STUDY OF LIGHT NUCLEI (ANTINUCLEI) PRODUCTION AND PHOTON MULTIPLICITY DETECTOR IN ALICE AT THE LHC

A THESIS

submitted to the

FACULTY OF SCIENCE

PANJAB UNIVERSITY, CHANDIGARH

for the degree of

DOCTOR OF PHILOSOPHY

2011

NATASHA SHARMA

DEPARTMENT OF PHYSICS

CENTRE OF ADVANCED STUDY IN PHYSICS

PANJAB UNIVERSITY, CHANDIGARH, INDIA

Dedicated

to

The Almighty God

and

My Beloved Family

Acknowledgements

First and foremost I would like to thank God, who gave me strength and courage to pursue my dreams and complete this thesis work.

My deepest gratitude to Prof. M. M. Aggarwal, my supervisor, for his encouragement, tremendous support and guidance during my research work. I am very thankful to him as because of him I was able to work in such a wonderful experiment and could learn a lot about different exciting physics topics related to this field. I would like to specially thank Prof. A. K. Bhati for his unconditional support and help both academically and non-academically during my research work.

It is my pleasure to have been associated with Department of Physics, Panjab University, Chandigarh. I would like to thank Prof. C. S. Aulakh, Chairperson, Department of Physics, Panjab University, Chandigarh, for providing me various opportunities during my research. I would also like to thank Prof. R. C. Sobti, Vice-Chancellor, Panjab University, Chandigarh, for providing support during my research work.

I would like to express my sincere and heartfelt thanks to Prof. Helmut Oeschler, Technische Universität, Darmstadt, Germany. I have greatly benefited from his deep knowledge and practical experiences in high energy physics. His help, support, guidance, and motivation helped me a lot during my research career. I cherish the discussions I had with him and deeply acknowledge him for keeping me motivated to study heavy-ion physics. It is a real pleasure to have worked with such a wonderful physicist and a very nice person. This thesis would not have been possible without the essential and gracious support of Dr. Jean-Pierre Revol. The constant discussions with him guided me to have better understanding of the subject.

I would like to take this opportunity to express my sincere thanks to the ALICE experiment colleagues at CERN. I would like to thank Dr. Paolo Giubellino (ALICE spokesperson) who always has been approachable for any discussions and help. I am thankful to Dr. Jurgen Schukraft (ex-ALICE spokesperson), Dr. K. Safarik, and Dr. A. Morsch for some really nice physics discussions and help during my stay at CERN. Dr. Yves Schutz has been very supportive for my work. Special thanks goes to L. Betev for

from so many experts in various areas in PMD group while at VECC. These include Dr. A. Dubey, Dr. P Ghosh, Mr. G. S. N. Murthy, Mr. M. R. Dutta Majumdar, Mr. S. Pal, Mr. R. N. Singaraju, I would like to express my humble thanks to Prof. B. Sinha, the ex-Director of VECC, for his unconditional support to the research and scholars coming to work in VECC.

It was a very nice experience to work in a team effort in the PMD group. I would like to thank our PMD collaborators with whom I was involved in many projects and discussions. These include Prof. S. Raniwala and his group at University of Rajasthan, Jaipur; Prof. (Ms.) A. Bhasin and her group at University of Jammu, Jammu; Prof. D. P. Mahapatra and his group at Institute of Physics, Bhubaneswar, Orissa; Prof. R. Varma and his group at Indian Institute of Technology Bombay, Mumbai.

I would like to acknowledge the support and encouragement of PMD research scholars during my research work. These include Dr. N. K. Pruthi, Dr. S. K. Prasad, Dr. M. M. Mondal, Dr. A. K. Dash, Dr. S. Sharma.

I am very thankful to the research scholars within the Chandigarh group for their cordial and co-operative attitude throughout my stay at Chandigarh.

My research work would not have been possible without the technical support provided by Mr. Dinesh Kumar Gupta, Mr. Satish Sharma, Mr. Ajit Singh and all the members of purchase section in the Department of Physics, Panjab University, Chandigarh. I am very thankful to them for their help and support.

I would like to express my heartiest thanks to my friends Ms. Phanouria Antoniou, Ms. Miriam Fitterer, Ms. Rajbir Kaur, Ms. Payal Mohanty, Mr. Kapil Kaushik, Mr. Sudeep Jain and Dr. Vishal Bhardwaj. They were always there whenever I needed them. They always encouraged me, and believed in me and my capabilities. I will always remember the days I spent with these guys no matter wherever I go.

I would like to take this opportunity to express my humble thanks to all those who have contributed in some way or the other in my thesis completion. Here I could list only few names but of-course there are many more who have contributed and helped me till now and will continue to do so. I would like to thank all those my well wishers here.

I would like to gratefully acknowledge the financial support from the Department of

Date: (Natasha Sharma)

Abstract

The primary goal of the heavy-ion program at the Large Hadron Collider (LHC) at CERN, Geneva, Switzerland is to search for the possible formation of Quark-Gluon Plasma. It also aims to understand the production mechanism of matter and antimatter in a collision.

The details of the ALICE detector and its subsystems are presented in this thesis. The details of the fabrication, electronics, readout and installation of the PMD (Photon Multiplicity Detector) in the ALICE experiment are also presented. The PMD detector measures the photons in the $2.3 < \eta < 3.7$ region. The software details including the reconstruction chain are also discussed. The detailed study of efficiency and purity calculation for the PMD detector using the embedding technique are also presented for pp and Pb-Pb collisions.

The detailed study of nuclei and anti-nuclei production using the statistical-thermal model (THERMUS) is discussed. Their ratios are compared with the existing experimental data and predictions are made for pp and heavy-ion collisions at RHIC and LHC energies.

The first measurements of nuclei and anti-nuclei like d ($\bar{\mathrm{d}}$), t ($\bar{\mathrm{t}}$) and ^{3}He ($^3\overline{\mathrm{He}}$) production in the ALICE experiment for pp and Pb-Pb collisions at $\sqrt{s} = 7$ TeV and $\sqrt{s_{NN}} = 2.76$ TeV respectively, are shown. The final spectra for nuclei are obtained and the particle ratios are compared with the statistical-thermal model predictions. The dependence of nuclei ratio on the chemical freeze-out temperature is also investigated. The year 2011 is marked with the discovery of anti-alpha by the STAR and ALICE experiments. The data analysis for the observation of anti-alpha ($^4\overline{\mathrm{He}}$) in Pb-Pb collisions at $\sqrt{s_{NN}} = 2.76$ TeV by the ALICE experiment is presented in this thesis.

List of Publications

1. **Investigation of high p_t events in Nucleus-Nucleus collisions using the Hijing event generator**,

   Natasha Sharma and Madan M. Aggarwal ,

   Indian J. Phys. **85**, 971 (2011).

2. **Antimatter production in proton-proton and heavy-ion collisions at ultrarelativistic energies**,

   J. Cleymans, S. Kabana, I. Kraus, H. Oeschler, K. Redlich, and N. Sharma,

   Accepted in Phys. Rev. C, arXiv:1105.3719 [hep-ph].

3. **Particle Production in p-p and Heavy Ion Collisions at Ultrarelativistic Energies**,

   J. Cleymans, S. Kabana, I. Kraus, H. Oeschler, K. Redlich, and N. Sharma,

   PoS KRUGER 2010 **043** (2011), arXiv:1107.0450 [hep-ph].

4. **Production of nuclei and antinuclei in pp and Pb-Pb collisions with ALICE at the LHC**,

   N. Sharma, for the ALICE Collaboration,

   Accepted in J. Phys. G, arXiv:1109.4836 [nucl-ex].

5. **Production of antinuclei in pp collisions at $\sqrt{s} = 7$ TeV with ALICE at the LHC**,

   N. Sharma, for the ALICE Collaboration,

   arXiv:1104.3311 [nucl-ex].

6. **Rapidity and transverse momentum dependence of inclusive J/psi production in pp collisions at $\sqrt{s}$= 7 TeV**,

   K. Aamodt *et al.* (ALICE Collaboration),

   Phys. Lett. B **704**, 442 (2011).

7. **Centrality dependence of the charged-particle multiplicity density at mid-rapidity in Pb-Pb collisions at $\sqrt{s_{NN}} = 2.76$ TeV**,

   K. Aamodt *et al.* (ALICE Collaboration),

   Phys. Rev. Lett. **106**, 032301 (2011).

8. **Production of pions, kaons and protons in pp collisions at $\sqrt{s} = 900$ GeV with ALICE at the LHC.**,

   K. Aamodt *et al.* (ALICE Collaboration),

   Eur. Phys. J. **C71**, 1655 (2011).

9. **Two-pion Bose-Einstein correlations in central Pb-Pb collisions at $\sqrt{s_{NN}} = 2.76$ TeV**,

   K. Aamodt *et al.* (ALICE Collaboration),

   Phys. Lett. B **696**, 328 (2011).

10. **Charged-particle multiplicity density at mid-rapidity in central Pb-Pb collisions at $\sqrt{s_{NN}} = 2.76$ TeV**,

    K. Aamodt *et al.* (ALICE Collaboration),

    Phys. Rev. Lett. **105**, 252301 (2010).

11. **Elliptic flow of charged particles in Pb-Pb collisions at 2.76 TeV**,

    K. Aamodt *et al.* (ALICE Collaboration),

    Phys. Rev. Lett. **105**, 252302 (2010).

12. **Transverse momentum spectra of charged particles in proton-proton collisions at $\sqrt{s} = 900$ GeV with ALICE at the LHC.**,

    K. Aamodt *et al.* (ALICE Collaboration),

    Phys. Lett. B **693**, 53 (2010).

13. **Midrapidity antiproton-to-proton ratio in pp collisions at $\sqrt{s} = 0.9$ and 7 TeV measured by the ALICE experiment**,

    K. Aamodt *et al.* (ALICE Collaboration),

    Phys. Rev. Lett. **105**, 072002 (2010).

14. **Charged-particle multiplicity measurement in proton-proton collisions at $\sqrt{s} = 0.9$ and 2.36 TeV with ALICE at LHC**,

    K. Aamodt *et al.* (ALICE Collaboration),

    Eur. Phys. J. **C68**, 89 (2010).

15. **First proton-proton collisions at the LHC as observed with the ALICE detector: Measurement of the charged particle pseudorapidity density at $\sqrt{s} = 900$ GeV**,

    K. Aamodt *et al.* (ALICE Collaboration),

    Eur. Phys. J. **C65**, 111 (2010).

16. **Two-pion Bose-Einstein correlations in pp collisions at $\sqrt{s} = 900$ GeV**,

    K. Aamodt *et al.* (ALICE Collaboration),

    Phys. Rev. D **82**, 052001 (2010).

Contents

List of Figures

List of Tables

Chapter 1

INTRODUCTION

The high energy heavy-ion collision experiments aim to study the fundamental constituents of matter or radiation and their interactions with each other. The matter is made up of molecules which are composed of atoms. The atoms contains protons and neutrons confined in nucleus and electrons revolving around it. The neutrons and protons are also not the fundamental particles and are bound states of quarks and gluons, collectively called as *partons* [1, 2]. Quarks are not observed as free particles and are confined in hadrons by the inter quark potential. Baryons are made up of three quarks (qqq) and mesons consist of a quark-antiquark pair ($q\bar{q}$). The deep-inelastic electron scattering experiments [3] showed that constituent quarks have fractional electric charges, $+2/3$ or $-1/3$, and carry effective mass (m^*) of about one third of the nucleon mass and only half of the nucleon's momentum. It was proposed that the other half of the nucleon's momentum is ascribed to the force carriers called as *gluons* which are responsible for the inter quark binding.

The discovery of Δ^{++} (uuu), Δ^{-} (ddd) and Ω^{-} (sss), particles lead to the new quantum number called the color quantum number [4, 5] for quarks so that the Pauli exclusion principle is not violated. The quark colors have nothing to do with the visible colors, they are only the quantum numbers. The quark color charge is denoted by red, blue, and green with the corresponding anti-colors antired, antiblue and antigreen. Since baryons and mesons are color neutral, the color charge combination forming a baryon or meson must sum to zero. Therefore, baryons consist of red, blue and green color charges having overall color charge zero. Similarly, anti-baryons have antired, antiblue

1

and antigreen color charges. Mesons have red-antired or blue-antiblue or green-antigreen
color charges combination.

1.1   The Quark-Gluon Plasma and the QCD

It is believed that the universe originated from a "Big-Bang" and after the few microsec-
onds of the Big-Bang, the quarks and gluons existed in the free state or de-confined
state [6]. This state of matter is also known as Quark-Gluon Plasma (QGP). De-
confinement or the formation of QGP can also be achieved in the laboratory. It can
be possible in two cases: either at very high energies where the partons effective color
charge approaches zero (asymptotic freedom), or at very high density where the hadronic
wave functions overlap delocalising the partons (Debye screening). Experiments such as
Relativistic Heavy Ion Collider (RHIC) at Brookhaven National Laboratory and A Large
Ion Collider Experiment (ALICE) at LHC (Large Hadron Collider) at CERN are the
facilities which work on the principle of creating QGP by increasing the center of mass
energy ($\sqrt{s_{NN}}$) to a high value. Maximum center of mass energy that can be achieved for
heavy-ion collisions at RHIC is $\sqrt{s_{NN}} = 200$ GeV and that at ALICE can be 5.5 TeV.
In addition to heavy ions, nucleon-nucleon e.g. pp collisions are also performed in these
experiments. The pp collisions are useful for the reference studies to compare with those
of heavy ions. Compressed Baryonic Matter (CBM) at FAIR (Facility for Antiproton and
Ion Research) in Germany will exploit the baryon density rich region for its physics pro-
grams [7]. The major goals of the CBM experiment include determination of the nuclear
equation of state at high baryon density, search for the existence of the first order phase
transition from hadronic to partonic matter and the location of the critical point in the
phase diagram. The CBM experiment will be the fixed target experiment in contrast to
collider experiments at RHIC and LHC. The results presented in this thesis are obtained
by analyzing the data recorded by the ALICE Experiment at the LHC.

     The theory which describes the interaction of color charges of quarks and gluons
is called *Quantum Chromodynamics* (*QCD*). The main goals of lattice QCD are to
calculate the masses and decay properties of the hadrons. Its another major goal is to
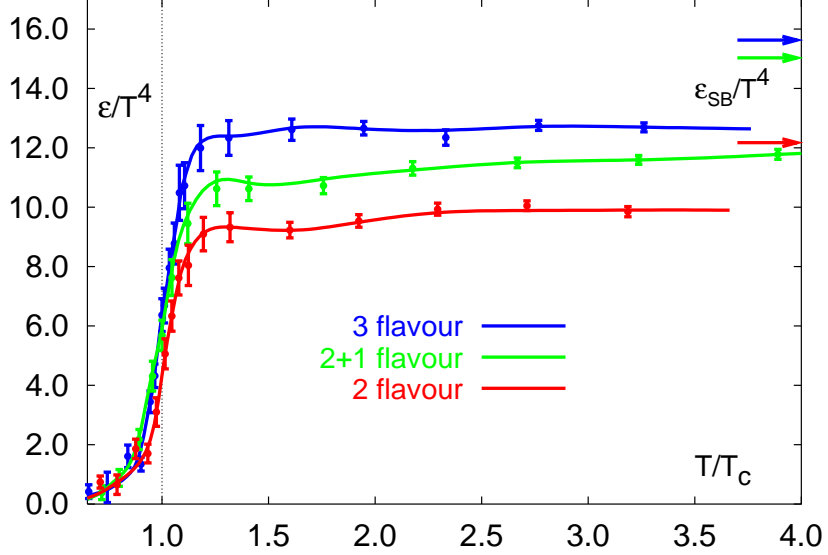
Figure 1.1: Energy density as a function of temperature as per the lattice QCD calculations [8].

determine the properties of QGP, which is assumed to be formed just after the collision of two high energy heavy-ion nuclei.

Figure 1.1 shows the equation of state (energy density versus temperature) from the lattice QCD calculations [8]. Here, ϵ/T^4 is plotted as a function of T/T_c, where T_c represents the critical temperature. These calculations are performed for non-zero temperatures and non-zero chemical potentials. The ϵ/T^4 is proportional to the number of degrees of freedom. The significant increase of ϵ/T^4 around critical temperature indicates the increase in the number of degrees of freedom, showing the quarks and gluons become the relevant degrees of freedom. The arrows indicate the Stefan-Boltzmann limit:

$$\epsilon = g\frac{\pi^2}{30}T^4,\tag{1.1}$$

where g is the number of degrees of freedom. For a hadron gas, the number of degrees of freedom are given by the three pion states (π^+, π^-, π^0), so $g = 3$ for this case:

$$\epsilon = 3\frac{\pi^2}{30}T^4,\tag{1.2}$$

In the QGP phase, the relative number of degrees of freedom are the quarks and gluons.
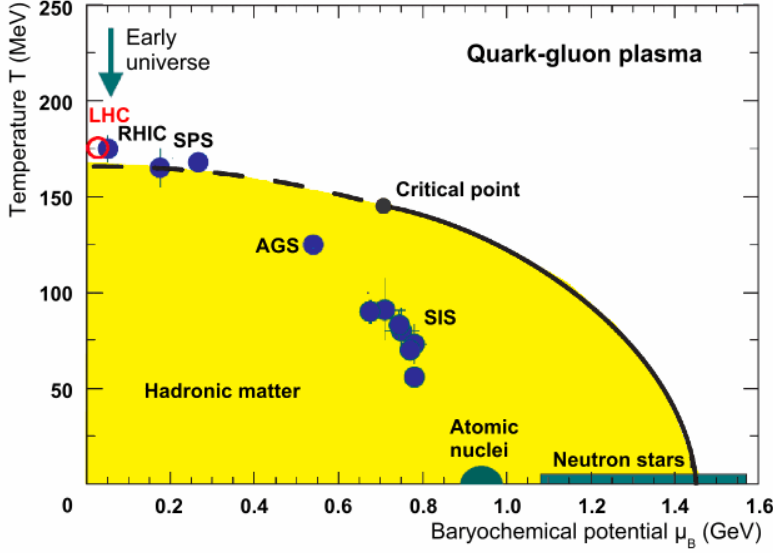
Figure 1.2: Schematic view of the QCD phase diagram shown in $T - \mu_B$ space. Also shown are the hadronization (chemical freeze-out) points measured by various experiments.

This number is much larger in case of QGP as compared to hadron gas phase:

$$\epsilon_{\text{QGP}} = \left(16 + \frac{21}{2} n_{flavor} \right) \frac{\pi^2}{30} T^4. \tag{1.3}$$

The critical temperature depends on the number of flavors and the mass of quarks. The blue curve in the Fig. 1.1 shows the expectation for the three light quark flavors, the red curve shows the two light quarks calculation. The green curve shows the more realistic calculation with two light quarks (u, d) and a heavy quark (s).

Figure 1.2 shows the phase diagram with the regions of hadronic matter and of the QGP. Chemical freeze-out points measured by various experiments are also shown as the solid circles. The existence and position of the critical point as well as the nature of the phase transition are only indicative and still under intensive study and discussion. Lattice QCD calculations predict the crossover from hadronic phase to the QGP for $\mu_B \sim 0$ at approximately 150 MeV [9] to 190 MeV [10]. The energy range of the ALICE experiment corresponds to $\mu_B \sim 0$ and is suitable for studying the properties of QGP and transition from hadrons to QGP phase.

1.2 Space-Time Evolution

The QGP is expected to have existed shortly after the Big-Bang. Currently, it may exist in the very dense cores of neutron stars [11]. In the high energy heavy-ion collision experiments, two nuclei are accelerated to a very high energy and made to collide with each other with velocities close to the speed of light. As a result, these nuclei, which are spherical in shape are Lorentz contracted along the direction of motion (beam direction or z-axis by convention). When the two nuclei collide, there is an overlap region depending upon the impact parameter. The nucleons which are in this overlap region are called *participants* and those which do not participate are called *spectators*.

Figure 1.3 shows the space-time evolution of the matter created in the heavy-ion collisions. One of the important requirement in creating the QGP phase in high energy nucleus-nucleus collisions is to achieve sufficient energy density. Consider the head-on collision of two Lorentz contracted (in the longitudinal direction) similar nuclei in the centre-of-mass frame at very high energy. The projectile nucleus A and the target nucleus B come from $z = -\infty$ and $+\infty$, respectively, at a speed closer to the speed of light and undergo collision at z=0 and at time t=0. The baryons lose energy and momentum and get slowed-down after the collision. At very high energies, the slowed-down baryons can still have enough momentum to proceed forward, and move away from the collision region. The energy lost by the baryons is deposited in the collision region around $z = 0$. As the colliding nuclear matter recede away from each other after the collision, a large amount of energy is deposited in a small region of space in a short duration of time. This energy density might be sufficiently high to create QGP.

The plasma initially may not be in the thermal equilibrium, but subsequently equilibration may bring it to local thermal equilibrium at the proper time τ_0, and the plasma may then evolve according to the laws of hydrodynamics thereafter. As the plasma expands, it cools down and the hadronization of plasma will take place at a later proper time. The hadrons will stream out of the collision region when the temperature falls below the freeze-out temperature.

The particles coming out from the collision region are then measured in the experi-
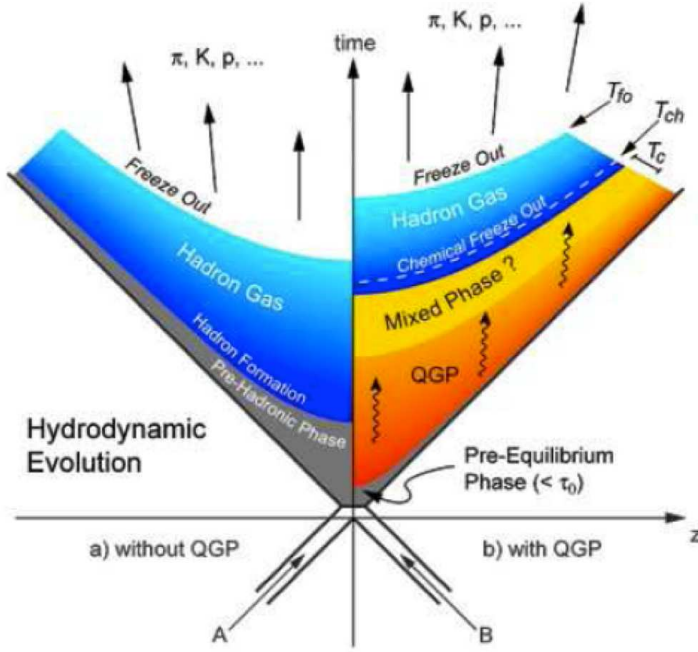
Figure 1.3: Schematic view of the QCD phase diagram shown in $T-\mu_B$ space. Also shown are the hadronization (chemical freeze-out) points measured by various experiments.

ment and they provide only indirect evidence for the QGP. These signatures may already have been distorted by interactions during and after the freeze-out. Thus, a QGP phase cannot be detected directly in a high energy physics experiment. Instead a set of signatures provide evidence. The main signatures of QGP formation are discussed briefly in the following subsections.

1.2.1 Quarkonia Yields

Quarkonia (J/Ψ, Ψ', Υ, Υ', Υ'') particles are made up of quark and anti-quark pairs like $c\bar{c}$ and $b\bar{b}$. These particles are created in the initial phase of the collision. In a quark-gluon plasma phase, the color charge of a quark is subject to screening due to the presence of quarks and gluons in the plasma, which weaken the interaction between quark and anti-quark pairs. This is called the *Debye screening*. Color screening in the de-confined phase leads to melting of quarkonia states (particles) [12, 13]. The freed c and b quarks are unlikely to recombine with anti-quarks to form quarkonia during freeze-out if their concentrations are small. In this case, the quarkonia yield in the presence of a

QGP compared to pp collisions should be suppressed with a characteristic dependence on the size of the specific quarkonium. This is called *quarkonia suppression*. Thus, the suppression of quarkonia particle in heavy-ion collisions, compared to pp collisions may be used as signature of the quark-gluon plasma formation [14]. The quarkonia suppression has been observed at the SPS [15]. Statistical hadronization assesses the probability for recombination into $c\bar{c}$ and $b\bar{b}$ pairs (so-called *quarkonia regeneration*) [16]. At much higher energies c and b quarks are produced in large abundances and statistical hadronization may even lead to enhanced quarkonia production at freeze-out.

1.2.2 Azimuthal Anisotropy

The particles in the overlap region for the non-central collisions in the relativistic heavy-ion collisions are subjected to the spatial anisotropy. This is because of the almond-shape of the overlap region formed after the collision. The particles which are along the short axis are subject to the more pressure gradient as compared to those along the long axis. As a result, the initial spatial anisotropy is converted into the anisotropy in the momentum space. This momentum anisotropy will reflect the time evolution of pressure gradients generated in the system at very early time [17, 18].

1.2.2.1 Directed Flow

Directed flow (v_1) describes collective side-ward motion of the produced particles and nuclear fragments. It carries the information of the very early stages of the collision [19]. A first order phase transition is associated with the presence of 'softest point' in the equation of state (EOS) and in the transition region, the tendency of matter to expand is reduced [20, 21]. It was proposed that the softening of equation of state can be deduced experimentally by observing a minimum in the directed flow as a function of beam energy [22, 23]. It was also suggested that the softening of EOS, which shows a distinct flow pattern, is due to the possible formation of QGP [24]. Also the hydrodynamic calculations assuming QGP show that the directed flow when plotted as a function of rapidity, crosses zero three times around mid-rapidity, displaying a *wiggle* shape which is predicted to occur in the close-to-central collisions. However, it was shown that wiggle shape can

also be produced by models which do not include QGP formation [25] .

1.2.2.2   Elliptic Flow

Elliptic flow (v_2) measurements carry the information from the partonic and hadronic level of the collision [26] as it is expected to develop early in the collision and survives the hadronization. Elliptic flow is "self-quenching" [19, 27], and any flow anisotropy measured in the final state must have been generated early when the collision fireball was still spatially deformed.
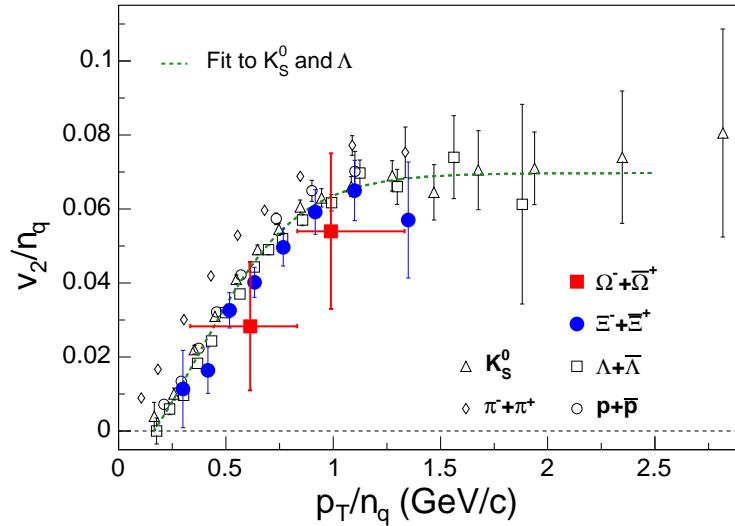
Figure 1.4: v_2 scaled by number of quarks (n_q) as a function of p_t scaled by n_q for various particles measured in the STAR experiment [28].

Elliptic flow results from the STAR show that the elliptic flow as a function of p_t follow distinct curves for mesons and baryons [28, 29]. STAR also reported a non-zero elliptic flow for strange baryons (Ω, Ξ, Λ) and mesons (K_S^0) [28, 29]. In this scenario, where multi-strange baryons are less affected by the hadronic stage [30] and where v_2 develops primarily at the early stage of the collision [27, 31], the large v_2 of multi-strange baryons shows that the partonic collectivity is generated at RHIC.

Figure 1.4 shows very interesting result for elliptic flow which is called the constituent quark scaling. In this figure, n_q-scaled v_2 is plotted as a function of n_q-scaled p_t for π, K_S^0, p, Λ, Ξ, and Ω. We observe that all hadrons except for pions, fall on a common curve.

This suggests that partonic degrees of freedom are the constituent quarks. In addition, the good agreement for $p(uud)$, $\Lambda(uds)$, $\Xi(dss)$, and $\Omega(sss)$ suggests that s quark flows similarly to u, d quarks.
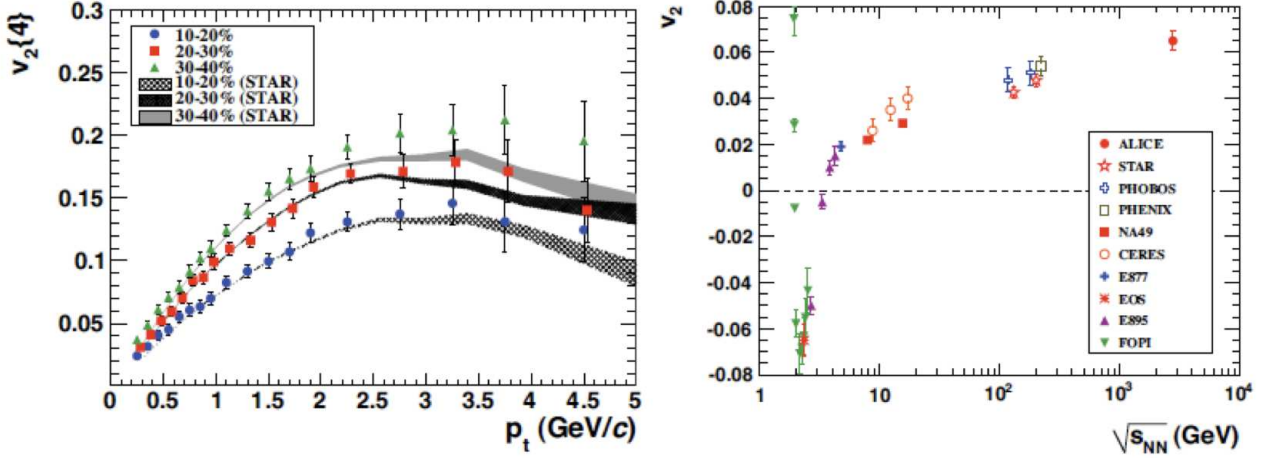
Figure 1.5: Left: $v_2\{4\}(p_t)$ for various centralities compared to STAR measurements. Right: Integrated elliptic flow at 2.76 TeV in Pb-Pb 20-30% centrality class compared with results from lower energies taken at similar centralities [32].

Figure 1.5 (left) presents $v_2(p_t)$ obtained with the 4-particle cumulant method for three different centralities by the ALICE for Pb-Pb collisions at $\sqrt{s_{NN}} = 2.76$ TeV [32]. The results are compared to STAR measurements at RHIC. The transverse momentum dependence is qualitatively similar for all three centrality classes. The observed similarity at RHIC and the LHC of the p_t-differential elliptic flow at low p_t is consistent with predictions of hydrodynamic models [33]. The integrated elliptic flow measured in the 20-30% centrality class is compared to results from lower energies in Fig. 1.5 (right). The figure shows that there is a continuous increase in the magnitude of the elliptic flow for this centrality region from RHIC to LHC energies. We find that the integrated elliptic flow increases by about 30% from $\sqrt{s_{NN}} = 200$ GeV at RHIC to 2.76 TeV at LHC [34–36].

1.2.3 Strangeness Enhancement

The strangeness enhancement is studied through the strangeness enhancement factor. It is defined as the yield per participating nucleon of a given type of strange particle in the

heavy-ion collisions (e.g. Au-Au or Pb-Pb collisions) relative to strange particle yield in a light reference system collisions (e.g. pp or p$\bar{\text{p}}$ collisions). The strangeness content in hadronic matter and quark-gluon plasma are different. The s and $\bar{s}$ quarks are enhanced in quark-gluon plasma in chemical and thermal equilibrium [37]. As, in QGP scenario, quarks and gluons are produced in abundance. The two possible main production channels for $s\bar{s}$ pairs are $q\bar{q} \rightarrow s\bar{s}$ and $gg \rightarrow s\bar{s}$.
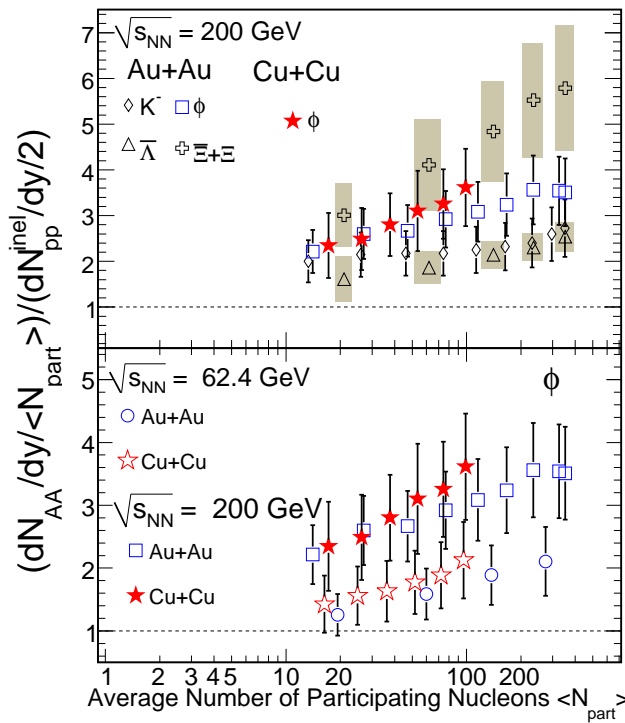
Figure 1.6: Upper panel: The ratio of the yields of K, ϕ, $\bar{\Lambda}$ and $\Xi + \bar{\Xi}$ normalized to $\langle N_{\text{part}} \rangle$ in Au-Au and Cu-Cu collisions to corresponding yields in inelastic pp collisions at 200 GeV. Lower panel: Same as above for only ϕ mesons at 200 and 62.4 GeV. The error bars represent the statistical and systematic errors added in quadrature.

Figure 1.6 shows the strangeness enhancement as a function of average number of participating nucleons ($\langle N_{\text{part}} \rangle$) for K, ϕ, $\bar{\Lambda}$ and $\Xi + \bar{\Xi}$ for Au-Au and Cu-Cu collisions relative to pp collisions at 200 and 62.4 GeV in STAR experiment [38].

1.2.4   Direct Photons

Direct photons are created in the thermally equilibrated quark-gluon plasma through the channels: $q\bar{q} \to \gamma g$, $gq \to \gamma q$ and $g\bar{q} \to \gamma\bar{q}$. They are supposed to carry information about the early stages of the relativistic heavy-ion collisions.

It is known that the photons interact with the particles through the electromagnetic interaction. When photons are produced in the quark-gluon plasma region, they do not participate much in the strong interactions with the quarks and gluons. Consequently, their mean-free path is quite large and they may not suffer a collision after they are produced. As a result, they would keep the memory of the temperature at which they were produced. In this way, they may provide the information about the quark-gluon plasma created in the early stages of collisions and hence can serve as a signal of the QGP [39].
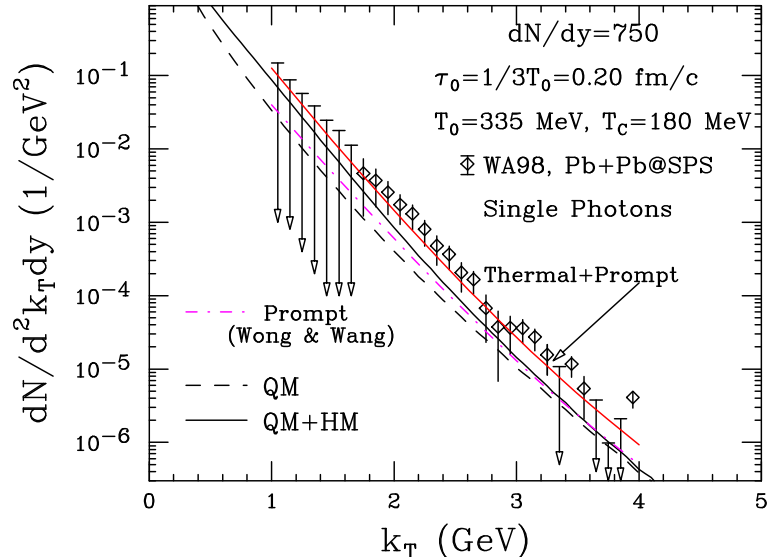
Figure 1.7: The invariant direct photon multiplicity for central Pb-Pb collisions at $\sqrt{s_{NN}} = 17.3$ GeV [40]. The model calculations [41] are shown in the form of lines.

Direct photons have been measured in the WA98 experiment at SPS at $\sqrt{s_{NN}} = 17.3$ GeV [40]. Figure 1.7 shows the invariant direct photon multiplicity for central Pb-Pb collisions at $\sqrt{s_{NN}} = 17.3$ GeV [40]. The figure also shows the model calculations [41] with the assumption that a chemically and thermally equilibrated quark-gluon plasma is formed at $\tau_0 = 1/3T_0$. The QGP is assumed to expand, cool, enter into a mixed phase

and attain freeze-out from a hadronic phase. QM represents the radiations from quark matter in the QGP and mixed phase. HM represents the radiations from the hadronic matter in the mixed and hadronic phase. T_0 is the initial temperature of the system and τ_0 is the initial time.

1.2.5   Jet Quenching

It was proposed that the energy loss of partons in QGP is much higher than that in hadronic matter [42]. Highly energetic partons when propagating through a dense medium lose energy via the two phenomena - collisional energy loss due to elastic scattering, and multiple scattering and induced gluon radiation [43]. This phenomenon leads to the *jet quenching* [44, 45], which is defined as the suppression of high p_t hadron yields in nucleus-nucleus (e.g. Au-Au or Pb-Pb) collisions relative to that in a pp collisions scaled by the number of elementary nucleon-nucleon collisions. The observable used to measure such an effect is called the Nuclear Modification Factor (R_{AA}) and is defined as -

$$R_{AA} = \frac{d^2 N^{AA}/dp_T d\eta}{T_{AA} d^2 \sigma^{NN}/dp_T d\eta} \tag{1.4}$$

where $T_{AA} = \langle N_{\mathrm{bin}} \rangle / \sigma_{\mathrm{inel}}^{NN}$ from a Glauber calculation accounts for the nuclear collision geometry.

Figure 1.8 shows the nuclear modification factor R_{AA} of charged hadrons for central Pb-Pb collisions, compared to that from the PHENIX and STAR experiments at RHIC. In central collisions at the LHC, R_{AA} exhibits a very strong suppression, reaching a minimum of ≈ 0.14 at $p_t = $ 6-7 GeV/c. Despite the much flatter p_t spectrum in pp at the LHC, the nuclear modification factor at $p_t = $ 6-7 GeV/c is smaller than at RHIC. This suggests an enhanced energy loss at LHC and therefore a denser medium. A significant rise by about a factor of two is observed for $7 < p_t < 20$ GeV/c. This pattern is very intriguing, because it suggests that very high momentum partons may lose only a small fraction of their energy in the medium and, thus, be sensitive probes of its properties.

Figure 1.9 shows the jet azimuthal correlations in Au-Au, d-Au and pp collisions at $\sqrt{s_{NN}} = 200$ GeV, as measured by STAR experiment [47]. The upper panel (a) shows the distributions for central and minimum bias d-Au collisions, and the lower panel (b) shows
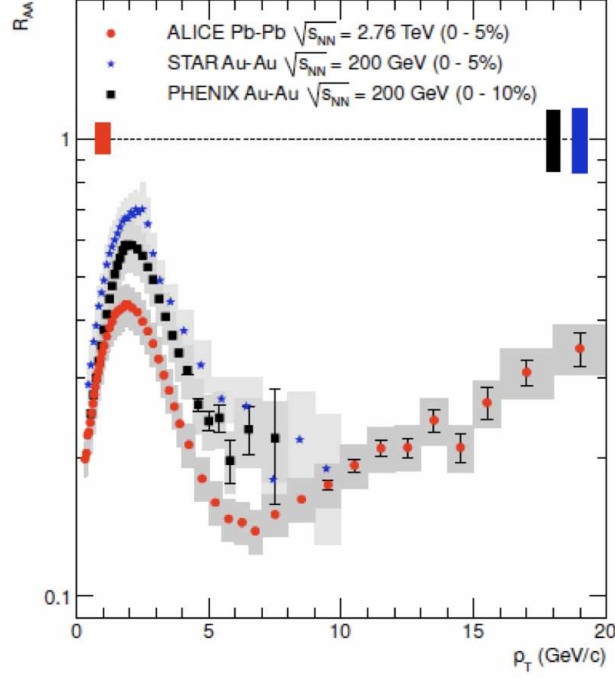
Figure 1.8: Nuclear modification factor R_{AA} for charged hadrons in central Pb-Pb collisions at the LHC, compared to measurements at $\sqrt{s_{NN}} = 200$ GeV by the PHENIX and STAR experiments [46].
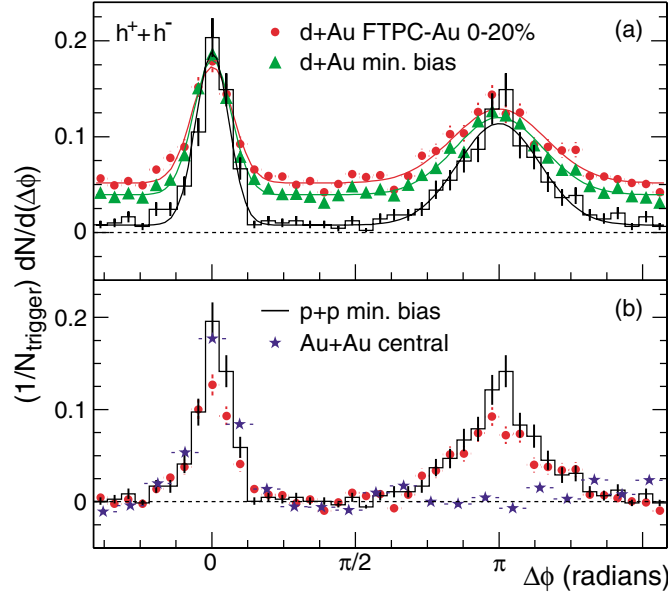
Figure 1.9: Jet azimuthal correlations for Au-Au, d-Au and pp collisions at $\sqrt{s_{NN}} = 200$ GeV measured in the STAR experiment [47].

these distributions for the central Au-Au and minimum bias pp collisions. In central Au-Au collisions, it is found that the away side correlations are totally quenched, whereas large away side correlations exist for d-Au and pp collisions. These measurements indicate that the medium created in central Au-Au collisions causes a strong suppression effect on the away side correlation. The suppression of away side correlations is simply due to the fact that particles emitted on the away sides always need to travel a longer distance through the medium compared to the same side particles. Such a geometry effect is confirmed by measuring the difference in suppression between particles close to the reaction plane (in plane) and perpendicular to the reaction plane (out of plane) [48]. The suppression at high p_t suggests that it is a final state effect and is due to the medium induced energy loss. However, it was also shown that if the p_t thresholds of the triggered and associated particles are increased, away-side partner fragmenting as in vacuum can be recovered [49].

1.3   Photon Multiplicity Measurements

Measurement of particle multiplicity provides information on particle production mechanisms in heavy-ion collisions [50]. The event-by-event fluctuations in the multiplicity of produced particles within a thermodynamic picture could be related to matter compressibility [51]. The event-by-event correlation between photon and charged particle multiplicities can be used to test the predictions of formation of disoriented chiral condensates [52]. The variation of particle density in pseudo-rapidity (η) with collision centrality can shed light on the relative contribution of soft and hard (perturbative QCD jets) processes in particle production [53]. Multiplicity measurements can provide tests of ideas on initial conditions in heavy-ion collisions based on parton saturation [54] and color glass condensates [55]. Under certain model assumptions, the particle density in pseudo-rapidity can provide information on the initial temperature and velocity of sound in the medium [56]. The pseudo-rapidity distributions are found to be sensitive to the effects of re-scattering, hadronic final-state interactions, and longitudinal flow [57].

Photon multiplicity is measured using the Photon Multiplicity Detector (PMD) [58]. The details about PMD hardware, testing and simulation form the major part of this thesis

and discussed in the later chapters. Photon multiplicity and pseudo-rapidity distributions have been obtained previously in experiments e.g. at CERN at SPS and at STAR experiment at RHIC. The PMD is also fabricated and installed for the ALICE experiment. Preliminary results of multiplicity measurements from the ALICE show that the system created at the LHC initially has much higher energy density and is at least 30% hotter than at RHIC, resulting in about double the particle multiplicity for each colliding nucleon pair [59]. In view of this, the photon multiplicity results from the ALICE-PMD will provide further understanding of the nucleus-nucleus collisions at very high energies of the order of TeV range.

The photon measurements using the PMD are useful to study various important physics goals of the high energy heavy-ion collision experiments as discussed below. PMD is helpful in the determination of reaction plane and probes of thermalization via studies of azimuthal anisotropy and flow. As we mentioned earlier, the flow measurements could provide a possible signature of the QGP. It is suggested that if flow occurs in the plasma state, then the subsequent hadronization may affect the kinematic quantities of different particle species differently. It is therefore desirable to measure the azimuthal anisotropy of different particle species in the final state. It is advantageous to study the event shapes with photons because their transverse distribution and that of the parent pions is not affected by the final-state Coulomb effects. Collective flow measurements at the SPS [60] and RHIC energies [61] have been studied using the photon measurements from PMD using the Fourier expansion technique.

It is proposed that the chiral symmetry is restored in the QGP scenario. After the initial stage of the collision, the system cools and expands leading to normal QCD vacuum in which the chiral symmetry is spontaneously broken. During this process, a metastable state may be formed in which the chiral condensate is disoriented from the true vacuum direction. This transient state would subsequently decay by emitting coherent pions within finite sub-volumes or domains of the collision region [62]. This possibility of formation of disoriented chiral condensate (DCC) would lead to a large imbalances in the production of charged and neutral pions. The primary signature of DCC is a large event-by-event fluctuation in photon to charged-particle multiplicity by measuring photons and

charged particles in a common coverage.
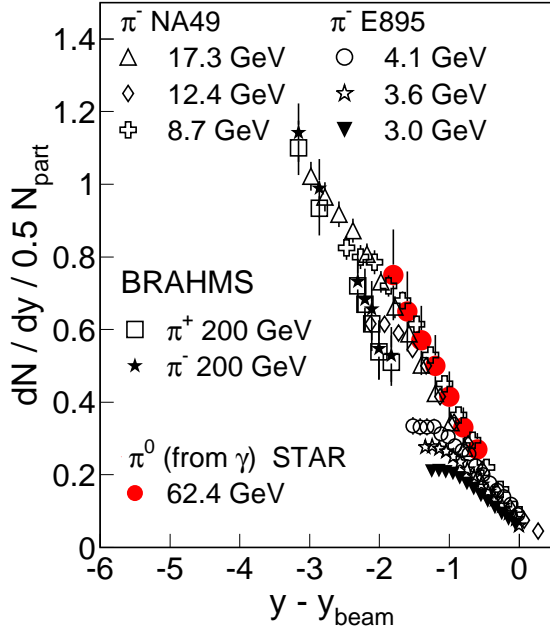
Figure 1.10: Estimated $\frac{dN_{\pi^0}}{dy}$ from $\frac{dN_\gamma}{dy}$ normalized to N_{part}, as compared to $\frac{dN_{\pi^\pm}}{dy}$ normalized to N_{part}, as a function of $y - y_{\text{beam}}$ for central collisions at various collision energies.

Several interesting features of the dependence of particle density in pseudo-rapidity have been observed in earlier measurements from the PMD [63]. Particle production is found to follow a unique, collision energy independent, longitudinal scaling [64] in pp and d-Au, as well as in heavy-ion collisions [65, 66]. Such longitudinal scaling is also found to be independent of collision centrality for photons [63, 67]. The total charged particle multiplicity (integrated over the full pseudo-rapidity range) per average number of participating nucleon ($\langle N_{\text{part}} \rangle$) pair is found to be independent of collision centrality [65]. However, at mid-rapidity ($|\eta| < 1$), charged particle multiplicity per $\langle N_{\text{part}} \rangle$ is observed to increase from peripheral to central collisions [65]. This clearly indicates that the mechanism of particle production could be different in different pseudo-rapidity regions. It will be interesting to see the similar measurements employing the ALICE-PMD at the LHC energies.

Figure 1.10 shows the charged pion rapidity density in Au-Au collisions at RHIC [68],

Pb-Pb collisions at the SPS [69], Au-Au collisions at AGS [70], and estimated π^0 rapidity density from the photon measurement (photon rapidity density) at $\sqrt{s_{NN}} = 62.4$ GeV, all as a function of $y - y_{\mathrm{beam}}$. HIJING calculations indicate that about 93-96% of photons are from π^0 decays. From HIJING, the ratio of photons to π^0 yields are obtained. This ratio is used to estimate the π^0 yield from the measured photon yield. The BRAHMS results at forward rapidities are slightly lower compared to the results from SPS energies. However, in general, the results show that pion production in heavy ion collisions in the fragmentation region agrees with the longitudinal scaling picture.

1.4 Freeze-Out Properties

The high energy heavy-ion collisions lead to a fireball in the collision region, which undergo expansion with time. The pressure generated in the fireball during the collision process boosts the produced particle away from the center of the collision. In this process, the particles interact among themselves elastically and in-elastically. This leads to the chemical and thermal equilibrium among the produced particles. Specifically these equilibria are called as "chemical and kinetic freeze-out" in heavy-ion collisions. Chemical freeze-out represents the point in time where inelastic processes that convert one kind of hadronic species into a different one, cease and the hadron abundances stop changing. The kinetic freeze-out defines the point in time where the momenta of the particles stop changing, i.e. where all types of momentum-changing collisions, elastic and inelastic cease.

The measured particle abundance ratios are fitted using the statistical or chemical equilibrium model [71–75]. The model assumes that the system is in thermal and chemical equilibrium at that stage. The model fit parameters are the chemical freeze-out temperature (T_{ch}), the baryon and strangeness chemical potentials (μ_B and μ_S), and the *ad hoc* strangeness suppression factor, γ_S.

The p_t spectra of the particles are well described by the hydrodynamics-motivated blast-wave model [18, 76–81]. The blast wave model makes the simple assumption that particles are locally thermalized at a kinetic freeze-out temperature and are moving with a common collective transverse radial flow velocity field. The common flow velocity field
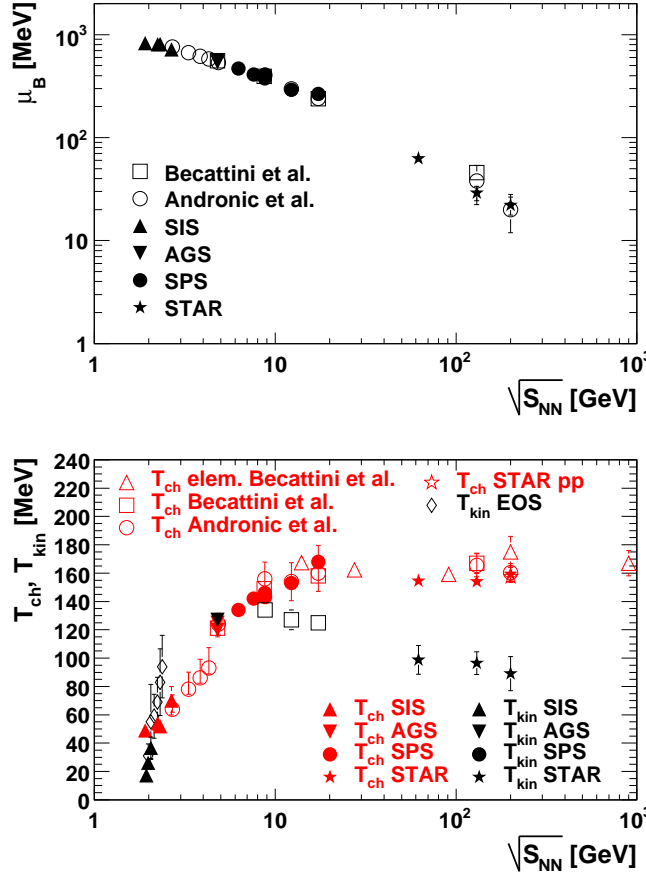
Figure 1.11: Top panel: Baryon chemical potential extracted for central heavy-ion colli-
sions as a function of the collision energy. Bottom panel: The extracted chemical (red
points) and kinetic (black points) freeze-out temperatures for central heavy-ion collisions
as a function of the collision energy. The figure is taken from the Ref. [82].

results in a larger transverse momentum of heavier particles, leading to the change in the

observed spectral shape with increasing particle mass. The measured spectra of all the

particle species are simultaneously fitted with blast wave model. The fit parameters are

the kinetic freeze-out temperature (T_{kin}), the average transverse flow velocity ($\langle \beta \rangle$) and

the exponent of the assumed flow velocity profile (n).

Figure 1.11 (top panel) shows the baryon chemical potential extracted from chem-

ical equilibrium model fits to central heavy-ion data at various energies. The extracted

μ_B falls monotonically from low to high energies. The low value of μ_B at mid-rapidity at

high energy is because fewer baryons can transport over the larger rapidity gap. Fig. 1.11

(bottom panel) shows the evolution of the extracted chemical and kinetic freeze-out temperatures as a function of the collision energy in central heavy-ion collisions. The extracted T_{ch} rapidly rises at SIS and AGS energy range, and saturates at SPS and RHIC energies. This suggests that the central heavy-ion collisions can be characterized by a unique, energy independent chemical freeze-out temperature. The value of T_{ch} at higher energies is close to the phase transition temperature predicted by Lattice QCD [83]. This suggests the collision system at high energies decouples chemically at the phase boundary. On the other hand, the extracted kinetic freeze-out temperature rises at SIS and AGS energies, and decreases at higher energies, especially at RHIC energies. At low energies, the extracted T_{kin} is similar to T_{ch}. This suggests that kinetic freeze-out happens relatively quickly after or concurrently with chemical freeze-out. As the collision energy increases, the two extracted temperatures begin to separate (around $\sqrt{s_{NN}} = 10$ GeV). The T_{ch} increases and T_{kin} decreases thereafter, suggesting that towards the higher energies, T_{kin} occurs long after the T_{ch}. This indicates that there is a longer time during which the particles scatter elastically, building up additional collective motion in the system while it undergoes further expansion and cooling.

1.5 (Anti) Nuclei Production Mechanisms

The major goal of this thesis is to study the production mechanism of the light (anti) nuclei. The light (anti) nuclei could be directly produced from the nucleus-nucleus collisions and then emitted from the thermal fireball formed during these collisions. This is called statistical-thermal approach [84]. However, the production of light nuclei and anti-nuclei can also be due to the coalescence of produced nucleons and anti-nucleons or participant nucleons. This is called the coalescence approach [85]. The results using these models are discussed in detail in chapter 5 of this thesis. In the following subsections, we will discuss about the details of these models.

1.5.1   Statistical Model

As discussed in the previous section, the hadron yields measured in the central heavy-ion collisions from AGS up to RHIC energies can be described very well [86–96] within a hadro-chemical equilibrium model or statistical model. We also observed in the previous section that the chemical freeze-out temperature increases sharply at low energies and then saturates at higher energies. This limiting temperature [97] behavior suggests a connection to the phase boundary and it was, argued [98] that quark-hadron phase transition drives the equilibration dynamically, at least for SPS energies and above. The importance of measurements at very high energies was felt to obtain the existence of a limiting temperature of the excited matter in the nuclear collisions [99–101]. Figure 1.12 shows the comparison of the yields of various particles at the top RHIC energy ($\sqrt{s_{NN}} = 200$ GeV) with statistical-thermal model. The model seems to explain the most of the yields reasonably well.
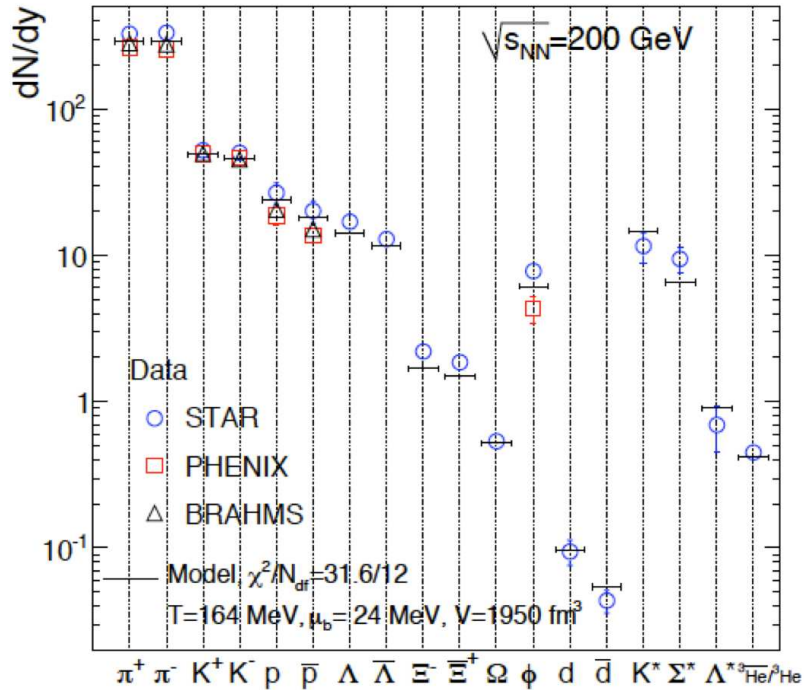
Figure 1.12: The thermal model fit to the yields of various particles at $\sqrt{s_{NN}} = 200$ GeV The figure is taken from the Ref. [102].

The thermal model also provided a good description of light nucleus production at AGS energies [103]. It is seen that yields obtained within thermal model are in close agreement to those obtained from the coalescence model [103, 104]. With the new measurements of nuclei and anti-nuclei (anti-hypertriton and anti-helium4) at RHIC and LHC, it is interesting to test the particle production at chemical equilibrium using thermal and coalescence models. At relatively low beam energies, where the baryon chemical potential and hence the baryon density is maximum, a large number of baryons and moderate strangeness may be abundantly produced. However, at RHIC and LHC energies, the production could lead to moderate (anti) baryons and large strangeness content.

The statistical models and their applications to the phenomenological description of particle production in nucleus nucleus collisions employ the conservation laws for different quantities [105–107]. The most recent software employing the statistical model approach is the THERMUS [75]. The results using the THERMUS package for pp, Au-Au and Pb-Pb collision systems at different center of mass energies are presented in details in chapter 5 of this thesis.

1.5.2   Coalescence Model

As mentioned before, the light nuclei and anti-nuclei in relativistic collisions can also be formed through coalescence of produced nucleons and anti-nucleons or participant nucleons. Since the binding energy is small, this formation process can only happen at the later stages of the evolution of the system when the interactions between nucleons and other particles are weak. This process is also known as final-state coalescence. The coalescence probability is related to the local nucleon density. Therefore, the production of light nuclei provide a tool to measure collective motion and freeze-out properties, such as particle density and correlation volume. In the most straight forward coalescence picture the ratios of different (anti)nuclei can be directly related to ratios of hadronic yields.

1.6   Matter and Anti-Matter Search

Along with the study of QGP formation, the heavy-ion experiments aim to study the production mechanism of matter and antimatter. The nucleus is made up of protons (p) and neutrons (n), and that of antimatter is composed of anti-protons ($\bar{p}$) and anti-neutrons ($\bar{n}$). It is believed that during the initial stage of the universe, matter and antimatter existed in equal abundance. It is still a mystery, how this symmetry got lost in the evolution of the universe with no significant amount of antimatter being present. The ultra-relativistic nuclear collisions could recreate energy density similar to that of the universe microseconds after the Big-Bang. One of the striking features of particle production at these high energies is the comparable abundance of matter and antimatter [108, 109]. These collisions generate hot and dense matter which contains equal number of quarks and anti-quarks (leading to matter and anti-matter production) and equal number of u, d and s quarks (ideal for hypernuclei and anti-hypernuclei production). Hypernuclei are nuclei which contain at least one hyperon in addition to nucleons.

In 1898, Franz Arthur Friedrich Schuster first thought of the concept of antimatter and published his ideas in *Nature* [110]. His hypothesis was given a mathematical foundation by the work of Paul Dirac in 1928. Till 2010, many antiparticles and anti-nuclei were discovered. Recently, STAR experiment at RHIC in BNL reported the first observation of anti-hypernuclei (anti-hypertritons) [111]. With the discovery of anti-nuclei, the plot of protons (Z) vs. neutrons (N) (Fig. 1.13) was extended to the negative axes. The discovery of hypernuclei had introduced the third axis to the plot for strangeness (S) and with the recent observation of anti-hypernuclei, the strangeness axis is also extrapolated to the negative direction as shown in the Fig. 1.13.

The study of (hyper)nuclei and anti (hyper)nuclei can also be useful in understanding the QGP properties. The hyperon-nucleon(Y-N) interaction is of great physical interest because it introduces a new quantum number strangeness in nuclear matter. It is predicted to be the decisive interaction in some high-density matter, such as neutron stars [112]. The LHC provides a good place to study Y-N interaction because hyperons and nucleons are abundantly produced at high energy nucleus-nucleus collisions. Due to the short
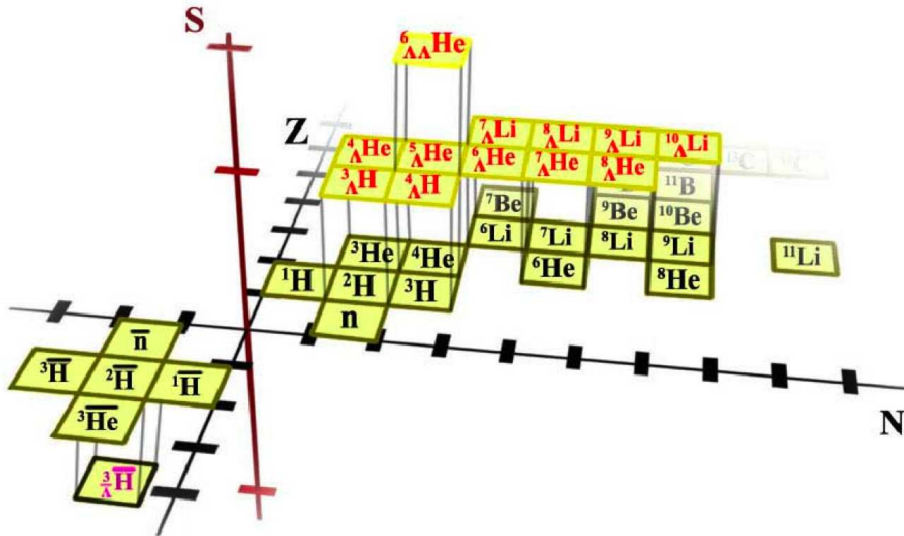
Figure 1.13: 3-dimensional chart (N, Z, S) plane of the nuclides, where N is the number of neutrons, Z is the number of protons and S is the number of strangeness in the nucleus. The figure is taken from Ref. [111].

lifetime of hyperons, it is hard to get direct cross section using hyperon beams. However, the hypertriton, the lightest hypernucleus, which consists of a proton, a neutron and the lightest hyperon Lambda, can give some hints on Y-N interaction.

It is suggested that the ratio S_3, represented as $S_3 = {}^3_\Lambda H / ({}^3He \times \frac{\Lambda}{p})$ is a good representation of the local correlation between baryon number and strangeness, and therefore is a valuable tool to probe the nature of the dense matter created in the high energy heavy-ion collision: quark-gluon plasma or hadron gas [113]. This ratio is also known as the Strangeness Population Factor (SPF). It shows the model dependent evidence of sensitivity to the local correlation strength between baryon number and strangeness, and is a promising tool to study the onset of de-confinement.

Figure 1.14 shows the ratio S_3 as a function of beam energy in minimum-bias Au-Au collisions from *A Multi Phase Transport Model (AMPT)* default version and AMPT with string melting scenario with coalescence model calculations. The figure shows that a prominent enhancement of the S_3 is expected, in a system that passes through a de-confined partonic state, relative to what would be observed in a system that always remained in a hadronic phase. It is interesting to note that S_3 increases with beam energy
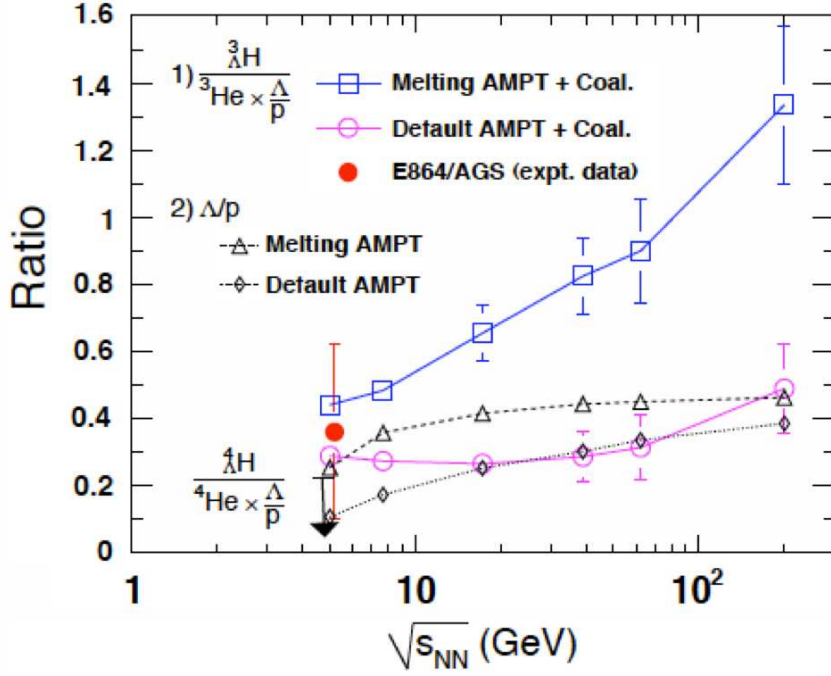
Figure 1.14: The ratio S_3 as a function of beam energy in minimum-bias Au-Au collisions from default AMPT (open circles) and melting AMPT (open squares) with coalescence model calculations. The figure is taken from the Ref. [113]. See text for details.

in a system with partonic interactions (melting AMPT) while it is almost unchanged in a purely hadronic system (default AMPT). Therefore, the Strangeness Population Factor S_3 when measured at high energies e.g. LHC or RHIC energies, could indicate the deconfinement or QGP phase.

The search of heavier anti-nuclei and anti-hypernuclei is still ongoing. Both STAR and ALICE have recently observed first time the anti-alpha $(^4\overline{He})$. The STAR experiment has observed 18 candidates [114] of anti-alpha in one billion events while the ALICE experiment with only first phase of data taking has found 4 anti-alpha candidates [115] in 16.5 M events. The anti-alpha results of the ALICE are obtained from the analysis presented in this thesis and discussed in chapter 6. The ALICE experiment at Large Hadron Collider (LHC) being taking data at very high energies has good possibility to collect large statistics for the anti-nuclei and study their production mechanism.

In a coalescence model, the light nucleus produced in the relativistic heavy-ion

collision is produced during the last stage of the collision process. The quantum wave functions of the constituent nucleons close enough in momentum and coordinate space will overlap and produce the nucleus. The production rate for a nucleus with baryon number B exhibits the exponential behavior as a function of B. In the thermodynamic model, a nucleus is assumed to have energy $E \approx |B|m_N$, where m_N is the nucleon mass. The production rate is determined by the Boltzmann factor $e^{-E/T}$, where T is the temperature. The nuclei yield predicted by this model also goes as exponential.

It is shown by the STAR experiment that the production rate of (anti) particles/(anti) nuclei reduces by a factor of $1.6^{+1.0}_{-0.6} \times 10^3$ and $1.1^{+0.3}_{-0.2} \times 10^3$ for each additional anti-nucleon and nucleon respectively. This trend is also expected from the coalescent nucleosynthesis models as well as from thermodynamic models. From the consistency of the measurements with thermodynamic and coalescent production, one could predict the yield of the next stable antimatter nucleus in the line ($B = -6$) which is found out to be 2.6×10^6 compared to anti-helium4. Therefore, the sensitivity of current space-based charged particle detectors (e.g. BESS, PaMela, and AMS) is below what would be needed to observe antihelium produced by nuclear interactions in the cosmos, and consequently, any observation of antihelium or even heavier anti-nuclei in space would indicate the existence of a large amount of antimatter elsewhere in the Universe.

Figure 1.15 shows discovery year versus the mass of antiparticles. The recent discoveries of anti-hypertriton and antihelium-4 nuclei happened in the year 2010 and 2011 respectively, are also shown.

1.7 Thesis Structure And Organization

This thesis deals with the study of various light nuclei and anti-nuclei production in the relativistic high energy collisions and the study of Photon Multiplicity Detector in the ALICE experiment. In chapter 2, the details of the LHC collider, ALICE detector and its various subsystems are discussed. The chapter 3 discusses the detailed description of the Photon Multiplicity Detector (PMD), its fabrication, electronics, module testing, test beam results, and installation in the ALICE experiments. In chapter 4, discussion of
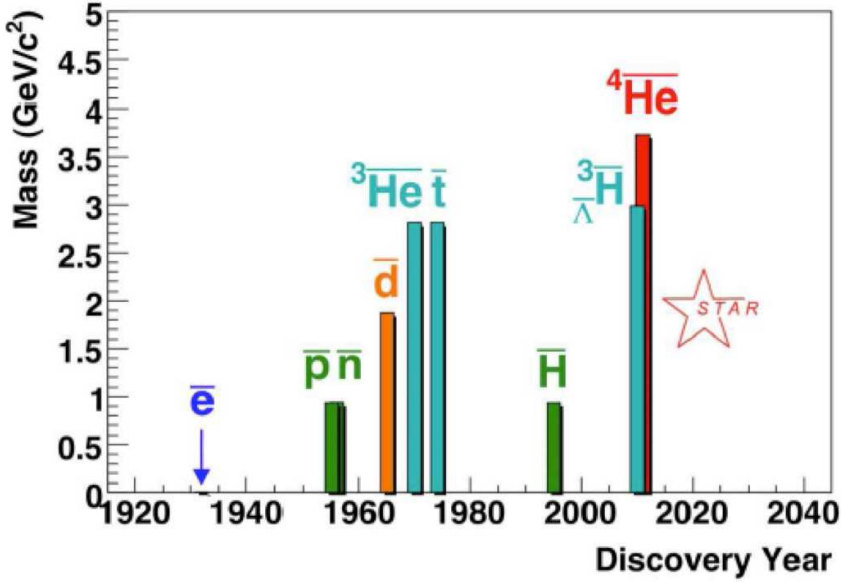
Figure 1.15: Discovery year versus the mass of antiparticles/antinuclei.

the PMD software framework including PMD reconstruction chain, efficiency and purity study using embedding technique are presented in detail. The chapter 5 contains the particle ratios predictions for various systems (pp, Au-Au and Pb-Pb) at different energies using the statistical thermal model, THERMUS. The existing experimental data are also compared with the THERMUS model predictions and with the coalescence model. The chapter 6 includes the techniques used in the data analysis for (anti) nuclei production. The spectra results for (anti)deuteron, (anti)tritons and (anti)helium3 in the ALICE for pp collisions and Pb-Pb collisions at $\sqrt{s} = 7$ TeV and 2.76 TeV, respectively are also presented. The chapter also discusses the observation of anti-alpha ($^4\overline{\text{He}}$) from the ALICE experiment.

Bibliography

[1] S. F. Novaes, Standard Model: An Introduction, hep-ex/0001283v1, (2000).

[2] D. P. Roy, Basic Constituents of Matter and their Interactions - A Progress Report, hep-ex/9912523v1, (1999).

[3] J. D. Bjorken and E. A. Paschos, Phys. Rev. **185**, (1969) 1975.

[4] D. H. Perkins, Introduction to High-Energy Physics, 4th edition, Cambride University Press (2000).

[5] M. Gell-Mann, Phys. Rev. **125**, (1962) 1067.

[6] N. Cabibbo and G. Parisi, Exponential Hadronic Spectrum and Quark Liberation, Phys. Lett. B **59** (1975) 67.

[7] C. Höhne, Internat. J. Mod. Phys. E **16**, 2419 (2007); Nucl. Phys. News **16**, 1 (2006).

[8] F. Karsch, Nucl. Phys. A **698**, (2002) 199.

[9] Y. Aoki, Z. Fodor, S. D. Katz and K. K. Szabo, The QCD transition temperature: Results with physical masses in the continuum limit, Phys. Lett. B **643** (2006) 46.

[10] M. Cheng *et al.*, The transition temperature in QCD, Phys. Rev. D **74** (2006) 054507.

[11] M. G. Alford, QCD at high density / temperature, Nucl. Phys. Proc. Suppl. **117** (2003) 65.

[12] T. Matsui and H. Satz, J/Ψ Suppression by Quark-Gluon Plasma Formation, Phys. Lett. B **178** (1986) 416.

[13] H. Satz, Color Screening and Quark Deconfinement in Nuclear Collisions, Adv. Ser. Direct. High-Energy Phys. **6** (1990) 593.

[14] T. Matsui and H. Satz, Phys. Lett. B **178** (1986) 416; T. Matsui, Zeit. Phys. C **38** (1988) 245.

[15] L. Ramello *et al.* (NA50 Collaboration), Quarkonium production and suppression in Pb-Pb and p-A collisions at SPS energies, Nucl. Phys. A **774** (2006) 59.

[16] A. Andronic, P. Braun-Munzinger, K. Redlich and J. Stachel, Statistical hadronization of heavy quarks in ultra-relativistic nucleus nucleus collisions, Nucl. Phys. A **789** (2007) 334.

[17] P. Huovinen, P. F. Kolb, U. W. Heinz, P. V. Ruuskanen and S. A. Voloshin, Phys. Lett. B **503**, (2001) 58.

[18] D. Teaney, J. Lauret and E. V. Shuryak, arXiv:nucl-th/0110037.

[19] H. Sorge, Phys. Rev. Lett. **78**, (1997) 2309.

[20] E. Shuryak and O. V. Zhirov, Phys. Lett. B **89**, (1979) 253.

[21] L. Van Hove, Z. Phys. C **21**, (1983) 93; K. Kajantie, M. Kataja, L. McLerran and P. V. Ruuskanen, Phys. Rev. D **34**, (1986) 2746; S. Chakrabarty, J. Alam, D. K. Srivastava and B. Sinha, Phys. Rev. D **46**, (1992) 3802.

[22] L. V. Bravina, N. S. Amelin, L. P. Csernai, P. Levai and D. Strottman, Nucl. Phys. A **566**, (1994) 461c; L. V. Bravina, L. P. Csernai, P. Levai and D. Strottman, Phys. Rev. C **50**, (1994) 2161.

[23] D. H. Rischke, Y. Pursun, J. A. Maruhn, H. Stoecker and W. Greiner, Heavy Ion Phys. **1**, (1995) 309, [arXiv:nucl-th/9505014].

[24] L. P. Csernai and D. Rohrich, Phys. Lett. B **458**, (1999) 454.

[25] A. Nyiri *et al.*, J. Phys. G **31**, (2005) S1045.

[26] P. F. Kolb and U. W. Heinz, arXiv:nucl-th/0305084v2.

[27] H. Sorge, Phys. Rev. Lett. **82**, (1999) 2048.

[28] J. Adams et al. (STAR Collaboration), Phys. Rev. Lett. **95** (2005) 122301 [arXiv:nucl-ex/0504022].

[29] J. Adams *et al.* (STAR Collaboration), Phys. Rev. Lett. **92**, (2004) 052302.

[30] J. Adams *et al.* (STAR Collaboration), Phys. Rev. Lett. **92**, (2004) 182301.

[31] J. Y. Ollitrault, Phys. Rev. D **46**, (1992) 229.

[32] Phys. Rev. Lett. **105**, (2010) 252302.

[33] G. Kestin and U. W. Heinz, Eur. Phys. J. C **61**, (2009) 545.

[34] H. Masui, J. Y. Ollitrault, R. Snellings and A. Tang, Nucl. Phys. A **830**, (2009) 463C.

[35] M. Luzum and P. Romatschke, Phys. Rev. Lett. **103**, (2009) 262302.

[36] T. Hirano, U. W. Heinz, D. Kharzeev, R. Lacey and Y. Nara, Phys. Lett. B **636**, (2006) 299.

[37] P. Koch, B. Müller and J. Rafelski, Phys. Rep. **142**, (1986) 167.

[38] B. I. Abelev *et al.* (STAR Collaboration), Phys. Lett. B **673**, (2009) 183.

[39] J. Alam, B. Sinha and S. Raha, Phys. Rept. **273** (1996) 243.

[40] M. M. Aggarwal *et al.* (WA98 Collaboration), Phys. Rev. Lett. **85**, (2000) 3595.

[41] D. K. Srivastava and B. Sinha, Phys. Rev. C **64**, (2001) 034902.

[42] M. H. Thoma and M. Gyulassy, Nucl. Phys. A **538**, (1991) 37c; S. Mrowczynski Phys. Lett. B **269**, (1991) 383; Y. Koike and T. Matsui, Phys. Rev. D **45**, (1992) 3237.

[43] R. Baier, D. Schi and B.G. Zakharov, Ann. Rev. Nucl. Part. Sci. **50**, (2000) 37.

[44] M. Gyulassy and M. Plumer, Phys. Lett. B **243**, (1990) 432.

[45] M. Gyulassy, I. Vitev, and X. N. Wang, Phys. Rev. Lett. **86**, (2001) 2537.

[46] K. Aamodt *et al.*, (ALICE Collaboration), Phys. Lett. B **696** (2011) 30.

[47] J. Adams *et al.* (STAR Collaboration), Phys. Rev. Lett. **91**, (2003) 072304.

[48] J. Adams *et al.* (STAR Collaboration), Phys. Rev. Lett. **93**, (2004) 252301.

[49] J. Adams *et al.* (STAR Collaboration), Phys. Rev. Lett. **97**, (2006) 162301.

[50] I. Arsene *et al.* (BRAHMS Collaboration), Nucl. Phys. A **757** (2005) 1; B. B. Back *et al.* (PHOBOS Collaboration), Nucl. Phys. A **757** (2005) 28; J. Adams *et al.* (STAR Collaboration), Nucl. Phys. A **757** (2005) 102; K. Adcox *et al.* (PHENIX Collaboration), Nucl. Phys. A **757** (2005) 184.

[51] H. Heiselberg, Phys. Rep. **351** (2001) 161; M. M. Aggarwal *et al.* (WA98 Collaboration), Phys. Rev. C **65** (2002) 054912.

[52] B. Mohanty and J. Serreau, Phys. Rep. **414** (2005) 263; WA98 Collaboration, M. M. Aggarwal *et al.*, Phys. Rev. C **64** (2001) 011901(R).

[53] K. Adcox *et al.* (PHENIX Collaboration), Phys. Rev. Lett. **86** (2001) 3500.

[54] L. V. Gribov, E. M. Levin and M. G. Ryskin, Phys. Rep. **100** (1983) 1; J. P. Blaizot and A. H. Mueller, Nucl. Phys. B **289** (1987) 847.

[55] L. McLerran and R. Venugopalan, Phys. Rev. D **49** (1994) 2233; L. McLerran and R. Venugopalan, Phys. Rev. D **50** (1994) 2225; Y. V. Kovchegov, Phys. Rev. D **54** (1996) 5463; E. Iancu and L. McLerran, Phys. Lett. B **510** (2001) 145; A. Krasnitz and R. Venugopalan, Phys. Rev. Lett. **84** (2000) 4309.

[56] J. D. Bjorken, Phys. Rev. D **27** (1983) 140; L. D. Landau, Izv. Akad. Nauk Ser. Fiz. 17 (1953) 51; S. Belenkij and L. D. Landau, Usp. Fiz. Nauk. **56** (1955) 309; Nuovo

Cim. Suppl. 3S10 (1956) 15; R. C. Hwa and K. Kajantie, Phys. Rev. D **32** (1985) 1109; J. Alam *et al.*, Annals of Phys. **286** (2000) 159; B. Mohanty and J. Alam, Phys. Rev. C **68** (2003) 064903.

[57] P. K. Netrakanti and B. Mohanty, Phys. Rev. C **71** (2005) 047901; J. Aichelin and K. Werner, Phys. Lett. B **300** (1993) 158.

[58] M. M. Aggarwal *et al.*, Nucl. Instr. Meth. A **499** (2003) 751; M. M. Aggarwal *et al.*, Nucl. Instr. Meth. A **488** (2002) 131.

[59] K Aamodt *et al.* (ALICE collaboration), Phys. Rev. Lett. **105** (2010) 252301.

[60] M. M. Aggarwal *et al.* (WA93 Collaboration), Phys. Lett. B **403**, 390 (1997); G. C. Mishra, Ph. D. Thesis, Utkal University (1999).

[61] R. Raniwala (for the STAR Collaboration), J. Phys. G **35**, (2008) 104104.

[62] B. Mohanty and J. Serreau, Phys. Rep. **414**, (2005) 263 and references therein.

[63] J. Adams *et al.* (STAR Collaboration), Phys. Rev. Lett. **95** (2005) 062301; B. I. Abelev *et al.* (STAR Collaboration), Nucl. Phys. A **832** (2010) 134; P. K. Netrakanti, Ph. D. Thesis, Jadavpur University (2008); M. Sharma, Ph. D. Thesis, Panjab University (2008); N. Gupta, Ph. D. Thesis, Jammu University (2008); D. Das, Ph. D. Thesis, Jadavpur University (2008); and S. M. Dogra, Ph. D. Thesis, Jammu University (2009). L. Kumar, Ph. D. Thesis, Panjab University (2009); http://drupal.star.bnl.gov/STAR/theses.

[64] J. Benecke *et al.*, Phys. Rev. **188** (1969) 2159.

[65] B.B. Back *et al.* (PHOBOS Collaboration), Phys. Rev. Lett. **87** (2001) 102303. B. B. Back *et al.* (PHOBOS Collaboration), Phys. Rev. Lett. **91** (2003) 052303.

[66] I. G. Bearden *et al.* (BRAHMS Collaboration), Phys. Lett. B **523** (2001) 227; I. G. Bearden *et al.*(BRAHMS Collaboration), Phys. Rev. Lett. **88** (2002) 202301.

[67] J. Adams *et al.* (STAR Collaboration), Phys. Rev. C **73** (2006) 034906.

[68] I.G. Bearden *et al.* (BRAHMS Collaboration), nucl-ex/0403050.

[69] S.V. Afanasiev *et al.*, (NA49 Collaboration), Phys. Rev. C **66**, 054902 (2002).

[70] J. L. Klay *et al.* (E895 Collaboration), Phys. Rev. Lett. **88**, (2002) 102301; J. L. Klay *et al.* (E895 Collaboration), Phys. Rev. C **68**, 054905 (2003).

[71] P. Braun-Munzinger, J. Stachel, J. P. Wessels, and N. Xu, Phys. Lett. B **344**, 43 (1995).

[72] P. Braun-Munzinger, J. Stachel, J. P. Wessels, and N. Xu, Phys. Lett. B **365**, 1 (1996).

[73] P. Braun-Munzinger, I. Heppe and J. Stachel, Phys. Lett. B **465**, 15 (1999).

[74] N. Xu and M. Kaneta, Nucl. Phys. A **698**, 306 (2002).

[75] S. Wheaton, J. Cleymans, and M. Hauer, Comp. Phys. Comm. 180 (2009) 84.

[76] E. Schnedermann, J. Sollfrank, and U. Heinz, Phys. Rev. C **48**, (1993) 2462.

[77] D. Teaney, J. Lauret, and E. V. Shuryak, Phys. Rev. Lett. **86**, (2002) 4783.

[78] P. Kolb *et al.* , Nucl. Phys. A **696**, (2001) 197.

[79] P. Huovinen *et al.* , Phys. Lett. B **503** (2001) 58.

[80] U. Heinz and P. Kolb, Nucl. Phys. A **702**, (2002) 269.

[81] F. Retiere and M. A. Lisa, Phys. Rev. C **70**, (2004) 044907.

[82] B. I. Abelev *et al.* (STAR Collaboration), Phys. Rev. C **79**, (2009) 034909.

[83] F. Karsch, Lecture Notes in Physics **583**, (2002) 209.

[84] P. Braun-Munzinger *et. al*, Nature **448** (2007) 302.

[85] H. Sato *et. al*, Phys. Lett. B **98** (1981) 153.

[86] P. Braun-Munzinger *et. al*, Phys. Lett. B **34** (1995) 43.

[87] J. Cleymans *et. al*, Z. Phys. C **74** (1997) 319.

[88] P. Braun-Munzinger *et. al*, Phys. Lett. B **465** (1999) 15.

[89] J. Cleymans *et. al*, Phys. Rev. C **60** (1999) 054908.

[90] F. Becattini *et. al*, Phys. Rev. C **64** (2001) 024901.

[91] P. Braun-Munzinger *et. al*, Phys. Lett. B **518** (2001) 41.

[92] N. Xu *et. al*, Nucl. Phys. A **698** (2002) 306c.

[93] F. Becattini, J. Phys. G **28** (2002) 1553.

[94] R. Rapp *et. al*, Phys. Rev. Lett **88** (2001) 2980.

[95] F. Becattini *et. al*, Phys. Rev. C **73** (2006) 044905.

[96] P. Braun-Munzinger *et. al*, Nucl. Phys. A **772** (2006) 167.

[97] R. Hagedron, CERN-TH-4100/85 (1985).

[98] P. Braun-Munzinger *et. al*, Phys. Lett. B **596** (2004) 61.

[99] H. Stöcker *et. al*, Phys. Rept. **303** (1981) 259.

[100] H. Stöcker *et. al*, Nucl. Phys. A **452** (1986) 723.

[101] H. Stöcker *et. al*, Nucl. Phys. A **476** (1988) 717.

[102] P. Braun-Munzinger *et. al*, Phys. Lett. B **697** (2011) 203.

[103] P. Braun-Munzinger *et. al*, J. Phys. G **21** (1995) L17.

[104] A. J. Baltz *et. al*, Phys. Lett. B **325** (1994) 7.

[105] P. Braun-Munzinger, I. Heppe, and J. Stachel, Phys. Lett. **B465**, 15 (1999); F. Becattini, J. Cleymans, A. Keranen, E. Suhonen, and K. Redlich, Phys. Rev. C **64**, 024901(2001); P. Braun-Munzinger, D. Magestro, K. Redlich, and J. Stachel, Phys. Lett. **B518**, 41 (2001); N. Xu and M. Kaneta, Nucl. Phys. **A698**, 306(2002); F. Becattini, J. Phys. G **28**, 1553(2002).

[106] P.Braun-Munzinger, K. Redlich,and J. Stachel, in *Quark-Gluon Plasma3*, edited by R.C.Hwa and X.N.Wang (WorldScientic Publishing, Singapore, 2004).

[107] For general reviews see e.g. K. Redlich, J. Cleymans, H. Oeschler, and A. Tounsi, Acta Phys. Pol. B **33** (2002) 1609.

[108] B. I. Abelev *et al.* (STAR Collaboration), Phys. Rev. C **79** (2009) 034909.

[109] K. Aamodt *et al.* (ALICE Collaboration)., Phys. Rev. Letters **106** (2010) 072002.

[110] A. Schuster, "Potential Matter.A Holiday Dream", Nature **58** (1898) 367.

[111] B.I. Abelev *et al.* (STAR Collaboration), Science **328** (2010) 58 .

[112] J. M. Lattimer, M. Prakash, Science **304** (2004) 536.

[113] S. Zhang, J. H. Chen, H. Crawford, D. Keane, Y. G. Ma and Z. B. Xu, Phys. Lett. B **684**, (2010) 224, [arXiv:0908.3357 [nucl-ex]].

[114] H. Agakishiev *et al.* (STAR Collaboration), Nature **473** (2011) 353.

[115] A. Kalweit, talk at QM2011; N. Sharma, poster presentation at QM2011.

Chapter 2

THE ALICE EXPERIMENT

2.1 Large Hadron Collider (LHC)

There have been many facilities in the world, built to study the properties of QGP and production mechanism of (anti) matter by looking at the collisions of heavy-ions at the relativistic speed. These were mainly - Alternating Gradient Synchrotron (AGS) [1] at Brookhaven National Laboratory (BNL) in USA; Bevatron-Bevalac [2] at Lawrence Berkeley Laboratory in USA; Super Proton Synchrotron (SPS) [3] at CERN, Switzerland; and Relativistic Heavy Ion Collider (RHIC) [4] in BNL, USA. The AGS and SPS were the fixed target experiment facilities while the RHIC is the collider accelerator facility. These experimental facilities covered the energy range from the lowest energy of $\sqrt{s_{NN}} \sim$ 2 GeV up to the highest energy of $\sqrt{s_{NN}} = 200$ GeV. The results from the experiments from these facilities have helped a lot in understanding the properties of matter created in heavy-ion collisions. But there was still need of very high energy collision experiments which could look for the rare or exotic particles, study their properties in detail and lead to larger lifetime and the volume of the QGP [5, 6] that could be created during the collisions.

In view of these, the need to further go to the very high-energy regime was felt and as a result the Large Hadron Collider (LHC) [7] was proposed. The first run of the LHC happened in the year 2008 but due to some technical problem [8] it had to be stopped. Till now LHC has collected data for proton-proton collisions at $\sqrt{s} = 7$ TeV and for Pb-Pb collisions at $\sqrt{s_{NN}} = 2.76$ TeV. Table 2.1 lists the operating parameters values that can

Table 2.1: Nominal LHC parameters for Pb-Pb collisions

Parameter	Nominal	units
$\sqrt{s_{NN}}$	5.5	TeV
Initial luminosity	1×10^{27}	cm^{-2}s^{-1}
Number of bunches	592	
Bunch spacing	99.8	ns
Pb ions per bunch	7×10^7	
LHC circumference	27	km

be achieved at LHC for the Pb-Pb collisions. The LHC and RHIC are the present collider accelerator facilities to search for the Quark Gluon Plasma (QGP) formation in the heavy ion collisions. Since both RHIC and LHC are the collider facilities and primarily look to study the properties of QGP produced in high energy heavy-ion collisions, it will be interesting to compare various parameters between the two facilities. Table 2.2 lists such a comparison for the top energies and the largest colliding systems that can be achieved for the RHIC and LHC. The parameters listed in the table are colliding systems, center of mass energy, maximum charged particle multiplicity, energy density, expected freeze-out volume and lifetime of the QGP attained in central collisions for two accelerator facilities. Clearly LHC is the ideal place to study the QGP and it's properties.

The LHC is a synchrotron accelerator of two counter-rotating beams moving in separate beam pipes. The circumference of LHC is about 27 km. Each beam contains bunches of particles rotated continuously in a circle by accelerating them before the collision energy is reached. The sets of magnetic and electric fields are needed to bend the beams around the ring, keep the bunches focused and accelerate them to their collision energy. Also the spatial dimension of the bunches is minimized to provide a high luminosity (number of collisions per time interval) at the collision points. The luminosity $\mathcal{L}$ can be given by the relation: $\mathcal{L}= fnN^2/A$, where n represents number of bunches in both beams, N is the

Table 2.2: Comparison between RHIC and LHC parameters

Central collisions	RHIC	LHC
Colliding System	Au-Au	Pb-Pb
E_{cm}	200	5500
dN_{ch}/dy	700	2000-8000
$\epsilon(t_{[0]} = 1\text{fm/c})[\text{GeV/fm}^3]$	3.5	15-40
$V_{\text{freeze}}[\text{fm}^3]$	7×10^3	2-5 $(\times 10^3)$
$\tau_{\text{QGP}}[\text{fm/c}]$	1.5–4	4–10

number of particles per bunch, A is the cross-sectional area of the the beams, and f is the frequency of revolution.

The schematic picture of LHC is shown in the Fig. 2.1. LHC is segmented into eight octants, each has a straight section in its center, referred to as pits or points. The two LHC rings cross at the four points (points 1, 2, 5, and 8) which contain the four major experiments. Particles are injected before point 2 and point 8 as shown in the figure. The radio-frequency (RF) system that accelerates the particles is located at point 4; the beam dumping system is located at point 6. At point 3 and 7 collimation systems are placed that clean the beam by removing particles that have either a too large spatial distance to their bunch (particles in the so-called beam-halo) or are too fast or too slow, thus separated in momentum-space. The cleaning prevents particles from being lost in an uncontrolled fashion within the accelerator.

To direct the beams around the accelerator, 1232 dipoles are employed so as to bend the beam trajectories. The LHC dipole has a length of 14.3m and contains superconducting magnets. These dipoles provide a magnetic filed of ~0.535T during injection and about ~8.33T during nominal collisions. In addition, about 392 quadrupole magnets, each 5-7 m long, are used to focus the beams. Prior to collisions, another magnet is used to squeeze the particles close together. Eight RF cavities per beam deliver radio-frequency power to accelerate the beams, keep the bunches of particles well-localized and
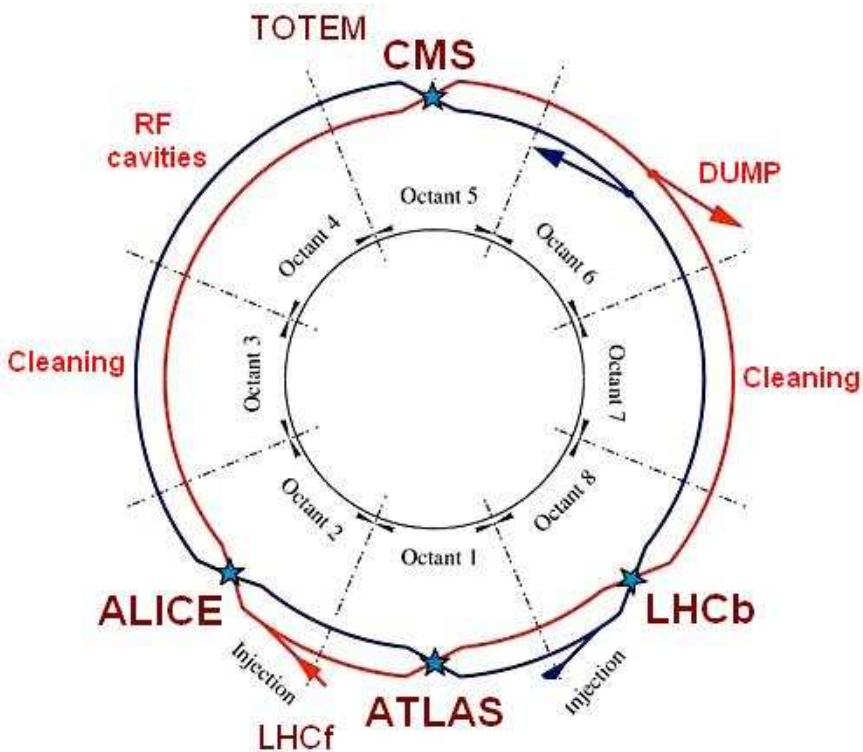
Figure 2.1: Layout picture of the LHC shown along with main experiments positions.

compensate for energy loss due to synchrotron radiation. The cavities produce a field of 5.5 MV/m.

Injection of bunches into the LHC is illustrated by the Fig. 2.2 and is described as following. The protons are obtained by knocking off the electrons from hydrogen atoms. These are accelerated in the linear accelerator (LINAC2) which fed them into the PS Booster, then into the Proton Synchrotron (PS), followed by the Super Proton Synchrotron (SPS) accelerator. Finally the bunches reach the LHC ring. Several injections to the LHC are needed until all bunches of both beams are filled. In the LHC rings, the beam may take about 20 minutes to reach the maximum speed and energy. Each beam is filled with 2808 bunches each consisting of 1.15×10^{11} protons. The time separation between two bunches is 25 ns. The Lead ions for the LHC enter LINAC3 before being collected and accelerated in the Low Energy Ion Ring (LEIR). Then they follow the same route to maximum acceleration as the protons.

When the beams reach the maximum speed and energy, they are collided at dif-
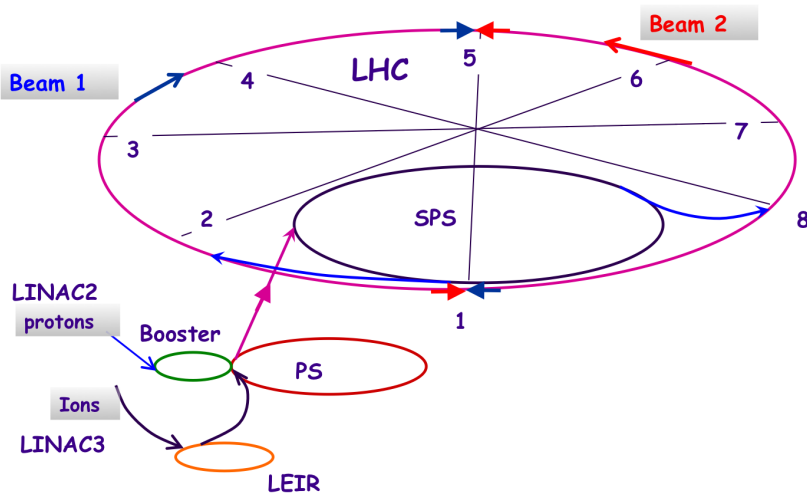
Figure 2.2: Schematic diagram showing the injection of protons or beam into the LHC ring.

ferent points containing the experiments. These experiments and their motivations are discussed below:

A Toroidal LHC ApparatuS (ATLAS) [9] and **Compact Muon Solenoid (CMS)** [10]: These are situated diametrically opposite in Pits 1 and 5, respectively. These two detectors are general-purpose proton-proton detectors that are built to cover the widest possible range of physics at the LHC. Specific topics are the search for the Higgs boson and physics beyond the Standard Model, e.g. new heavy particles postulated by super-symmetric extensions (SUSY) of the Standard Model, evidence of extra dimensions, and particles that could make up dark matter. The difference between ATLAS and CMS experiments is in the technical design of their detector magnet system. They also take the heavy-ion data.

Large Hadron Collider beauty (LHC-b) [11]: This experiment is dedicated to the study of CP violation and other rare phenomena in the decay of Beauty particles.

Large Hadron Collider forward (LHC-f) [12]: It measures forward particles created during LHC collisions to provide further understanding of high-energy cosmic rays.

The detector is placed close to the ATLAS experiment. Cosmic rays are naturally occurring charged particles from outer space that constantly bombard the Earths atmosphere. They collide with nuclei in the upper atmosphere, leading to a cascade of particles that reaches ground level. Studying how collisions inside the LHC cause similar cascades of particles will help scientists to interpret and calibrate large-scale cosmic-ray experiments that can cover thousands of kilometers.

TOTal Elastic and diffractive cross-section Measurement (TOTEM) [13]: This experiment studies forward particles to focus on physics that is not accessible to the general-purpose experiments. It measures the total cross-section, elastic scattering, and diffractive processes. Among a range of studies, it will measure, in effect, the size of the proton and also monitor accurately the LHCs luminosity. It shares intersection point Pits 5 with CMS.

A Large Ion Collider Experiment (ALICE) [14, 15]: This is a dedicated heavy-ion experiment designed to study strongly-interacting matter. It will explore the phase transition to the quark-gluon plasma, and its properties. Furthermore, ALICE will also study collisions of protons, on the one hand as a baseline for heavy- ion measurements and on the other hand to contribute in the analyses related to particle identification capabilities and acceptance at very low transverse momenta. The ALICE experiment is situated in pit2. The results presented in this thesis are based on the data taken by the ALICE detector so we explain the ALICE experiment in detail in the following sections.

2.2   The ALICE Experiment

ALICE is a general-purpose particle detector designed to study heavy-ion collisions. It is placed at one of the four collision points of LHC. ALICE collaboration involves more than 1000 members from about 30 countries. The ALICE was designed to study the strong interactions and to characterise the Quark-Gluon Plasma (QGP). It is the one of the experiment at LHC designed to study the heavy ion (Pb-Pb) collisions and has been

optimized for the very high multiplicity environment that is created in central heavy-ion collisions. The design was optimised for a multiplicity $dN_{\mathrm{ch}}/d\eta = 4000$, but tested by simulation up to $dN_{\mathrm{ch}}/d\eta = 8000$. The first results showed a lower $dN_{\mathrm{ch}}/d\eta \approx 1600$ at half energy [16]. The detectors unique features are the tracking and particle identification over a large range of momenta i.e., from tens of MeV/c to over 100 GeV/c, allowing physics topics involving soft, jet physics and high-p_T particle production.

Figure 2.3 shows the cross-sectional views of the ALICE detector. The detector is placed in the solenoid magnet from the old LEP experiment L3 which provides a relatively low magnetic field of 0.5 T. This allows the precise momentum measurements of the particles. Particles in ALICE are identified over the vast momentum range with various PID techniques: specific ionisation energy loss dE/dx, time-of-flight (TOF), transition and Cherenkov radiation, electromagnetic calorimetry, muon filters, and topological decay reconstruction. ALICE detector contains various subsystems focusing on different Physics analyses. These detectors are discussed briefly in the following subsections.

2.2.1   The Central Barrel

The Central Barrel includes the set of detectors which cover the central region of the ALICE detector inside the L3 magnet. These detectors mainly include the Inner Tracking System (ITS), the Time-Projection Chamber (TPC), the Transition-Radiation Detector (TRD), and the Time-Of-Flight (TOF), covering the pseudo-rapidity region of $|\eta| <0.9$.

2.2.1.1   Inner Tracking System (ITS)

The schematic view of the ITS [17] is shown in Fig. 2.4. ITS is placed closest to the inter-action point. It consists of 6 cylindrical layers of silicon detectors with radii from 3.9 to 43 *cm*, and covering the pseudo-rapidity region $|\eta| <0.9$. ITS is useful for the reconstruction of the primary vertex of the collision as well as the reconstruction of secondary vertices's of heavy-quark decays (B and D mesons) and hyperons with a resolution better than 100 μm in transverse direction. The ITS is very useful in the particle identification through the specific ionisation energy loss as well as for the particle tracking.

The two innermost layers consist of Silicon Pixel Detectors (SPD) in order to handle
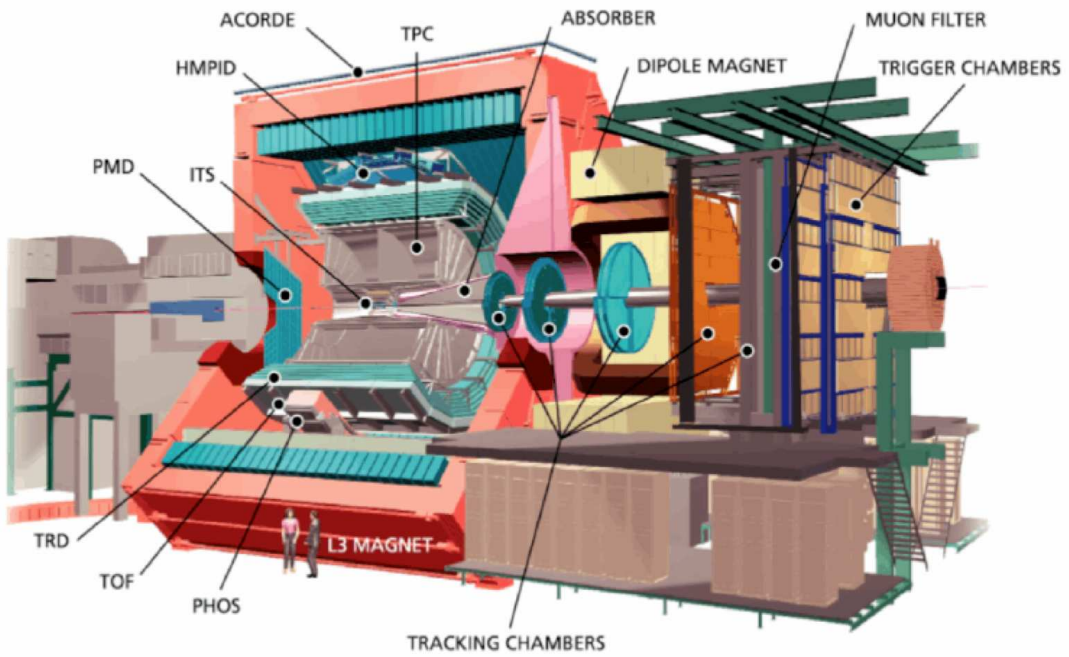
Figure 2.3: Perspective view of the ALICE detector, with a cutaway for viewing inner detector systems.

the high-particle density (as many as 50 particles per cm^2). The SPD is based on hybrid silicon pixels consisting of silicon detector diodes with a thickness of 200 μm. The SPD readout is in a binary fashion and thus does not provide energy-loss information. So the SPD does not contribute to the particle identification. The information from the SPD is used to measure the charged particle multiplicity. It can also be used as L0 trigger. The two middle layers (third and fourth layer) consist of Silicon Drift Detectors (SDD), with a 300 μm thick layer of homogeneous high-resistivity silicon. The readout of these two layers are of analog type therefore, they provide the energy-loss information and contribute towards the particle identification. The two outermost layers consist of double sided Silicon Strip Detectors (SSD). These provide the two-dimensional measurement of the track position along with energy-loss measurement for the particle identification. These are also important for track matching from the Time Projection Chamber to the ITS.
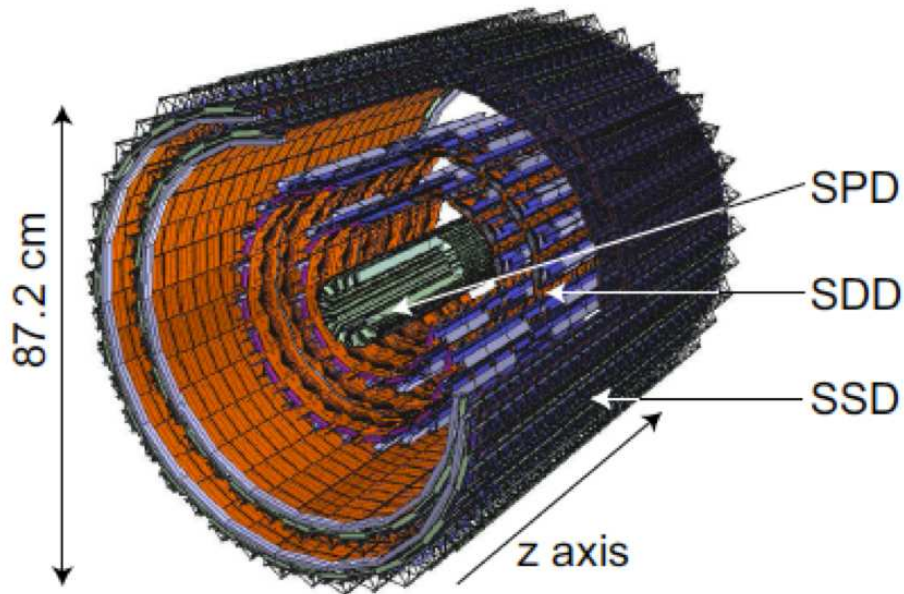
Figure 2.4: Schematic view of the ITS [17].

2.2.1.2 Time Projection Chamber (TPC)

The TPC [18, 19] is the main tracking device of the ALICE detector. The TPC is able to track charged particles in $|\eta| < 0.9$ with full azimuthal coverage. Particles with a p_T from about 200 MeV/c up to 100 GeV/c can be reconstructed in TPC with a good momentum resolution. In combination with the other central barrel detectors, TPC provides the measurement of charged-particles including their momentum, particle identification, and vertex reconstruction.

Figure 2.5 shows the schematic picture of the TPC. It is a gas detector with a volume of 90 m^3 which makes it the largest TPC of the world. The active volume has an inner radius of about 85 cm, an outer radius of about 250 cm, and an overall length along the beam direction of 500 cm. A conducting electrode at the center of the cylinder, charged to 100 kV, provides, together with a voltage dividing network at the surface of the outer and inner cylinder, a precise axial electric field of 400 V/cm. The active volume is filled with Neon (Ne), Carbon-dioxide (CO$_2$) and Nitrogen (N$_2$) gas mixture at atmospheric pressure. The charged particles traversing the TPC volume ionise the gas
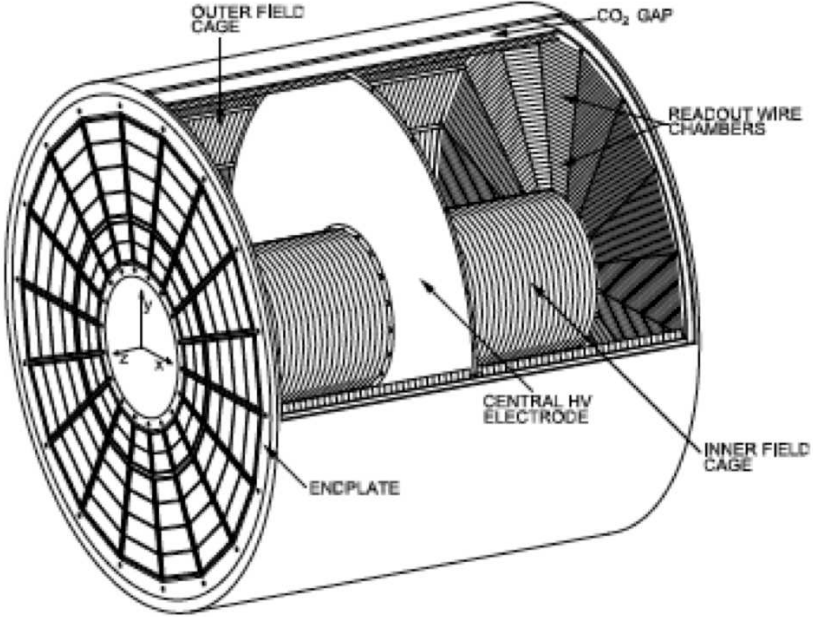
Figure 2.5: The ALICE Time Projection Chamber [18].

along their path, liberating electrons. The ionization electrons drift, under the influence of the electric field, to the end plates of the cylinder, where their arrival point in the cylinder plane is precisely measured. Together with an accurate measurement of the arrival time, the complete spatial trajectory of all charged particles traversing the TPC can be determined with precision.

Field Cage:

The purpose of the field cage is to define a uniform electrostatic field in the gas volume for the ionization electrons to transport from their point of creation to the readout chambers. It provides a stable mechanical structure for precise positioning of chambers and other detectors while being as thin as possible for minimum radiation length presented to tracks entering. The field cage also provides a gas-tight envelope and ensure appropriate electric isolation of the field cage from the rest of experiment.

The ALICE field cage consists of two parts: a field cage vessel with a set of coarsely segmented guard rings and a finely segmented field cage located inside the field cage vessel. Four cylinders are required to make the complete field cage structure: two field-

cage vessels (inner and outer) and two containment vessels (inner and outer). The inner and outer field-cage vessels define the gas volume of the TPC. The containment vessels surround the field cage vessels and they provide gas tight and grounded enclosures at the inner and outer diameters of the TPC. The containment vessels are separated from the field cage vessels by an insulating gap and these gaps are continuously flushed with CO_2 to isolate the field cage voltage from the grounded containment walls. The TPC contains a high voltage electrode in the middle of the detector called the *Central electrode*. Electrons drift to both end plates in a uniform electric field that runs parallel to the axis of the cylinder. The central electrode is made of a stretched 23 μm thick mylar foil which is aluminized on both sides and held flat by an inner and outer aluminum rim.

To align the cylinders for the field cage vessels and to hold the readout chambers in position, *Endplates* are used. They also provide feed-throughs and flanges for gas, laser and electrical connections. The four cylinders are screwed to the flanges that connect the field cage vessels and the containment vessels, and are made gas-tight. The aluminum structure of the endplate is 60 mm thick and the spokes are 30 mm wide. The gas tightness is achieved by a sealing foil and a double O-ring; one on the chamber and one on the endplate.

Readout Chambers:

The readout for the ALICE TPC was a challenging task because of the high particle densities and rates anticipated at the LHC. The readout chambers use Multi Wire Proportional Counters (MWPCs) with cathode pad readout. The azimuthal segmentation of the readout plane is common with subsequent detectors Transition Radiation Detector (TRD) and Time Of Flight (TOF) which includes 18 trapezoidal sectors each covering 20^0 in azimuth. The radial dependence of the track density required two different types of readout chambers namely Inner and Outer ReadOut Chamber (i.e., IROC and OROC).

The dead space between neighboring readout chambers is minimized by a special mounting technique by which the readout chambers are attached to the endplate from the inside of the drift volume. The dead space between two adjacent chambers in the azimuthal direction is 27 mm. This includes the width of the wire frames of 12 mm on
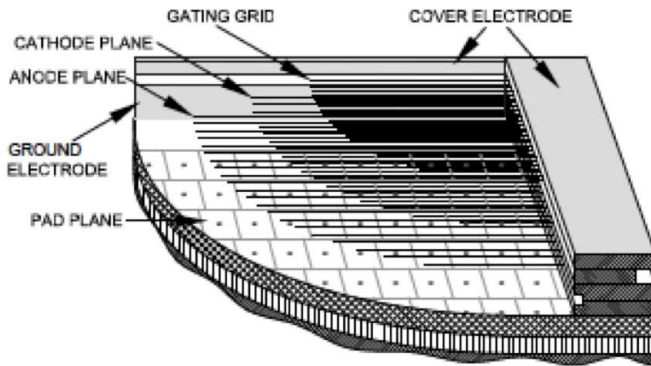
Figure 2.6: Cross-sectional view of readout chamber.

each chamber (Fig. 2.6) and a gap of 3 mm between two chambers. The total active area of the ALICE TPC readout chambers is 32.5 m^2, leaving a total insensitive area of about 10%. Since the magnetic field bends the tracks out of the insensitive region, the loss of efficiency is less than the 10%. However, the high-p_t tracks which mostly travel straight are bound to get lost if move into the insensitive area. The mechanical structure of the readout chamber itself consists of four main components: the wire planes, the pad plane, made of a multi-layer Printed Circuit Board (PCB), an additional 3 mm Stesalit insulation plate, and a trapezoidal aluminum frame.

The *anode wire* diameter is preferred to be small because of large gas gain at small wire diameter. The gold-plated tungsten because of it's superior strength is used for the anode wires. The material used for the thicker *cathode and gating grid* wires is copper-beryllium (an alloy of 98% Cu and 2% Be) since the gold-plated tungsten would require large tensions on the thin wire ledges. The typical diameters of anode wires and cathode or gating grid wires are 20 μm and 75 μm respectively.

Figure 2.7 shows the scheme used for the wire planes. It uses anode wires grid, a cathode-wire grid, and a gating grid. All wires run in the azimuthal direction. The wire geometry is different for the inner and outer chambers because of their different designs. The gap between the anode-wire grid and the pad plane is 3 mm for the outer chambers, and only 2 mm for the inner chambers. The cathode wire grid is at a distance of 3 mm
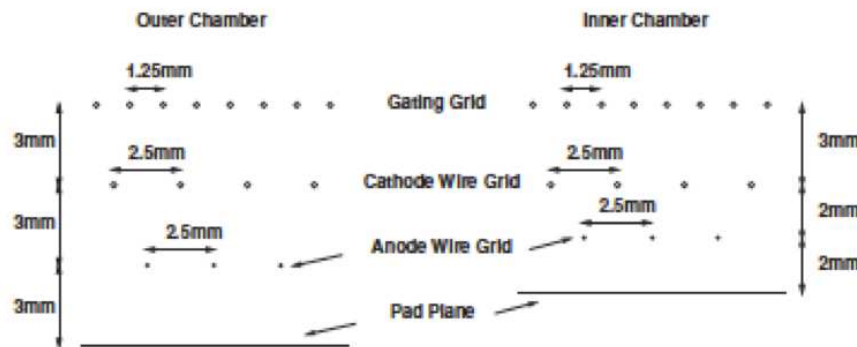
Figure 2.7: Wire geometries for inner and outer readout chambers

from the anode wire grid for the outer chamber but 2 *mm* for the inner chamber. The gating grid is located 3 *mm* above the cathode-wire grid in both types of chamber.

Since the particle multiplicity is expected to be high at ALICE and the gas gain is required to be large, a small anode-wire pitch of about 2.5 *mm* is used for the anode wires. The cathode-wire pitch is also 2.5 *mm*. The cathode-wire grid separates the drift volume from the amplification region near anode-wire grid. Cathode wires collect large number of the ions produced in the amplification avalanche without so much affecting electron transmission. The gating grid is located above the cathode-wire grid. The alternating wires of gating grid are connected together electrically.

In the open gate mode, when the gating grid wires are held at the same potential, the electrons from the drift volume are admitted into the amplification region. In the absence of a valid trigger, the gating grid is biased with a bipolar field and said to be in *closed gate* mode. At this time, electrons are prevented to enter the amplification region from the drift volume. This considerably reduces the integral charge deposit on the anode wires. In addition, the closed gate stops ions created in the avalanche processes of previous events from drifting back into the drift volume. This is important because escaping ions accumulate in the drift volume and can cause distortion in the field. To achieve an electron transparency close to 100% in the open mode while trapping ions and electrons in the closed mode, the offset and bias potentials of the gating grid are carefully adjusted. However, any ionization produced by particles traversing the gap between the

gating grid and pad plane will unavoidably be amplified at the anode wires and thus contribute to the integral charge accumulation. To minimize this effect, the gap between the gating and cathode-wire grid is only 3 mm, sufficient to trap the ions within a typical gate opening time of 100 μs. To keep the alternating bias voltages low, the pitch between the gating grid wires is 1.25 mm.

Moving from the anode wire towards the surrounding electrodes, positive ions, created in an avalanche process, induce a positive signal on the pad plane. The precise position of the avalanche is obtained from the induced signal distributed over several adjacent readout pads (charge sharing). The position of the particle track in the drift direction can be determined by sampling the time distribution of each pad signal. The resulting two dimensional pulse height distribution in pad-time space is called a *cluster*. A maximum of 160 clusters can be measured for a typical track which allows up to 20000 tracks in one event to be reconstructed and identified.

The pad shape is chosen based on the requirement of minimizing the occupancy and to maximize the momentum and dE/dx resolution within a reasonable budget. The average single track cluster area for different pad geometries show a minimum for a pad-size of $6 \times 10 \ mm^2$. Since the track density is not constant throughout the TPC, highest being at the small radii, smaller pad sizes at small radii are considered. On the other hand, the overall track density decreases by $1/r^2$, less stringent pad size for the outer radii of the TPC are considered. The total number of pads in the inner chamber is 5504, distributed over 63 pad rows running parallel to the wires. The pad size is $4 \times 7.5 \ mm^2$. The number of pads in the outer chamber is 9984, with a pad size of $6 \times 10 \ mm^2$ for 134.6 < r < 198.6 cm (64 rows) and $6 \times 15 \ mm^2$ for r > 198.6 cm (32 rows).

Front-End Electronics and Readout:

Charged particles traversing the TPC volume ionize the gas along their path, liberating electrons that drift towards the end-plate of the chamber. The signal amplification is provided through avalanche effect in the vicinity of the anode wires of the readout chambers. The electrons and positive ions created in the avalanche, which move respectively towards the anode wire and the surrounding electrodes, induce a positive current signal on the pad plane. The current signal of a single avalanche is characterized by a fast rise
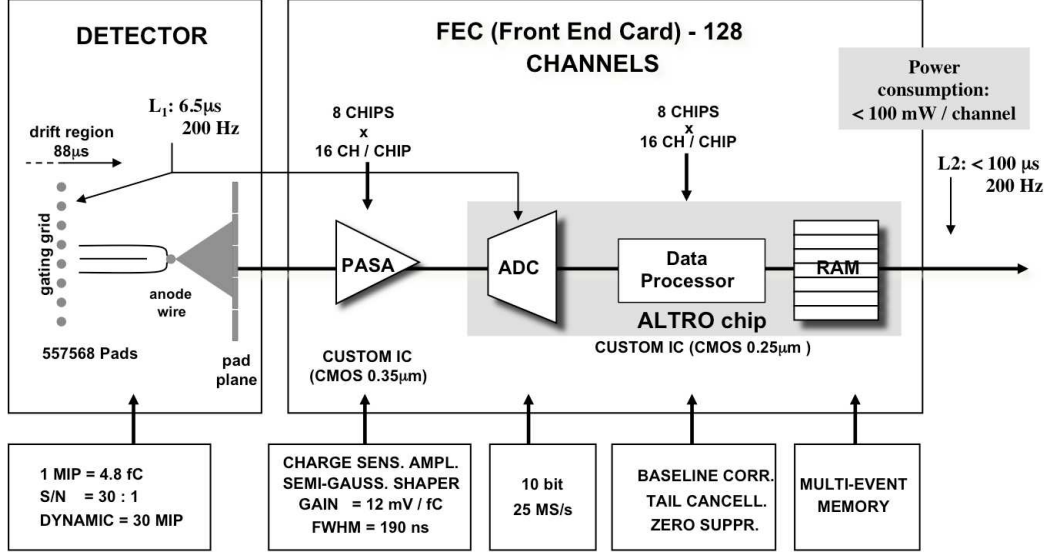
Figure 2.8: ALICE TPC frond end electronics.

time (less than 1 ns) and a long tail (of the order of 50 μs). The long tail is responsible for the pile-up effects.

Figure 2.8 shows the ALICE TPC front end electronics and readout functioning. The TPC readout is done by 557568 pads. The signals from the pads are passed to 4356 Front-End Cards (FECs), located 7 cm away from the pad plane, via flexible Kapton cables. In the FECs a custom-made charge-sensitive shaping amplifier, named PASA (PreAmplifier ShAper), transforms the charge signal induced in the pads into a differential semi-Gaussian voltage signal that is fed to the input of the ALTRO (ALice Tpc Read Out) chip. Each ALTRO contains 16 channels operating concurrently that digitize and process the input signals. Upon arrival of a first-level trigger, the data stream corresponding to the detector drift time ($\leq$100 μs) is stored in a memory. On receiving a second-level trigger (accept or reject) the latest event data stream is either frozen in the data memory, until its complete readout takes place, or discarded. The readout can take place at any time at a speed of up to 200 MByte/s through a 40-bit-wide backplane bus linking the FECs to the Readout Control Unit (RCU), which interfaces them to the Data AQuisition (DAQ), the Trigger and the Detector Control System (DCS). The tables 2.9 and 2.10 summarize the ALICE TPC electronics and ALICE TPC general parameters, respectively.

Front-End Cards (FECs)	121 per sector × 36 = 4356
Readout partitions	6 per sector, 18 to 25 FECs each
Total readout control units	216
Total pads — readout channels	557 568
Pad occupancy (for dN/dy = 8 000)	40 to 15% inner / outer radius
Pad occupancy (for pp)	5 to 2 × 10^{-4} inner / outer radius
Event size (for dN/dy = 8 000)	≈ 70 MByte
Event size (for pp)	0.1 – 0.2 MByte
Total bandwidth	35 GByte/s
Maximum trigger rate	300 Hz Pb–Pb central events
	1.4 kHz proton–proton events
ADC	10 bit
sampling frequency	5 – 10 MHz
time samples	500 – 1 000
Conversion gain	6 ADC counts/fC

Figure 2.9: ALICE TPC electronics parameters.

2.2.1.3   Transition Radiation Detector (TRD)

The ALICE TRD provides the the electron identification at high momenta above 1 GeV/c. TRD is very efficient in distinguishing electrons from pions above 1 GeV/c. The achieved pion rejection is better than 100 for particles above 1 GeV/c at an electron efficiency of 90% [20]. The detector is based on transition radiation (TR) e.g. photons with wavelengths in the region of soft X-rays. These radiations occurs when a charged particle propagates through boundaries between media that have different dielectric constants. The probability for the creation of such a photon is linearly dependent on the particles Lorentz factor γ. For example, particles with $p = 1$ GeV/c, : $\gamma(e\pm)/\gamma(\pi\pm) \approx 2000/7$.

TRD is located at radii from 2.9 m to 3.7 m. It consists of 540 individual readout detector modules and is segmented into 18 sectors called supermodules each containing 30 modules. In each sector, the modules are arranged in 5 stacks along z-direction forming six layers in radius. Figure 2.11 shows one layer that combines a radiator, a drift chamber, and readout electronics. The radiator facilitates the production of TR. The ionization radiation produces electrons in the counting gas (Xe/CO_2 (85:15)). Particles exceeding the threshold for TR production ($\gamma \sim 1000$) will in addition produce about 1.45 X-ray photons in the energy range of 1 to 30 keV. X-rays in this energy regime are efficiently converted by the high-Z counting gas with the largest conversion probability at the very beginning

Pseudo-rapidity coverage	$-0.9 < \eta < 0.9$ for full radial track length
	$-1.5 < \eta < 1.5$ for 1/3 radial track length
Azimuthal coverage	360°
Radial position (active volume)	$848 < r < 2466$ mm
Radial size of vessel (outer dimensions)	$610 < r < 2780$ mm
Radial size of vessel (gas volume)	$788 < r < 2580$ mm
Length (active volume)	2×2497 mm
Segmentation in φ	20°
Segmentation in r	2 chambers per sector
Total number of readout chambers	$2 \times 2 \times 18 = 72$
Inner readout chamber geometry	trapezoidal, $848 < r < 1321$ mm active area
pad size	4×7.5 mm² $(r\varphi \times r)$
pad rows	63
total pads	5504
Outer readout chamber geometry	trapezoidal, $1346 < r < 2466$ mm active area
pad size	6×10 and 6×15 mm² $(r\varphi \times r)$
pad rows	$64 + \quad 32 = \quad 96$ (small and large pads)
total pads	$5952 + 4032 = 9984$ (small and large pads)
Detector gas	Ne–CO_2–N_2 [85.7–9.5–4.8]
Gas volume	90 m³
Drift voltage	100 kV
Anode voltage (nominal)	1350 V (IROC)
	1570 V (OROC)
Gain (nominal)	$7000 - 8000$
Drift field	400 V/cm
Drift velocity (NTP)	2.65 cm/µs
Drift time (NTP)	94 µs
Diffusion (longitudinal and transversal)	220 µm/$\sqrt{\text{cm}}$
Material budget (including counting gas)	$X/X_0 = 3.5\%$ near $\eta = 0$

Figure 2.10: General parameters of ALICE TPC.

of the drift region. All electrons from ionization energy loss and X-ray conversions will drift towards the anode wires. After gas amplification in the vicinity of the anode wires the signal is induced on the readout pads. The readout electronics of TRD consists of 1.18 million channels.

The TRD is designed to derive a fast trigger for charged particles with high momentum. It is a part of Level 1 trigger. A built-in tracklet processor combines the information from the six layers to form tracklets which are used to identify high-momentum electrons which in turn provide a L1 trigger. Such a trigger is for example useful to increase the yield of Υs and high-p_T J/Ψs. The TRD needs a so-called pretrigger to wake up its electronics that is usually in standby to reduce the power consumption and thus heat production.
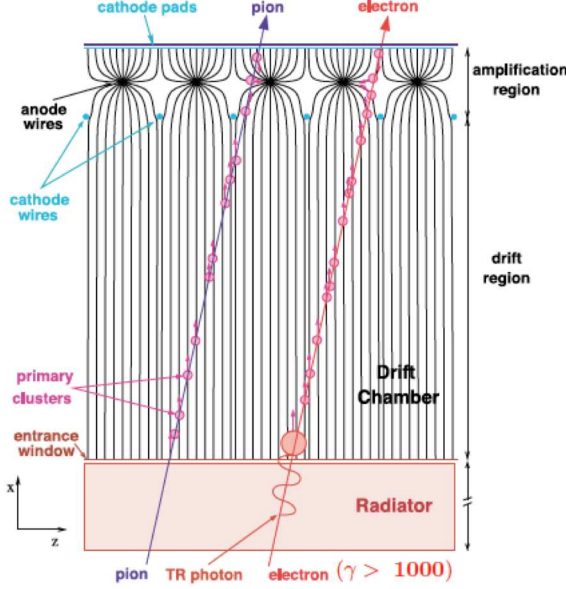
Figure 2.11: Schematic view of one TRD layer together with the clusters produced by an electron and a pion track.

2.2.1.4   Time Of Flight (TOF)

The TOF [21] detector uses the difference between the collision event time and time of arrival of the particles (pion, kaon, and proton) at the detector to identify them. It can provide the particle identification in the intermediate momentum range and extend the particle identification obtained using TPC at low momentum. The pions/kaons using TOF are well separated up to 2.5 GeV/c and kaons/protons can be separated up to momentum 4 GeV/c with better than 3σ. The TOF system provides the pretrigger signal to the TRD and an L0 trigger for the ultra-peripheral collisions.

The TOF is a gas detector based on Multi-gap Resistive Plate Chamber (MRPC). It is located at radii from 2.70 to 3.99 m and covers a pseudo-rapidity of $|\eta| < 0.9$. The basic unit of the TOF system is a 10-gap double-stack MRPC strip 122 cm long and 13 cm wide, with an active area of 120×7.4 cm^2 subdivided into two rows of 48 pads. The TOF consists of 90 modules. Every module of the TOF detector consists of a group of MRPC strips (15 in the central, 19 in the intermediate and external modules) closed inside a box that defines and seals the gas volume and supports the external front-end electronics and

services. The detector covers a cylindrical surface and the modules are arranged in 18 sectors in ϕ and in 5 segments in z-direction. Five modules of three different lengths are needed to cover the full cylinder along the z-direction. The length of the central module is 117 *cm*, the intermediate ones 137 *cm*, and the external ones 177 *cm*. The overall TOF barrel length is 741 *cm* (active region). The chambers have high and uniform electric field over the full sensitive gaseous volume of the detector. Any ionization produced by a traversing charged particle immediately starts a gas avalanche process which generates the observed signals on the pick-up strips. The setup achieves a very good time resolution of about 40 *ps*. The TOF detector has about 160 000 channels.
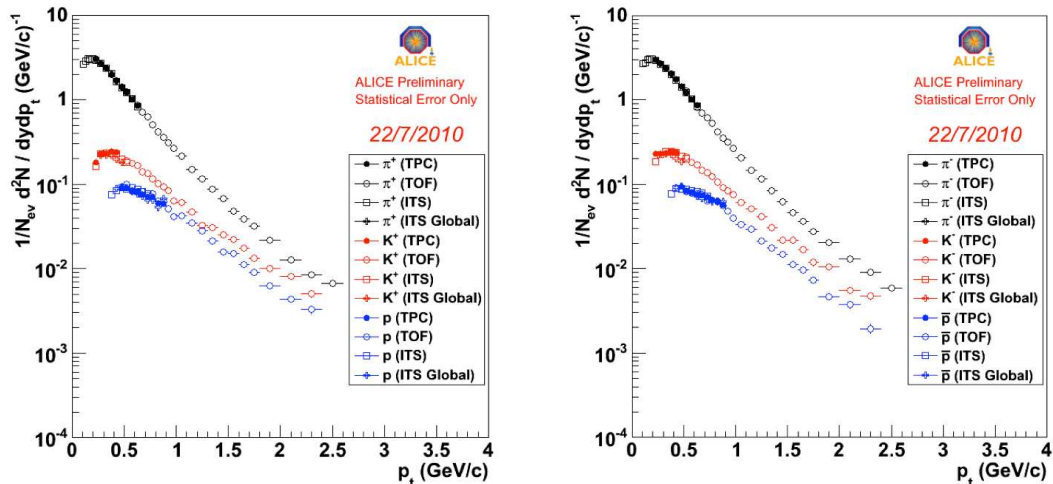
Figure 2.12: The spectra of pion, kaon, and proton for pp collisions at 900 GeV showing combined yields obtained from ITS, TPC, and TOF detectors covering different momentum regions. Left panel is for positively charged particles while the right panel is for the negatively charged particles.

The TOF along with ITS and TPC provides the nice particle identification of the particles over a large momentum range in the ALICE. As an example, Fig. 2.12 shows the spectra of pion, kaon, and proton for pp collisions at 900 GeV showing combined yields obtained from ITS, TPC, and TOF detectors covering different momentum regions. Clearly the three detectors complementary cover the wide range of momentum for the particle identification and are in well agreement with each other.

2.2.1.5   High Momentum Particle Identification Detector (HMPID)

The HMPID [22] is a proximity focusing Ring-Imaging Cherenkov (RICH) detector for particle identification of high-momentum hadrons. It extends ALICE PID capability of π/K and K/p-separation to 3 and 5 GeV/c, respectively, and therefore allows the inclusive measurement of charged particles within 1-5 GeV/c. The detectors acceptance covers about 5% of the central region phase space. The HMPID consists of 10m^2 of active CsI photocathode area.

2.2.1.6   PHOton Spectrometer (PHOS)

The PHOS [23] is a high resolution electromagnetic calorimeter primarily measures photons. By measuring the decay photons of e.g. π^0 and η, it provides their indirect measurements. The photons are discriminated from charged hadrons and neutrons partly with the topological shower analysis. The PHOS consists of 17920 detection channels based on lead-tungstate crystals, $PbWO_4$ (or PWO). It is positioned on the bottom of ALICE set-up at a distance of 460 cm from the interaction point and covers the region with -0.12 $< \eta < 0.12$ and 100° in azimuthal angle.

The detector is arranged in 5 modules with 3584 crystals in each. In front of PHOS, at a distance of about 5 mm, a Charged Particle Veto (CPV) detector is used to reject the charged particles. CPV is a Multi-Wire Proportional Chamber (MWPC) with cathode pad readout. The active volume is 14 mm thick gas mixture of Ar and CO_2 in the ratio 80:20 at a pressure slightly above atmospheric pressure.

2.2.1.7   ElectroMagnetic CALorimeter (EMCAL)

The EMCal [24] is a Pb-scintillator sampling calorimeter that measures photons, π^0, and η via their decay photons like the PHOS detector. It is, however, larger than PHOS with an acceptance of about 23% of phase space of the central region, but offers lower granularity and resolution. It covers a pseudorapidity range $|\eta| \leq 0.7$ and $\Delta\phi = 107^o$, and is placed almost opposite to the PHOS. It is arranged in 12 supermodule units of two types: full size which span $\Delta\eta = 0.7$ and $\Delta\phi = 20^o$, and one-third size which span $\Delta\eta = 0.7$ and $\Delta\phi = 7^o$. The lower 2 supermodules are one-third size type while the rest 10 are

of full size type. These supermodules are segmented into 12288 towers. The PHOS can provide a L0 and L1 trigger based on sums of deposited energy (towers) in sliding regions of the detector.

2.2.1.8   ALICE COsmic Ray DEtector (ACORDE)

ACORDE [25] provides a fast (Level-0) trigger signal, for the commissioning, calibration and alignment procedures of some of the ALICE tracking detectors, and it also detects in combination with the TPC, TRD, and TOF, single atmospheric muons and multi-muon events (so-called muon bundles) thus allowing to study high-energy cosmic rays in the energy region of knee in the cosmic ray spectrum. ACORDE is an array of plastic scintillator counters placed on the upper surface of the L3 magnet. It consists of two scintillator counters, each with $190 \times 20 \ cm^2$ effective area, placed on top of each other and read out in coincidence. The detector is arranged in 60 modules covering a pseudorapidity range of $|\eta| < 1.3$.

2.2.2   Forward Detectors

We now discuss the detectors located in the forward η region of the ALICE experiment.

2.2.2.1   Photon Multiplicity Detector

The PMD [26] measures the multiplicity distribution of inclusive photons (mainly decay from π^0) in the forward region ($2.3 < \eta < 3.7$, full azimuth). It consists of two gas chambers/planes with a lead converter of thickness $3X_0$ radiation length sandwiched between them. The two planes of the PMD are called Preshower plane and Charged Particle Veto (CPV). Each plane consists of large number of cells acting as individual gaseous proportional counters. The CPV is located twoards the interaction point (IR) and is used for improving the photon-hadron discrimination. Preshower plane is behind the lead plates.

The particles incident on PMD provide hit information on the CPV plane, passes through the lead converter and finally give hits at the preshower plane. If the incident particle is a charged hadron it will pass as it is through the lead converter and hit mostly one cell in the preshower plane. On the other hadron, the photons while passing through

the lead plates give electromagnetic shower and in principle hit more than one cells in the preshower plane. These hits produce signals in the preshower plane which is read by the Front End Electronics (FEE) consisting main component as MANAS chips. The PMD detector details and simulation part form the major part of this thesis and are discussed in details in chapters 3 and 4.

2.2.2.2   Forward Multiplicity Detector

The FMD [27] measures the charged-particle multiplicity over a large fraction of phase space, $3.4 < \eta < 1.7$ and $1.7 < \eta < 5.0$, both in full azimuth. The FMD can provide the measurements of event-by-event charged particle multiple fluctuations, determination of reaction plane and hence elliptic flow measurements. The PMD and FMD together can be used to study the correlation between photons and charged particles at forward rapidity.

The detector is composed of silicon strips located in five rings at z = 3.2 m, 0.83 m, 0.75 m, 0.63 m and 0.75 m. The total number of strips are 51200. The rings are of two types: the inner type consist of 10 wafers subdivided into 20 sectors with 1024 strips each. The outer type are subdivided into 40 sectors each with 512 strips. The Si wafers are 300 μm thick and are manufactured out of 6 diameter Si disks. FMD consists of three groups of detectors namely FMD1, FMD2, and FMD3. The FMD2 and FMD3 are located either side of the IR, while FMD1 is at 3.2 m from the IR towards FMD2 side.

2.2.2.3 V_0 Detector

The V_0 [27] detector is used to provide minimum bias trigger, reject beam-gas events, and provide pretrigger to the TRD. The V0 consists of two arrays of scintillator counters, called as V0A and V0C, which are installed on two sides of the ALICE interaction point. The V0A is located 340 cm from the IP in front of PMD covering a pseudorapidity range $2.8 < \eta < 5.1$ while the V0C is located at 90 cm from the IP on the side of muon spectrometer covering a pseudorapidity range -3.7 $< \eta <$-1.7. Both V0A and V0C, are segmented into 32 individual counters which are distributed into four rings. The time resolution is about 1 ns [28] which allows to identify the beam-gas events that occurred

outside of the nominal interaction region.

2.2.2.4 T_0 **Detector**

The T_0 [27] or ('time 0') detector performs several tasks in the ALICE trigger. It can measure the collision time with a precision of 25 ps. This information is used as a time reference for the TOF detector and to determine the vertex position with a precision of about 1.5 cm. If the vertex position is inside a window where interactions are expected an L0 trigger is issued. A vertex position outside the region where collisions happens is used as a beam-gas rejection signal. Furthermore, the T0 detector can also send a pretrigger to the TRD. It can also generate minimum bias and multiplicity triggers (semi-central and central).

The T0 consists of two arrays of Cherenkov Counters with 12 counters per array. The two arrays are called as T0-A and T0-C, which are installed on two sides of the ALICE interaction point. The T0-A is located 375 cm from the IP covering a pseudorapidity range $4.61 < \eta < 4.92$ while the T0-C is located at 72.7 cm from the IP on the side of muon spectrometer covering a pseudorapidity range $-3.28 < \eta < -2.97$. The T0 signal is generated online by a mean timer. The position of the T0 signal on the time axis is equal to (T0-C + T0-A)/2 +T_{delay}, where T_{delay} is the fixed delay of the analog mean timer. The position of vertex is measured as (T0-A) - (T0-C) and this value is sent to a digital discriminator with preset upper and lower limits thus providing the T0vertex trigger signal.

2.2.2.5 **Zero Degree Calorimeter (ZDC)**

The ZDCs [29] are the two identical sets of detectors located on either side of the IP at a distance of 116 m. The ZDCs provide an estimate of the impact parameter or centrality of heavy-ion collisions by the measurement of the number of spectator nucleons which is related to the energy carried forward, i.e. in beam direction.

ZDCs are composed of four calorimeters, two to detect neutrons (ZN) placed between the beam pipes at 0° relative to the LHC axis and two to detect protons (ZP) placed externally to the outgoing beam pipe on the side where positive particles are deflected.

The measurement is complemented by an electromagnetic calorimeter (called ZEM, 4.8 $< \eta < 5.7$) which measures the total forward energy at z $= 7.25\ m$. The ZDCs are "spaghetti calorimeters", made by a stack of heavy metal plates grooved to allocate a matrix of quartz fibres. The metal plates are made of a special material namely a tungsten alloy for neutrons and brass for protons. The material of the metal plates is known as "passive material", while the quartz fibres are known as "active material". High energy protons and neutrons hitting the passive material create a cascade of particle, called "shower". When one of these shower particles crosses a fibre, if its speed is high enough, it can produce light (Cherenkov effect). This light propagates in the fibre by total reflection up to its end, where a photomultiplier converts the light into an electric signal. The amplitude of the electric signal is proportional to the energy of the incoming protons and neutrons allowing to measure the energy carried away by the spectator nucleons and therefore, indirectly the size of the overlap region of the two colliding nuclei.
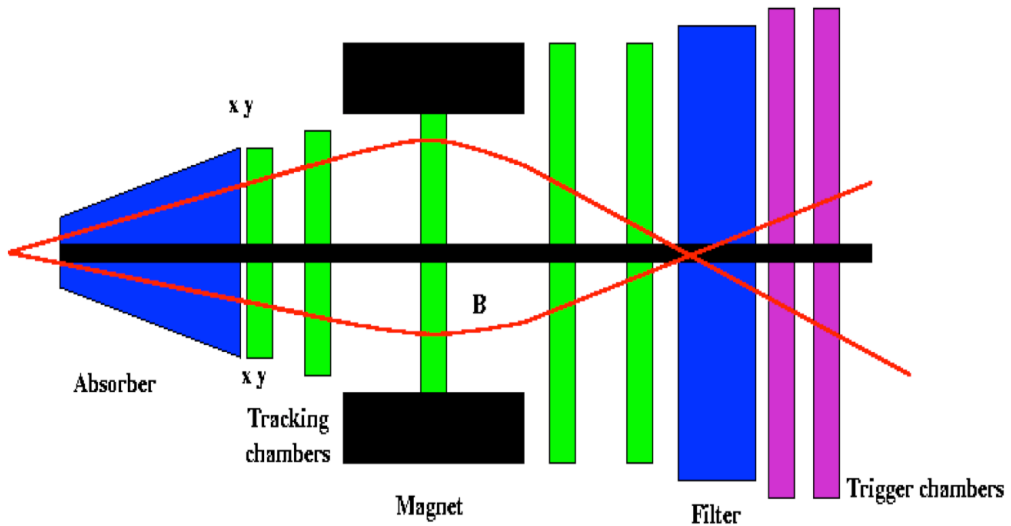
Figure 2.13: Schematic diagram showing main components of ALICE muon spectrometer.

2.2.3   Muon Spectrometer

The Muon Spectrometer [30] is used to measure the complete spectrum of quarkonia $(J/\Psi, \Psi', \Upsilon, \Upsilon', \Upsilon'')$, as well as ϕ mesons with good resolution. It can also be useful to

study open charm and beauty.

The spectrometer is located on the C side of the ALICE experiment. It accepts particles in $4 < \eta < 2.5$ and has full azimuthal coverage for muons with $p > 4$ GeV/c. This cut-off is due to the fact that to reach the spectrometer, muons first have to pass through the front absorber made of carbon, concrete, and steel (see Fig. 2.13). Successively they are measured by five tracking stations with two planes each made of very thin, high-granularity, cathode strip tracking stations. A dipole magnet is located outside of the L3 magnet to allow the muons momenta to be reconstructed. Two tracking stations are located in front of the dipole magnet. One tracking station is in its center; two are positioned behind the magnet. An iron wall of 1.2 m acts as a further muon filter after which two trigger stations with two planes each of resistive plate chambers are located. The whole spectrometer is shielded by means of a dense absorber tube against particles emerging from the beam pipe.

2.3 ALICE Subdetectors Acceptance

The ALICE subdetectors combinedly cover large phase space area to detect the particles produced in the high-energy collisions. Figure 2.14 shows the pseudorapidity distribution for the ALICE subdetectors. All the detectors except labelled with asterisk have the full azimuthal acceptance. The figure shows that the ALICE covers broad pseudorapidity range for particle detection.

2.4 ALICE Trigger, Computing and Software

As discussed before, the average particle multiplicity produced at the LHC is very large. As a result, ALICE detector has a challenging task of handling the large volumes of data. The data sharing and processing requires large resources. In the following sections and subsections, we discuss about the ALICE data collection, triggering, offline framework and finally the data analysis procedure for the final Physics results.
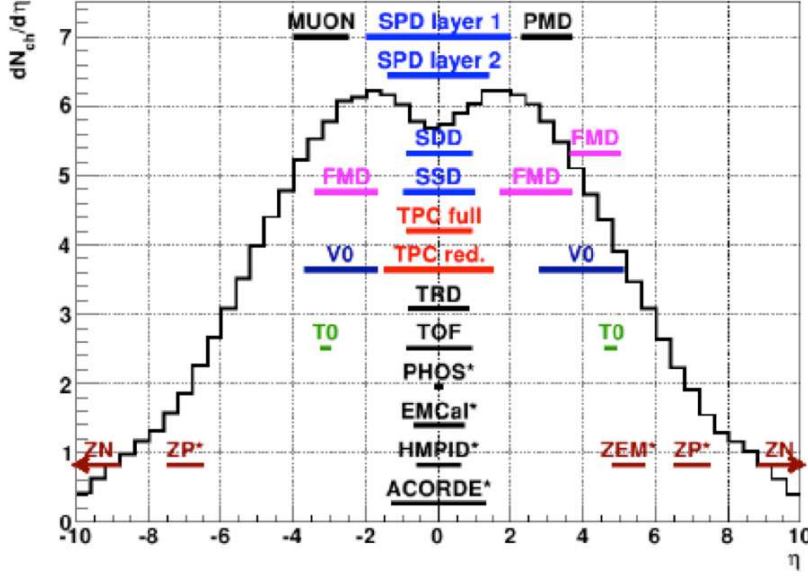
Figure 2.14: The pseudo-rapidity coverage of the ALICE subdetectors. Figure is adopted from the Ref. [31].

2.4.1   Data Acquisition (DAQ)

The main task of the DAQ system [13, 32] is to collect the data from individual subdetectors and build them into complete events (event building). The DAQ also provides buffering and exporting of assembled events to permanent storage. The ALICE DAQ is designed to process a data rate of up to 1.25 GB/s in heavy-ion runs. Event building is done in two steps. Data from the subdetectors is received by Detector Data Links (DDLs) on Local Data Concentrators (LDCs). The LDCs assemble the data into sub-events that are then shipped to Global Data Collectors (GDCs). A GDC receives all sub-events from a given event and assembles them into a complete event. Subsequently, these events are stored on a system called Transient Data Storage (TDS) that provides at present 45 TB of data storage. The DAQ has at present 83 LDCs and 43 GDCs while the fully equipped DAQ setup will comprise 200 LDCs and 60 GDCs.

ALICE can simultaneously take data in several partitions, where each partition consists of a set of subdetectors. Obviously a given subdetector can only be active in one partition at a time. The active subdetectors in a given partition are grouped into clusters

for which triggers can be defined. Therefore, upon a trigger only a subset of the whole partition may be read out. Furthermore, a triggering detector does not have to be necessarily part of the partition.

The Data Acquisition and Test Environment (DATE)

The DATE [13, 32] performs the processing, synchronization and data transmission tasks. DATE is the DAQ software framework. It is a distributed, process-oriented system designed to run on Unix platforms connected by an IP-capable network. The system configuration is realized with MySQL. The DATE controls and synchronizes the processes running in the LDCs and the GDCs. It can be run on the LDC or GDC or on a computer.

Monitoring Of Online Data (MOOD)

The MOOD [34, 35] is the DAQ framework for monitoring the quality of the data stream created by any ALICE detector. MOOD is the data visualization and data quality monitoring tool which includes a generic part implementing interface with DATE and a detector-specific part that can be tailored to detector-specific requirements and setups. The MOOD is fully integrated with the ROOT development toolkit, the AliRoot environment, and uses the ALICE common event data format. MOOD can handle on-line and off-line data streams, available on the LDCs and on the GDCs.

Automatic MOnitoR Environment (AMORE)

The AMORE [36] is also the DAQ framework which automizes the data quality monitoring. Each detector defines a set of physics plots which have to be continuously filled and checked against reference ones. The AMORE framework includes three components: the client part which collects the data, the server part which accumulates the plots and archives them, and the display program which provides an interactive distributed access to the plots archives. It employs alarm system which provide alarm in case the plots

do not conform anymore to the expected reference. These alarms are displayed on the operator screens and initiate automatic recovery actions.

2.4.2   Trigger System

The ALICE trigger system [37] is a two layer architecture. The Central Trigger Processor (CTP) is a ow-level trigger while the High-Level Trigger (HLT) is implemented as a pure software trigger. The CTP combines inputs from different trigger sources, i.e. the readout of various subdetectors and governs their readout. The HLT allows the implementation of sophisticated logic for the triggering. It receives a copy of the data read out from the subdetectors and processes it. The CTP and HLT triggers are briefly discussed below.

2.4.2.1   Central Trigger Processor (CTP)

The CTP trigger [38] combines the trigger signals of the various subdetectors to decide if an event is to be accepted which means that it is read out and written to disk. The accepted events have to pass different levels. The first level, called L0, is delivered after 1.2 μs, the second, called L1, after 6.5 μs. The final trigger, L2, is delivered after 100 μs (completion of the drift time in the TPC). The event is finally stored after the L2 trigger. The trigger logic acts upon numerous inputs: up to 24 L0, 24 L1, and 12 L2 input signals. These inputs can define up to 50 trigger classes but the inputs cannot be connected in an arbitrary way. Another task of the hardware trigger is to issue a pretrigger to wake up the TRD electronics which is needed in less than 900 ns after the interaction

The events having too many pile-ups are provided a past-future protection. The readout times of the different detectors vary significantly, therefore the window in which pile-up is recognized depends on the detectors that are part of the current partition as well as on the collision system. The rates of different trigger classes are very different. By definition minimum-bias triggers have the highest rate, other triggers that look for rare signals have much lower rates. Therefore, downscaling factors can be applied to the trigger classes individually. The total recording rate is limited by the maximum bandwidth of data that can be recorded to disk and tape. To prevent losing precious events and proper utilization of disk space, trigger classes are grouped into common triggers and rare triggers.

This ensures that if the utilization of the temporary storage is above a certain value (high water mark) then only rare triggers are accepted otherwise all triggers are accepted (low water mark).

2.4.2.2 High Level Trigger (HLT)

The HLT [39] is ALICE's software trigger consisting of farm of multiprocessor computers. It allows for more sophisticated triggers and can significantly reduce the event size by selecting regions of interest (partial readout of subdetectors) and by further compression of the data. The HLT system receives a copy of all relevant raw data via DDLs and the HLT Readout Receiver Card (H-RORC) into the Front-End Processors (FEP). The HLT is meant for online processing of a part of raw data and making decisions in order to select the relevant events or sub-events and to compress the data without loosing their physics content. The generated data and decisions are transferred to dedicated LDCs.

2.4.3 Data Handling

The raw data processing in ALICE is done in various steps as shown in Fig. 2.15. These steps are described below [40]. The raw data obtained from the subdetectors are processed by LDCs (Labelled as 1 in the Fig. 2.15). The GDCs (labelled as 2) build the global events from the data. Then the assembled events are registered into the AliEn system (labelled as 3) by the publish agents and shipped to the CERN computing center where they are stored on disks (labelled as 4). Finally the data are shipped permanently on to the tapes (labelled as 5) by the CASTOR system [41].

It is very important to have the information about the detector status and environmental conditions during data-taking. This information is provided by the subdetectors as *conditions data* and is relevant for the calibration of individual detector signals. Conditions data is produced by special programs that process the raw data stream and extract the needed values. These programs work in the realm of DAQ, DCS (Detector Control System), and HLT and store their output on to File eXchange Servers (FXS) (labelled 6-8). A dedicated program called Shuttle collects these outputs and makes them available to the reconstruction program. Furthermore, it retrieves information about the run
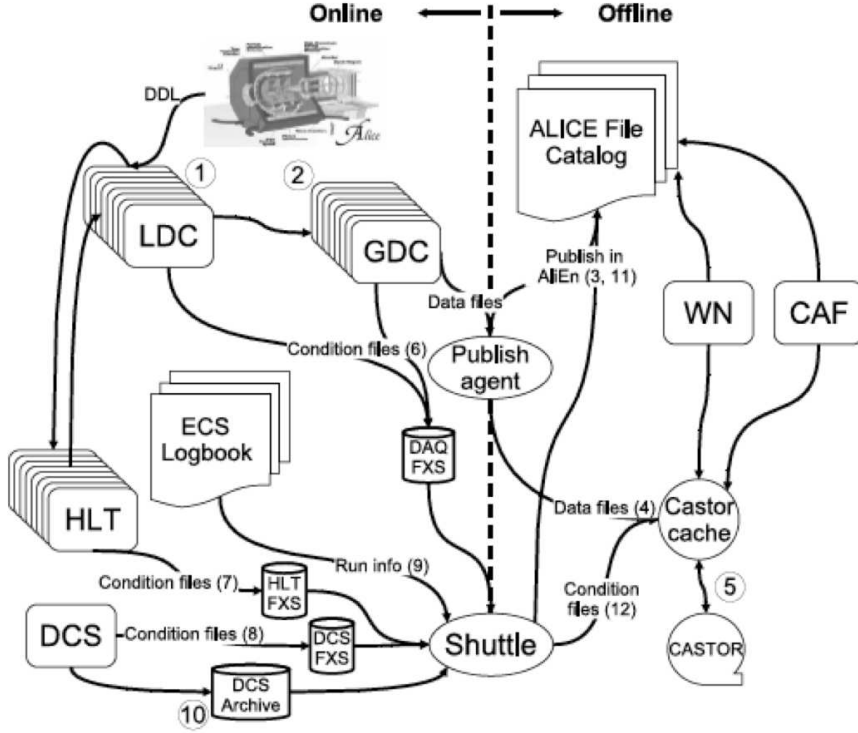
Figure 2.15: The ALICE data flow [40].

from the ECS logbook (labelled as 9) and collects continuously monitored values that are written by DCS into the DCS Archive (labelled as 10). After processing the data, the Shuttle registers the produced condition files in AliEn (labelled as 11) and stores the data in CASTOR (labelled as 12).

The transition from online to offline world is said to be done when the raw and conditions data have been registered. The online actions are performed in the real time while the offline processing is the subsequent step.

2.4.4 Offline Software Framework

The offline software framework includes main tasks such as simulation, reconstruction, calibration, alignment, visualization and analyses of the data. The data production of the LHC experiments is at the large scale. In ALICE, an average Pb-Pb event size is of about 13.75 MB and on average a pp event is about 1.1 MB. The challenging task is the reconstruction and analysis of this huge amount of raw data as well as the production

of simulated events needed for the understanding of the data. The required computing resources for these tasks are large and are beyond the capacity of a single institute or computing centre. Therefore data processing is distributed onto several computing centres located worldwide. There are around 80 such centres. The sharing and processing of data are provided through the Grid [42].

The Grid Middleware allows treatment of this collection of distributed computing resources as an integrated computing centre. ALICE uses the ALICE Environment (AliEn) system as a user interface to connect to the Grid composed of ALICE-specific services that are part of the AliEn framework and basic services of Grid middleware. The distributed computing infrastructure serving the LHC experimental program is coordinated by the Worldwide LHC Computing Grid (WLCG). The WLCG is highly hierarchical by nature. All real data originate from CERN, with a very large computing centre called Tier-0. Large regional computing centres, called Tier-1, share with CERN the role of a safe storage of the data. Smaller centres, called Tier-2, are logically clustered around the tier-1's. The main difference between the two is the availability of high reliability mass-storage media at Tier-1's. The major role of Tier-2's is simulation and end-user analysis. Smaller centre, corresponding to departmental computing centre and sometimes called Tier-3's, contribute to the computing resources but there is no definite role or definition for them.

2.4.4.1   AliEn Framework

The ALiEn is the ALICE Grid Environment [43]. It is basically a set of middleware tools and services that implement a Grid infrastructure. The AliEn framework works on three different levels - Central Services, VO-box, and Job Agent. Central services are the services running on a set of computers at CERN, managing and optimising the jobs and data distribution on the Grid. The VObox are the services running on a front end machine in each cluster providing resources to AliEn and managing the jobs on the cluster. The Job Agent is the service started by the VO-box on individual computing nodes, to run and manage single jobs.

AliEn has been used for both data production and end-user analysis. The AliEn

system is built around Open Source components, uses Web services models and standard protocols. AliEn web services play a central role in enabling AliEn as distributed computing environment. The user interacts with them by the exchange of Simple Object Access Protocols (SOAP) messages and they constantly exchange messages between themselves behaving like a true Web of collaborating services. The AliEn has been extensively tested and used for producing the large amount of simulated data and processing the data recorded in pp and in Pb-Pb collisions.

2.4.4.2   AliRoot Framework

AliRoot [44] is the ALICE offline framework based on ROOT framework [45]. AliRoot uses the C++ coding with some parts written in Fortran language. It is used for simulation, alignment, calibration, reconstruction, visualization, quality assurance, and analysis of experimental and simulated data. AliRoot has been used for the large-scale productions called Physics Data Challenge (PDCs) where millions of events are produced. These events are very useful in terms of optimizing experiment's design, physics performances, develop analysis procedures, and to estimate the associated errors. After data production from the detectors, AliRoot is used to reconstruct events that occurred in the detector.

The simulation framework includes following functions:

- **Event Generation**: The event generation involving generators such as Pythia [46], Phojet [47], or HIJING [48], is interfaced with AliRoot. The output is stored in the *kinematics tree* containing the full information about the generated particles.

- **Detector response**: The particles generated through the event generators are propagated through the detector material modeled as realistically as possible. The packages used to model the detector material and transport of the particles are Geant3 [49], Geant4 [50], and Fluka [51]. During the propagation, the particles undergo all possible interactions which they would undergo during the real experiment. The information is recorded as *hits* that contain the position, time, and energy deposit by due to interaction. Also the *track references* are stored that can be used to follow a track's trajectory, mainly needed for the debugging of the reconstruction

algorithms.

- **Digitization**: The hits are stored as a summable digit taking into account the detectors response function. Possible noise is then added to the summable digit and it is stored as a digit. Summable digits allow events to be merged without duplication of noise. In the last step, the data is stored in the specific hardware format of the detector (raw data).

  The raw data from the simulation at this stage corresponds to the signals that would be produced by an interaction of the same kind within the detector in real experiment. After this step, the reconstruction is identical, both for simulated as well as real events.

- **Cluster Finding**: Particles that interact with the detector usually leave a signal (hits) in several adjacent detecting elements or in several time bins of the detector. These signals are combined to form *clusters*. This allows the exact position or time of the traversing particle to be determined and reduces the effect of random noise. Overlapping signals from several particles in a single cluster are unfolded. This step is performed for each subdetector.

- **Track Reconstruction**: The tracking is done globally as well as for the individual detector. The global central barrel tracking starts from track seeds in the TPC which are found by combining information from a few outermost pad rows under the assumption that the track originated from the primary vertex. Tracks are then followed inwards using a procedure called the Kalman filter [52]. Any cluster that fits to the track is added to the track.

  Afterwards the same procedure is repeated by starting the seeding closer to the collision point. In a final step all clusters already associated to tracks are removed and the procedure is repeated without requiring that the seeds point to the primary vertex. The result, the so-called TPC-only tracks to which only TPC information contributed, is saved in the reconstruction output. Subsequently, these tracks are complemented with information from the ITS, TRD, and TOF as well as HMPID

and the CPV of PHOS if the track is in their acceptance which produces so-called *global tracks.* Tracks can also be formed using the information from the ITS only. Further details about tracking can be found in the Ref. [53].

- **Primary Vertex Reconstruction**: The various informations are used to find the primary vertex position of the collision. These include the clusters in the SPD, tracks in the TPC and global tracks. When a vertex position is found the tracks are constrained to it. This constraint is only used for tracks that actually pass in vicinity of the vertex. The vertex position is used as an additional point to estimate the track parameters. The TPC-only tracks are constrained with the vertex position found with TPC-only tracks while the global tracks are constrained with the vertex position found with global tracks.

- **Secondary Vertex Reconstruction**: The secondary vertices are formed to reconstruct the particles which get decayed to daughter particles prior to their detection. This is done by combining the tracks of unlike sign particles originating away from the primary vertex. A pair is accepted as potential secondary vertex if it satisfies certain criteria based on distance of closest approach and the topology of two tracks for decay.

When the full reconstruction is done, the information is stored as Event-Summary Data (ESD). It contains the high level or complete information for each event. For analysis purpose, all the information is not needed but rather less variables are needed. So the data is further filtered to Analysis-Object Data (AOD) format.

2.4.4.3   CERN Analysis Facility (CAF)

As discussed previously, the processing of large amount of data in ALICE is done through Grid using the AliEN framework. It requires the jobs to be submitted in Grid using batch-type approach. The jobs have to be submitted through a queue which is often long. Furthermore, if there is bug in the code or is in the developing stage, it becomes time consuming using the Grid.

In view of this, a system called CAF was set up. The main tasks which can be performed with CAF are as follows. It provides fast processing of the medium size data and allows interactive processing hence minimizing execution time. It is very useful to speed-up the code developing and fast debugging. In addition to prompt analysis of pp data and pilot analysis of Pb-Pb data, CAF also provides the fast event reconstruction, calibration and alignment. A fraction of the total data recorded by the experiment as well as some simulated data are available on the CAF. After all checks and debugging, the analysis code can be sent as a Grid job to subsequently process larger sets of data.

The access to the CAF data and perform analysis is provided by the parallel computing facility based on ROOT framework, called Parallel ROOT Facility (PROOF) [54]. It enables interactive parallel data processing on a computing cluster. The system works on the principle that the events can be processed in an arbitrary order and results obtained in parallel can be summed up after processing (event-based parallelism). The details of the implementation and performances of these facilities can be found in the Ref. [31].

Bibliography

[1] *http://www.bnl.gov/rhic/AGS.asp.*

[2] UC Radiation Lab Document UCRL-3369, "Experiences with the BEVATRON", E.J. Lofgren, 1956; Segré Nobel Lecture, 1960; "Bevalac Had 40-Year Record of Historic Discoveries" Goldhaber, J. (1992) Berkeley Lab Archive.

[3] *http://public.web.cern.ch/public/en/research/SPS-en.html.*

[4] *http://www.bnl.gov/rhic/*; M. Harrison, M. Harrison, T. Ludlam, and S. Ozaki, Nucl. Instr. Meth. A **499**, (2003) 235.

[5] J. P. Blaizot and E. Iancu, Phys. Rept. **359**, (2002) 355.

[6] J. Adams *et al.* (STAR Collaboration), Nucl. Phys. A **757** (2005) 102;

[7] T. S. Pettersson (ed.), P. Lef'evre (ed.), CERN-AC-95-05 LHC (1995); LHC Design Report Volume I+II+III, CERN-2004-003-V-1, CERN-2004- 003-V-2, CERN-2004-003-V-3 (2004), *http://ab-div.web.cern.ch/ab-div/Publications/LHC-DesignReport.html.*

[8] P. Lebrun, Interim Summary Report on the Analysis of the 19 September 2008 Incident at the LHC, CERN EDMS document no. 973073, ver. 1, https://edms.cern.ch/document/973073/1 (2008).

[9] ATLAS Collaboration, ATLAS Technical Proposal, CERN/LHCC 94-43 (1994).

[10] CMS Collaboration, The Compact Muon Solenoid Technical Proposal, CERN/LHCC 94-38 (1994).

[11] LHCb Collaboration, LHCb Technical Proposal, CERN/LHCC 98-4 (1998).

[12] LHCf Collaboration, Technical Proposal for the CERN LHCf Experiment, CERN/LHCC 2005-032 (2005).

[13] TOTEM Collaboration, TOTEM Technical Proposal, CERN/LHCC 99-7 (1999).

[14] ALICE Collaboration, "ALICE Technical Proposal for A Large Ion Collider Experiment at the CERN LHC", CERN/LHCC 95-71 (1995).

[15] K. Aamodt *et al.* (ALICE Collaboration),The ALICE Experiment at the CERN LHC, JINST 3 (2008) S08002.

[16] K. Aamodt *et al.* (ALICE Collaboration), Phys. Rev. Lett., vol. 105, p. 252301, 2010.

[17] ALICE Collaboration, ALICE Inner Tracking System (ITS): Technical Design Report, CERN-LHCC-99-012, *http://edms.cern.ch/file/398932/1.*

[18] ALICE Collaboration, ALICE Time Projection Chamber: Technical Design Report, CERN-LHCC-2000-001, *http://cdsweb.cern.ch/record/451098.*

[19] J. Alme *et al.*, Nucl. Instrum. Meth. A **622**, (2010) 316.

[20] A. Andronic et al. (ALICE TRD Collaboration), Electron identification performance with ALICE TRD prototypes, Nucl. Instrum. Meth. A 522 (2004) 40; C. Adler et al. (ALICE Collaboration), Electron / Pion Identification with ALICE TRD Prototypes using a Neural Network Algorithm, Nucl. Instrum. Meth. A 552 (2005) 364. A. Wilk, Particle Identification using a Neural Network Algorithm in the ALICE TRD, Ph.D. Thesis, University of Muńster, (2009).

[21] ALICE Collaboration, ALICE Time-Of-Flight system (TOF): Technical Design Report, CERN-LHCC-2000-012; http://cdsweb.cern.ch/record/430132; ALICE Time-Of Flight system (TOF): addendum to the technical design report, CERN-LHCC-2002-016, *http://cdsweb.cern.ch/record/545834.*

[22] ALICE Collaboration, ALICE high-momentum particle identication: Technical Design Report, CERN-LHCC-98-019, *http://cdsweb.cern.ch/record/381431.*

[23] ALICE Collaboration, ALICE Technical Design Report of the Photon Spectrometer (PHOS), CERN/LHCC 99-4 (1999), *https://edms.cern.ch/document/398934/1.*

[24] ALICE Collaboration, ALICE electromagnetic calorimeter: addendum to the ALICE technical proposal, CERN-LHCC-2006-014, *http://cdsweb.cern.ch/record/932676.*

[25] A. Fern'andez et al., Cosmic ray physics with the ALICE detectors, Czech. J. Phys. 55 (2005) B801; A. Fern'andez et al., ACORDE a cosmic ray detector for ALICE, Nucl. Instrum. Meth. A572, 102 (2007).

[26] ALICE Collaboration, ALICE Photon Multiplicity Detector (PMD): Technical Design Report, CERN-LHCC-99-032; http://cdsweb.cern.ch/record/451099; ALICE Photon Multiplicity Detector (PMD): addendum to the technical design report, CERN-LHCC-2003-038, *http://cdsweb.cern.ch/record/642177.*

[27] ALICE Collaboration, ALICE forward detectors: FMD, TO and VO: Technical Design Report, CERN-LHCC-2004-025, *http://cdsweb.cern.ch/record/781854.*

[28] F. Carminati *et al.* (ALICE Collaboration), ALICE: Physics Performance Report, Volume I, J. Phys. G 30 (2004) 1517.

[29] ALICE Collaboration, ALICE Zero-Degree Calorimeter (ZDC): Technical Design Report, CERN-LHCC-99-005, *http://cdsweb.cern.ch/record/381433.*

[30] ALICE Collaboration, ALICE dimuon forward spectrometer: Technical Design Report, CERN-LHCC-99-022; http://cdsweb.cern.ch/record/401974; ALICE dimuon forward spectrometer: addendum to the Technical Design Report, CERN-LHCC-2000-046, *http://cdsweb.cern.ch/record/494265.*

[31] J. F. Grosse-Oetringhaus, PhD thesis, University of Munster, Germany, 2009.

[32] F. Bergsma *et al.*, CERN ALICE DAQ Group, ALICE DAQ and ECS users guide, ALICE Internal Note ALICE-INT-2005-015, *http://cdsweb.cern.ch/record/960457.*

[33] J. P. Baud et al., ALICE data challenge III, ALICE Internal Note ALICE-INT-2001-36, *https://edms.cern.ch/document/336659/1.*

[34] O. Cobanoglu, et al., Development of an on-Line data quality monitor for the relativistic heavy-ion experiment ALICE, Proceedings of the IEEE RT2005, Real Time Systems conference, Stockholm Sweden (2005), *http://dx.doi.org/10.1109/RTC.2005.1547409*

[35] O. Cobanoglu, et al., The ALICE-LHC online data quality monitoring framework: present and future, Proceedings of the IEEE RT2007, Real Time Systems conference, Fermilab, Batavia Illinois U.S.A. (2007).

[36] F. Roukoutakis et al., The ALICE-LHC online data quality monitoring framework, Proceedings of the Computing in High Energy Physics (CHEP2007), Victoria BC Canada (2007), *http://cdsweb.cern.ch/record/1066450.*

[37] ALICE Collaboration, ALICE Technical Design Report of the Trigger, Data Acquisition, High-Level Trigger, Control System, CERN/LHCC 2003/062 (2004), https://edms.cern.ch/document/456354/2.

[38] ALICE Collaboration, JINST 3 S08002 (2008).

[39] A. Vestbo et al., The ALICE high level trigger, J. Phys. G30, s1097 (2004).

[40] K. Aamodt et al. (ALICE Collaboration), The ALICE Experiment at the CERN LHC, JINST 3 (2008) S08002.

[41] J. Durand, O. Barring, S. Ponce and B. Couturier, CASTOR: Operational issues and new developments, in Interlaken, Computing in high-energy physics and nuclear physics, 1221-1226 (2004).

[42] I. Foster and C. Kesselmann, The Grid Blueprint for a New Computing Infrastructure, 2nd edition, Morgan Kaufmann Publishers (2004).

[43] P. Saiz et al., AliEn ALICE environment on the GRID, Nucl. Instrum. Meth. A502, 437 (2003); *AliEn home page, http://alien.cern.ch/.*

[44] The ALICE experiment offline project,
     http://www.cern.ch/ALICE/Projects/offline/aliroot/Welcome.html

[45] R. Brun and F. Rademakers, ROOT: An object oriented data analysis framework,
     Nucl. Instrum. Meth. A 389, 81 (1997).

[46] H. -U. Bengtsson and T. Sjostrand, The Lund Monte Carlo for hadronic processes:
     Pythia version 4.8, Comput. Phys. Commun. 46, 43 (1987).

[47] R. Engel, Photoproduction within the two-component dual parton model. 1. Ampli-
     tudes and cross-sections, Z. Phys. C 66 (1995) 203. R. Engel and J. Ranft, Hadronic
     photon-photon interactions at high ener- gies, Phys. Rev. D 54 (1996) 4244.

[48] X. N. Wang and M. Gyulassy, HIJING: a Monte Carlo model for multiple jet produc-
     tion in pp, pA and AA collisions, Phys. Rev. D44, 3501 (1991); M. Gyulassy and X.
     N. Wang, HIJING1.0: a Monte Carlo program for parton and particle production in
     high-energy hadronic and nuclear collisions, Comput. Phys. Commun. 83, 307 (1994);
     http://www-nsdth.lbl.gov/xnwang/hijing.

[49] R. Brun, F. Bruyant, M. Maire, A. C. McPherson and P. Zanarini,
     GEANT3 user guide, CERN data handling division DD/EE/84-1 (1985),
     http://wwwinfo.cern.ch/asdoc/geantold/GEANTMAIN.html; M. Goossens et al.,
     GEANT detector description and simulation tool, CERN program library long write-
     up W5013 (1994), http://cdsweb.cern.ch/record/1073159.

[50] S. Agostinelli et al., Geant4, a simulation toolkit, Nucl. Instrum. Meth.
     A506, 250 (2003), CERN-IT-2002-003, http://cdsweb.cern.ch/record/602040;
     http://wwwinfo.cern.ch/asd/geant4/geant4.html.

[51] A. Fasso et al., FLUKA: present status and future developments, Proceedings of the
     IV International Conference on Calorimeters and their Applications, World Scientific,
     Singapore (1994).

[52] P. Billoir, Progressive track recognition with a Kalman like fitting procedure, Com-
     put. Phys. Commun. 57 (1989) 390.

[53] B. Alessandro et al. (ALICE Collaboration]) ALICE: Physics Performance Report, Volume II, J. Phys. G 32 (2006) 1295.

[54] M. Ballintijn, R. Brun, F. Rademakers and G. Roland, Distributed parallel analysis framework with PROOF, *http://root.cern.ch/twiki/bin/view/ROOT/PROOF.*

Chapter 3

PHOTON MULTIPLICITY DETECTOR (PMD)

3.1   Introduction

The Photon Multiplicity Detector (PMD) is a preshower detector, designed for the measurements of photon multiplicity and its pseudo-rapidity distributions in the forward rapidity region produced in nuclear collisions. PMD detector is designed and fabricated in India. It was first installed at the CERN SPS in the WA93 experiment [1], and then in WA98 experiment [2]. Later on PMD was installed in the STAR experiment at RHIC, BNL [3] and in the ALICE experiment at LHC, CERN [4] with the better fabrication, electronics and readout techniques which suit the high energy heavy-ion collision experiments. PMD is a gas detector which operates in the proportional counter region. It has a lead converter plate of three radiation length ($3X_0$) sandwich between two proportional counter planes. The front plane (closer to the interaction point) acts as a Charged Particle Veto (CPV) and the plane behind the converter act as the preshower plane [1, 5].

The PMD detector is installed in the ALICE experiment at the LHC. It enhances the phase space coverage of the ALICE experiment by covering the pseudo-rapidity region of $2.3 \leq \eta \leq 3.9$ with full azimuthal acceptance ($0 \leq \phi \leq 360$). It uses the gas mixture of Ar (70%) and CO_2 (30%) as the sensitive medium. The detector consists of an array of cellular hexagonal proportional counters with extended cathode design. The PMD in ALICE is positioned at a distance of 367.2 cm from the interaction point, in the opposite direction of the Muon Arm detector [2, 3] . The mechanical design, assembly,

Table 3.1: Response of a photon and hadron in the PMD

Incident particle	Signal in veto	Signal in preshower	Energy deposited	Number of cells hit
Hadron	yes	yes	MIP	~1
Photon	no	yes	Large (>MIP)	>1

signal processing, readout architecture and the software details are discussed in the later sections of this chapter.

3.2   Principle of photon detection

ALICE PMD has very fine granular structure. The principle of a preshower detector is schematically depicted in Fig. 3.1. The PMD consists of highly segmented detector called as preshower detector, placed behind a lead converter of thickness three radiation length. A photon produces an electromagnetic shower on passing through the converter (see Fig. 3.1). These shower particles produce signals in several cells of the sensitive volume of the detector [11]. Charged hadrons usually affect only one cell and produce a signal resembling those of Minimum Ionizing Particles (MIPs) [1]. The thickness of converter is optimized such that the conversion probability of photons is high and transverse shower spread is small to minimize shower overlap in high multiplicity environment [1]. In order to have better hadron rejection capability, another plane of the detector of identical dimension as of the preshower part is placed before the lead plate. This acts as a veto for charged particles, and accordingly called as Charged Particle Veto (CPV). The photon-hadron discrimination in the PMD is also illustrated in the Table 3.1.

---

[1]Minimum Ionizing Particle (MIP): The mean rate of energy loss for charged particles in a medium is given by Bethe-Bloch equation. Most of the relativistic particles have energy loss rates close to a minimum value, and are said to be minimum ionizing particles or mips [10].
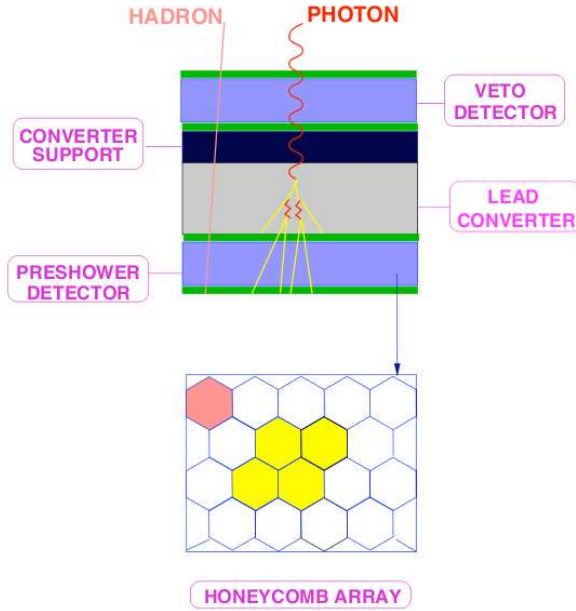
Figure 3.1: Schematic diagram showing a hadron and a photon track passing through a converter and hitting the preshower detector. The hadron track hits only one cell whereas the the photon track initiates an electromagnetic shower in the converter and hits several cells

3.3   Fabrication, Assembly and Readout

The PMD detector is fully fabricated and assembled in India at Variable Energy Cyclotron Center (VECC), Kolkata. A honeycomb chamber is a rectangular shape matrix of 48×96 (rows, columns) or 96×48 unit cells made up of a thin copper sheet of $0.2\ mm$ thickness. Each module is designed as an independent gas-tight unit, so that it can be fabricated, tested and installed individually. The module with 48 rows and 96 columns is known as "Short" type module, whereas module with 96 rows and 48 columns is called as "Long" type module. Figure 3.2 shows an unit cell, which is hexagonal in shape. Each module contains 4608 hexagonal cells as a basic unit, having $0.23\ cm^2$ cross-section and $0.5\ cm$ depth (shown in Fig. 3.2). PMD has total active area of $2\ m^2$ and total readout channels $\sim$182,000. Each plane (CPV and preshower) contain four super modules (SM) and each super module has six unit modules. This makes 48 total unit modules for PMD with each CPV and preshower plane containing about 24 unit modules. The lead plate of thickness
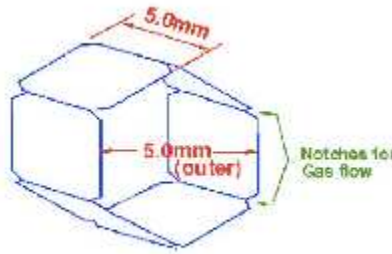
Figure 3.2: Schematic diagram of ALICE PMD unit cell.

1.5 *cm* is chosen so that it can meet the requirement of $3X_0$ thick material in front of the PMD for photon conversion while taking into account the 0.5 *cm* thick stainless steel support structure [2]. Each unit module is fabricated, tested and installed independently.

3.3.1 PMD Modules Assembly

The procedure for PMD module assembly is described below. The honeycomb chambers are first properly cleaned up using sand-blasting technique and then are made smooth using filling. Chambers dimensions are checked using a GO/NO-go jig, since they may get deformed during the cleaning process. These chambers are then properly cleaned using alcohol. The top and the bottom PCBs (Printed Circuit Board) are visually inspected and checked for correct dimensions. The leakage current between the anode island and the extended copper is measured [2].

The impurities present at the island adds to the leakage current and therefore need to be cleaned properly with alcohol to minimize the leakage current. The leakage current observed after such operations is of negligible amount, of the order of nano amperes.

The honeycomb chamber is placed over the bottom PCB. If the anode points on the PCB and the cell centres of the chamber matches properly then the top PCB is placed over it, as shown in Fig. 3.3 otherwise the honeycomb chamber is rejected. The top and the bottom PCBs are connected together with the help of 24 screws of diameter 1 *mm* and 12 wires of diameter 0.25 *mm* for Short type module while for Long type module 16 screws and 20 wires are used. All the screws and the wires are connected in the boundary
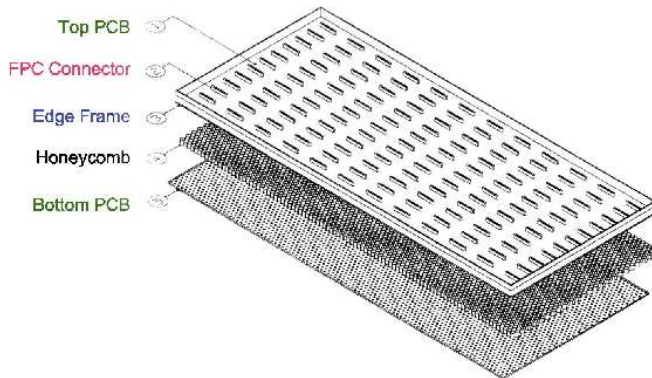
Figure 3.3: Assembly of unit module

region without disturbing the honeycomb cells except the six screws that are connected through the centre of the cell in place of anode wire. Therefore, each module contains six dead cells from the beginning. In the next step, gold plated tungsten wires of diameter 20 μm are inserted through the centre of each cell with the help of fine gauge hypodermic needle. Proper tension is applied on the wire during the soldering using a calibrated tensioning jig. It takes around 18 to 20 days for wire insertion for one module. Thirty two pin FPC connectors are then fixed on the top PCB at their appropriate position. One connector covers 32 cells. There are 72 connectors in a module. It takes 2 to 3 days in fixing all the connectors on one module. A visual inspection is performed with the help of a video zoom magnifier and any discrepancy in the soldering is rectified. To cut the extra wire projecting after the soldering point a resistive heating technique is used. Now again the visual inspection is performed from both top and bottom side. These modules are then kept in an air tight container filled with Ar-gas.

The modules are made gas tight with a proper mechanism for gas inflow and outflow. For this stainless steel (SS) rectangular frame with a base plate of 2 mm thick FR4 material is made. It contains the nozzles for gas inflow and outflow and also a place is kept to mount the high voltage box to the chamber. The SS frame contains groove from inside all along its length for gas flow which is covered by a perforated strip of FR4 material to ensure uniform gas flow throughout the module. This also acts as an insulation between the honeycomb chamber and the SS frame [2, 3].
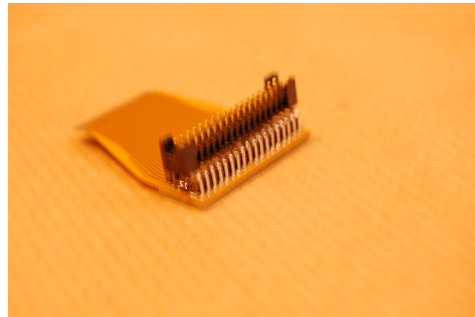
Figure 3.4: View of Kapton cable, which connects FEE board to translator board.

3.3.2 Front End Electronics and Readout

The honeycomb structure forms a common cathode, operated at a high negative voltage. The signal is read out from the anode wires at ground potential. The signals from the anode wire is collected by the Front End Electronic Boards (FEE boards) connected to the detector with the help of flexible kapton cables, shown in Fig. 3.4. Signals are then processed and digitized by the FEE boards and then sent to the Translator Board (TB) via. back plane. Figure 3.5 show the pictorial representation of the FEE board (Left panel) and the translator board (Right panel). Translator board sends these signals to the Cluster Readout Concentrator Unit System (CROCUS) with the help of Patch Bus cables. The CROCUS transfers these signals further to the Data Acquisition System (DAQ) with the help of Detector Data Link (DDL) [11]. All these readout components are discussed below in details.

Front End Electronics (FEE) Board

The left panel of the Fig. 3.5 shows the front view of the Front End Electronics (FEE) board. The block diagram of the operation of FEE board is shown in Fig. 3.6. Each Front End Electronics (FEE) board of PMD consists of the following:

- Four Multiplexed ANAlog Signal Processor (MANAS) chips [12]

- two inverting buffer amplifiers

- two serial 12bit ADCs (AD7476) and
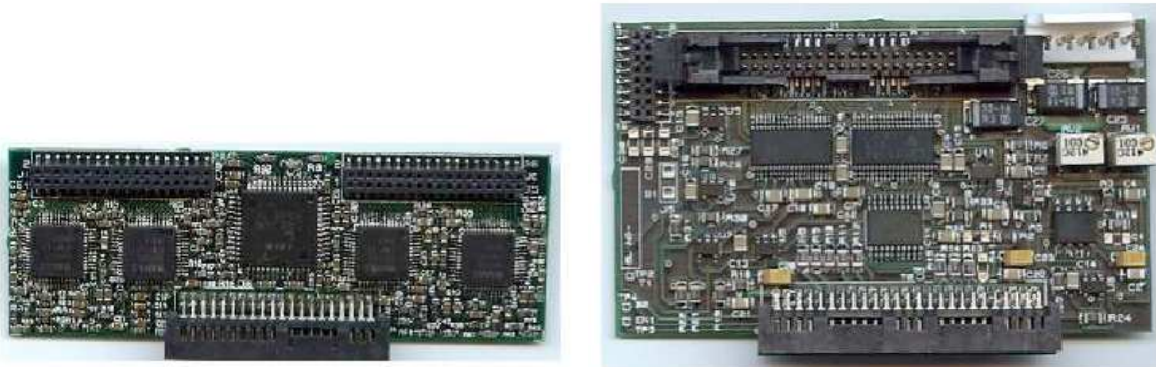
Figure 3.5: Left: Front End Electronics (FEE) board and Right: Translator Board.

- a Muon Arm Readout Chip (MARC).

  The basic functions of the Front End Electronics (FEE) board are as follows:

 i) Reads 64 analog signals from the honeycomb cells

 ii) Converts Analog to digital by serial 12 bit ADC (AD7476)

iii) Communicate with CROCUS-DAQ through link port bus (4 bit)

The MANAS chip has sixteen input channels and one output channel. Figure 3.7 shows the operation of MANAS chip in the form of block diagram. The Charge Sensitive Amplier (CSA), Deconvolution Filter (DF), Semi Gaussian Shaper (SGS), Track/Hold and the analog multiplexers are the main components of the MANAS chip. The input charge collected from the anode wire of the honeycomb proportional counters is integrated by the CSA on its feedback capacitor. The signals from the gas detector contains hyperbolic tails due to slow motion of ions. The DF removes this long tail and ensures base line restoration. The SGS shapes the pulses to Semi Gaussian shape which is essential to avoid pile up. It improves the signal-to-noise ratio and ensures faster base line restoration. The time constant of the shaper is kept large to avoid ballistic decit and ensure maximum charge collection. A properly timed Track/Hold pulse opens the switch at the instant when the peak of the input signal arrives. The analog multiplexer consists of 16 switches. Output of these switches are connected together and this line forms the output line from the chip. Switches are controlled by clock (CLK) signals.
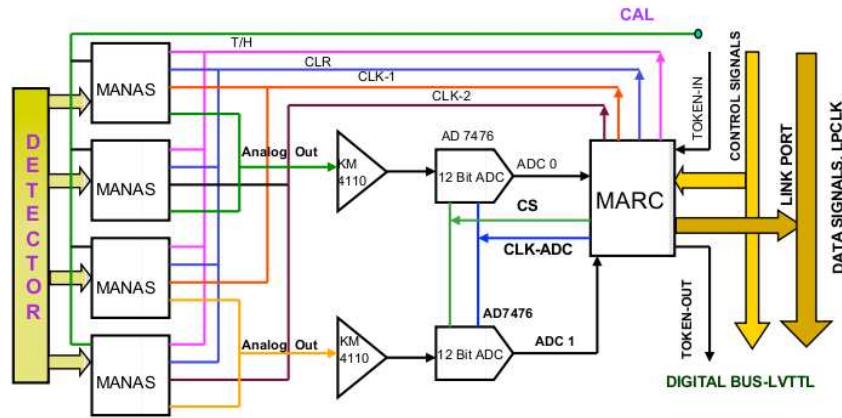
Figure 3.6: Block diagram of the Front End Electronics (FEE) board.
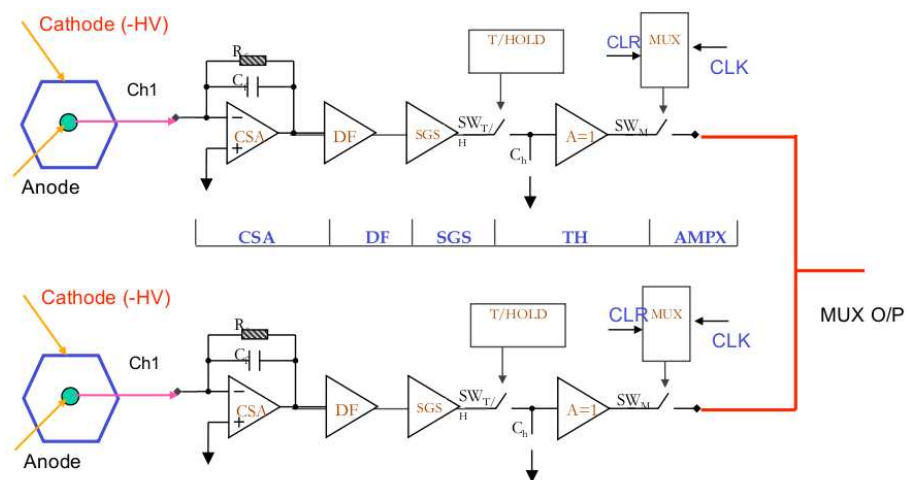
Figure 3.7: Block diagram of MANAS chip.

As explained in Fig. 3.6, buffer amplifiers are of inverting type. The signal coming from the detector is negative. It is needed to be inverted since the ADCs can accept only the positive signals. This buffer amplifier performs the inversion. ADCs convert the analog signal coming from MANAS. The ADCs are 12-bit serial ADCs with analog input and digital output. The digitized output signal is sent to the MARC. The functions of MARC are listed below:

- Controls 4 MANAS Chips by generating CLK, CLR, Track/Hold for MANAS on receipt of trigger.

- Controls two serial 12-bit ADCs by generating Chip select and reading from ADC by sending the clock (SCLK).

- Channelised threshold values are stored in a 64×12-bit word RAM.

- 12-bit ADC words are stored in a temporary register (Shift Register) and compared with threshold RAM words.

- Data above threshold are stored in a 64 word $\times$ 18 bit FIFO (First In First Out) together with a 6-bit channel address (6-bit for 64 channels).

- The 64×18-bit words are merged with 11-bit module address (FEE address) along with one parity and two control bits forming 32-bit word.

- The resulting 32-bit word is then sent through a Link Port (LP) as 8-nibbles of 4-bits each.

- Performs zero suppression on data.

- Communicates with ADSP 2106N through a 4-bit bus i.e Link Port bus.

Translator Board

The right panel of Fig. 3.5 shows the view of translator board. The function of translator board can be explained using Fig. 3.8. All the signals: four data bits (LPD0, LPD1, LPD2, and LPD3) , CLK (LPCLK) and token back) from the FEE board are of Low
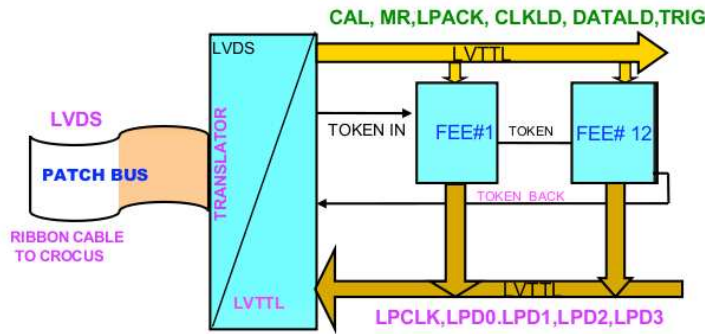
Figure 3.8: Schematic diagram of patch bus cable, translator board and FEE boards.

Voltage TTL (LVTTL) type and all the signals from CROCUS are of Low Voltage Differential Signals (LVDS) type. The Translator Board (TB) converts all LVTTL signals from the FEE board to LVDS levels before sending to the CROCUS. It also translates all the LVDS signals from CROCUS (i.e TRIG, MR, CLKLD, DATALD, LPACKL, and TOKEN IN) to LVTTL and send it to FEE board. The low voltages to the chain (one chain consists of 12 FEE boards) is fed through the translator boards using the backplane PCB. For adjusting the threshold levels of the signals Trim pots are available on the translator board [3].

Patch Bus Cable

To transfer the LVDS signals from the translator board to CROCUS and vise-versa flexible flat and twisted pair cables known as PATCH BUS cables are used. It is a halogen free forty core cable with 1.27 mm pitch having 40-pin female type SAMTEC connectors at both ends. The cable is shielded with aluminium tape to minimize the Electro-Magnetic Interference (EMI). The length of these cables are kept around 8.5 m. There are 200 patch bus cables used for the readout of PMD.

CROCUS

The Cluster Readout Concentrator Unit System (CROCUS) is one of the main readout components of the ALICE-PMD detector. It is composed of the three main boards the CROCUS-Back board, the CROCUS-FRT board (Frontal board) and the CROCUS-CRT
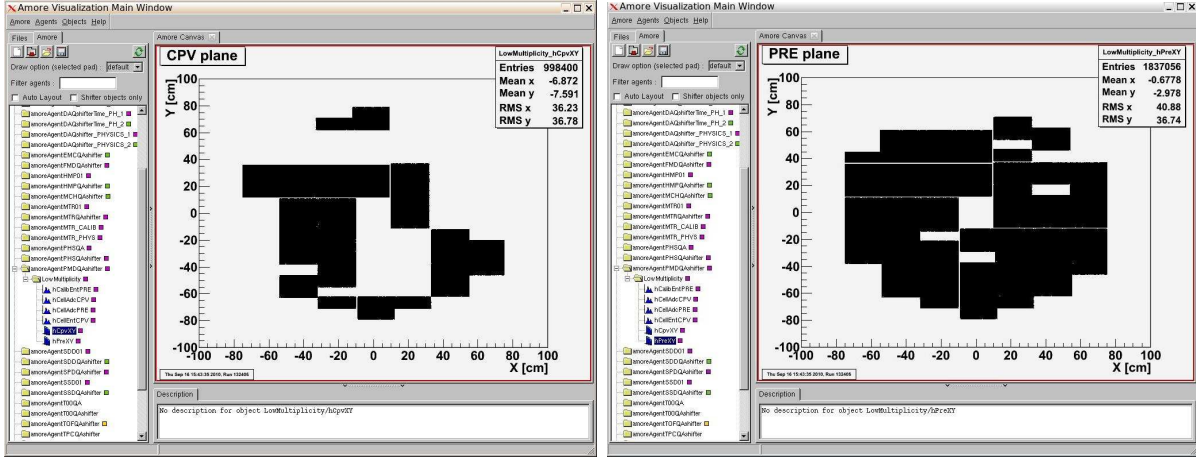
Figure 3.9: 2-D pedestal plot for CPV and preshower plane in AMORE.

board (Concentrator board). One CROCUS consist of five FRT boards and one CRT board. The main features of the CROCUS are

- gather and concentrate the information coded on the FEE boards,

- pass the data to the Data Acquisition System (DAQ),

- drive the FEE boards via patch bus controllers,

- receive and distribute the trigger signals,

- allow the calibration of the detector, and

- detect the breakdown in the data acquisition chain.

Data Acquisition (DAQ) System

The details of the ALICE DAQ [11] system are given in section 2.4.1 of the previous chapter. The main task of the DAQ system is to collect the data from individual sub-detectors and build them into complete events. This is called event building. The DAQ utilizes three frameworks: Data Acquisition and Test Environment (DATE) [13], Monitoring Of Online Data (MOOD) [14, 15], and Automatic MOnitor Environment (AMORE) [16]. The DATE performs the processing, synchronization and data transmission tasks. The MOOD monitors the quality of the data stream created by any ALICE detector and used for data visualization. The AMORE automizes the data quality monitoring.

The PMD detector being one of the sub-detector of the ALICE takes part in the event building through DAQ and utilizes its various frameworks. The DAQ is also used for the testing purpose of the modules. For ALICE-PMD the output is in terms of ADC channel number obtained from the FEE boards. The intrinsic noise of electronics of each channel gives rise to a finite read out value known as "pedestal". Pedestal values depend on the design of the electronics and the operating environment. During final data recording, the raw data is not pedestal subtracted, therefore before doing any analysis on raw data, the first step is to subtract the pedestal. A dedicated data taking known as pedestal run are taken in the absence of beams for a large number of events. From the pedestal distribution, mean and the rms of the pedestals are calculated for each channel and stored in a file for offline use. It is found that the pedestal of each channel is reasonably stable (~ 250 ADC) with a very small fluctuation (rms = ~ 1). The data quality monitoring is automatized through AMORE. Each detector defines a set of physics plots which have to be continuously filled and checked against reference ones. Figure 3.9 shows one of the example of 2-D plot of pedestal hits on CPV and preshower plane.

3.3.3 Support Structure (SS)

The main structural support for the PMD detector is a twin boxed stainless steel girder which is designed to move on the rails of the ALICE experiment mini-frame and can carry the weight of the ALICE-PMD. This girder can transport the PMD in z-direction, using a sprocket-chain system, from the beginning of the rails to the final position. Two movable carriages are provided on this girder and stainless steel support plates of 5 mm thickness are attached to these carriages. The suspension screws on these carriages can provide leveling adjustment to the SS support plate and the plates can be side open or closed around the beam pipe using a hand operated screw mechanism.

Ten unit modules are mounted on either side of each support plate at specied locations using guide rail fixtures. Space is provided on the sides of the plates to accommodate all the Low Voltage Distribution Boards (LVDB). Patch panels mounted on the sides of these plates carry all the LV, sense and HV connectors. All the Embedded Local Monitor Board (ELMB) modules which are used for the Detector Control System (DCS) are

mounted at the bottom of these support sheets.

A thin FR4 copper clad sheet covers each side of these sheets and act as a cooling enclosure and also as EMI shield. Cooled air is forced from the bottom of the support plates to reduce the heating caused by thermal dissipation of the front end electronic boards. Hot air travels upwards and enters the hollow boxed girder through the holes provided on the bottom face of the girder and is extracted out through ports provided on the girder. The support structure can be moved about a meter away from the final position to facilitate servicing on both sides of the detector.

3.4 PMD Modules Testing and Quality Assurance

The modules are fabricated in India at VECC center, Kolkata and tested properly and then dispatched to CERN for installation in the ALICE experiment. Before installation, all the modules and their electronic parts are tested again at CERN.

3.4.1 Gas Leak Test and Insulation Test

A mixture of Ar + CO_2 (in the ratio 70:30 by weight) is flushed through the module at a pressure slightly greater than the atmospheric pressure. The gas leakage from the module is detected using a leak detector. If leakage is found at any point, then it is fixed using the araldite. Gas flushing helps in removing out the small impurities and moisture from the detector and in maintaining the equilibrium state of the gas mixture.

Leakage current is also measured during gas flushing which is essentially the boundary leakage current. The boundary leakage current normally decreases with time which is also known as seasoning of the module. The module is kept for few days under this condition depending upon the value of the leakage current. If there leakage current is very high and does not decrease with time then the module is rejected.

3.4.2 Leakage Current and Spark Rate Test

The modules which passes through gas leakage and current leakage test are put to next step. High voltage is applied in steps with the help of shorting connectors and the Dual In-line Package (DIP) switches. The high voltage is raised till 1700 V and kept it for three

to four days. The modules are kept in gas flushing condition with shorting connectors. Followings points are monitored:

- If the module does not trip for 3-4 days and shows nearly zero leakage current then this module is considered as good module.

- If the module shows high leakage current i.e. $\sim 5 \; \mu A$ in the beginning and $\sim 3 \; \mu A$ in later stage of the testing, then the procedure is to look for the channel or zone responsible for this high current. This channel or zone is referred to as hot channel or zone. Once, the hot channel or zone is detected, the ground connection of this channel or zone is cut and made inactive. In this way, the high leakage current in the module is avoided. This process introduces some dead cells in a module.

- It is recommended that the modules should be kept under high voltage (HV) and gas flushing condition for longer period. It helps in reducing the leakage current and the conditioning of the module due to continuous flushing of impurities and stabilizing the high voltage conditions of the honeycomb cells.

- It should be noted that, sometimes there are many hot channels or zones in a module which produces high leakage current and module keeps on tripping. These type of modules take longer time ($\sim$ few weeks) to pass through leakage current and spark rate tests. If the cutting of hot channels and zone does not reduce leakage current below 5 μA value, this module is rejected and considered as bad module.

- After the above tests on modules, they are tested with readout channels. The backplane, FEE boards, kapton cables and translator boards are mounted on the modules which are considered as good modules. Figure 3.10 shows one of such example of a long type module. The high voltage (HV) of module is raised till 1400-1425 V slowly, with the current trip limit set to 4-5 μA. If the module does not trip for 2-3 days and sustain this HV, then this module is considered as ready for the installation in the ALICE experiment.
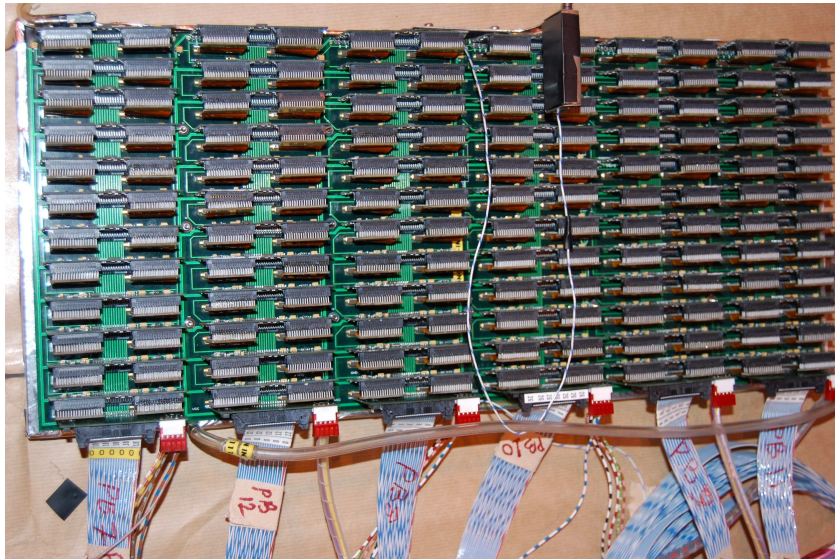
Figure 3.10: A long type module with backplane, HV box, FEE boards, kapton cables, translator boards and patch bus cables mounted on it.

3.4.3   Few Problems

Some of the problems which are normally faced during PMD module testing and quality assurance tests are as follows:

CROCUS BUSY

When the modules are kept at high voltage near to 1000 V value with CROCUS connected through patch bus cables and Data Acquisition System is run, the CROCUS never become busy. If the high voltage to modules are increased to 1350 V or higher, CROCUS become BUSY after few hours of DAQ running. This problem could be due to HV sparks, as the spark rate increases with the high voltage and could produce EMI (Electro Magnetic Interference) radiation. The CROCUS has to be hard reset to run DAQ again.

MARC Address Loss

It is observed that sometimes the MARC (Muon Arm Readout Chip) address of some of the FEE boards is lost. It mostly occurs when there is a spark in the module. In this
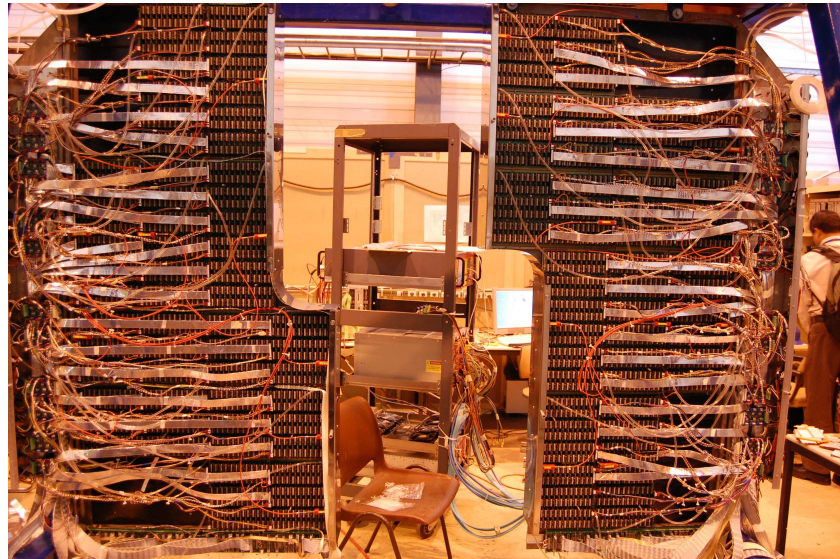
Figure 3.11: PMD prepared to be installed in the ALICE experiment.

situation the pedestal of PMD detector is taken so as to load the MARC address again.

The modules which pass through all the above explained quality assurance tests are mounted on the CPV and preshower planes of the PMD. The black color plates in the figure are the three radiation length lead converter.

3.5 Installation and commissioning of the PMD in ALICE at LHC

Figure 3.11 shows the picture of PMD on support structure in the surface area at point-2, CERN. The detector is almost prepared to be install in the ALICE experiment. In the installed version, there are 20 modules in each plane, four corner modules are not installed. Some chains in modules situated on the periphery are not connected as the four CROCUS units can only service up to maximum of 200 chains. Five modules each on top left and bottom right are of short type and the rest are of long type. Overall this provide almost full azimuthal coverage ($\geq$90%) in the pseudo-rapidity region 2.3 to 3.9.

3.6 Test Results for the ALICE-PMD

The performance of the ALICE-PMD has been studied with some of the PMD modules using the pion and electron beams at various energies and for different detector configurations at the T10 beam line at the CERN PS. The main aim of the ALICE-PMD modules testing are:

1. to understand the response of the detector to the MIPs,

2. to optimize the detector operational parameters e.g., the operating voltage, etc.

3. to understand the uniformity of cells over a module, and

4. to understand the interaction properties of hadrons.

As a result, a calibration relation between the energy deposition calculated in GEANT (in keV units) and the digitized electronic signal (in ADC units) had been obtained. This relation is fed to AliRoot-PMD software to simulate energy deposition in ADC units.

3.6.1 Test Beam Set Up

The PMD test beam experiment set up in May 2009 is shown in the Fig. 3.12. The detector modules are mounted exactly in the same fashion as in the real experiment. There are two modules and a lead converter sandwiched in between them. The module facing the beam pipe acts as the CPV plane while the other which is behind the lead converter works as the preshower plane. A charged hadron passing through the CPV and preshower plane in general, deposits energy like a minimum ionizing particle (MIP) in both the detectors. Photons do not deposit any energy in the CPV plane but deposit large energy in a number of cells in the preshower plane. Different values of lead thickness $(2X_0, 3X_0$ and $4X_0)$ in addition to no lead, in between CPV and preshower plane are used to study the response of the detector to MIPs. The detector modules are mounted on the X-Y stand which have the movement facility along both horizontal and vertical directions, so as to expose a desired cell to the beam. The high voltage (HV) to the detector modules

Figure 3.12: Picture of Test Beam Setup in 2009 in T10 area.

is applied by SY1527-CAEN high voltage power supply (HVPS) and low voltages (LV) through 3009-B CAEN modules which are being used in the real experiment as well. The data was readout by the CROCUS using the patch bus cables of similar length as being used in the real experiment.

The trigger requirements were different for pion and the electron beams. Figure 3.13 shows the schematic diagram of different trigger signals generated using scintillator paddles. For triggering a pion beam, we have used a five fold coincidence from a set of scintillators. As shown in the top panel of Fig. 3.13, the set of scintillators P1 and P2 are the two crossed scintillators kept near the beam pipe and P3 and P4 are another two crossed scintillators kept near the detector end. These crossed scintillators are placed in a straight line. There is a small scintillator of 0.3 cm × 0.3 cm size, also known as Finger Scintillator (FP), is kept just in front of the detector module. The finger scintillator is used to make sure that the incident particles fall in one detector cell (note that detector cell diameter is 0.5 cm). The coincidence of these five scintillators are used for triggering a pion beam.

For electron triggers, a Cherenkov detector is introduced in between the two pairs of crossed scintillators and the finger scintillator (FP). The threshold in Cherenkov detector
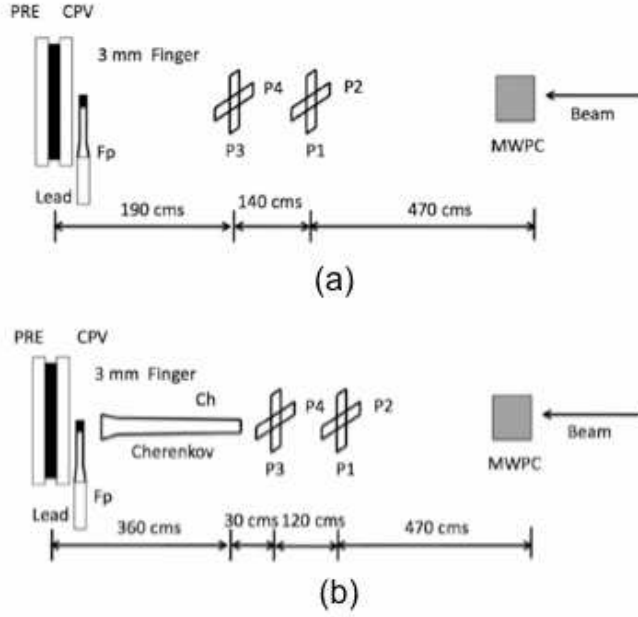
Figure 3.13: Schematic view of PMD test beam 2010 setup. (a) Pion beam triggered using five fold scintillators coincidence. (b) Electron beam triggered using four fold scintillators coincidence.

is set such that it signals an electron beam. The coincidence of P3, P4, Cherenkov and the Finger Scintillator (a four fold coincidence) is used as a trigger for electron beam, as shown in the bottom panel of Fig. 3.13. The pion beam of 3 and 5 GeV energy and the electron beams of energies 2, 3, 4 and 5 GeV are used for this study.

3.6.2   Simulation Study and Data Analysis

One of the aims of the test beam experiment is to test the software framework. Therefore, the data are analyzed in the AliRoot framework using the full reconstruction chain. Clustering was done with the default setting of "Crude Clustering" as used for the analysis of LHC pp data. The details of the reconstruction chain and the clustering routine are discussed in the next chapter of the thesis. The data is recorded by the CROCUS and are reconstructed. The properties of the reconstructed clusters are then studied. A calibration relation between the energy deposition calculated in GEANT (in keV units) and the digitized electronic signal (in ADC units) is required to transform the simulated data
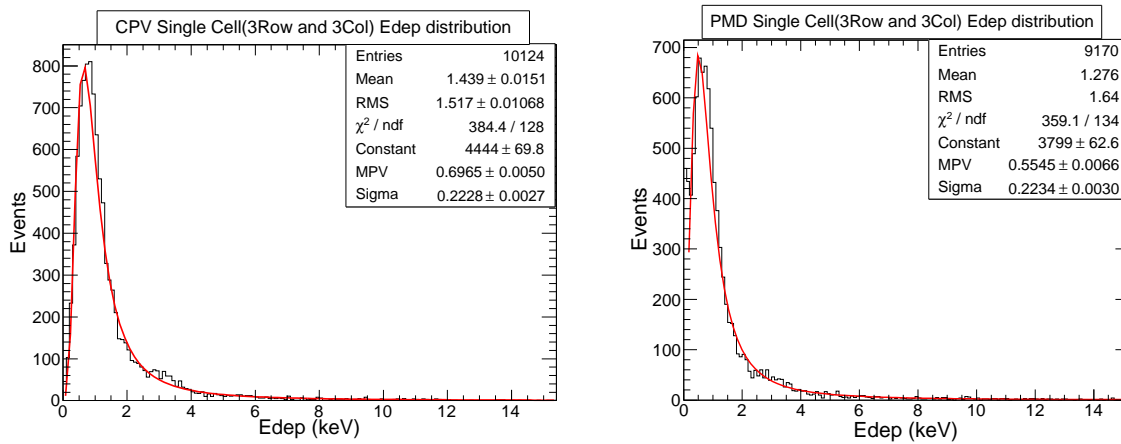
Figure 3.14: Energy deposition in a cell for the CPV and preshower planes by 5 GeV pion (π^-) beam.

in 'RAW' format so that the same reconstruction chain is employed to analyse both the simulated and LHC data. The calibration relation for a wide range of energy deposition and ADC values is deduced from the preshower data.

3.6.2.1   Simulation Study

To simulate the test beam setup, we have generated pion (π^-) and electron (e^-) particles in a small pseudo-rapidity and azimuthal window ($\Delta\eta$, $\Delta\phi$) using the single particle box generator in the AliRoot framework [17]. In total 10k events are generated for pions and electrons separately.

Pion Beam

The response of the charged particles (hadrons) to the PMD modules is studied using pion (π^-) beam of energy 5 GeV. The setup of the detector is shown in the top panel of Fig. 3.13. Figure 3.14 shows the energy deposition in a cell distribution for 3 rows and 3 columns around the maximum ADC cell as center for the CPV and preshower planes with $3X_0$ lead converter. The distributions are fitted with the Landau function. The total number of cells hit for 10k events are shown in Fig. 3.15 on the CPV and preshower planes with $3X_0$ lead converter. It can be seen from the figure, that in more than 90% of the cases pions are confined to a single cell. While calculating the MIP value maximum
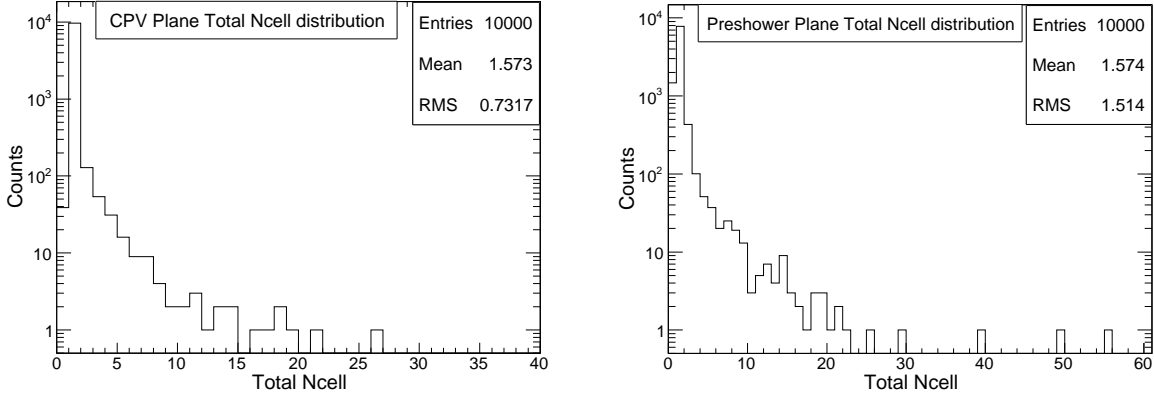
Figure 3.15: Total number of cells hit distribution on the CPV and preshower plane for 5 GeV pion (π^-) beam.

three cells contribution is taken.

The left panel of Fig. 3.16 shows the variation of MPV as a function of operating voltage for 3 GeV pion beam. It is seen that the MPV value increases with the operating voltage. Efficiency of the PMD modules for charged particles is calculated by taking the ratio of the detected events and the incident events for the pion beam. The incident events are defined as the triggered pion beam events. The right panel of Fig.. 3.16 shows the charged particle efficiency of the PMD modules as a function of operating voltage for 3 GeV pion beam. It is observed that the efficiency increases with the increase in operating voltages and becomes almost constant beyond 1300 Volts.

To understand the uniformity of the cells over a module the most probable value (MPV) of the ADC distribution for different cells are studied. Figure 3.17 shows the MPV distribution for 81 randomly selected cells on the CPV plane (top panel) and 76 randomly selected cells on the preshower plane (bottom panel). It is observed from the mean and the sigma of the distribution that the cell-to-cell gain variation is small i.e. about 6.85% for the preshower plane and 10.72% for the CPV plane.

Electron Beam

The main aims of the electron test beam is to understand the electromagnetic shower properties and to compare the cluster ADC in simulation and data, and thereby estab-
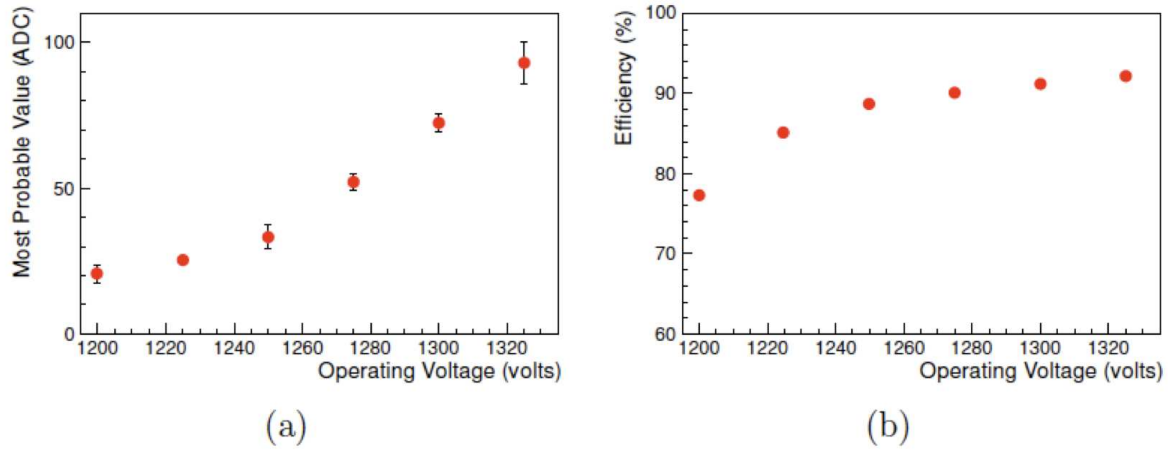
Figure 3.16: (a) Variation of Most Probable Value (MPV) as a function of operating voltage; and (b) Charged particle efficiency as a function of operating voltage of the PMD modules for 3 GeV pion beam.
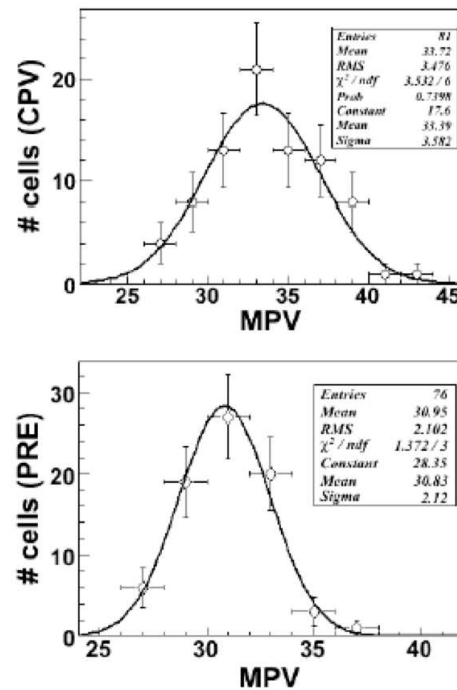
Figure 3.17: The MPV value of the ADC distribution is plotted for 81 randomly selected cells on the CPV plane (top) and for 76 randomly selected cells on the preshower plane (bottom). The figure is taken from the Ref. [20].

lishing a calibration relation between the energy deposition in terms of keV to the energy deposition in terms of ADC. It should be noted that the electron beam produce electromagnetic showers while passing through the lead converter. During the data taking, the trigger condition is defined in such a way that only one electron falls on the detector for most of the time. It is therefore, expected that one cluster should form near the finger position in each event. Figure 3.18 show the energy deposition in a cell distribution for 3 rows and 3 columns around the maximum ADC cell as center on the CPV and preshower planes for the electron beam. The left plots show the energy deposition for the test beam data collected at an operating voltage of 1350 V and the right plots are the simulation results. The top panel show the plots for electron beam of energy 3 GeV and $3X_0$ as lead thickness and the bottom panel show the similar plots but with $4X_0$ as lead thickness. The energy deposition distributions are fitted with the Gaussian function. More details of data analysis for the pion and electron test beam experiment can be found in the Refs. [17, 18, 20].

3.6.2.2   Edep to ADC Conversion

Now we discuss the results from the test beam which lead to the conversion relation of energy deposition (Edep) in the PMD in keV units to ADC values. This relation is important and useful while analyzing the real data.

The left panel of the Fig. 3.19 shows the variation of most probable value (MPV) of the energy deposition as a function of different electron beam energy. The results taking energy deposition distribution taking all hit cells, cell with maximum ADC, cell with maximum ADC and 1 cell around it (cluster 1) and taking 2 cells around it (cluster 2) are shown by different labels. The right panel of the figure show the variation of MPV value of energy deposition as a function of different lead thickness (X_0) for electron beam of 3 GeV energy.

The detector was tested in the year 2009 at an operating voltage of 1350 V and a calibration relation had been obtained during that run [17]. However, it was noted during the LHC pp run that (a) the MIP signal being deduced from data was different from that obtained in the test run and, (b) the detector was not running smoothly at the
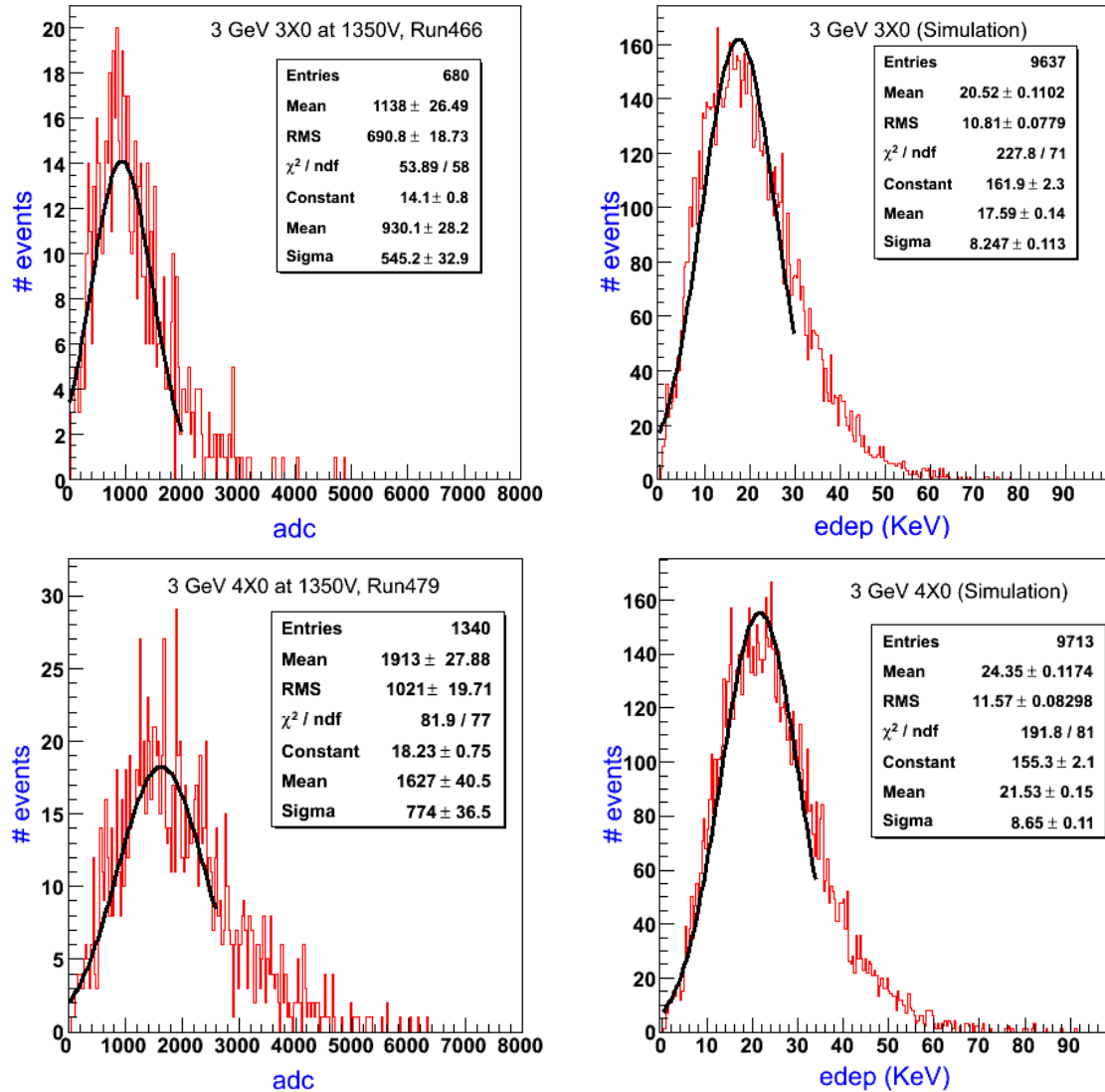
Figure 3.18: Energy deposition in a cell for the CPV and preshower planes by 3 GeV electron (e^-) beam. Left panel: For the test beam data collected at an operating voltage of 1350 V; Right panel: For the simulation data.
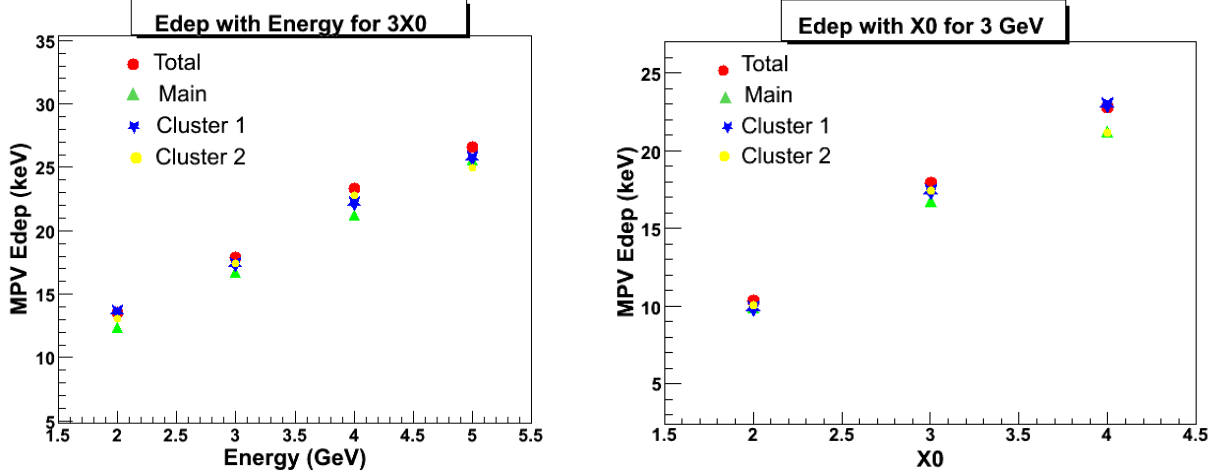
Figure 3.19: Left plot: The variation of MPV value of energy deposition as a function of different electron beam energy is shown. Right plot: The variation of MPV value of energy deposition as a function of different lead thickness for electron beam of 3 GeV energy is shown.

operating voltage of 1350 V. After various investigations, one of the prime suspects for the difference in the values of MIP signal obtained during LHC pp runs and the earlier test beam runs was found to be the composition of the gas mixture. In the 2009 PS tests, the gas handling system used rotameters where there had been some instability of the readings, particularly for CO_2 line, which affected the ionization process significantly. The effect of this instability could not be gauzed till data analysis was complete and a discrepancy was noted between the MIP values obtained in test beam runs and the LHC pp runs.

In order to understand the issue of MIPs and to investigate the possibility of a lower operating voltage, another test beam run was planned in June, 2010 in the CERN PS area. An important component of the tests was to study the MIP response for various gas mixtures. The pion beam of 3 GeV energy and the electron beams of energies 1 GeV, 2 GeV and 3 GeV are used for this study.

The obtained relation between the mean energy deposition in the detector as given by GEANT Monte Carlo simulation (in keV units) and the mean ADC in test beam for the operating voltage of 1300 V (in ADC units) is displayed in Fig. 3.20. A straight line
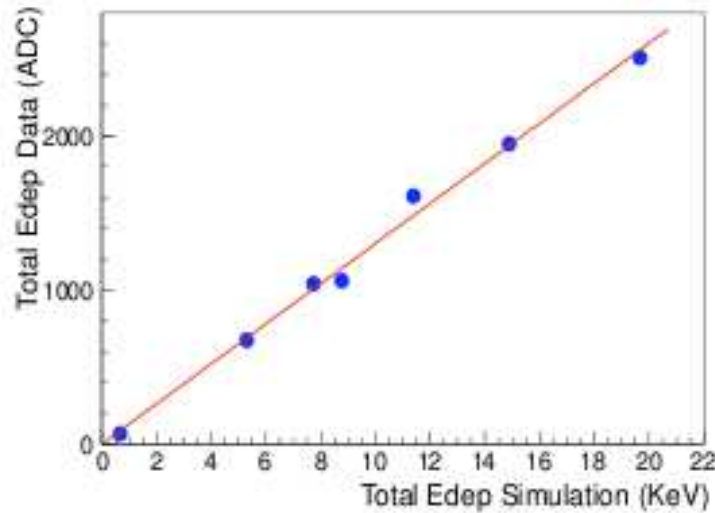
Figure 3.20: The calibration relation obtained in 2010 test run for 1300 V operating voltage.

fit well describes the data points and denotes the calibration relation as shown below:

$$ADC = slope \times Edep + y - intercept \tag{3.1}$$

The parameters obtained from the straight line fit are used to convert GEANT energy deposition in keV to ADC in the ALICE-PMD simulation study. The calibration relation has subsequently been incorporated in the AliRoot reconstruction chain. To check the compatibility of obtained new calibration relation with the data, we have generated simulated data and applied the conversion relation as in Eq. 3.1. The simulation results are then compared with the data and shown in the Fig. 3.21. It is observed that both the Monte Carlo and the data do agree quite well.

3.6.3   Summary

Testing of the PMD detector which is installed in the ALICE experiment is done at the PS Test Beam line, at CERN in May 2009 and June 2010. The pion and electron beams of varying energy were used to carry out this study. It helped to understand the response of the PMD modules to the charged particles. The charged particle efficiency as a function of operating voltage and cell to cell gain variation in the CPV and preshower planes is
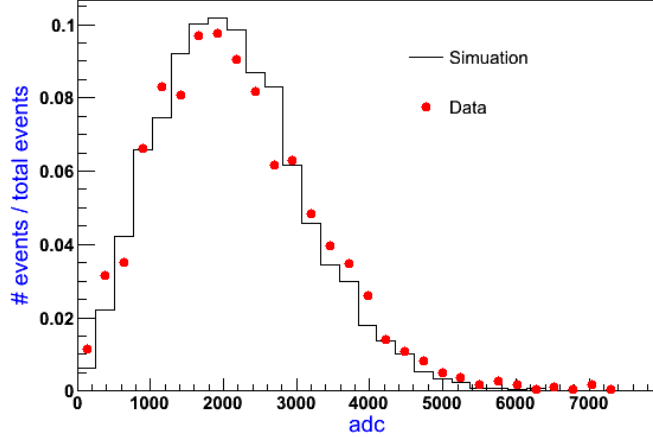
Figure 3.21: The comparison of energy deposition in data and simulation framework after including calibration relation.

studied. The efficiency increases with the operating voltage and becomes constant after 1300 Volts. Hence, the optimized operational voltage of the PMD detector is taken as 1300 Volts. The cell to cell gain variation in a module is found to be very small ($\sim 10\%$). The conversion relation of energy deposition (Edep) on the PMD modules in keV units to ADC values is also obtained, shows linear behavior of the form Eq. 3.1. This relation is used for the PMD simulation studies to compare the simulation results with the real data.

Bibliography

[1] WA93 Collaboration, CERN/SPSC/90-14, SPSC/P-252, 1990.

[2] H.H. Gutbrod *et al.*, Proposal for a large acceptance hadron and photon spectrometer, CERN/SPSLC/91-17, CERN-P260, 1991, 87p.

[3] K. H. Ackermann *et al.*, Nucl. Instr. Meth. **A499** (2003) 624.

[4] ALICE Collaboration, JINST **3** (2000) S08002.

[5] M.M. Aggarwal *et al.*, Nucl. Instr. Meth. in Phys. Res. **A372** (1996) 143.

[6] M.M. Aggarwal *et al.*, Nucl. Instr. Meth. **A488** (2002) 131.

[7] ALICE Technical Design Report on Photon Multiplicity Detector, CERN/LHCC/99-32 (1999).

[8] ALICE Technical Design Report on Photon Multiplicity Detector, Addendum-1, CERN/LHCC 2003-038 (2003).

[9] William R. Leo, Techniques for Nuclear and Particle Physics Experiments, First Narosa Publishing House Reprint (1995).

[10] C. Caso *et al.* Particle Data Group, Eur. J. Phys. C **3** (1998) 1.

[11] CERN ALICE DAQ Group, ALICE DAQ and ECS users guide, ALICE Internal Note ALICE-INT-2005-015, *http://cdsweb.cern.ch/record/960457*.

[12] ALICE Dimuon Forward Spectrometer Technical Design Report, CERN/LHCC 99-22.

[13] J. P. Baud *et al.*, ALICE data challenge III, ALICE Internal Note ALICE-INT-2001-36, *https://edms.cern.ch/document/336659/1.*

[14] O. Cobanoglu *et al.*, Development of an on-Line data quality monitor for the relativistic heavy-ion experiment ALICE, Proceedings of the IEEE RT2005, Real Time Systems conference, Stockholm Sweden (2005), *http://dx.doi.org/10.1109/RTC.2005.1547409.*

[15] O. Cobanoglu *et al.*, The ALICE-LHC online data quality monitoring framework: present and future, Proceedings of the IEEE RT2007, Real Time Systems conference, Fermilab, Batavia Illinois U.S.A. (2007).

[16] F. Roukoutakis *et al.*, The ALICE-LHC online data quality monitoring framework, Proceedings of the Computing in High Energy Physics (CHEP2007), Victoria BC Canada (2007), *http://cdsweb.cern.ch/record/1066450.*

[17] Test Beam simulation results 2009, *http://nsharma.web.cern.ch/nsharma/TestBeam2009/Simulation/electron/TestBeam2009_new1.html.*

[18] A.K. Dash, Institute of Physics Bhubaneswar Internal Report IP/BBSR/2009-7, Ph.D. Thesis Utkal University, 2009.

[19] M.M. Mondal, Ph.D. Thesis, Univ. of Calcutta, 2010.

[20] S. K. Prasad, Ph.D. Thesis, Univ. of Calcutta, 2011.

Chapter 4

PMD Simulation

A photon passing through the lead converter in front of the preshower plane of the PMD produce electromagnetic showers. However, most of the hadrons pass through the converter plate without any interaction [1–3]. Test beam and simulation studies have revealed that incident photons deposit signal in more than one cell since the electrons and positrons coming out of the shower deposit energies in a group of cells on the preshower plane whereas charged hadrons deposit energy typically in a single cell. It is necessary to study the interaction of photons and charge hadrons with the converter and to adapt some algorithm to obtain the photon clusters in each event and reject the hadrons (hadron clusters). The main steps for photon reconstruction followed for the PMD detector is schematically shown in the Fig. 4.1.

In this chapter results on the simulation study are presented using AliRoot (ALICE Software) framework. It is the ALICE offline framework based on ROOT [4] and uses C++ programing [5]. AliRoot enables the simulation and reconstruction of the collisions and act as a basis for data analysis framework. In simulation framework, particles are generated by event generators such as GUN, BOX, PYTHIA [6], HIJING [7], PHOJET [8], HERWIG [9] etc. These particles passing through the detector geometry in the ALICE experiment using GEANT3 code [10] produce signal (hits) in the ALICE sub-detectors, which are reconstructed further using software.

4.1   Simulation Framework

The particles produced using the event generator pass through the detector and produces detectable signals. Figure 4.1 depict the steps followed for photon reconstruction in the ALICE-PMD detector in the form of flow chart. These steps are discussed in detail as follow:

- The particles passing through the PMD detector hit the cells (of CPV and preshower plane) and deposit energy which are stored as hits in a ROOT compatible file known as 'PMD.Hits.root'.

- All the energies deposited in a cell in one event are then summed together and the output is stored in other file known as 'PMD.SDigits.root', which is also ROOT compatible.

- The energy deposition are recorded in the units of GeV. These signals are then digitized using the parameters of keV-ADC conversion relation obtained in the test beam, which is discussed in details in the section 3.6 of the previous chapter. The digital output in terms of ADC channel number are stored in another root file known as 'PMD.Digits.root'.

- As a next step the row, column and z position (x, y, z) of each cell is converted into the global (x, y, z) coordinates and we get complete address of each cell with respect to the ALICE experiment. This is also known as 'hardware mapping information'. This leads to the conversion of PMD.Digits.root file into another format which is exactly same as that of the real data (raw data) obtained during the real experiment, known as 'PMD.Raw.root'.

- During the real data taking or experiment, we subtract pedestal from the raw data and then do gain calibration at this step. The raw data is then reconstructed using 'Clustering Algorithm'. The clustering algorithm is discussed in details in the next section of this chapter. We get clusters information like cluster position, ADC value, number of cells in a cluster etc. In simulation, we associate each cluster to
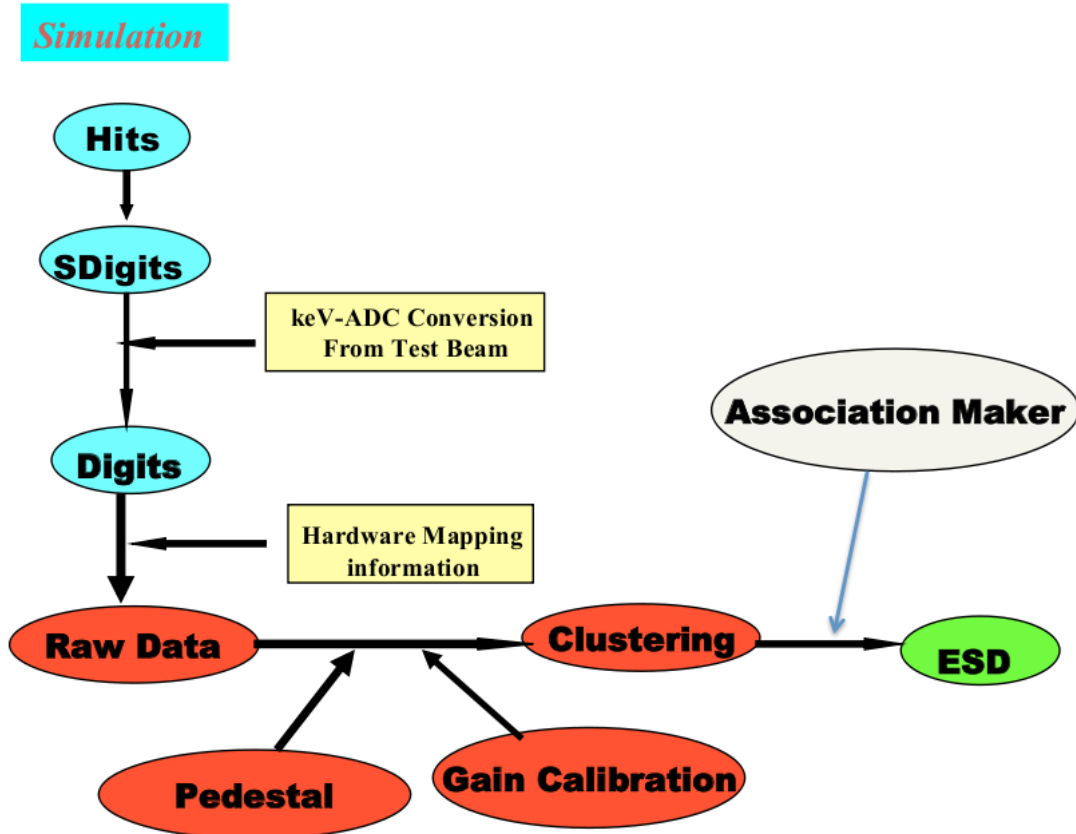
Figure 4.1: Flow chart of photon reconstruction used for simulation and during real data taking for the PMD detector.

the incident photon or hadron and use this to calculate the efficiency and purity of photon detection using PMD detector.

- The final output in terms of cluster information are stored in a root file known as 'Event Summary Data (ESD)' file. During real data taking, we get the data in ESD file format only. It contains the cluster information where each cluster is characterized by its ADC, transverse spread (number of cells), pseudo-rapidity (η) and azimuthal angle (ϕ).

4.2   Clustering Routine

A photon passing through the lead converter in front of the preshower plane produces electromagnetic showers [11]. The electrons and positrons coming out of the shower hit a

group of cells on the preshower plane. These group of cells are called "clusters". A cluster can be associated to the photon or to the charge particle incident on the PMD detector. It is very important to identify photons and hadrons, so as to study the multiplicity and pseudo-rapidity distribution of the photons during real data taking. We get high multiplicity of produced particles in the heavy-ion collisions, because of which clusters formed by the produced photons may superimpose and mimic like a single cluster. Clustering routine is used to split the merged cluster into split clusters and these split clusters can be assigned to the incident photons. Different algorithms are studied to split the super clusters, thereby correcting the effect of photon overlap. For the pp collisions, because of low particle density the cluster overlap probability is low. The splitting of a cluster is not required for pp data.

Each cluster is characterized by its total ADC (or energy deposition (E_{dep})), total number of cells associated to it and (η, ϕ) position of its center. The clustering is done module wise. The first step is to collect all the contagious cells having non-zero value of the ADC (E_{dep}). This group of cells is referred to as a "Super Cluster", also termed as "Crude Cluster". Thus the super clusters are separated by cells having zero ADC (E_{dep}) value, or part of their boundary coincides with the module boundary. Super clusters are made starting from the cell with largest ADC (E_{dep}) and forming a cluster with contagious non-zero ADC (E_{dep}) cells. For making the subsequent super clusters we search for the next largest ADC (E_{dep}) cell in a module and follow the same procedure of collecting contagious non-zero ADC (E_{dep}) cells. This process is repeated till all the non-zero ADC (E_{dep}) cells in a module are exhausted [12].

If the total number of cells in a super cluster is one or two, then this super cluster is identified as 'charged hadron' cluster. The super clusters having large number of cells could arise from a photon cluster or may have arisen due to overlap of electromagnetic showers of different particles as a result of large particle density. In such a case, there is a need of breaking the super clusters further. If the super cluster has more than two cells then it is broken into a number of clusters, known as "Refined Cluster".

Various algorithm have been studied to break a super cluster into 'clusters'. The final selection of clustering algorithm is based on the criteria that the efficiency of photon

detection should be high with little contamination from the hadron like cluster. Figure 4.2 shows the block diagram of the one of the clustering routine algorithm. For breaking up the super cluster, we assume that the super cluster consists of overlapping clusters. First of all the cells in a super cluster are arranged in the descending order of their ADC (E_{dep}) value. Cell with largest ADC value is taken as first cluster center, also known as 'first local maxima'. More local maxima in the super cluster are searched with the condition that newly proposed center should be at least one cell unit away from the previously determined cluster center. That is, neighboring cells cannot be cluster centers. It is also assumed that if the distance between the proposed center and the previously accepted center is between 1 and 2 cell units, the strength of the (new) cluster center should be larger than 25% of the previously accepted center cell. This is to ensure that fluctuations do not give rise to clusters. The number 25% is adhoc and is tuned depending on the particle density. This distance condition implies the two cells are next nearest neighbours. If the distance between the proposed center and the previously accepted center is 2 cell units (next-to-next nearest neighbor), the cell strength should be larger than 10% of the strength of the previously accepted cell. If the distance is larger than 2 cell units, it is accepted as new cluster center [12]. Note that total number of local maxima formed from a crude cluster (super cluster) is the final number of refined clusters and each local maximum is cluster center. The strength i.e. ADC value and total number of cells associated to each cluster center is calculated. In a crude cluster the fractional ADC weight of each cell to each refined cluster center is calculated as [13]:

$$W_{ij} = zc_j \times exp(\frac{-r_i^2}{2\sigma^2}) \tag{4.1}$$

Here, W_{ij} is the ADC weight of ith cell (x_i, y_i) to the jth cluster center, zc_j is ADC of jth cluster center, $r_i^2 = (x_i - xc_j)^2 + (y_i - yc_j)^2$ and $\sigma = 1.2$. The cell is assigned to the cluster center getting maximum ADC weight.

Cluster center position (X_c, Y_c) and cluster ADC value are calculated using two different methods as shown in step number 10 and 11 of the flowchart in Fig. 4.2. Detailed study is done to finalise one of the methods and is discussed in section 4.2.2. Finally, cluster center position (X_c, Y_c) is taken as

1. Order the cells in the descending order of their ADC

2. All the contiguous cells having non-zero ADC forms super-cluster

3. number of cells in super-cluster is 1

4. number of cells in super-cluster is 2

5. number of cells in super-cluster > 2

6. Go to step 10.

7. In a super-cluster arrange the cells in decreasing order of ADC. Cell having largest adc is taken as first cluster center or first local maxima.

8. Find out other local maxima in the super-cluster, by searching for a cell which is not nearest neighbor to the previously accepted local maxima and its adc is greater than 50% of previously accepted local maxima.
Note: Total number of local maxima is the number of refined clusters formed from crude cluster and each local maximum is cluster center.

9. The fractional adc weight of each cell to each cluster center is calculated.
$W_{ij} = zc_j \times \exp(-r_i^2/2\sigma^2)$
Where, W_{ij} is the adc weight of ith cell (xi, yi) to the jth cluster center, zc_j is ADC of jth cluster center, $r_i^2 = (x_i-xc_j)^2 + (y_i-yc_j)^2$
and $\sigma = 1.2$
The cell is assigned to the cluster getting maximum ADC weight.

10. Then,
Cluster $X_c = \Sigma(x_i z_i) / \Sigma z_i$
Cluster $Y_c = \Sigma(y_i z_i) / \Sigma z_i$
Cluster ADC = Σz_i
sum i is over all the cells assigned to a cluster from step 9 and z_i is i^{th} cell ADC

11. Then,
j^{th} cluster $X_c = ax_j / az_j$

j^{th} cluster $Y_c = ay_j / az_j$

j^{th} cluster ADC = az_j

where,
$ax_j = \Sigma (x_i \times z_i \times W_{ij} / S_i)$ sum over i

$ay_j = \Sigma (y_i \times z_i \times W_{ij} / S_i)$ sum over i

$az_j = \Sigma (z_i \times W_{ij} / S_i)$ sum over i

sum i is over all the cells in the crude cluster. z_i is i^{th} cell ADC.

$S_i = \Sigma W_{ij}$ sum over cluster centers.

Figure 4.2: Block diagram of PMD Clustering routine.

$$X_c = \frac{\Sigma(x_i z_i)}{\Sigma z_i},$$ (4.2)

$$Y_c = \frac{\Sigma(y_i z_i)}{\Sigma z_i}$$ (4.3)

and,

$$\text{Cluster ADC} = \Sigma z_i$$ (4.4)

Here, sum 'i' is over all the cells assigned to the cluster and z_i is the ADC value of the ith cell. In order to understand the photon multiplicity and determination of photon spatial position, detailed simulation study is required. We have carried out this detailed simulation study using ALICE Software (AliRoot). To carry out this study we have used the following parameters in the AliRoot framework:

- Single particle Box Generator;

- Photons are generated;

- Particles are generated in the PMD pseudo-rapidity region: $2.3 \leq \eta \leq 3.7$, with full azimuthal coverage ϕ: (0, 360);

- Only PMD detector is switched ON; and

- 1000 events are generated with photons at various energies (E_γ): 100 MeV, 200 MeV, 400 MeV, 800 MeV and 1600 MeV.

Full reconstruction chain is run on each event and the cluster properties are studied and discussed in next subsection.

4.2.1 Study of Crude Clusters

The total number of super clusters formed on the CPV and preshower planes in an event for different incident photon energy (for 1000 events) are studied and the plots are shown in the Fig. 4.3. It can be seen from the left panel of the Fig. 4.3, that as the incident photon energy (E_γ) increases the number of super clusters formed also increases. The
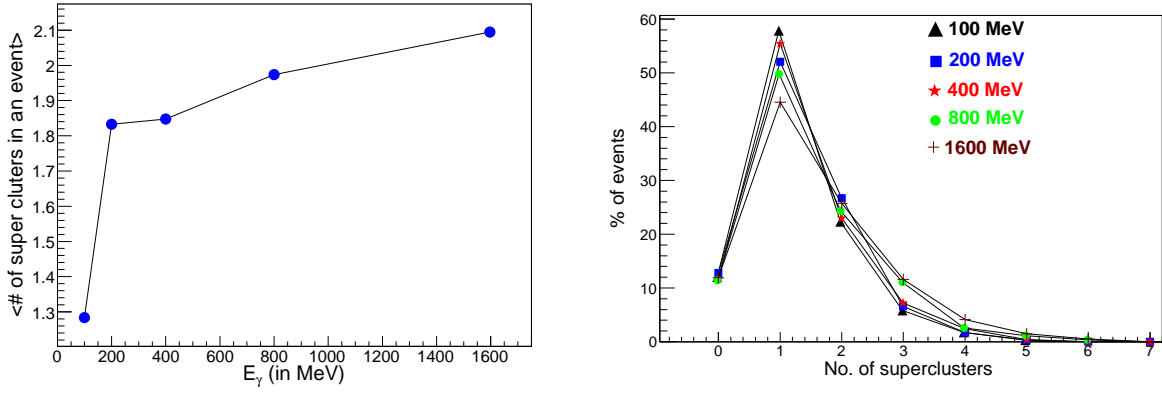
Figure 4.3: Left Panel: Average number of super clusters in an event as a function of incident photon energy (E_γ). Right Panel: The fraction of total number of events (out of 1000 events) is plotted as a function of total number of super clusters formed.

right panel shows the fraction of events (out of 1000 events) as a function of total number of super clusters in an event. It should be noted that, nearly 10% of events have no super cluster (no hit on PMD), that means 10% of photons are not identified at all for all energies. With increase in the photon energy (E_γ), the number of events with single super cluster decreases. In ideal case, a single photon should produce electromagnetic shower which, should produce one super cluster. But with single photon per event, we see that more than one super clusters are also formed. This will increase the amount of split clusters for a single photon. However, 40-60% of photons forms a single super cluster at all energies. As seen from the right plot of Fig. 4.3, there are more than one super cluster in some of the events.

The total number of cells in a super cluster are also studied and found to increase with increase in energy of the incident photon as shown in Fig. 4.4. Furthermore, the total number of cells in a super cluster are studied for the three different cases: events having all super clusters, events having maximum ADC super clusters, and events with only one super cluster. Figure 4.5 shows the conclusive plot of the average number of cells in a super cluster as a function of incident photon energy. The average number of cells in a super cluster increases with increase in E_γ and is high for super cluster with maximum ADC value.

The mean ADC of a super cluster is also studied as a function of photon energy for
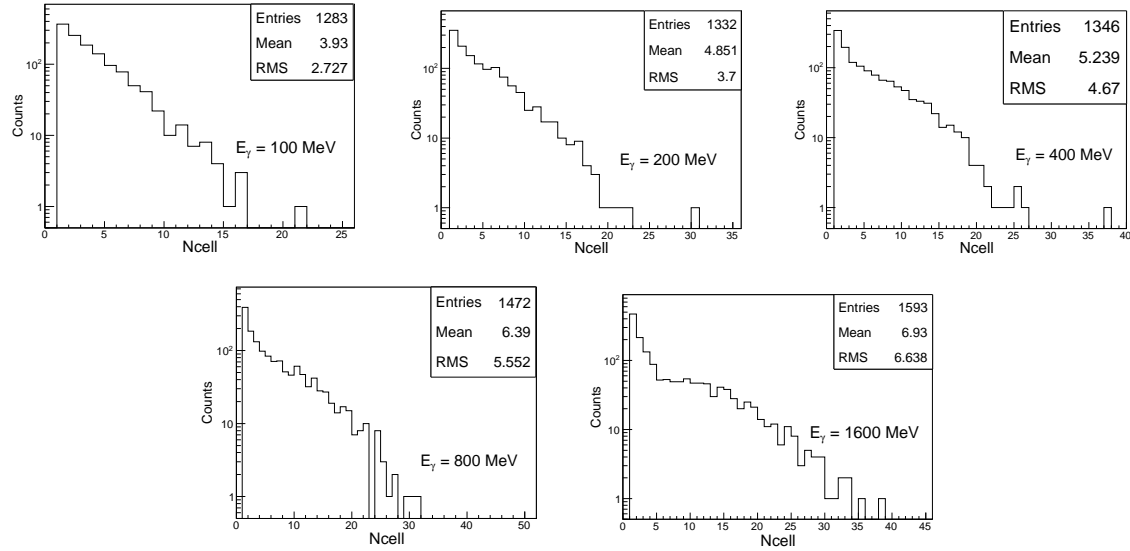
Figure 4.4: Total number of cells in a super cluster.
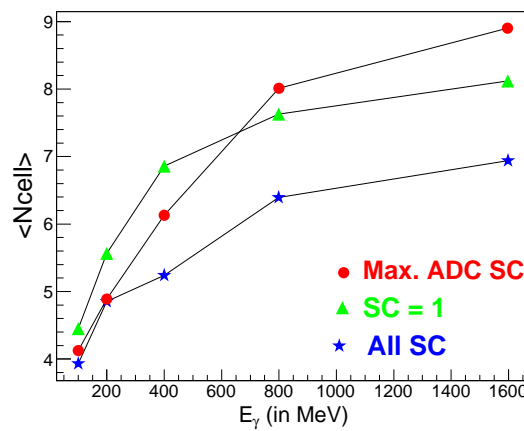
Figure 4.5: Average number of cells in a super cluster is plotted as a function of incident photon energy (E_γ) for three different cases.
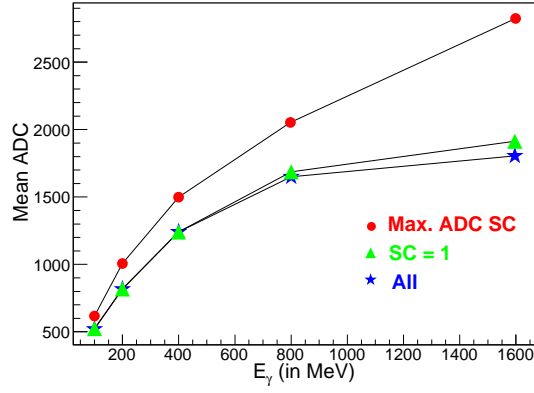
Figure 4.6: Mean ADC of a super cluster is plotted as a function of incident photon energy (E_γ) for three different cases.

three different cases as discussed above. Figure 4.6 shows that the mean ADC of a super cluster increases with increase in the incident photon energy. As observed in the average number of cells also, the mean ADC value is higher for those super cluster with maximum ADC as compared to other two cases.

The difference between incident photon pseudo-rapidity (η_{inc}) position and super cluster center pseudo rapidity (η_{clu}) is defined as:

$$\delta\eta = \eta_{inc} - \eta_{clu} \tag{4.5}$$

As expected, when only one super cluster is formed for single incident photon, the spread in super cluster centers is much narrow or close to the incident photon direction, as can be seen from Fig. 4.7 .

The difference between incident photon azimuthal (ϕ_{inc}) angle and super cluster center azimuthal (ϕ_{clu}) angle is defined as:

$$\delta\phi = \phi_{inc} - \phi_{clu} \tag{4.6}$$

The super cluster with maximum ADC value looks closer to the incident photon in azimuthal plane as compared to other case where, only one super cluster is formed for single incident photon, as can be seen in Fig. 4.8 .

The distance between the super cluster center position (X_c, Y_c) and any cell position
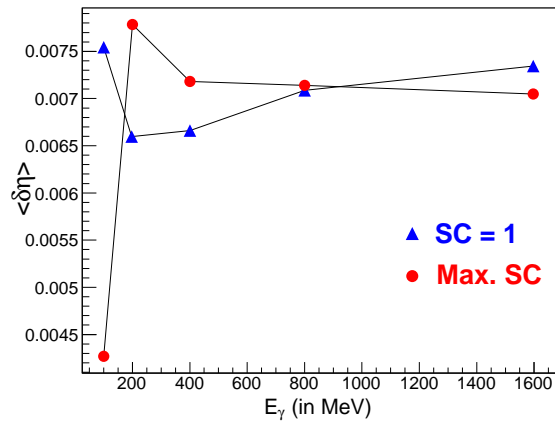
Figure 4.7: Difference between incident photon and super cluster position is plotted as a function of incident photon energy (E_γ) in pseudo-rapidity plane $(\delta\eta)$.
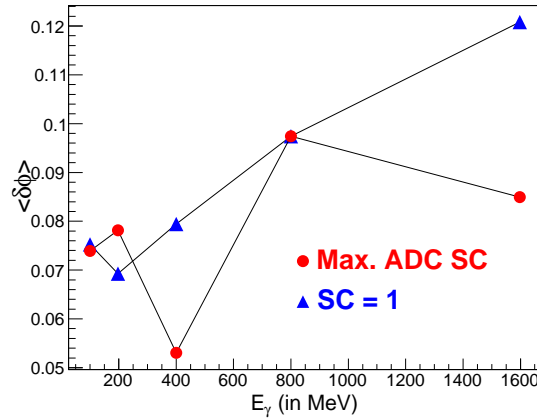
Figure 4.8: Difference between incident photon and super cluster position is plotted as a function of incident photon energy (E_γ) in azimuthal plane $(\delta\phi)$.
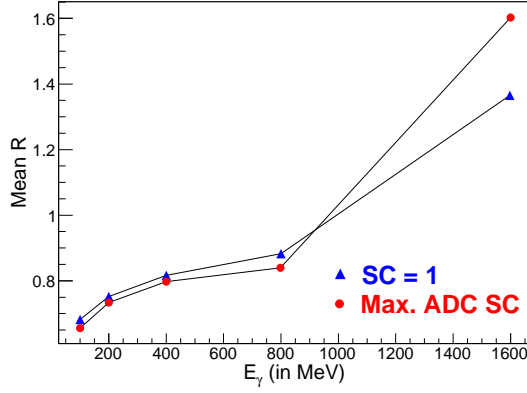
Figure 4.9: The mean distance between super cluster center and the position of cells in a super cluster is plotted as a function of incident photon energy (E_γ).

(x, y) in the super cluster is defined as:

$$R = \sqrt{(X_c - x)^2 + (Y_c - y)^2} \tag{4.7}$$

Same as the other cases, this study is also performed for two different cases, if there is a single super cluster in an event, then R is calculated between super cluster center and all the cells in the cluster. Or, if there are more than one super cluster in an event, then R is calculated between the super cluster center having maximum ADC value and the cells in this cluster. Figure 4.9 shows that with increase in incident photon energy (E_γ), the mean distance (R) between super cluster center and its cell increases. The mean distance increases rapidly when the energy of the incident photon is greater than 800 MeV.

4.2.2   Study of Refined Clusters

The ALICE experiment is designed to take data in high multiplicity environment. Pb-Pb collisions at $\sqrt{s_{NN}} = 2.76$ GeV produces large number of charged and neutral particles. In the high particle density, clusters formed by different incident photons on PMD detector may superimpose and appear as a single super cluster. Refined clustering is required to split this overlap clusters and these split cluster can be further assigned to the incident photons.

As is seen in the Fig. 4.2, we have two different procedure to calculate cluster position (X_c, Y_c) and cluster ADC value. The step number 11 in the flowchart is the old procedure
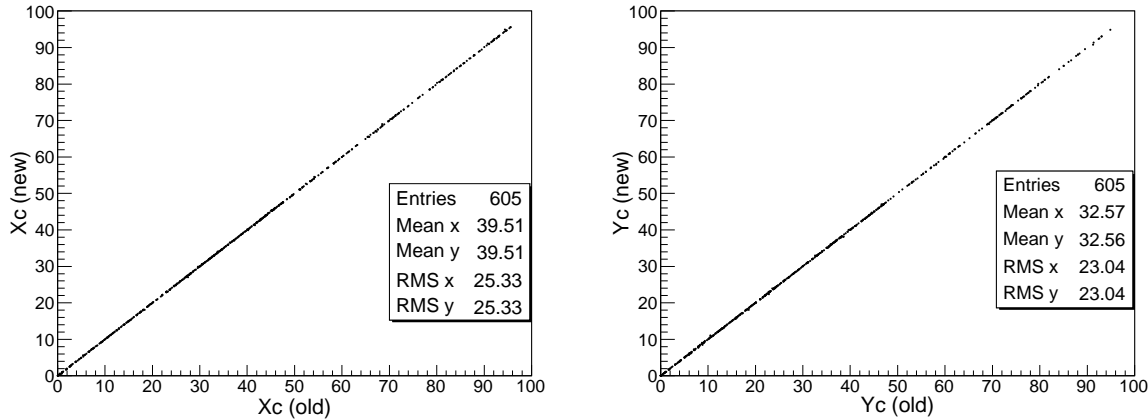
Figure 4.10: Left Plot: Row position (X_c) of a refined cluster using old routine is plotted corresponding to row position using new routine. Right Plot: Similar plot for column position (Y_c).

and step number 10 is the new procedure. In order to finalise one routine, various cluster properties are compared using old and new procedures and are discussed below. For this study we have used those events which has only one super cluster and incident photon energy (E_γ) as 1600 MeV.

1. Figure 4.10 show that comparison of row and column position of cluster formed using old and new clustering routine. Here, X_c is row number and Y_c is the column number of the cell in unit module. The (x, y) position of the cluster in two routines are almost same.

2. The ADC of cluster formed using old clustering routine vs. ADC of the cluster formed using new clustering routine is shown in Fig. 4.11. There is not huge difference in ADC value of cluster using new and old clustering routine.

3. To have a closer look into the difference between old and new clustering routine, the fraction of entries having zero difference between old and new clustering routine is shown in tabular form in Table 4.1. The cluster position and ADC values are almost similar in the two procedure.

4. The difference between (η, ϕ) position of the refined cluster formed using old clustering routine and new clustering routine is shown in Fig.4.12. The spatial position
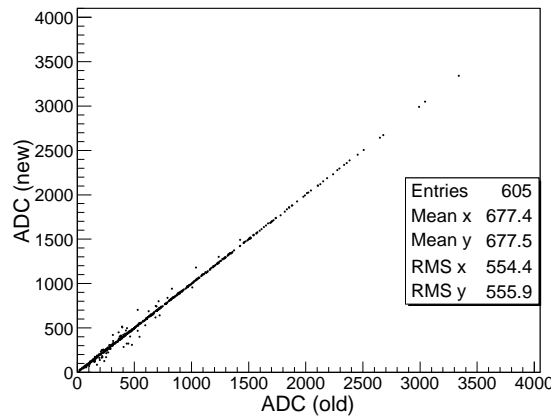
Figure 4.11: The cluster ADC using new routine is plotted as function of old clustering routine.

Table 4.1: Fraction of entries having zero difference between old and new clustering routine:

	No. of entries with zero difference	Total Entries	Fraction
$\Delta x \ (x_{new} - x_{old})$	503	605	0.831
$\Delta y \ (y_{new} - y_{old})$	506	605	0.836
$\Delta ADC \ (ADC_{new} - ADC_{old})$	503	605	0.831
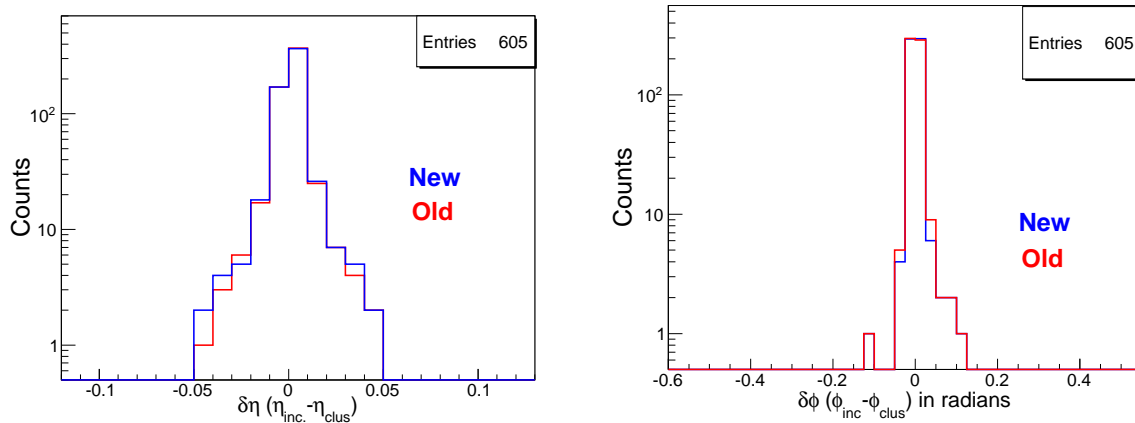
Figure 4.12: Blue line is for new and red line is for old clustering routine. Left Plot: Difference between incident photon pseudo-rapidity (η_{inc}) and refined cluster pseudo-rapidity (η_{clus}) is plotted. Right Plot: Difference between incident photon azimuthal angle (ϕ_{inc}) and refined cluster azimuthal angle (ϕ_{clus}) is plotted.

of the refined cluster using new and old clustering routine are almost same.

5. The comparison of refine cluster ADC value and total ADC of all the cells in a refine cluster for new and old routine is studied. Figure 4.13 shows the the fraction of cluster ADC to the total ADC of all the cells for new and old clustering routine. For old routine the sum of cell ADC assigned to a cluster is not always equal to the cluster ADC whereas the sum of cell ADC is always equal to the cluster ADC for new routine.

A clustering algorithm is adopted to reconstruct photon clusters on an event-by-event basis. In order to discriminate between charged hadrons and photon signals, a suitable discriminating threshold is applied to the reconstructed photon clusters. For the PMD to count photons on an event-by-event basis and measure their spatial distribution (x, y) or (η, ϕ), it is necessary to know the following parameters :

- Photon counting efficiency and purity of the photon samples.

- Accuracy of the spatial distribution of the detected photons relative to the incident photons. Specially one needs to calculate the resolution i.e., (η_{track} - η_{cluster}) and (ϕ_{track} - ϕ_{cluster}), where (η_{track}, ϕ_{track}) are the original η, phi position of the incident
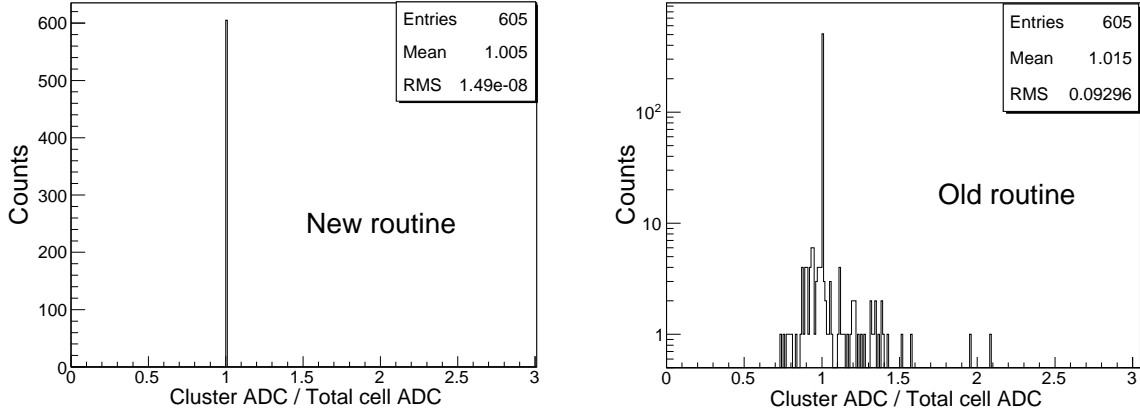
Figure 4.13: Fraction of cluster ADC to total ADC of cells in a cluster is plotted. Left Plot: For new clustering routine. Right Plot: For old clustering routine.

track and $(\eta_{\text{cluster}}, \phi_{\text{cluster}})$ denotes the η, phi position of a cluster associated to the track.

All these above mentioned steps are included in the 'association maker', shown in the Fig. 4.1.

4.3   Material in front of PMD

Since one of the main aim of the PMD detector in the ALICE experiment is to study the multiplicity and pseudo-rapidity distribution of photons produced in a collision in the forward rapidity region. It is crucial to see if we have most of the photon clusters from the photons produced in a collision or from the photons produced after secondary interactions in the other detector material of the ALICE experiment.

The ALICE vacuum chamber, beam pipe, and the support structures of the central barrel detectors like TPC and ITS are the important components of the upstream material in front of the PMD. The secondary particles produced by the interactions taking place in the upstream material could deviates the incoming particles and sometimes produce the secondary which finally effects the photon counting efficiency and purity of the PMD detector.

Th radiation length (X_0) of the upstream material is needed to be study in details to reject the secondary photons produced in PMD spatial (η, ϕ) position. All the ALICE
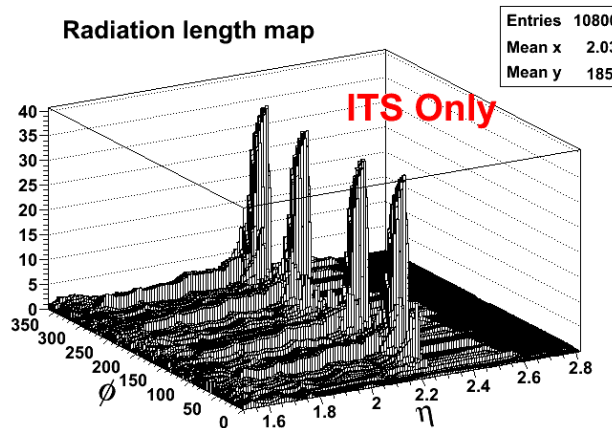
Figure 4.14: ITS detector and support cables and structure material radiation length (X_0) distribution in the (η, ϕ) plane at a distance of 360 cm from the interaction point.

detectors along with their support cables, structure geometry and material are included in the Geant3 code, so that the secondary interaction which will take place during the real data taking can be simulated in the AliRoot framework. We study the various detector's material radiation length (X_0) in their pseudo-rapidity and azimuthal (η, ϕ) plane in front of the PMD. Some of the material budget Lego plots made using the AliRoot version dated: 05.07.2010 are discussed below:

1. **ITS** (Inner Tracking System): The support structure and the cables of the ITS detector are the major source of secondary particles falling on the lower pseudo-rapidity (η) region. Figure 4.14 shows the material radiation length (X_0) plot of the ITS detector and its support structure. This plot is with fine binning of the pseudo-rapidity axis. The figure shows that at $\eta = 2.3$ and at regular ϕ intervals, there is a material with very high radiation length of ~ 34 X_0. This is due to the support structure of the ITS detector. This will affect the photon detection efficiency in the lower PMD η region.

2. **PIPE** (Beam Pipe): Figure 4.15 shows the beam pipe material's radiation length plot at a distance of 360 cm from the interaction point $(Z = 360$ $cm)$. We note that beam pipe has material of radiation length, $X_0 \sim 0.8$ in the pseudo-rapidity region $\eta = 4.4$ in full azimuthal range. It deviate the particles falling in this re-
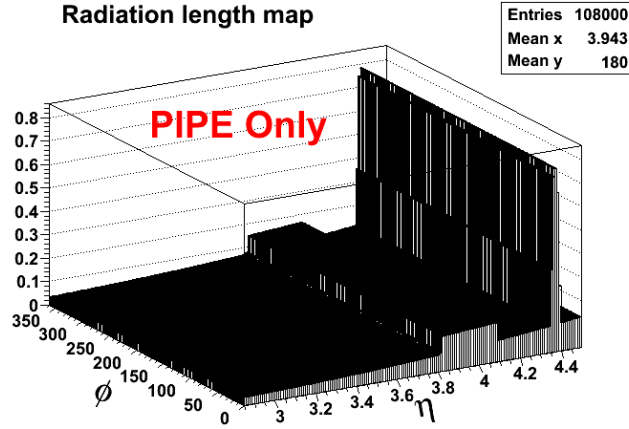
Figure 4.15: Beam pipe material radiation length (X_0) plot in the (η, ϕ) plane at a distance of 360 *cm* from the interaction point.

gion and sometimes these particles fall on the PMD η region which introduce the contamination in the higher PMD η region.

3. **V0**: If we look from the interaction point to the PMD direction, V0 detector is installed in front of the PMD. Figure 4.16 shows the V0 detector material radiation length (X_0) plot. The left plot shows that there is some V0 detector of nearly one radiation length at pseudo-rapidity region $\eta \sim 2.3$ which overlaps with the PMD η region. The right plot of the figure confirms that there is some boxes structure in regular azimuthal interval.

Figure 4.17 shows the upstream material radiation length plot of the V0, ITS detector and beam pipe at a distance (Z) of 360 *cm* from the interaction point, i.e. in front of the PMD detector. This will effect the efficiency and the purity calculation of the photons detection in the lower η region.

4.4   Photon Hadron Discrimination

The PMD consists of highly segmented detector called as preshower detector, placed behind a lead converter of thickness three radiation length. A photon produces an electromagnetic shower on passing through the converter. These shower particles produce
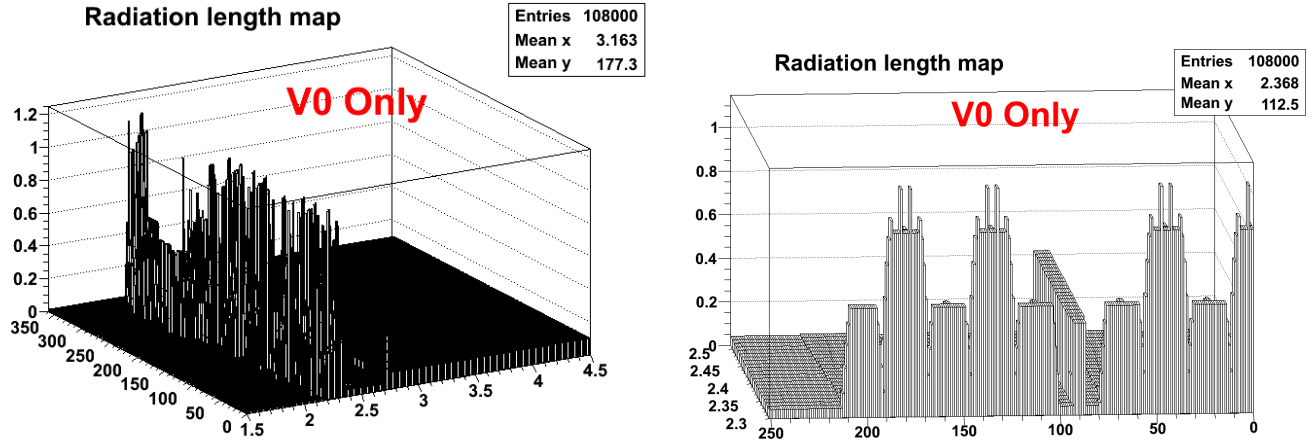
Figure 4.16: Radiation length (X_0) plot of the V0 detector at a distance of 360 cm from the interaction point. Left plot: In the (η, ϕ) plane. Right plot: Shows the azimuthal (ϕ) axis in front.
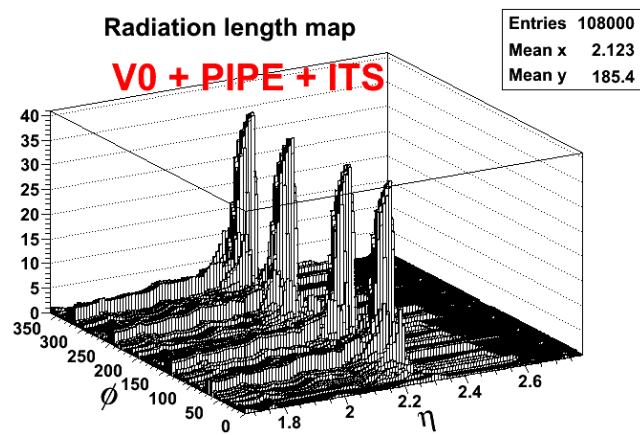
Figure 4.17: Lego plot of material radiation length (X_0) of the V0, ITS detectors and the beam pipe in the (η, ϕ) plane in front of the PMD (Z = 360 cm).

signals in several cells of the sensitive volume of the detector. Charged hadrons usually affect only one cell and produce a signal resembling those of Minimum Ionizing Particles (MIPs). It is seen in section 4.2, that charged hadron sometime hits more than one cell, thus forms a cluster and can mimic like a photon cluster.

4.4.1   Optimization of Photon-Hadron Discrimination

In order to discriminate clusters due to photon track and clusters due to charged hadron track, we need to know the properties of photon clusters and charged hadron clusters. Some of these features are listed below -

- Photon cluster will deposit more energy in the sensitive medium of the detector as compared to the cluster formed due to charged hadron.

- Photon cluster will have more number of cells hit in the preshower plane due to the electromagnetic shower coming from photon conversion in the $3X_0$ material of the lead converter. The charged hadrons, which essentially hit single cell, will form cluster with single isolated cell in the preshower plane.

These features are used to discriminate a photon cluster from a charged hadron cluster. One expects a hadron to deposit signal in the sensitive volume corresponding to a MIP mostly in one cell. But the following points are needed to be considered for photon hadron discrimination [14–16].

- A charge particle may interact with the converter material (for $3X_0$ the interaction probability is about 10%) and can also interact with the honeycomb cell boundary walls of the charged particle veto (CPV) plane. It may give signal in larger number of cells in the preshower plane and can form a cluster with $N_{cell} > 1$, and hence deposit more energy (> 1 MIP).

- The clustering algorithm in its attempt to separate overlapping clusters (expected in high particle density at forward rapidity) may split a photon cluster into many small clusters. This results in the formation of clusters having smaller energy deposition and less number of cells. These clusters are also known as 'split clusters'.

The photon hadron discrimination threshold cuts are optimised using simulation, so that we have high efficiency and purity of photon detection for the PMD detector. The effect of these threshold cuts on efficiency and purity calculations are discussed in detail in section 4.5.2.

4.5 Photon Detection Efficiency and Purity

In simulation, we have the information of the tracks which deposit energy on the CPV and preshower planes. After clustering, each cluster is assigned identification (IDs), such as hadron or photons on the basis of their Monte Carlo track information. A photon hadron discrimination threshold is applied to get γ-like clusters ($N_{\gamma-like}$) and finally, the efficiency and purity are calculated. During the real data taking, we do not know if the cluster formed on the preshower plane is due to hadron or primary photon. We apply the photon hadron discrimination threshold cut to reject most of the hadron cluster and get the γ-like clusters. These clusters are then corrected for efficiency, purity and geometrical acceptance factors obtained from the simulation and we get the final counts of photons produced in collisions in the PMD pseudo-rapidity (η) region.

4.5.1 Efficiency and Purity

All the clusters which are above the discrimination threshold are known as the 'γ-like' clusters. The efficiency (ϵ_γ) is defined as the ratio of the number of photons detected above the discrimination threshold within a given coverage to the number of incident photons within the same coverage:

$$\epsilon_\gamma = \frac{N_{clus}^{\gamma,th}}{N_{\gamma-inc}} \tag{4.8}$$

where, $N_{clus}^{\gamma,th}$ is the number of photon clusters above threshold and $N_{\gamma-inc}$ is the number of incident photons in the same coverage.

The purity (f_p) is defined as the ratio of the number of photons detected above the discrimination threshold within a given coverage to the number of γ-like clusters within the same coverage:

$$f_p = \frac{N_{clus}^{\gamma,th}}{N_{\gamma-like}} \tag{4.9}$$

From the experimental data one can determines the $N_{\gamma-like}$, the number of clusters above the photon hadron discrimination threshold. Using the estimated values of ϵ_γ and f_p from the simulation study, one obtains the number of photons incident on the PMD detector by the relation:

$$N_\gamma = N_{\gamma-like} \times \frac{f_p}{\epsilon_\gamma}. \tag{4.10}$$

Various procedures are studied using simulation in the AliRoot framework to get the efficiency and purity correction values for the PMD detector [16–18]. In this thesis, one of the methods 'efficiency and purity calculation using embedding technique' is discussed in details in the next section.

4.5.2   The Embedding Technique

The basic principle of the embedding technique [19] is to embed a small event (a single tagged photon or hadron) in a big event (HIJING or PYTHIA) and run the full reconstruction chain (Fig. 4.1). At the end, one has to see if the tagged particle remain or got lost in the finally obtained '$\gamma - like$' clusters. The main purpose of this technique is to study the following:

1. Obtain the efficiency (ϵ_γ) and the purity (f_p) of the photon detection as the function of pseudo-rapidity (η).

2. Study the energy and multiplicity dependence of the photons detection efficiency using this method.

For our purpose, we have embed a single photon/hadron in an event, known as 'parent' event (PYTHIA for pp collisions or HIJING for Pb-Pb collisions). The transverse momentum (p_t) of the embedded particle is randomly selected from the p_t distribution of the same particle (photon/hadron) in the parent event. This selection helps to simulate the parent event without distorting the transverse momentum shape of the particle. The pseudo-rapidity (η) and azimuthal angel (ϕ) are also randomly selected within the PMD acceptance region i.e. $2.3 \leq \eta \leq 3.7$ with full ϕ coverage. The photon detection efficiency and purity are calculated using Eqs. 6.2 and 4.9.
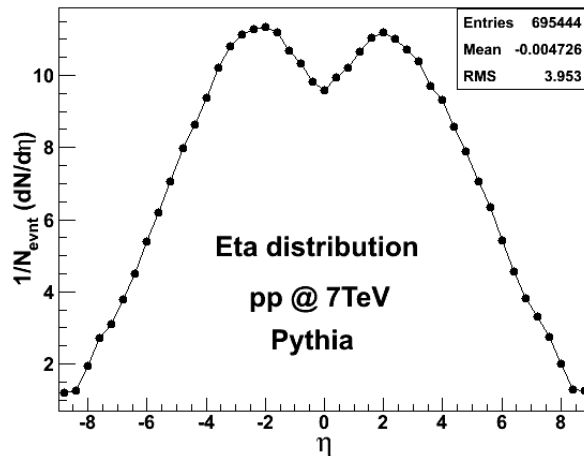
Figure 4.18: The charge particle $(\mathrm{d}N/\mathrm{d}\eta)$ distribution for generated PYTHIA events for pp collisions at $\sqrt{s} = 7\mathrm{TeV}$.

4.5.2.1 PYTHIA Generator for pp collisions at $\sqrt{s} = 7$ TeV

We have used PYTHIA generator in AliRoot framework to study the photon detection efficiency and purity for low multiplicity event. About 5000 minimum bias events are generated using the PYTHIA with π^0 decay ON, for pp collisions at $\sqrt{s} = 7$ TeV with the following conditions:

- Detectors: PMD, TPC, ITS, V0, T0, Beam pipe, FMD, Hall and Dipole

- Pseudo-rapidity Range: -0.8 to 0.8 with 2π azimuthal coverage

Figure 4.18 shows the pseudo-rapidity distribution $(\mathrm{d}N/\mathrm{d}\eta)$ of the generated charge particles in the PYTHIA events for pp collisions at $\sqrt{s} = 7$ TeV. To embed single particle we need to first generate single particle event with the same parameters. Since we want to calculate the efficiency and purity of photons detection for the PMD detector, so it is sufficient to generate single particle in the PMD pseudo-rapidity region.

4.5.2.2 Single Particle Photon Generator

Box Generator is used to generate single photon (γ) in the PMD pseudo-rapidity region $(2.3 \leq \eta \leq 4.1)$ with full azimuthal range $(0 \leq \phi \leq 360)$. We have generated 100k
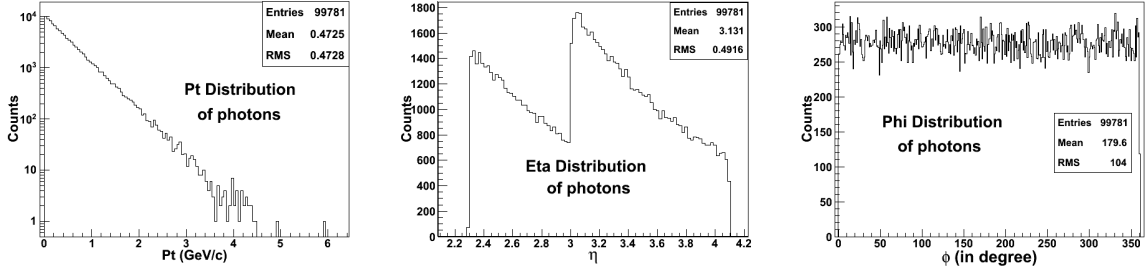
Figure 4.19: The transverse momentum (p_t), pseudo-rapidity (η), and azimuthal (ϕ) distributions of generated single photon in the PMD pseudo-rapidity region.

events with the same detectors ON as for PYTHIA event generation. The left plot of the Fig. 4.19 shows the transverse momentum (p_t) distribution of the generated photons. As discussed in the section (4.5.2), the transverse momentum of the generated photon is randomly selected from the p_t distribution of the photons from the generated PYTHIA events (see section 4.5.2.1). The middle and the right plots of the Fig. 4.19 show the pseudo-rapidity (η) and azimuthal (ϕ) distributions of the generated photons. To get the sufficient statistics covering full PMD η coverage, we generate photons for the two regions: 2.3–3.0 and 3.0–4.1, separately and combine them together, as shown in the middle plot of Fig. 4.19.

The next step is to embed these generated single photons in PYTHIA events. First, 5000 photon events are embedded in 5000 PYTHIA events, this gives us 5000 embedded events. Then, next 5000 single photon events are embedded into the same 5000 generated PYTHIA events. The process is repeated again and again and finally we get 100 k different embedded events. Embedding is done in the hits level of the reconstruction chain (see Fig. 4.1), all the steps like digitization, clustering is done afterwards. Each cluster is then associated to incident particle using existing algorithm, we then look for clusters formed by the embedded photons.

Efficiency: As discussed in Eq. 6.2, Efficiency ($\epsilon_{\gamma-det}$) is defined as the ratio of total number of detected embedded photons above the photon hadron discrimination threshold ($N^{th}_{\gamma-det}$) to the total number of incident embedded photons ($N_{\gamma-inc}$) in the same coverage, as shown below:

$$\text{Efficiency} = \epsilon_{\gamma-det} = \frac{N^{th}_{\gamma-det}}{N_{\gamma-inc}} \tag{4.11}$$
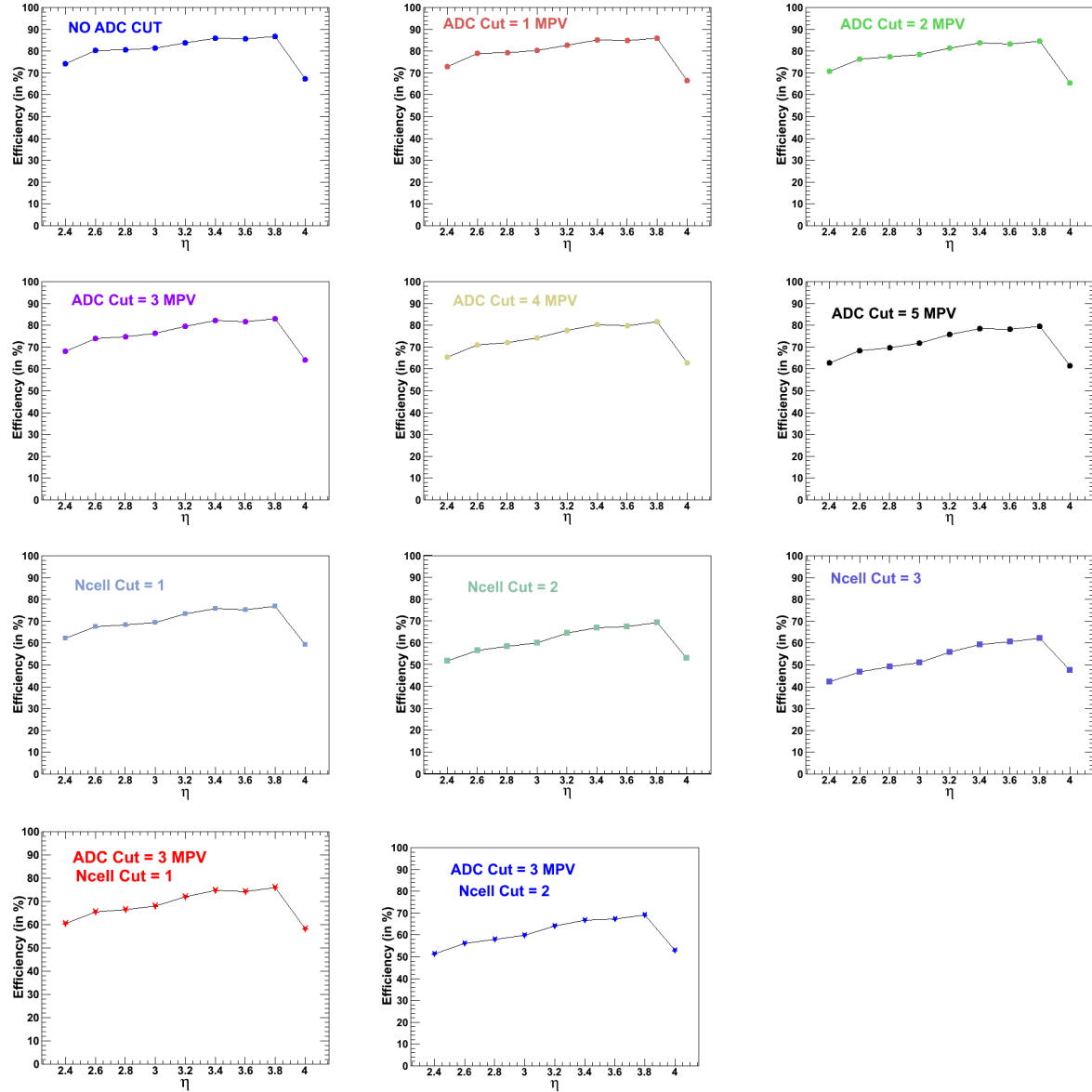
Figure 4.20: Photons detection efficiency ($\epsilon_{\gamma-det}$) as a function of pseudo-rapidity (η) for pp collisions at $\sqrt{s} = 7$ TeV, using embedding technique. Various plots are for different photon hadron discrimination cuts.
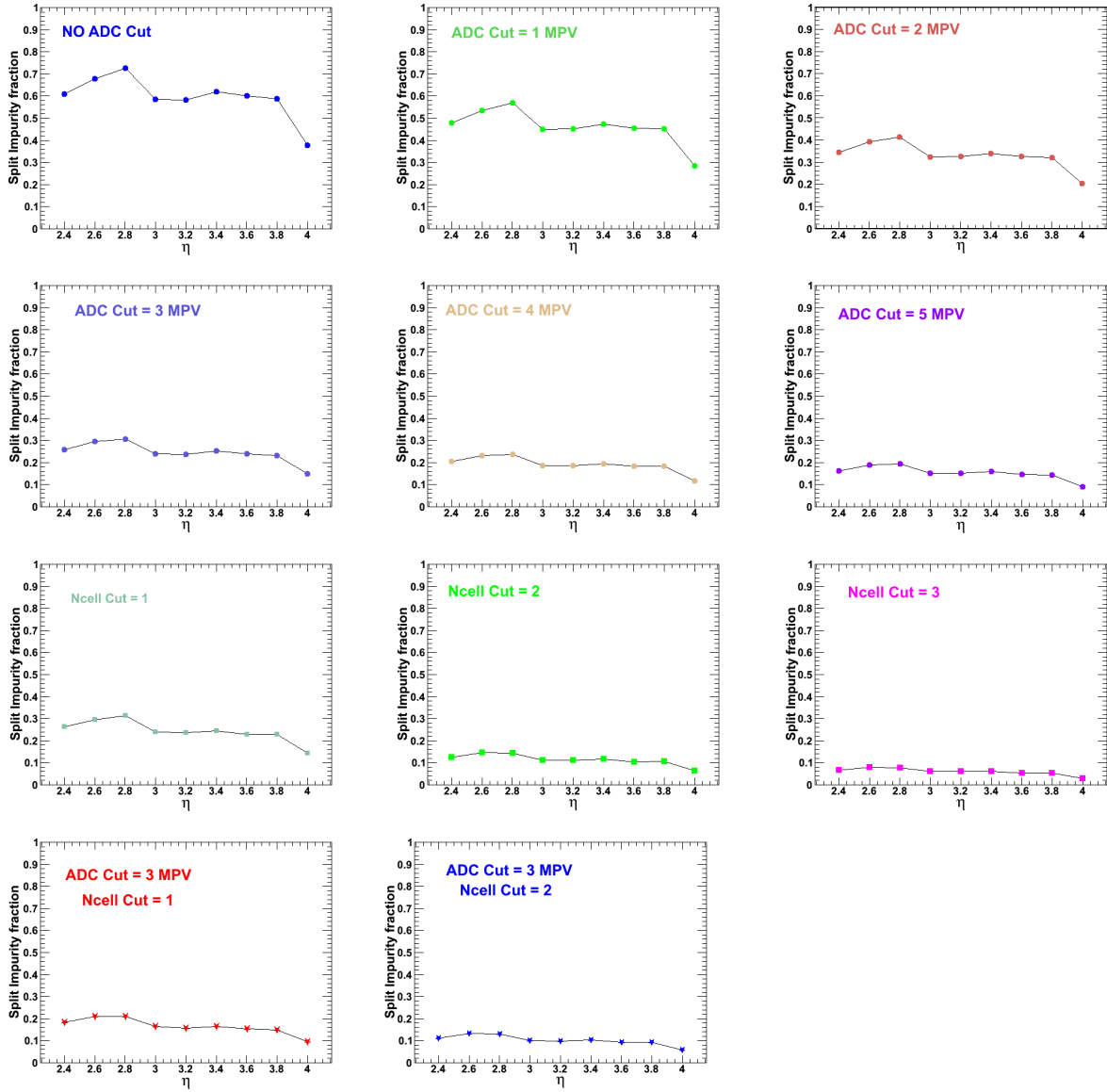
Figure 4.21: The fraction of photon split clusters as a function of pseudo-rapidity (η) calculated using embedding technique for pp collisions at $\sqrt{s} = 7$ TeV. Various plots are for different photon hadron discrimination cuts.

To calculate the embedding photons efficiency we have taken only the primary cluster, i.e. a single cluster is associated to one embedded photon. $\epsilon_{\gamma-det}$ is calculated for pseudo-rapidity (η) rings of size 0.2. Figure 4.20 show the efficiency ($\epsilon_{\gamma-det}$) plots for the PMD detector assuming various photon hadron discrimination threshold value, as a function of pseudo-rapidity (η) for pp collisions at $\sqrt{s} = 7$ TeV, using the embedding technique. The Most Probable Value (MPV) used in the plots is the minimum ionizing particle value of charged particle in the preshower detector. We have chosen this value to be 35 ADC based on the simulation studies.

Figure 4.20 shows the photon detection efficiency of the PMD detector for the various cluster ADC and number of cells in a cluster i.e., no cut on cluster ADC, cluster ADC cut of 1 MPV (Most Probable value in a MIP) to 5 MPV with no cut on number of cells (Top two rows of the Fig. 4.20). Third row of the figure shows the plots for the number of cells cut of 1 to 3, in a cluster with no cut on cluster ADC. Bottom row displays simulation plots with cuts on the number of cells in a cluster along with cluster ADC cut.

We find that the efficiency shows small variation within 20% in all PMD pseudo-rapidity region. The efficiency decreases for the last bin i.e. $\eta = 4.0$. As discussed in section 4.3, the efficiency decreases in the pseudo-rapidity ($\eta = 4.0$) region because this region is close to beam pipe and some of the particles produced due to secondary interactions in the beam pipe material fall in this η region.

Split Cluster Impurity: In the process of association of each cluster to a incident photon, two or more cluster can also get associated to a single photon. The cluster with maximum ADC value is called as primary cluster and is associated to the incident photon track, the remaining clusters are known as split clusters which decrease the purity of photon detection and therefore adds to the photon detection as impurity. The split cluster impurity fraction ($\text{Imp}_{\text{split}}$) is defined as the ratio of total number of split clusters detected which are associated to the embedded photons above the photon hadron discrimination threshold (N^{th}_{split}) to the total number of incident embedded photons ($N_{\gamma-inc}$) in the same coverage, as shown below:

$$\text{Imp}_{\text{split}} = \frac{N^{th}_{\text{split}}}{N_{\gamma-inc}} \tag{4.12}$$

Figure 4.21 shows the split clusters impurity fraction as a function of pseudo-rapidity
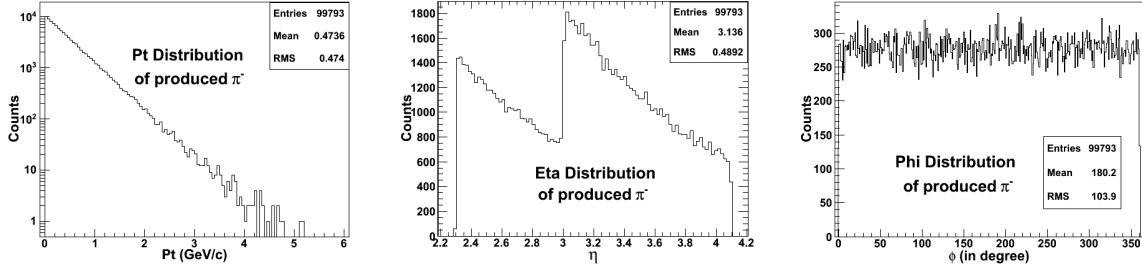
Figure 4.22: The transverse momentum (p_t), pseudo-rapidity (η), and azimuthal (ϕ) distributions of generated single π^- particle in the PMD pseudo-rapidity region.

(η) for pp collisions at $\sqrt{s} = 7$ TeV, using the embedding technique. The figure shows split clusters impurity fraction plots for various photon hadron discrimination threshold cuts. The cuts used are similar to what we used for the study for efficiency. It can be seen from the plots in Fig. 4.21 that with increase in ADC or N_{cell} cuts, the fraction of split clusters decreases. For a given η region e.g. 2.8, the 3 MPV cut reduces the split cluster fraction to nearly 30% from about 70% with no cut. Similarly, with one Ncell cut, the fraction of split clusters reduces to 30% from about 70% when no cut applied. Since the fraction of split clusters reduces significantly with 3MPV and/or one N_{cell} cuts, we can conclude that most of the split clusters are single cell cluster.

4.5.2.3   Single Charged Particle Generator

Box Generator is used to generate single charge particle in the PMD pseudo-rapidity region with full azimuthal coverage. In total 100k events of single π^- particle are generated with the same detectors configuration as used for the PYTHIA and the single photon event generators. The left panel of the Fig. 4.22 shows the transverse momentum (p_t) distribution of generated π^- charge particle. The transverse momentum is randomly selected from the p_t distribution of π^- from the generated PYTHIA events (see section 4.5.2.1). The right panel of the figure shows the azimuthal (ϕ) distributions of the generated π^- particles. The middle panel of the Fig. 4.22 shows the pseudo-rapidity (η) distribution of the generated π^- particle. As we did for photons, to increase the statistics in the PMD η coverage, we have generated single π^- particle for the two η regions separately.

In the similar way, as single photon was embedded in each PYTHIA events and in

total we got 100k photon embedded events in PYTHIA. We embed charge particle (π^-) event in PYTHIA event again in the hits level and we got 100k π^- embedded PYTHIA events. Whole reconstruction chain (Fig. 4.1) is run on each event and then each cluster is associated to the incident track. Our next job is to study the number of events where clusters get associated to the incident embedded π^- particle.

Charge Impurity fraction: The charge impurity fraction is defined as the ratio of total number of clusters which are associated to the embedded charge particle (π^-) above the photon hadron discrimination threshold (N_{charge}^{th}) to the total number of incident embedded charge particles π^- $(N_{\text{charge-inc}})$ in the same coverage, as shown below:

$$\text{Imp}_{\text{charge}} = \frac{N_{\text{charge}}^{th}}{N_{\text{charge-inc}}} \tag{4.13}$$

Figure 4.23 shows the plots for the charge impurity fraction $(\text{Imp}_{\text{charge}})$ as the function of pseudo-rapidity (η). This ratio is calculated in the pseudo-rapidity ring of size 0.2. The charge impurity fraction is very high $\sim$1.2 if no cut is applied, as shown in the top left plot of the Fig. 4.23. This shows that more than one cluster get associated to the embedded π^- particle. This impurity fraction keeps on decreasing as the photon hadron discrimination threshold ADC cut is increased, same behaviour is seen when the threshold cut as number of cells (N_{cell}) in a cluster is increased.

Purity: As discussed in Eq. 4.9, Purity (f_p) using embedding technique is defined as the ratio of total number of detected embedded photons above the photon hadron discrimination threshold $(N_{\gamma-det}^{th})$ to the total number of clusters formed by the embedded photons and embedded charge particle above the hadron discrimination threshold $(N_{\gamma-like}^{th})$. To calculate purity we have used the following method. From Eq. 4.9,

$$\text{Purity} = \frac{N_{\gamma-det}^{th}}{N_{\gamma-like}^{th}} \tag{4.14}$$

We know that γ-like clusters above discrimination threshold are clusters associated to the incident photons (primary + split) and to the incident charge particles above the threshold, so

$$N_{\gamma-like}^{th} = N_{\gamma-det}^{th} + N_{\text{split}}^{th} + N_{\text{charge}}^{th} \tag{4.15}$$
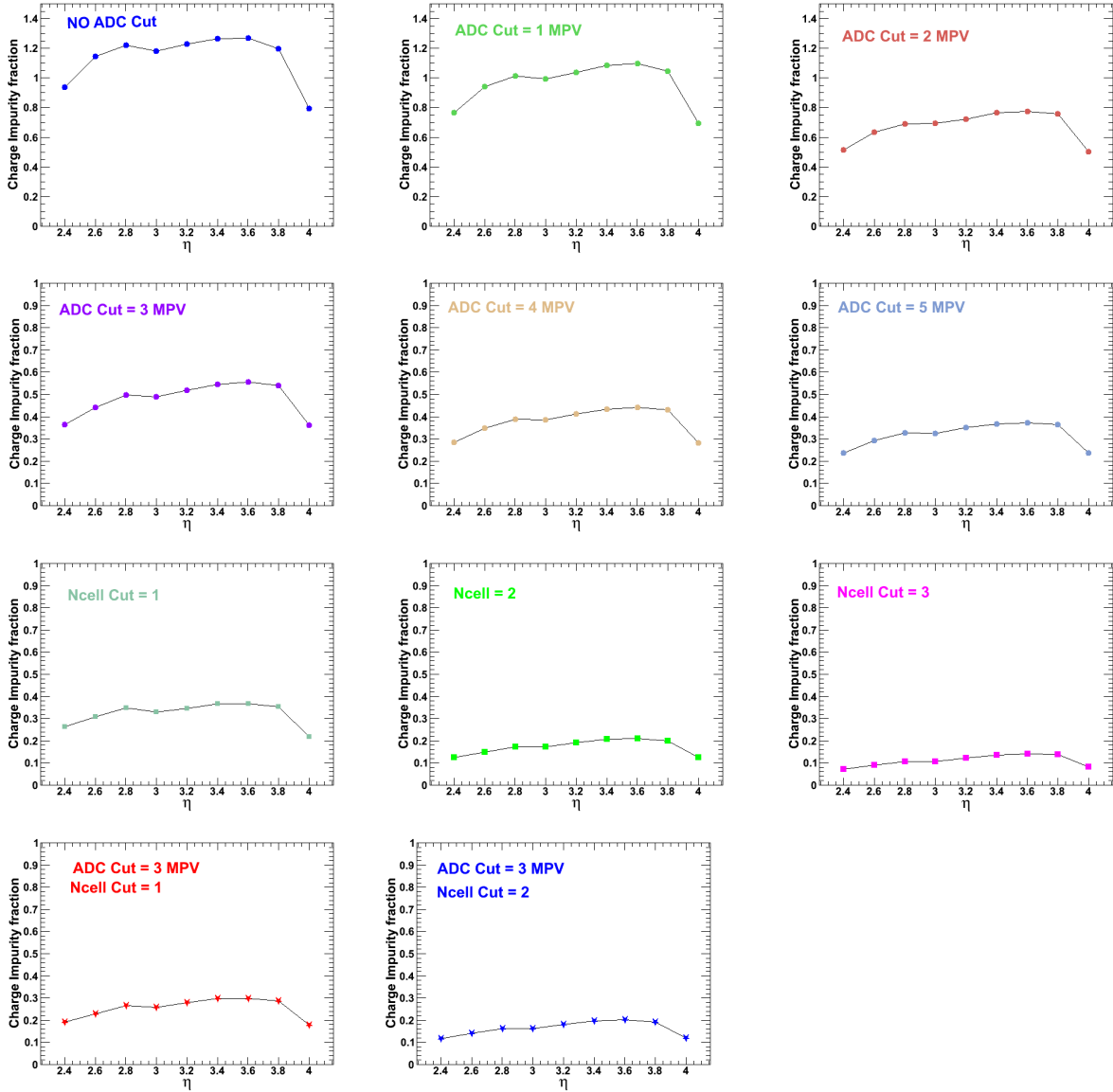
Figure 4.23: The fraction of charge particle clusters as a function of pseudo-rapidity (η) calculated using embedding technique for pp collisions at $\sqrt{s} = 7$ TeV. Various plots are for different photon hadron discrimination cuts.
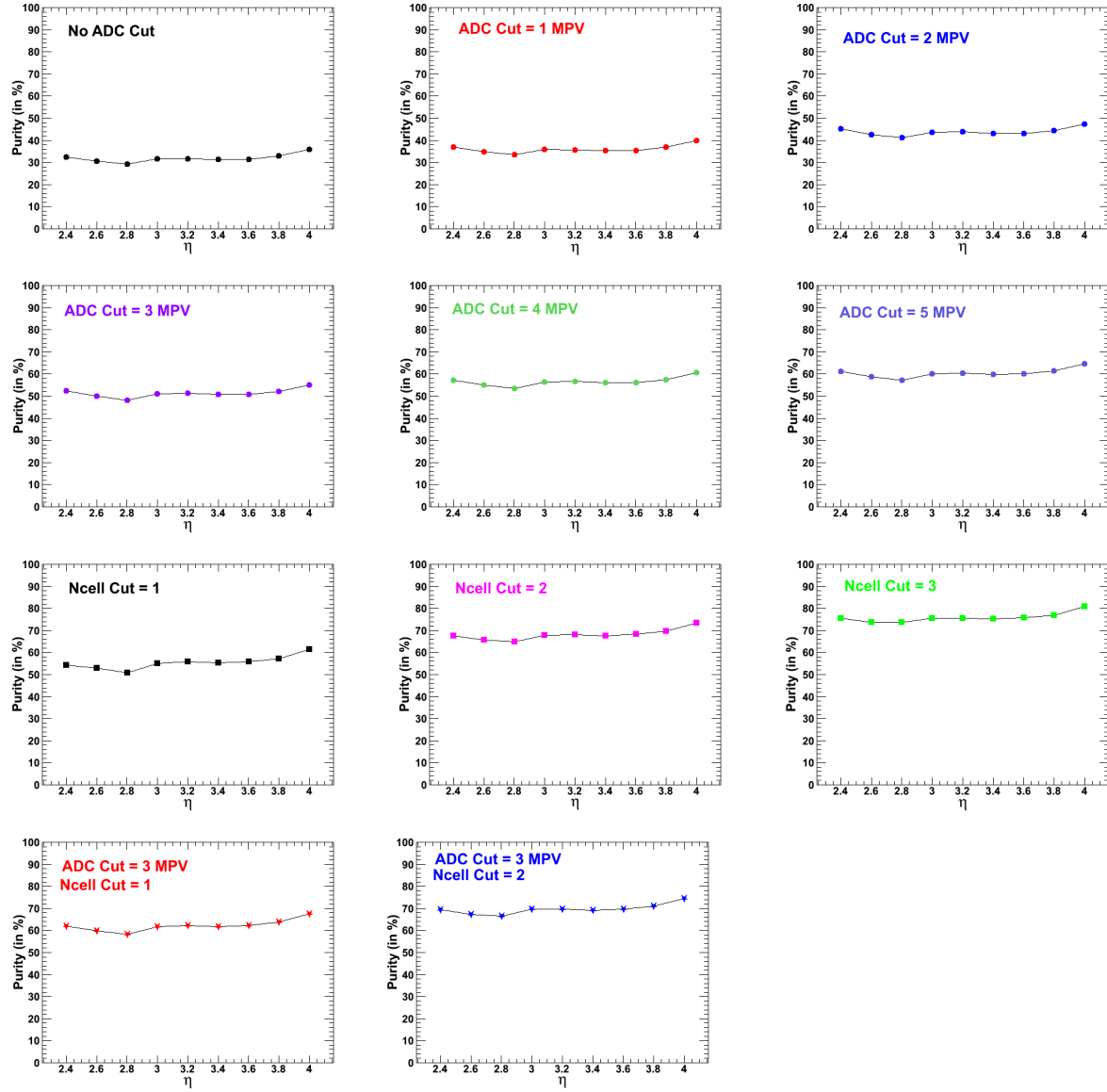
Figure 4.24: Photons detection efficiency ($\epsilon_{\gamma-det}$) as a function of pseudo-rapidity (η) for pp collisions at $\sqrt{s} = 7$ TeV, using embedding technique. Various plots are for different photon hadron discrimination cuts.
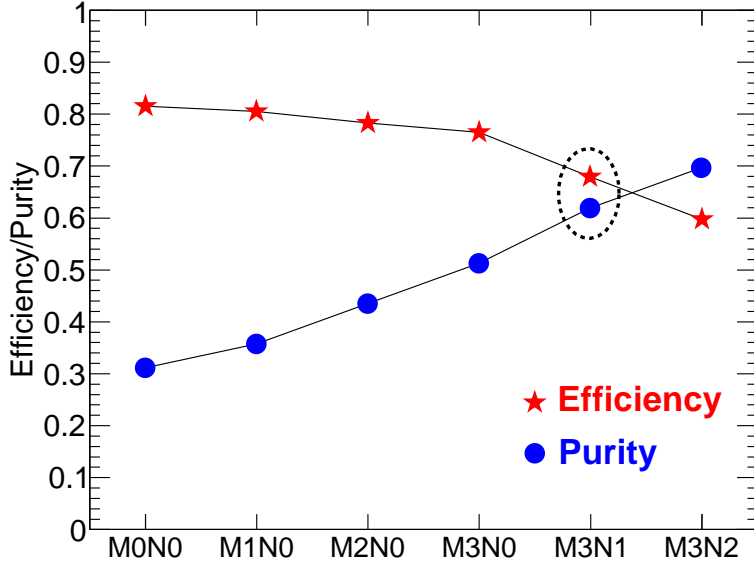
Figure 4.25: Efficiency (solid stars) and purity (solid circle)of photon counting as a function of MIP (or MPV) and N_{cell} cuts for pp collisions at $\sqrt{s} = 7$ TeV, using embedding technique.

In total we have generated 100k photon embedded events and charge particles embedded events separately, so dividing Eq. 4.15 by total number of events (N_{total}) and using Eqs. (4.11, 4.12, and 4.13), we get

$$\frac{N^{th}_{\gamma-like}}{N_{total}} = \epsilon_{\gamma-det} + \mathrm{Imp}^{th}_{\mathrm{split}} + \mathrm{Imp}^{th}_{\mathrm{charge}} \tag{4.16}$$

so, purity of photon detection is calculation as follows using embedding technique:

$$\mathrm{Purity} = \frac{(N^{th}_{\gamma-det}/N_{total})}{(N^{th}_{\gamma-like}/N_{total})} = \frac{\epsilon_{\gamma-det}}{(\epsilon_{\gamma-det} + \mathrm{Imp}^{th}_{\mathrm{split}} + \mathrm{Imp}^{th}_{\mathrm{charge}})} \tag{4.17}$$

All the above parameters are calculated for various discrimination threshold cuts and for various pseudo-rapidity region. Figure 4.24 show the purity of photon detection as a function of pseudo-rapidity for the PMD detector for various threshold cuts.

Figure 4.25 shows the efficiency of photon counting and purity of photon sample as a function of MIP (or MPV) and N_{cell} cuts. The X-axis labels M0N0, M1N0, M2N0, M3N0, M3N1, and M3N2 represent the MIP=0 and N_{cell}=0, MIP=1 and N_{cell}=0, MIP=2 and N_{cell}=0, MIP=3 and N_{cell}=0, MIP=3 and N_{cell}=1, and MIP=3 and N_{cell}=2 cuts
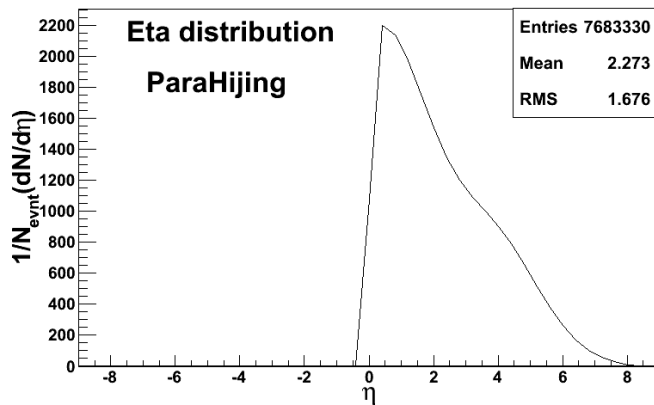
Figure 4.26: The charge particle $(\mathrm{d}N/\mathrm{d}\eta)$ distribution of generated parametrised HIJING events for Pb-Pb collisions.

respectively. We observe that the efficiency of photon counting varies from greater than 80% to less than 60% as a function of these cuts while Purity of the photon sample varies from 30% to 70%. Since we do not want the cases of low efficiency and purity, it is appropriate to use the threshold values for photon-hadron discrimination to be close to 3×MIP and number of cells in a cluster greater than one as marked by the dotted circle in the figure.

4.5.3 Parametrized HIJING for Pb-Pb collisions

Parametrized HIJING event generator is a HIJING event generator in which one can set the number of produced particles in the mid-rapidity region parameter according to need. We have used the parametrized HIJING event generator to study the photon detection efficiency and purity of the PMD detector for the heavy-ion collisions. Since the PMD detector is installed in the forward pseudo-rapidity region, so it is sufficient to generate particles in the forward region only. Events are generated for Pb-Pb collisions with the following parameters. Number of events generated are 1000, detectors included in the simulation are PMD, TPC, ITS, V0, T0, Beam pipe, FMD, Hall and Dipole, and pseudo-rapidity coverage used is 0.0 to 0.8 with 2π azimuthal angle. The parametrized HIJING is used with dN/dη = 2000 in the mid-rapidity region with π^0 decay ON.

The pseudo-rapidity distribution $(\mathrm{d}N/\mathrm{d}\eta)$ of the generated charge particles in the
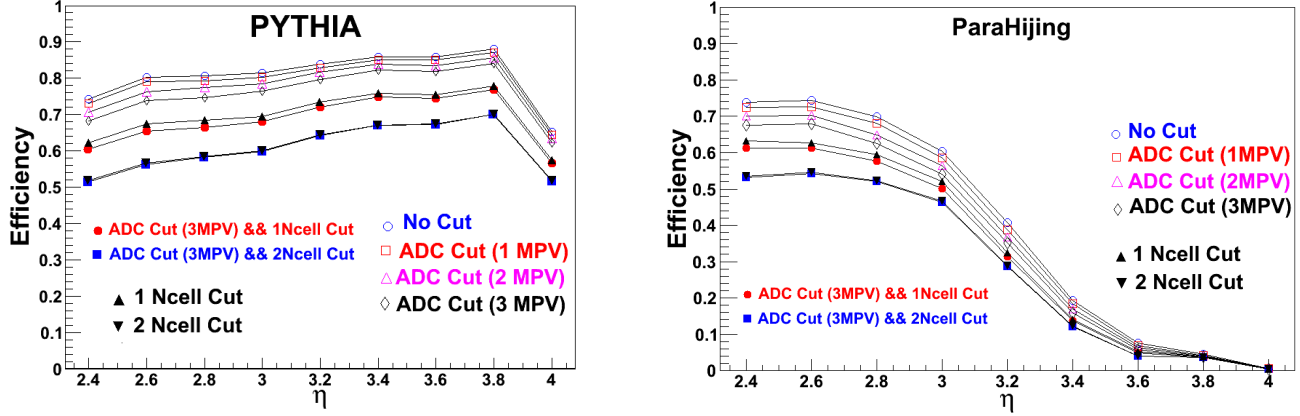
Figure 4.27: The comparison of efficiency as a function of pseudo-rapidity with different photon hadron threshold cuts. Left plot: for PYTHIA; Right plot: for parametrised HIJING (p = 2000).

parametrised HIJING events are shown in Fig. 4.26. The particles are generated only in the forward pseudo-rapidity region and the number of charged particles in the mid-rapidity region is nearly 2000. To embed single particle we need to first generate single particle event with the same parameters. Since we want to calculate the efficiency and purity of photons detection for the PMD detector, so it is sufficient to generate single particle in the PMD pseudo-rapidity region.

A single particle (photon/hadron) is embedded in the parametrised HIJING event. About 20K different embedded events for photon embedding as well as for charged particle embedding are generated. Embedding is done in the hits level. Then, we do digitisation and run full reconstruction chain. After association we look for clusters formed by the embedded particle (photon/hadron). Finally, the efficiency and purity using HIJING embedding are obtained employing the similar procedure as used for PYTHIA. The comparison between the results from PYTHIA and HIJING embedding are discussed in the next section.

4.5.4   Comparison between PYTHIA and HIJING embedding results

The comparison of efficiency of photon detection with different photon hadron detection cuts using PMD detector are shown in Fig. 4.27. Efficiency as a function of pseudo-

rapidity is shown for PYTHIA in the left figure and for parametrised HIJING (p = 2000) in the right. For PYTHIA, the efficiency increases with pseudo-rapidity and suddenly drops at $\eta \sim 4$ because of upstream material (beam pipe). For parametrised HIJING, the efficiency is decreasing with η. Figure 4.28 shows the comparison of purity with different cuts as a function of η for PYTHIA (left) and for parametrised HIJING (right). For PYTHIA, the purity is almost constant as a function of η for different cuts. However, for HIJING, purity is almost flat up to $\eta = 3.4$ for different cuts. After $\eta = 3.4$, it shows fluctuations.

Figure 4.27 (right plot) is obtained using parametrised HIJING with primary particles as 2000 in the mid-rapidity region. Since the particle density in the HIJING events is greater compared to those in PYTHIA events, the different behaviour of efficiency between the PYTHIA and HIJING could be due to the different particle densities used in these generators. Figure 4.29 (top panels) shows the X-Y display of hits on the preshower plane at digits level (left panel) and efficiency as a function of η with no ADC and no number of cells cuts (right panel) for the PYTHIA generator. Similarly, middle panels represent the X-Y display and efficiency as a function of η for HIJING generator with primary particles as 2000. From these plots, it can be seen that when the multiplicity is less, the efficiency is high. This can also be confirmed from the middle panels of Fig. 4.29. The plots suggest that when we go from lower η value towards the higher η (close to beam pipe) , the multiplicity increases (see left panel) and the efficiency decreases (see right panel). Now, it will be interesting to see the behaviour of efficiency by varying the particle density in HIJING. Therefore, to study the decrease of efficiency with pseudo-rapidity in HIJING, we have generated parametrised HIJING events with primary particles as 8000.

Figure 4.29 (bottom panels) shows the X-Y display of hits on the preshower plane at digits level. The left panel show the X-Y display for parametrised HIJING with primary particles as 8000 in the mid rapidity region. Now we observe that the efficiency shows similar trend as observed for the previous case, but overall efficiency is less compared to previous case.

Hence, we find that for photon multiplicity and pseudo-rapidity distribution measurements using PMD in pp collisions in the ALICE experiment, the embedding technique
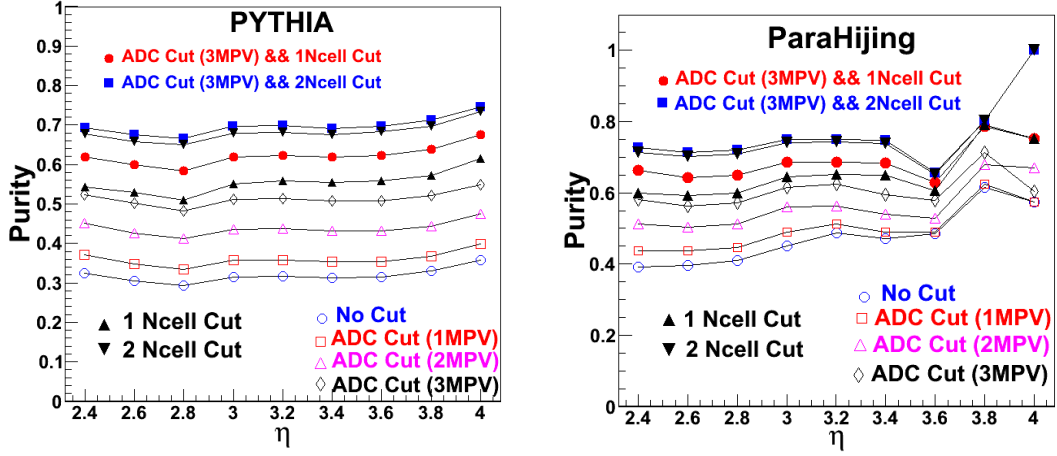
Figure 4.28: The comparison of purity as a function of pseudo-rapidity with different photon hadron threshold cuts. Left plot: for PYTHIA; Right plot: for parametrised HIJING (p = 2000).

using PYTHIA event generator provides reasonable results of efficiency and purity. The HIJING is mostly used as event generator for the heavy-ion collisions but embedding technique using HIJING shows decreasing trend with increasing η. However, previous studies of PMD efficiency and purity with HIJING event generator in the STAR experiment [15, 20] without using embedding technique give reasonable results with no such decrease in efficiency as shown in the Fig. 4.30. So embedding technique using HIJING is not suitable for studying PMD efficiency and purity in heavy-ion collisions at the ALICE experiment. Other techniques (e.g. two fold method) may be used to further investigate the PMD efficiency and purity calculations.

4.6   Summary

In summary, the ALICE-PMD simulation framework and full reconstruction chain used for simulation and real data are discussed in details in this chapter.

Different clustering algorithms are discussed by performing various checks to study the properties of crude clusters and refined clusters. Two different methods of refined clustering are discussed. One of the method is developed from the work presented in this thesis and compared with the previously existing refined clustering routine. We find that
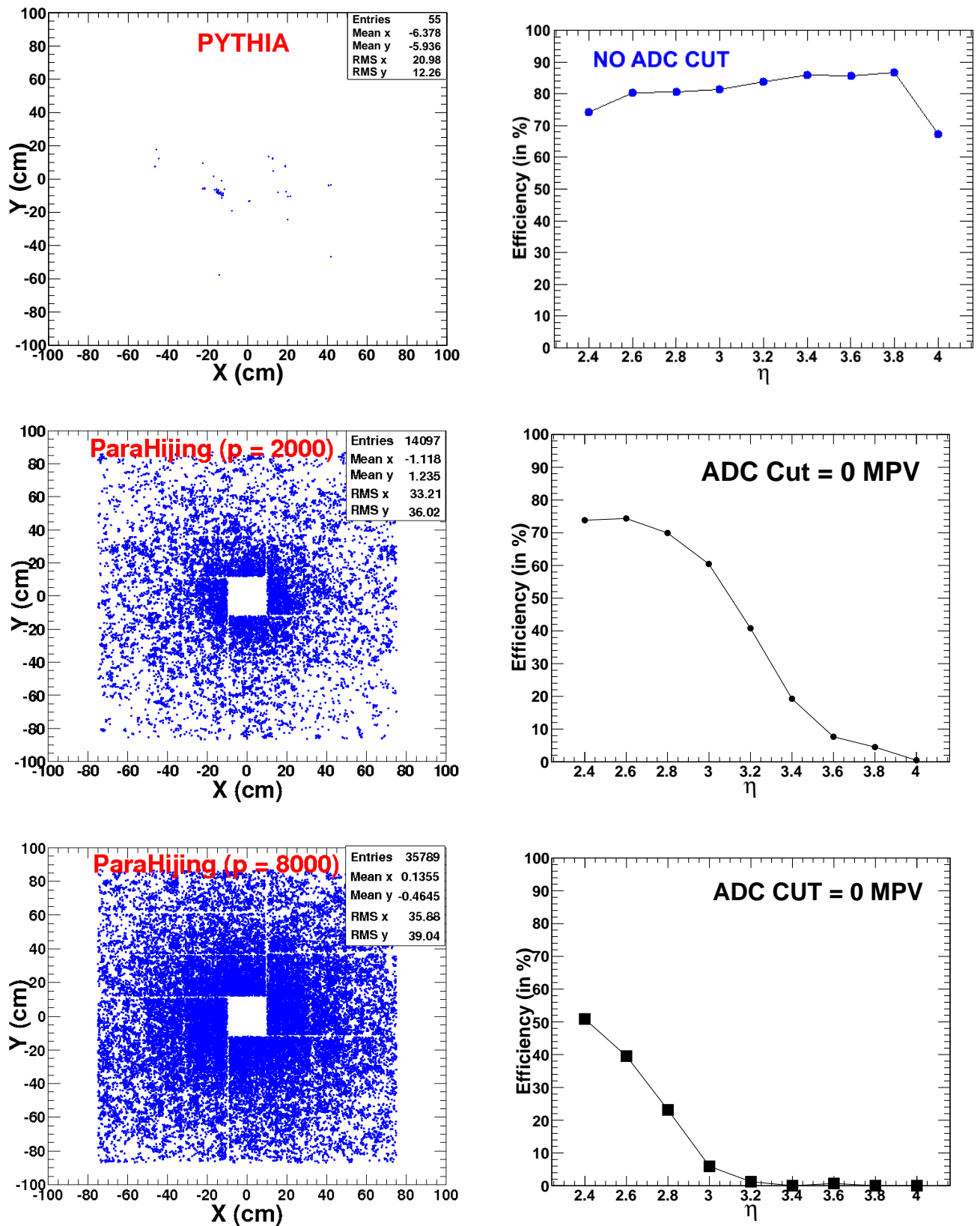
Figure 4.29: Left panel: Show the X-Y display of the hits on preshower plane for different generators. Right panel: Show the efficiency as a function of pseudo-rapidity with no ADC cut for different generator.
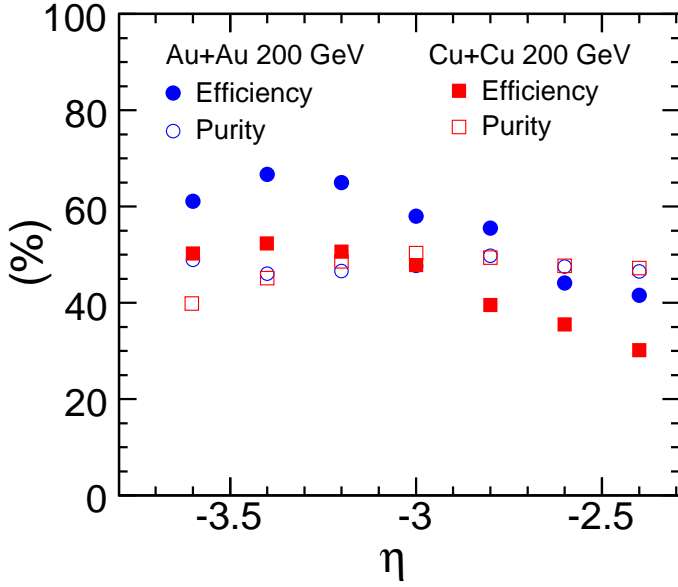
Figure 4.30: PMD Efficiency and purity as a function of η for Au-Au and Cu-Cu collisions at 200 GeV using HIJING event generator in the STAR experiment [15, 20].

although the two methods are similar in most of the ways, the sum of cell ADC assigned to a cluster is not always equal to the cluster ADC for old or existing routine which should not be the case. However, the new method gives sum of cell ADC always equal to the cluster ADC.

Effect of upstream material in front of the PMD is also studied. We find that the major contribution of the material in front of the PMD is due to the ALICE-ITS detector which corresponds to a radiation length of ~ 34 X_0 at $\eta=2.3$ and at regular ϕ intervals. This will affect the photon detection efficiency in the lower η region of the PMD.

The photon hadron discrimination threshold cuts are also discussed and optimised. After detailed study of N_{cell} and ADC cuts, we found that the best optimised cut for the photon hadron discrimination should be cluster ADC > 3MIP and number of cells in a cluster greater than one.

Finally, the photon detection efficiency and purity of the photon sample are studied using the embedding technique with PYTHIA (for pp collisions) and HIJING (for Pb-Pb

collisions) event generators. It is observed that embedding technique works well for the low multiplicity events such as pp collisions.

Bibliography

[1] M. M. Aggarwal *et al.*, Nucl. Instr. Meth. **A488** (2002) 131.

[2] ALICE Technical Design Report on Photon Multiplicity Detector, CERN/LHCC/99-32 (1999).

[3] ALICE Technical Design Report on Photon Multiplicity Detector, Addendum-1, CERN/LHCC 2003-038 (2003).

[4] R. Brun and F. Rademakers, ROOT: An object oriented data analysis framework, Nucl. Instrum. Meth. A **389** (1997) 81.

[5] The ALICE experiment offline project,
http://www.cern.ch/ALICE/Projects/offline/aliroot/Welcome.html

[6] T. Sjostrand *et al.*, Comput. Phys. Commun. **135** (2001) 238; T. Sjostrand and M. van Zijl, Phys. Rev. D **36** (1987) 2019; T. Sjostrand and P. Skands, Eur. Phys. J. C **39** (2005) 129; J. High Energy Phys. **05** (2006) 026.

[7] S. E. Vance, M. Gyulassy, and X. N. Wang, Phys. Lett. B **443** (1998) 45.

[8] R. Engel, Z. Phys. C **66** (1995) 203; R. Engel, J. Ranft, and S. Roesler, Phys. Rev. D **52** (1995) 1459.

[9] G. Marchesini, B. R. Webber, Cavendish-HEP-87/9. Dec 1987.

[10] R. Brun *et al.* CERN-DD-78-2-REV (1978).

[11] William R. Leo, Techniques for Nuclear and Particle Physics Experiments, First Narosa Publishing House Reprint (1995).

[12] S. C. Phatak, Clustering Algorithm for PMD,
http://www.iopb.res.in/phatak/cluster/.

[13] T. K. Nayak and B. Mohanty, private communication.

[14] P. K. Netrakanti, Ph.D. Thesis, Jadavpur University 2008.

[15] L. Kumar, Ph.D. Thesis, Panjab University, Chandigarh 2010.

[16] S. K. Prasad, Ph.D. Thesis, Univ. of Calcutta, 2011.

[17] A. K. Dash, Institute of Physics Bhubaneswar Internal Report IP/BBSR/2009-7, Ph.D. Thesis Utkal University, 2009.

[18] M. M. Mondal, Ph.D. Thesis, Univ. of Calcutta, 2010.

[19] PMD Efficiency and Purity
https://nsharma.web.cern.ch/nsharma/Embedding/embedding.html

[20] B. I. Abelev *et al.* (STAR Collaboration), Nucl. Phys. A **832** (2010) 134.

Chapter 5

(ANTI)MATTER PRODUCTION USING STATISTICAL AND COALESCENCE MODELS

5.1 Introduction

One of the striking features of particle production at high energy collisions is the nearly equal abundance of matter and antimatter in the central rapidity region [1, 2]. It is believed that a similar symmetry existed in the initial stage of the universe. It remains a mystery how this symmetry got lost in the evolution of the universe reaching a stage with no visible amounts of antimatter being present. The ultra-relativistic nuclear collisions could recreate energy density similar to that of the universe few microseconds after the Big-Bang. These collisions generate hot and dense matter which contains equal number of quarks and anti-quarks leading to matter and antimatter production. In such collisions the u, d and s quarks are produced in equal number which is ideal for hypernuclei and anti-hypernuclei production. Hypernuclei are nuclei which contain at least one hyperon (particles with s quark) in addition to nucleons.

The STAR Collaboration at RHIC has reported the first observation of anti-hypertriton ($^3_\Lambda \overline{\text{H}}$) in Au-Au collisions at $\sqrt{s_{NN}} = 200$ GeV in 2010 [3]. Recently, both the STAR [4] and the ALICE Collaboration have observed first time the anti-alpha ($^4\overline{\text{He}}$) particle in the heavy-ion collisions, in the year 2011. The ALICE experiment have also observed light anti-nuclei: anti-deuterons (d), anti-tritons ($^3\overline{\text{H}}$) and anti-helium3 ($^3\overline{\text{He}}$) in pp collisions at $\sqrt{s} = 7$ TeV and in Pb-Pb collisions at $\sqrt{s_{NN}} = 2.76$ TeV. The data

analysis to identify these light nuclei and anti-nuclei in the ALICE experiment are discussed in details in the next chapter of this thesis. The production mechanism of these (anti)nuclei and (anti)hypernuclei in a collision is still not understood. Till now, the statistical-thermal model and the coalescence model have been very successful in describing the hadron yields and ratios in elementary (pp, p$\bar{\text{p}}$ and e^+e^-) collisions as well as in the central heavy-ion collisions over the wide range of energies. The statistical-thermal model has provided us useful framework to describe the centrality and system size dependence of particle production in low and high energy collisions [1, 5].

In this chapter, we will discuss the formulation of statistical-thermal model and its applications to the phenomenological description of (anti)particles and (anti)nuclei production in pp as well as in heavy-ion collisions. More emphasise is given on the importance of conservation laws and their implementations in the statistical-thermal approach. The formulation of coalescence model and its application on the anti-nuclei production in the heavy-ion collisions are also discussed.

5.2 The Statistical Thermal Model

The statistical-thermal model assumes that in a high energy collision at freeze-out all hadrons follow equilibrium distributions. The conditions at chemical freeze-out where inelastic collisions cease are governed by the hadron abundances, while the particle spectra offer insight into the conditions at thermal freeze-out where elastic collisions cease. Once thermal parameters are fixed, the hadron gas partition function gives all primordial thermodynamic observables of the system.

The equilibrium behavior of thermodynamical observables can be evaluated as an average over statistical ensembles (rather than as a time average for a particular state) [6]. The equilibrium distribution is thus obtained by an average over all accessible phase space. Furthermore, the ensemble corresponding to thermodynamic equilibrium is that for which the phase space density is uniform over the accessible phase space. In this sense, filling the accessible phase space uniformly is both a necessary and sufficient condition for equilibrium. Consequently, the agreement between observables and predictions using the

statistical operator imply equilibrium (to the accuracy with which agreement is observed).

The particle yields in the relativistic heavy-ion collisions over past two decades shows striking regularity at all beam energies [7]. Particle ratios and yields are found to be described with remarkable precision, by the statistical-thermal model [8]. This fact allows to estimate thermal parameters characterizing the particle source for each colliding system which is relevant for the understanding of the thermal properties of dense and hot matter and for the studies of QCD phase transitions [9–12]. For a given collision energy, the statistical-thermal model with only two parameters, the chemical freeze-out temperature (T) and baryon chemical potential (μ_B), provides a very systematic description of the particle yields. As the model considers integrated particle multiplicities, it is not sensitive to local inhomogeneities and/or fluctuations as these will mainly disappear after integration over particles. Local inhomogeneities have been considered in recent years in detail in Refs. [13, 14].

With the increasing collision energy, there is an increase of the chemical freeze-out temperature, T, and a corresponding decrease of the baryon chemical potential, μ_B. In the (T, μ_B)-plane the freeze-out parameters lie on a curve connecting the lowest data points taken at the SIS through the data points taken at the BNL Alternating Gradient Synchrotron (AGS), at the CERN Super Proton Synchrotron (SPS), and at RHIC with a temperature that corresponds to the critical temperature expected for de-confinement [15]. Within the grand-canonical (GC) ensemble, the quantum numbers of the system are conserved on an average through the action of chemical potentials [16]. In other words, the baryon B, strangeness S and the charge content Q are fixed on average by the μ_B, μ_S and μ_Q chemical potentials respectively. For each chemical potential one can introduce the corresponding fugacity $\lambda = e^{\mu/T}$ where, T is the temperature of the system. In the GC ensemble the density of hadron species i with the mass m_i, the quantum numbers B_i, S_i and Q_i and with the spin-isospin degeneracy factor g_i is express as

$$n_i(T, \mu_B, \mu_S, \mu_Q) = \frac{<N_i>}{V} = \frac{g_i}{2\pi^2} m_i^2 T \lambda_B^{B_i} \lambda_S^{S_i} \lambda_Q^{Q_i} K_2\left(\frac{m_i}{T}\right). \tag{5.1}$$

Here, $K_2(x)$ is the modified Bessel function, $K_2(x) = \sqrt{\frac{\pi}{2x}} e^{-x}$, and g_i is degeneracy factor defined as $(2J + 1) \times (2I + 1)$. Then,

$$n_i(T, \overrightarrow{\mu}) = \frac{g_i}{2\pi^2}\sqrt{\frac{\pi}{2}}(Tm_i)^{\frac{3}{2}}e^{\frac{-m_i+B_i\mu_B+S_i\mu_S+Q_i\mu_Q}{T}} \tag{5.2}$$

The above form is valid only in the Boltzmann approximation and is easily general-ized to the quantum statistics [17, 18].

In the application of the statistical-thermal model, the chemical potentials μ_S and μ_Q are typically constrained in the initial stage by the strangeness neutrality condition and by the fixed baryon-to-charge ratio. However, it is well established, that the usual form of the statistical-thermal model formulated in the grand canonical ensemble cannot be used when either the temperature T or the volume parameter V or both are small [16, 19]. As a thumb rule one needs $VT^3 > 1$ for a grand canonical description to hold [20–22]. This condition is not usually justified in pp collisions (where volume is very small), requiring canonical (C) formulation of strangeness conservation. The exact strangeness conservation causes a suppression in particle ratios of strange (or multi-strange) hadrons to pions or to any strangeness neutral particles as compared to the corresponding ratio in the grand canonical limit. The key parameter governing this effect can be quantified by the strangeness correlation volume [19]. The effect of this parameter is seen and discussed in the later section of this chapter.

The statistical-thermal model, THERMUS [18] is used to perform various calcula-tions for pp and heavy-ion collisions system at various energies. The details of THERMUS model is discussed below.

5.2.1   THERMUS

With an appropriate choice of ensemble, the statistical-thermal model has been extremely successful in describing the hadron multiplicities in relativistic collisions for both heavy-ion and elementary collisions over a wide range of energies.

This motivated the development of THERMUS – a thermal model analysis package of $C++$ classes and functions for incorporation into the object oriented ROOT framework. All THERMUS C++ classes inherit from the ROOT base class TObject. This allows them to be fully integrated into the interactive ROOT environment. They are compiled into shared libraries which can be loaded in a ROOT session allowing all the ROOT

functionality in a thermal analysis of particle production in the relativistic elementary
and heavy-ion collisions.

   This model is capable of performing calculations within three different statistical
ensembles; a grand-canonical treatment of the conserved quantities as baryon number
(B), strangeness number (S) and charge (Q), a fully canonical treatment of the conserved
quantities, and a mixed-canonical (also known as strangeness canonical) ensemble com-
bining a canonical treatment of strangeness with a grand-canonical treatment of baryon
number and electric charge. THERMUS also allows for the assignment of decay chains
and detector efficiencies specific to each particle yield, which enables sensible fitting of
model parameters to the experimental data. Currently, THERMUS performs only chem-
ical freeze-out analyses. In other words, no kinetic freeze-out analysis or momentum
spectra calculations are performed.

   In order to calculate the thermal properties of a system, one starts with an evaluation
of its partition function. The form of the partition function obviously depends on the
choice of ensemble.

5.2.1.1   The Grand Canonical (GC) ensemble

This ensemble is the most widely used in the applications of heavy-ion collisions [9, 10, 16].
Within this ensemble, conservation laws for energy and quantum numbers are enforced on
average i.e. the baryon number (B), strangeness content (S) and charge (Q) are conserved
on an average.

   The parameters used in the grand canonical ensemble are T, μ_B, μ_S, μ_Q, γ_s, and R.
These represent respectively, the chemical freeze-out temperature, baryon chemical po-
tential, strangeness chemical potential, charge chemical potential, strangeness suppression
factor, and radius of the fireball.

5.2.1.2   The Canonical ensemble

Within this ensemble, quantum number conservation is exactly enforced i.e. B, S and Q
are all treated canonically.

   The parameters used in the canonical ensemble are T, B, S, Q, γ_s, and R. Since all

conservation is exact, there is no chemical potential to satisfy constraints.

5.2.1.3 The Strangeness Canonical (SC) or Mixed Canonical ensemble

Within this ensemble, the strangeness in the system is fixed exactly by its initial value of S , while the baryon and charge content are treated grand canonically.

The parameters used in the strangeness canonical ensemble are T, μ_B, μ_S, μ_Q, γ_s, R_c, and R. Here, R_c represents the correlation or *canonical radius* which is the radius inside which strangeness is exactly conserved.

Using techniques of the THERMUS model, one can make predictions for various particle ratios, chemical freeze-out temperatures, baryon chemical potentials and radius of the fireball at different center of mass energies.

5.2.2 Particle Ratios Predictions Using GC

THERMUS model can be used to predict the ratios for various anti-nuclei to nuclei at different center of mass energies. Figure 5.1 shows various anti-nuclei to nuclei ratios as a function of center of mass energy. The black symbols represent the data (solid circles represent the $\bar{p}/p$ ratio and solid square symbol represents the $^3\overline{\text{He}}/^3\text{He}$ ratio from the experiments) while other colored symbols are the predictions from the THERMUS model as shown in the legend. The figure suggests that the ratios $\bar{\text{p}}/\text{p}$, $\bar{\text{d}}/\text{d}$, and $^3\overline{\text{He}}/^3\text{He}$, have different values at the lower energies. With increase in energy, the difference between these ratios decreases and their values reaches unity at very high energies. It can also be seen that the predictions from the THERMUS give similar results to those measured by the experiments within errors. These results are obtained using the grand canonical approach of the THERMUS model. The input parameters T and μ_B in the model, at different energies, for the ratio predictions are obtained using Eqs. 5.3 and 5.4, respectively, discussed in next subsection.

5.2.3 Parametrization of T and μ_B in heavy-ions

The statistical-thermal model, outlined above, was applied to describe particle yields in the heavy-ion collisions. The model was compared with all available experimental data
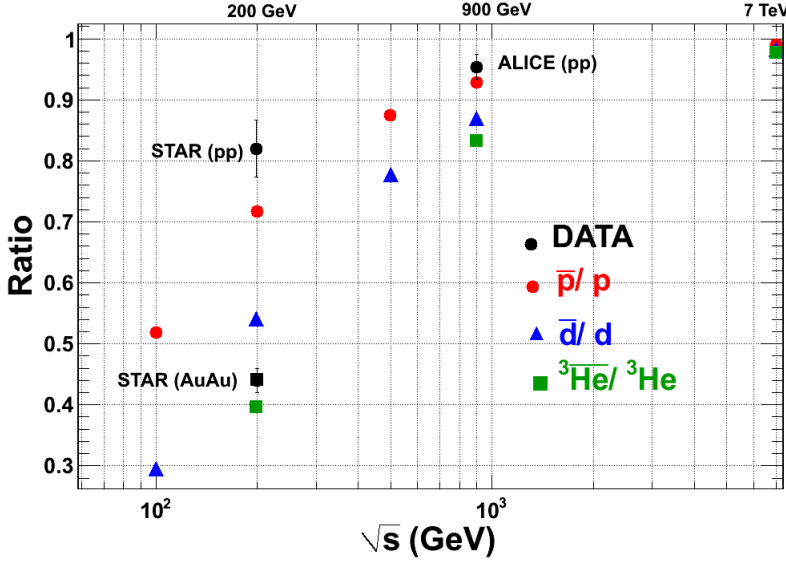
Figure 5.1: Various anti-nuclei to nuclei ratios predictions using THERMUS plotted as a function of center of mass energy. See text for details.

obtained in the energy range from AGS up to RHIC energy. Hadron multiplicities ranging from pions to omega baryons and their ratios were used to verify that there is a set of chemical freeze-out parameters (T, μ_B) which can simultaneously reproduce all measured yields [15, 23]. The corresponding plot is shown in Fig. 5.2. The phenomenologically representation of these parameters are [15]

$$T(\mu_B) = a - b\mu_B^2 - c\mu_B^4 \tag{5.3}$$

$$\mu_B = d/(1 + e\sqrt{s_{NN}}) \tag{5.4}$$

with $a = 0.166 \pm 0.002$ GeV, $b = 0.139 \pm 0.016$ GeV^{-1}, $c = 0.053 \pm 0.021$ GeV^{-3}, $d = 1.308 \pm 0.028$ GeV and $e = 0.273 \pm 0.008$ GeV^{-1}. As can be seen from the Fig. 5.2, the above parametrizations describe the data very well. These parametrizations are quantitatively similar to the those proposed in Ref. [24] and result in a very satisfactory description of different particle excitation functions measured in nucleus-nucleus collisions.
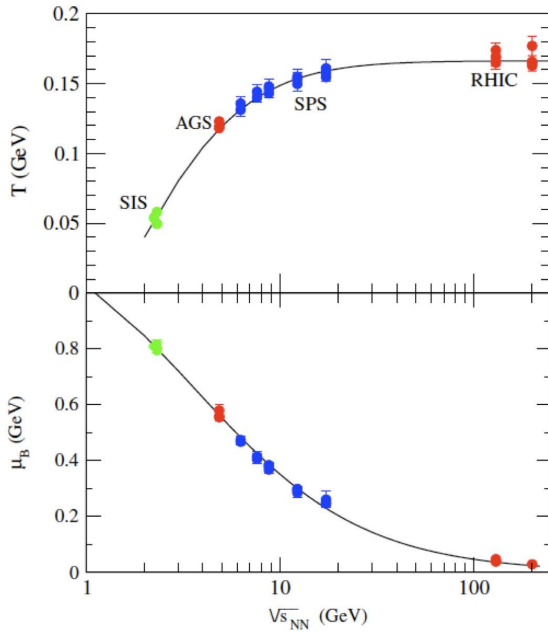
Figure 5.2: The chemical freeze-out parameters, T and μ_B as a function of center of mass energy. The curves have been obtained using parametrization in Eqs. 5.3 and 5.4. This figure is taken from the Ref. [15].

5.2.4 Parametrization of T and μ_B in pp

The phenomenological representation of chemical freeze-out parameters (T, μ_B) does not existed so far for pp collisions. We have used the existing data (of pp collisions) to obtained new parameters which could reproduce the measured yields in pp collisions. Fig. 5.3 (a) shows the change of $\bar{p}/p$ ratio with collision energy at mid-rapidity in central heavy-ion and in pp collisions. The data from NA49 and STAR Collaboration are compared with new results from the ALICE Collaboration [2]. The solid circles represent data for pp collisions and open squares for heavy ion collisions. There is a clear increase of this ratio towards unity, indicating approximate symmetry of matter and antimatter at the LHC energy. There is also a clear increase of the $\bar{p}/p$ ratio when going from heavy-ion towards pp collisions.

If (anti)nucleons are directly originating from a thermal source, then from Eq. (5.1)

(i.e. neglecting feed-down from resonances) it is obvious, that the $\bar{p}/p$ densities ratio

$$\frac{n_{\bar{p}}}{n_p} = \exp[-2\mu_B/T], \tag{5.5}$$

is entirely quantified by the μ_B/T value. Thus, an increase in the $\bar{p}/p$ ratio from heavy-ion to pp collisions, seen in Fig. 5.3 (a), is due to a decrease in the μ_B/T value.

In Fig. 5.3 (a), the heavy-ion data (open squares) are compared with the statistical-thermal model results (dashed line). In heavy-ion collisions these model calculations are done using the energy dependence of model parameters as described by Eqs. (5.3) and (5.4). There is a clear agreement of model predictions with data. For pp collisions no systematic analysis of such model parameters with energy were performed till now.

To extract the corresponding μ_B and T at fixed energy in pp collisions, we have used one of the statistical-thermal model, THERMUS [17, 18] which correctly accounts for feeding corrections to (anti)nucleons from decays of heavier resonances. The $\bar{p}/p$ ratios measured in pp collisions, shown in Fig. 5.3 (a), have been fitted using the statistical-thermal model. The resulting baryon chemical potential μ_B is shown in the Fig. 5.3 (b) by filled circles. In addition, applying the parametrization of $\mu_B(\sqrt{s_{NN}})$ as in Eq. (5.4) we have found that the parameters corresponding to pp collisions are

$$\mu_B = d_{pp}/(1 + e_{pp}\sqrt{s_{NN}}) \tag{5.6}$$

with $d_{pp} = 0.4$ GeV and $e_{pp} = 0.1599$ GeV^{-1}. The solid line in the Fig. 5.3 (b) represents the energy dependence of μ_B in pp collisions obtained with the above new parameters. For comparison also shown in this figure is the energy dependence of the value of μ_B in heavy-ion collisions. It is also clear that at mid-rapidity region, μ_B is always lower in pp than in heavy-ion collisions. This observation reflect the fact that at mid-rapidity the stopping power in pp collisions is less than in heavy-ion reactions, as can be seen in Fig. 5.3 (a).

We have used the same T ($\sqrt{s_{NN}}$) dependence for pp as for heavy-ion collisions. This is justified by the observation that at high energies there is no noticeable change in T between central and peripheral heavy-ion collisions as well as for pp collisions [28]. The
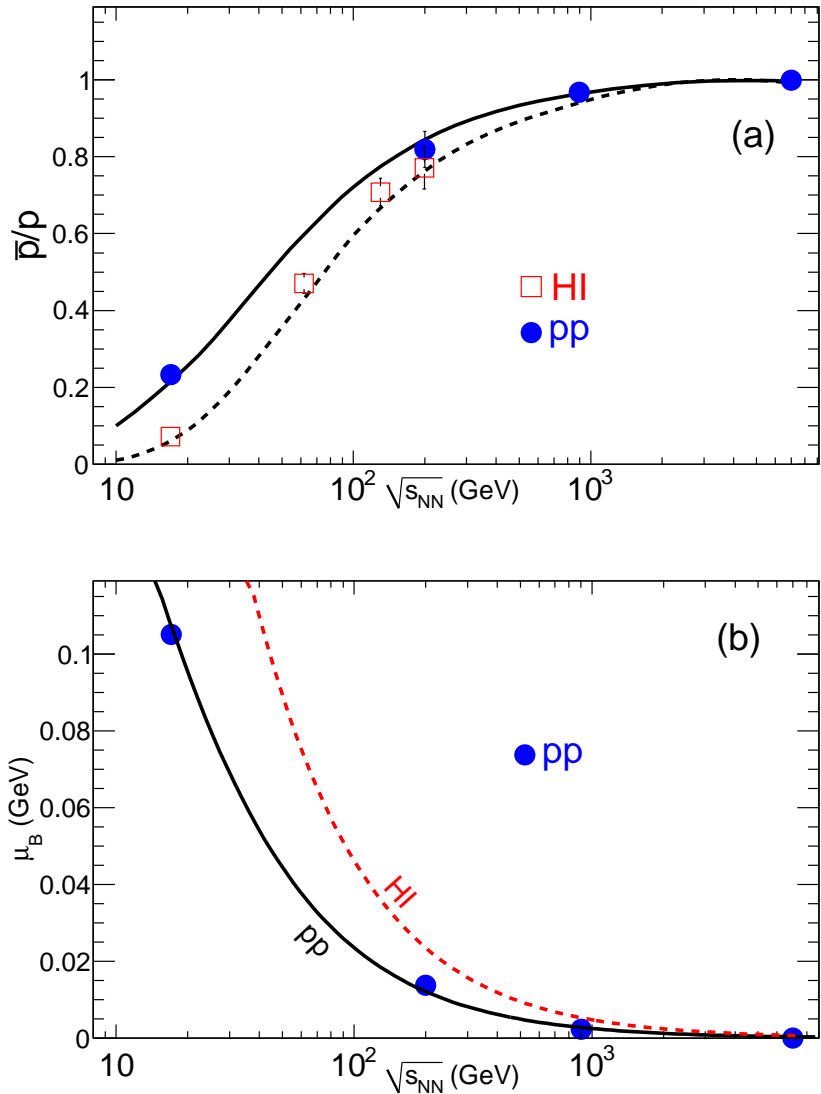
Figure 5.3: (a) The $\bar{\mathrm{p}}/\mathrm{p}$ ratio and (b) μ_B as a function of $\sqrt{s_{NN}}$. The solid circles are results from pp collisions and the open squares are results from heavy-ion collisions [1, 2, 25–27]. The dashed line is the parametrization for heavy-ion collisions from Ref. [15] while the solid line is the new parametrization for pp collisions (Eq. 5.6).

change of $\bar{\mathrm{p}}/\mathrm{p}$ ratio with energy in pp collisions is quantified in Fig. 5.3 (a) (as solid line) using parametrization of μ_B ($\sqrt{s_{\mathrm{NN}}}$) adjusted for pp collisions, as in Eq. (5.6).

5.3 Antibaryon to Baryon Ratio Comparison With Thermus Predictions

In the previous section, we have derived a new parametrization for baryon chemical potential (μ_B) as in Eq. 5.6 for pp collisions. In this section we will study the trend of antibaryon-to-baryon ratio with the strangeness content (S) and in addition, we will compare the statistical-thermal model calculations with our new parametrization with the existing data for pp collisions. For baryons carrying N_S as (anti)strange quarks, the antibaryon/baryon ratio using Eq. (5.1) (again neglecting feed-down from resonances) is given by:

$$\frac{n_{\overline{\mathrm{B}}}}{n_{\mathrm{B}}} = \exp[-2(\mu_B - N_S\mu_S)/T], \tag{5.7}$$

This equation is modified by the strange chemical potential (μ_S). As μ_S is always smaller than μ_B [16, 29], the above ratios should appear ordered with the strangeness quantum numbers, i.e. the higher N_S, the smaller the difference between antibaryon and baryon, because of negative exponential term.

Figure 5.4 show the comparison of antibaryon/baryon ratio as increasing strangeness quantum number (S) for pp and heavy-ion collisions. The left plot is for SPS energy ($\sqrt{s_{NN}} = 17.3$ GeV) and the right plot is for RHIC energy ($\sqrt{s_{NN}} = 200$ GeV). The solid points represent particle ratios from data for pp collision system and open squares for heavy-ion collision system. The comparison of data with the statistical-thermal model calculations using the THERMUS code are shown as solid line for pp system and dashed line for heavy-ion system. The data and the model results both for pp and heavy-ion collisions are in good agreement. The clear trends in strange antibaryon/baryon ratios already expected from the simplified Eq. (5.7). Following interpretations are made from the two panels in Fig. 5.4.

- With increasing strangeness content, the antibaryon/baryon ratios are increasing
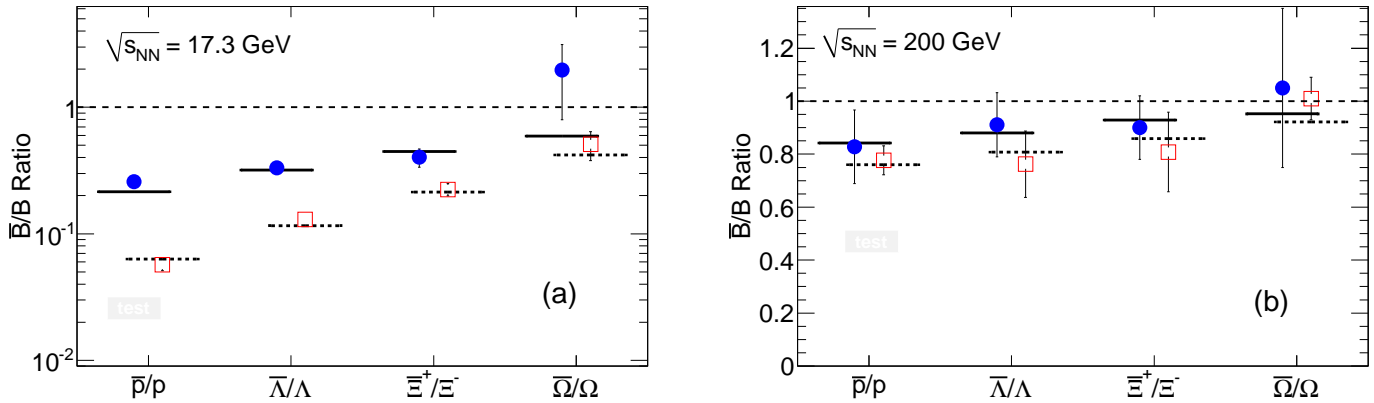
Figure 5.4: Antibaryon to baryon ratios sorted according to their strangeness content. Circles (solid horizontal line) refer to pp collisions data (model calculations) and open squares (dashed horizontal line) refer to heavy-ion collisions data (model calculations). The left panel shows results at the SPS and the right panel at the RHIC energy.

and approaching to unity.

- Heavy-ion collisions exhibit smaller $\bar{B}/B$ ratios as compared to pp collisions due to different μ_B values as mentioned in the previous section. This is well seen at SPS energies, as the difference in μ_B in pp and Pb-Pb systems is larger than that at RHIC.

- The differences between heavy-ion and pp collisions decrease with increasing energy ($\sqrt{s_{NN}}$). Since at LHC energies the $\bar{p}/p$ ratio is close to unity [2] and therefore, the abundances of strange baryons are roughly as large as those of anti-strange baryons.

5.4 Ratio Comparison With Models in Au-Au at $\sqrt{s_{NN}} = 200$ GeV

The production of matter and antimatter with strangeness content, expressed as antibaryon-to-baryon ratios is well described by the statistical-thermal model. Thus, it is of interest to verify whether the recently observed production of light (anti)nuclei including (anti)hypertritons ($^3_\Lambda$H) in heavy-ion collisions (Au-Au, $\sqrt{s_{NN}} = 200$ GeV) at RHIC by the STAR Collaboration [3] also follows the pattern expected in the statistical-thermal model and the coalescence model frameworks. Figure 5.5 shows the antiparticle-to-particle

ratios for heavy-ion collisions (Au-Au collisions) at the RHIC energy ($\sqrt{s_{NN}} = 200$ GeV). The open square symbols represent the experimental data values [30, 31]. The interpretations of these results are given using the Statistical-Thermal and the Coalescence model approaches in the following subsections.

5.4.1 Statistical-Thermal Model Approach

Studying the antinuclei-to-nuclei ratio in the statistical-thermal model picture, we observed that an extra factor of μ_B is picked up each time the baryon number is increased. Thus, each nucleon adds a factor of μ_B in the exponent of the Boltzmann factor in Eq. (5.1). The production of nuclear fragments is therefore very sensitive to the value of the baryon chemical potential (μ_B) and thus could be useful for the precise determination of μ_B of the system.

The deuterium has an additional neutron and the antideuterium-to-deuterium ratio in the statistical-thermal model is given by

$$\frac{n_{\overline{\mathrm{d}}}}{n_{\mathrm{d}}} = \exp[-4\mu_B/T], \tag{5.8}$$

thus should be similar to the square of the antiproton-to-proton ratio if decay contributions of heavier resonances to nucleon yields are neglected.

The ^{3}He has three nucleons and the corresponding $^3\overline{\mathrm{He}}/^3\mathrm{He}$ ratio is given by

$$\frac{n_{^3\overline{\mathrm{He}}}}{n_{^3\mathrm{He}}} = \exp[-6\mu_B/T], \tag{5.9}$$

which is then similar to $(\bar{\mathrm{p}}/\mathrm{p})^3$.

If the nuclei carry strangeness, then this leads to an extra term μ_S and therefore the ratio of antihypertriton-to-hypertriton reads

$$\frac{n_{^3_{\overline{\Lambda}}\overline{\mathrm{H}}}}{n_{^3_{\Lambda}\mathrm{H}}} = \exp[-(6\mu_B - 2\mu_S)/T]. \tag{5.10}$$

In mixed ratios, i.e. ratios of nuclei (or anti-nuclei) with different mass, there appears an extra factor due to different degeneracy and masses, e.g. in the statistical-thermal model

$$\frac{n_{^3_{\Lambda}\mathrm{H}}}{n_{^3\mathrm{He}}} = \frac{g_{^3_{\Lambda}\mathrm{H}}}{g_{^3\mathrm{He}}} \frac{(m_{^3_{\Lambda}\mathrm{H}})^2}{(m_{^3\mathrm{He}})^2} \frac{K_2(m_{^3_{\Lambda}\mathrm{H}}/T)}{K_2(m_{^3\mathrm{He}}/T)} \exp[-\mu_S/T]. \tag{5.11}$$
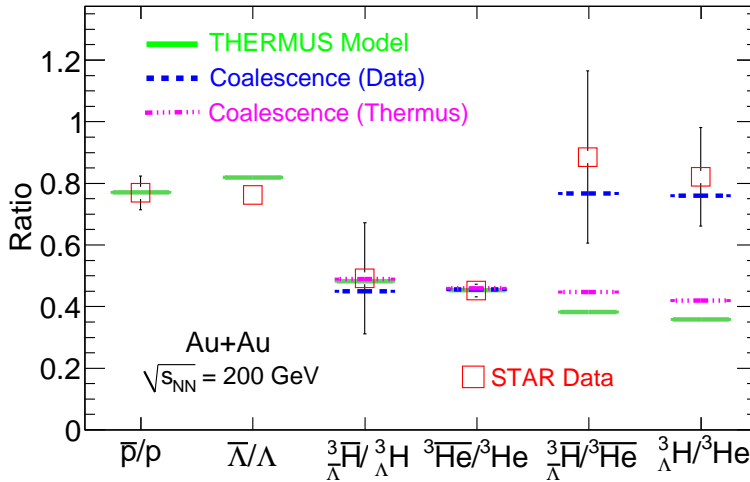
Figure 5.5: Comparison of data from the STAR Collaboration with the statistical-thermal and the coalescence model. For the coalescence approach both experimental values [30, 31] (dashed lines) and values from the statistical-thermal model (dash-dotted lines) have been used.

Figure 5.5 shows the comparisons of statistical-thermal model results on different (anti)nuclei ratios with the recent experimental data from the STAR Collaboration. The open squares represent RHIC data and the solid line represent model calculation of various particle ratios. Yields of ^{3}He and $^3\overline{\text{He}}$ have been corrected for contamination from hypertriton and antihypertriton decays assuming the decay branching ratio of 25% and consequently in the model calculations such decays have not been included.

In the statistical-thermal model, following Eqs. (5.9) and (5.10), ratios of (anti)nuclei-to-nuclei are entirely quantified by the μ_B/T and μ_S/T values. From Fig. 5.5 it clear that using the thermal parameters at chemical freeze-out obtained from the analysis of particle yields at RHIC, there is an excellent description of measured ratios of $^3\overline{\text{He}}/^3$He and $^3_{\overline{\Lambda}}\overline{\text{H}}/^3_{\Lambda}$H. However, deviations are seen on the level of mixed ratios, $^3_{\overline{\Lambda}}\overline{\text{H}}/^3\overline{\text{He}}$ and $^3_{\Lambda}$H/^{3}He.

In elementary collisions, nuclei and anti-nuclei as well as hypernuclei and antihypernuclei can be produced by direct pair production. In heavy-ion collisions, due to final state correlations, a different production mechanism opens up through hadron coalescence. Indeed, production of nuclei in Pb-Pb collisions at $\sqrt{s_{NN}} = 17.3$ GeV at CERN

SPS [32] have been found to be consistent with a coalescence picture, while this was not the case in p-Be collisions at the same energy.

5.4.2   Coalescence Model Approach

In relativistic heavy-ion collisions, light nuclei and anti-nuclei can be formed through coalescence of produced nucleons and anti-nucleons or participant nucleons. Since the binding energy is small, this formation process can only happen at a late stage of the evolution of the system when interactions between nucleons and other particles are weak. This process is also known as final-state coalescence. The coalescence probability is related to the local nucleon density. Therefore, the production of light nuclei provide a tool to measure collective motion and freeze-out properties, such as particle density and correlation volume. In the most straight forward coalescence picture the ratios of different (anti)nuclei can be directly related to ratios of hadronic yields. In particular,

$$\frac{^3\overline{\text{He}}}{^3\text{He}} = \frac{\bar{\text{p}}\bar{\text{p}}\bar{\text{n}}}{\text{ppn}} \simeq \left(\frac{\bar{\text{p}}}{\text{p}}\right)^3 \tag{5.12}$$

$$\frac{^3_{\bar{\Lambda}}\overline{\text{H}}}{^3_{\Lambda}\text{H}} = \frac{\bar{\text{p}}\bar{\text{n}}\bar{\Lambda}}{\text{pn}\Lambda} \simeq \left(\frac{\bar{\text{p}}}{\text{p}}\right)^2 \frac{\overline{\Lambda}}{\Lambda} \tag{5.13}$$

$$\frac{^3_{\Lambda}\text{H}}{^3\text{He}} = \frac{\text{pn}\Lambda}{\text{ppn}} \simeq \frac{\Lambda}{\text{p}} \tag{5.14}$$

and

$$\frac{^3_{\bar{\Lambda}}\overline{\text{H}}}{^3\overline{\text{He}}} = \frac{\bar{\text{p}}\bar{\text{n}}\bar{\Lambda}}{\bar{\text{p}}\bar{\text{p}}\bar{\text{n}}} \simeq \frac{\overline{\Lambda}}{\bar{\text{p}}}. \tag{5.15}$$

From Eqs. (5.9) and (5.12) as well as from Eqs. (5.10) and (5.13) it is clear that neglecting feed-down from resonance decays the statistical-thermal model coincides with coalescence predictions on the level of $^3\overline{\text{He}}/^3\text{He}$ and $^3_{\bar{\Lambda}}\overline{\text{H}}/^3_{\Lambda}\text{H}$ ratios (see also Ref. [33]). The coalescence expectation of various (anti)nuclei ratios using Au-Au ($\sqrt{s_{NN}} = 200$ GeV RHIC data is shown as dashed line (blue color) in Fig. 5.5. Thus, as long as the key input ratios $\bar{\text{p}}/\text{p}$ and $\overline{\Lambda}/\Lambda$ are in agreement with a thermal descriptions, the measured ratios do not allow to distinguish the two mechanisms. However, differences between

these models are seen on the level of mixed ratios, $^3_\Lambda\overline{\text{H}}/^3\overline{\text{He}}$ and $^3_\Lambda\text{H}/^3\text{He}$, due to different masses of nuclei. From Eqs. (5.11) and (5.14) one finds that when neglecting binding energy of nuclei and feed-down corrections the statistical-thermal model differs from the coalescence framework by a factor of $(1/3 + 2\text{m}_\text{p}/3\text{m}_\Lambda)^{3/2}$. The coalescence expectation of various (anti)nuclei ratios using the statistical-thermal model calculation is shown as dash-dotted line (pink color) in Fig. 5.5. Consequently, the statistical-thermal model results for $^3_\Lambda\overline{\text{H}}/^3\overline{\text{He}}$ and $^3_\Lambda\text{H}/^3\text{He}$ ratios (solid lines in Fig. 5.5) are lower than those obtained in the coalescence picture using the (anti)Λ/p ratios from THERMUS.

The results from the coalescence model [34, 35] are compared to data from the STAR Collaboration and the statistical-thermal model predictions in Fig. 5.5. The coalescence estimate has been done using the $\bar{\text{p}}$/p, $\bar{\Lambda}/\Lambda$, $\bar{\Lambda}/\bar{p}$ and Λ/p ratios both measured by the STAR Collaboration [3, 30, 31] (dashed lines) and from the THERMUS calculations (dash-dotted lines).

We note that in coalescence picture the equilibrium abundances of particle yields are not required. Consequently, (anti)nuclei produced from the off-equilibrium medium can lead to particle ratios being in agreement with the simple coalescence estimate discussed above. However, this is not anymore the case for statistical-thermal model which requires statistical order of particle yields in the final state.

5.4.3 Canonical Radius (R_c) Study for pp Collisions

As mentioned before, for elementary systems (like pp system), the grand canonical ensemble cannot be used. The strangeness has to be treated canonically for pp collisions. Thus for pp systems, to apply the statistical-thermal model, one has to provide the correlation volume or canonical radius (R_c) as the input parameter. Since the exact value of R_c is not know for the pp collisions, we study different antiparticle ratios in the strangeness canonical formulation in the THERMUS with different values of R_c. For the other input parameters, we have used T and μ_B from Eqs. 5.3 and 5.6 respectively, and R is fixed as 4 fm. Figure 5.6 shows the various antiparticle ratios for different canonical radius assumptions. It can be seen that for most cases, the ratios are similar for different R_c values. The difference observed for ratios involving antihypernuclei to anti-nuclei could
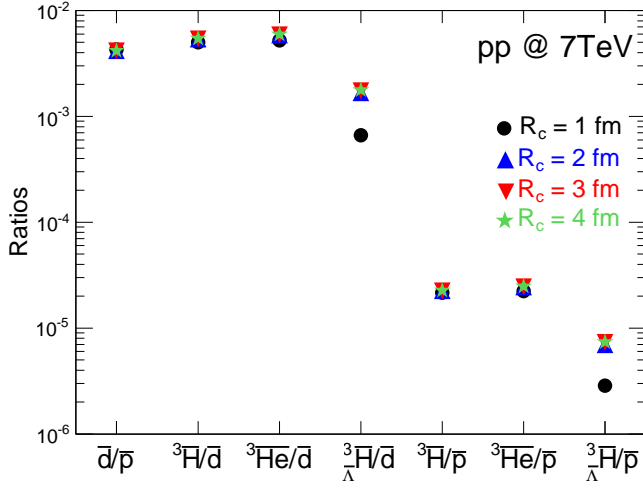
Figure 5.6: Comparison of data from the STAR Collaboration with the statistical-thermal and the coalescence model. For the coalescence approach both experimental values [30, 31] (dashed lines) and values from the statistical-thermal model (dash-dotted lines) have been used.

be due to the dependence on the strangeness. In view of these, we take the value of $R_c = 1.5$ fm for pp systems. The results presented from here onwards use this value of R_c for the pp collisions.

5.5   Statistical-Thermal Model Predictions for RHIC and LHC

In the previous section, the statistical-thermal model and the coalescence descriptions of (anti)matter production in the heavy-ion collisions up to RHIC energies was discussed. In this section, we have concentrated on the predictions of various particle ratios at higher incident energies (LHC energy). The quantify differences between pp and heavy-ion collisions is also discussed in this section. The statistical-thermal model calculations of various particle ratios are performed, assuming chemical freeze-out temperature (T) as 170 MeV, and baryon chemical potential (μ_B) from Eqs. 5.4 and 5.6 for heavy-ion and pp collisions system, respectively.
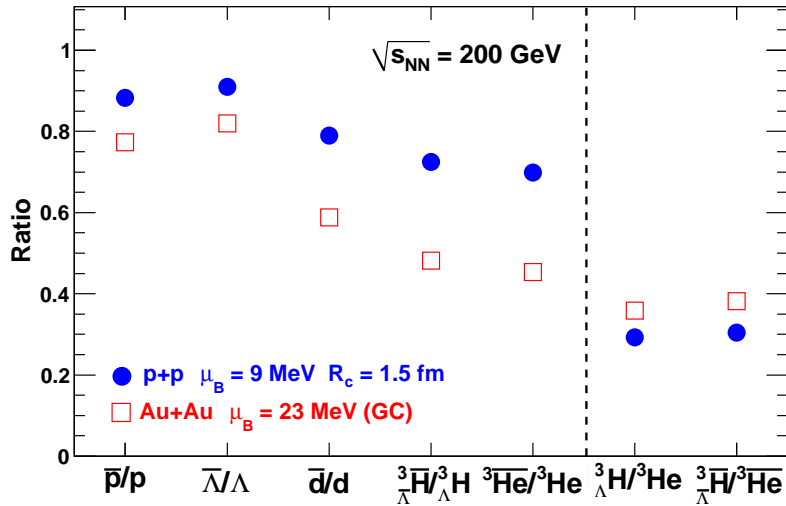
Figure 5.7: Comparison of different particle ratios calculated in the statistical-thermal model using $T = 170$ MeV for pp and heavy-ion collisions at $\sqrt{s_{\mathrm{NN}}} = 200$ GeV.

5.5.1 Predictions for pp and Au-Au at 200 GeV

Figure 5.7 shows the comparison of particle ratios calculated using the statistical-thermal model (THERMUS) assuming $T = 170$ MeV. The solid circles represent pp collisions and open squares symbol are for heavy-ion collisions (Au-Au) at $\sqrt{s_{\mathrm{NN}}} = 200$ GeV. The Grand Canonical (GC) approach is used for Au-Au collisions and the Strangeness Canonical (SC) approach is used for pp collisions. Figure 5.7 nicely demonstrates that with increasing mass the effect of μ_B becomes stronger and the difference between particle ratios increases as we go from heavy-ion to pp collision system at fixed energy ($\sqrt{s_{\mathrm{NN}}} = 200$ GeV). Yet a strangeness content causes an opposite trend as discussed earlier, the ratio of hypertriton-to-^{3}He and the corresponding antimatter ratio show the effect of the canonical suppression, which reduces the yield of (anti)baryons carrying strangeness. For pp calculations we have used the correlation volume with canonical radius $(R_c) = 1.5 \ fm$. The canonical or correlation radius is defined as the radius inside which strangeness is exactly conserved. The difference between the hypertriton-to-^{3}He ratio for pp and heavy-ion systems is not dramatic but very noticeable.
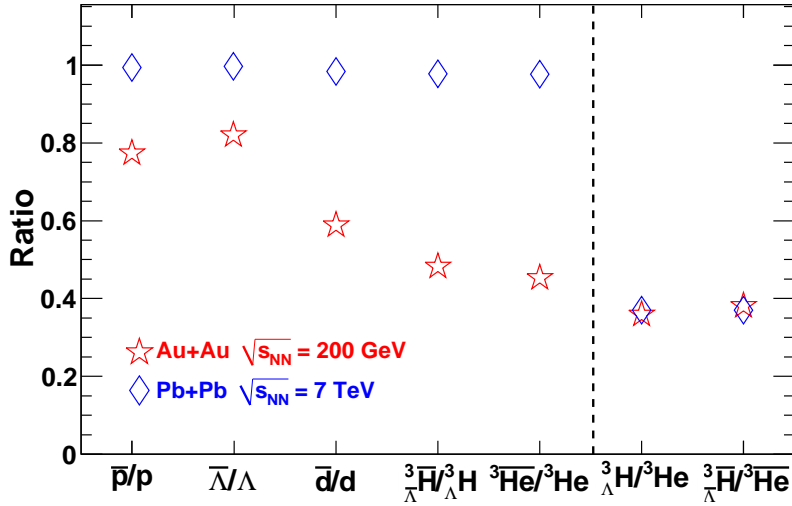
Figure 5.8: Comparison of different particle ratios calculated in the statistical-thermal model using $T = 170$ MeV for heavy-ion collisions at different collision energies.

5.5.2 Predictions for Au-Au at 200 GeV and Pb-Pb at 7 TeV

Figure. 5.8 demonstrates the comparison of heavy-ion collisions at $\sqrt{s_{NN}} = 200$ GeV (Au-Au system) and at 7 TeV (Pb-Pb system). The open diamond symbols represent particle ratios for Pb-Pb collisions at $\sqrt{s_{NN}} = 7$ TeV and open star symbols for Au-Au collisions at $\sqrt{s_{NN}} = 200$ GeV. Here, the difference between the antimatter-to-matter ratios in the heavy-ion collisions at RHIC and LHC are essentially due to the decreasing value of μ_B. At LHC energy, the baryon chemical potential (μ_B) is smaller than 1 MeV resulting in the antimatter-to-matter ratio being close to unity. The ratios of the (anti)hypernuclei/^{3}(anti)He remain nearly unchanged from RHIC to LHC since here the effect of chemical potential is only due to the strange chemical potential (μ_S) which is small and baryon chemical potential (μ_B) is cancelled out (see Eq. 5.11). It is clear from the mathematical form (Eq. 5.11), that these ratios are dominated by the mass differences and degeneracy factors.

5.5.3 Predictions for pp and Pb-Pb at 7 TeV

In this section, the predictions for different colliding systems at LHC energy are discussed. Figure 5.9 show the particle ratios calculation using the statistical-thermal model for pp collision and Pb-Pb collisions at $\sqrt{s_{NN}} = 7$ TeV. For simplicity, in both cases the collision energy of 7 TeV has been chosen. The ratios do not change between $\sqrt{s_{NN}} = 2.76$ TeV and 7 TeV, since in both the energies the baryon chemical potential (μ_B) is less than 1 MeV. In Fig. 5.9, the open square represent particle ratios for Pb-Pb collisions and solid triangle for pp collisions at $\sqrt{s_{NN}} = 7$ TeV.

We have used the grand canonical (GC) approach for Pb-Pb collisions, since in heavy-ion collisions all the quantum numbers (B, S and Q) are conserved on an average through the action of chemical potential (μ_B, μ_S and μ_Q) respectively. We have assumed chemical freeze-out temperature (T) = 170 MeV, μ_B from Eq. 5.4, and radius of fireball (R) as 6 fm for our calculations.

In pp collisions, the volume (V) of the fireball is very small so exact strangeness conservation is required. We have used the strangeness canonical (SC) formulation for pp collisions and calculations are performed assuming $T = 170$ MeV, μ_B from Eq. 5.6, fireball radius (R) = 4 fm, and canonical radius (R_c) = 1.5 fm and 4.0 fm.

From Fig. 5.9 we note that antimatter-to-matter ratios shows very little change from pp to heavy-ion collisions. All antiparticle-to-particle ratios are close to unity. The ratios of (anti)hypernuclei/^{3}(anti)He exhibit the influence of the canonical suppression for the correlation volume (see Section 5.2) corresponding to $R_c = 1.5$ fm shown as inverted solid triangles in the figure [19]. However, for larger R_c the canonical effect is reduced and for $R_c = 4$ fm this effect is not visible (solid triangles).

5.6 Chemical Temperature Prediction Using THER-MUS

In the previous section, we have discussed in detail the comparison of various particle ratios for pp and heavy-ion collisions at RHIC and LHC energies. In this section, we will give the prediction of chemical freeze-out temperature (T) using statistical-thermal model
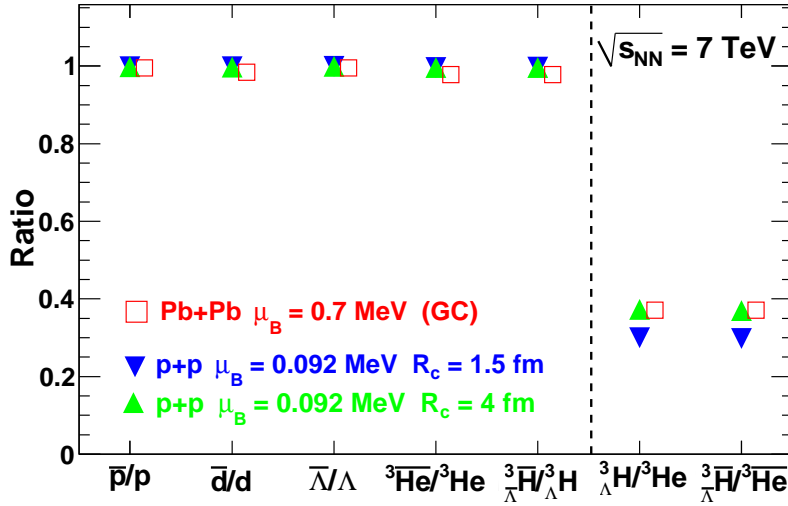
Figure 5.9: Predictions of particle ratios calculated in the statistical-thermal model using $T = 170$ MeV. for pp and Pb-Pb collisions at $\sqrt{s_{\mathrm{NN}}} = 7$ TeV.

(THERMUS). At high energy collisions baryon chemical potential (μ_B) is very small. If we calculate the ratios of particles with different mass using Eq. 5.2, then the particle ratios is proportional to the exponential term, $\exp(-\Delta m/T)$.

To study these ratios the statistical-thermal model calculations are performed for Au-Au collisions at $\sqrt{s_{NN}} = 200$ GeV using grand canonical approach. We assume the chemical freeze-out temperature (T) between 110 and 170 MeV, baryon chemical potential (μ_B) from Eq. 5.4, and radius of fireball (R) as 6 fm. The antimatter ratios predicted by the model assuming different chemical freeze-out temperature (T) are shown in Fig. 5.10. The different line style represent particle ratios with different temperature. We observe that the ratios of (anti)nuclei with different mass depend on the value of chemical freeze-out temperature (T) used in the model calculations. The open square symbols represent the data from the STAR Collaboration [4, 36]. It also includes the recently measured $^4\overline{\mathrm{He}}/^3\overline{\mathrm{He}}$ ratio. It is the first time these anti-nuclei yields are/or ratios are measured by any experiment, but the statistics is very less. To make any conclusion on the chemical freeze-out temperature (T) for the anti-nuclei production more data with high precision is needed.
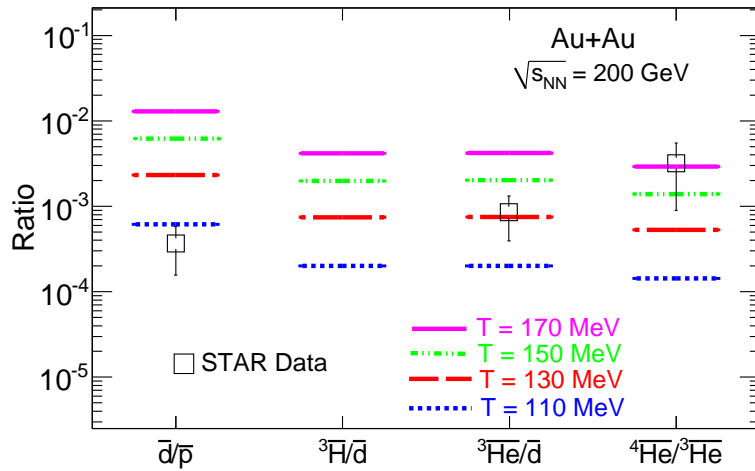
Figure 5.10: Comparison of model calculations of various anti-nuclei ratios with different masses for Au-Au collisions at $\sqrt{s_{\mathrm{NN}}} = 200$ GeV for different freeze-out temperatures and also comparison with the recently measured values by STAR Experiment [4, 36].

5.7 Summary

In this chapter, we have discussed in a systematic manner the production of (anti)matter in high energy collisions within the statistical-thermal model approach (THERMUS). The statistical-thermal model approach and the THERMUS package are discussed in detail.

The general comparison of the production of antibaryons and anti-nuclei is presented. The variation of the $\bar{p}/p$ ratios with $\sqrt{s_{NN}}$ being different for pp and heavy-ion collisions has been used to obtain the parametrization of the energy dependence of thermal parameters in pp collisions. We found the scaling behavior of the (anti)baryon/baryon ratios with the strangeness quantum number and the changes in these ratios between pp and heavy-ion collisions with $\sqrt{s_{NN}}$. The measured ratios of nuclear and anti-nuclear fragments in Au-Au collisions at $\sqrt{s_{NN}} = 200$ GeV are compared with the predictions from the statistical-thermal model and the coalescence concept.

We found that the statistical-thermal model gives successful description of existing data. Based on the success of this model, the predictions for (anti)matter production in pp and heavy-ion collisions at LHC energies are made.

Bibliography

[1] B. I. Abelev *et al.* (STAR Collaboration), Phys. Rev. C **79** (2009) 034909.

[2] K. Aamodt *et al.* (ALICE Collaboration), Phys. Rev. Lett. **106** (2010) 072002.

[3] B.I. Abelev *et al.* (STAR Collaboration), Science **328** (2010) 58 .

[4] H. Agakishiev *et al.* (STAR Collaboration), Nature **473** (2011) 353.

[5] B. I. Abelev *et al.* (STAR Collaboration), Phys. Rev. C **81** (2010) 024911.

[6] K. Huang, in *Statistical Mechanics, 2nd Edition-1987*, Wiley, New York Sect. 3,4.

[7] P. Braun-Munzinger, K. Redlich, and J. Stachel, arXiv:0304013 [nucl-th].

[8] F. Karsch, E. Laermann, and A. Peikert, Nucl. Phys. B **605** (2001) 579.

[9] P. Braun-Munzinger, I. Heppe, and J. Stachel, Phys. Lett. **B465** (1999) 15; F. Becattini, J. Cleymans, A. Keranen, E. Suhonen, and K. Redlich, Phys. Rev. C **64** (2001) 024901; P. Braun-Munzinger, D. Magestro, K. Redlich, and J. Stachel, Phys. Lett. **B518** (2001) 41; N. Xu and M. Kaneta, Nucl. Phys. **A698** (2002) 306; F. Becattini, J. Phys. G **28** (2002) 1553.

[10] P.Braun-Munzinger, K. Redlich, and J. Stachel, in *Quark-Gluon Plasma 3*, edited by R.C.Hwa and X.N.Wang (World Scientific Publishing, Singapore, 2004).

[11] A. Andronic, P. Braun-Munzinger, and J. Stachel, Nucl. Phys. **A772** (2006) 167.

[12] T.S. Biro, J.Phys. G **35** (2008) 044056.

[13] A. Dumitru, L. Portugal, and D. Zschiesche, nucl-th/0511084.

[14] L. V. Bravina, E. E. Zabrodin, S. A. Bass, M. Bleicher, M. Brandstetter, S. Soff, H. Stocker, and W. Greiner, Phys. Rev. C **62** (2000) 064906.

[15] J. Cleymans, S. Wheaton, H. Oeschler and K. Redlich, Phys. Rev. C **73**, (2006) 034905.

[16] K. Redlich, J. Cleymans, H. Oeschler, and A. Tounsi, Acta Phys. Pol. B **33** (2002) 1609;

[17] S. Wheaton, and J. Cleymans, J. Phys. G **31** (2005) S1069.

[18] S. Wheaton, J. Cleymans, and M. Hauer, Computer Physics Communications, **180** (2009) 84.

[19] S. Hamieh, K. Redlich, and A. Tounsi, Phys. Lett. B **486** (2000) 61.

[20] R. Hagedorn, and K. Redlich, Z. Phys. C **27** (1985) 541.

[21] J. Rafelski, and M. Danos, Phys. Lett. B **97** (1980) 279; B. Müller, and J. Rafelski, Phys. Lett. B **116** (1982) 274.

[22] J. Cleymans, H. Oeschler, and K. Redlich, Phys. Rev. C **59** (1999) 1663.

[23] F. Karsch and K. Redlich, arXiv:1007.2581 [hep-ph].

[24] A.Andronic, P. Braun-Munzinger, and J. Stachel, Nucl. Phys. A **772** (2006) 167.

[25] C. Alt *et al.* (NA49 Collaboration), arXiv:0512033 [nucl-ex].

[26] B.I. Abelev *et. al.* (STAR Collaboration), Phys. Rev. C **75** (2007) 064901, arXiv:0607033 [nucl-ex].

[27] C. Alt *et al.* (NA49 Collaboration), Phys. Rev. C **77** (2008) 024903, arXiv:0710.0118 [nucl-ex].

[28] I. Kraus, J. Cleymans, H. Oeschler, K. Redlich, and S. Wheaton, [arXiv:0902.0873 [hep-ph]].

[29] J. Cleymans, and H. Satz, Z. Phys. C **57** (1993) 135.

[30] B. I. Abelev *et al.* (STAR Collaboration), Phys. Rev. Lett. **97** (2006) 152301.

[31] J. Adams *et al.* (STAR Collaboration), Phys. Rev. Lett. **98** (2007) 062301.

[32] R. Arsenescu *et al.* (NA52 Collaboration), New J. Phys. **5** (2003) 150.

[33] A. Andronic, P. Braun-Munzinger, J. Stachel, and H. Stoecker, Phys. Lett. B **697** (2011) 203-207.

[34] H. Sato and K. Yazaki, Phys. Lett. B **98** (1981) 153.

[35] B. I. Ioffe, I. A. Shushpanov, and K. N. Zyablyuk, Phys. Atom. Nucl. **68** (2006) 326.

[36] C. Adler *et. al.* (STAR Collaboration), Phys. Rev. Lett. **87** (2001) 262301.

Chapter 6

(Anti)Nuclei Production in pp and Pb-Pb Collisions in ALICE

6.1 Introduction

One of the goals of ultra-relativistic nuclear collision experiments is to understand the production mechanism of matter and antimatter. The nucleus of matter is made up of protons (p) and neutrons (n), and that of antimatter is composed of antiprotons ($\bar{p}$) and antineutrons ($\bar{n}$). In the Big-Bang [1], matter and antimatter are supposed to be created with comparable abundance. However, our universe today consists almost entirely of matter rather than antimatter. It is therefore conjectured that the Big-Bang could have made antimatter somewhere else in the distant universe, and our observable universe happens to be in the matter zone.

The space-based experiments [2–4] aim to look for tiny antimatter fragments that travel from the primordial antimatter zone. If there is any primordial antimatter, antihelium is the most likely to be formed and can be detected in cosmic rays, likewise in matter nucleosynthesis, helium is the next most abundant element to hydrogen. Lighter antiparticles in cosmos such as antiprotons and positrons are primarily produced by collisions of the cosmic rays with the interstellar medium, thus they are not direct indicators for the existence of antimatter domain. Antihelium-4 ($\bar{\alpha}$) was not observed until the recent discovery [5], although the α-particle was identified a century ago by Rutherford and is present in cosmic radiation at the 10% level [6].

The relativistic heavy-ion collisions create suitable conditions for producing

(anti) nuclei, because large amounts of energy are deposited into a more extended volume than that achieved in elementary particle collisions. These nuclear interactions produce hot and dense matter for a short duration (10^{-23}s), containing roughly equal numbers of quarks and antiquarks. In contrast to the Big-Bang, nuclear collisions produce negligible gravitational attraction and allow the plasma to expand rapidly. The hot and dense matter cools down and undergoes a transition into a hadron gas, producing nucleons and their antiparticles. The production of (anti) nucleus could be due to the following mechanisms. (Anti) nucleus could be directly produced from the nucleus-nucleus collisions and then emitted from the thermal fireball formed during these collisions (following the thermal statistical approach [7–9]); or could be formed during the chemical and thermal freeze-out via the final state coalescence of the nucleons and anti-nucleons that are produced in the collision [10].

The spectra, yields and ratios of various nuclei and anti-nuclei could be used to provide valuable information about the final state freeze-out parameters like temperature (T) and chemical potentials (μ_B, μ_S) of the system [11, 12]. The particle spectra, yields and ratios for π, K, and p have been intensively studied at the RHIC as well as at the ALICE experiment at the LHC [13, 14]. These measurements have been very useful in understanding the particle production mechanisms and extracting information of the fireball created during the heavy-ion collisions. Similarly, studying the light (anti) nuclei produced in the heavy-ion collisions at ALICE can be very useful in understanding the production mechanisms and the fireball information at the LHC energies. These studies are also motivated for the discovery of the new particles e.g. observation of anti-hypertriton by the STAR experiment in the year 2010 [15] and of anti-alpha particle in the year 2011 [5] and confirmed by the ALICE experiment at the same time [16].

This chapter is devoted to the details of analysis technique used to extract raw and final spectra of the light (anti)nuclei; like (anti)deuterons, (anti)tritons and (anti)^{3}He for pp collisions at $\sqrt{s} = 7$ TeV and Pb-Pb collisions at $\sqrt{s_{NN}} = 2.76$ TeV at the mid-rapidity region. The observation of anti-alpha $^4\overline{\text{He}}$ using the similar technique in ALICE experiment is also discussed. The data used for this analysis are from Pb-Pb collisions at $\sqrt{s_{NN}} = 2.76$ TeV. The results were presented for the first time by both STAR experi-

ment [17] as well as by the ALICE experiment [16] at the Quark Matter-2011 conference held in Annecy, France in May 2011. The anti-alpha ($^4\overline{\text{He}}$) is the heaviest anti-nucleus (antimatter) observed by any experiment till date.

6.2 Experiment and Data Analysis

The results presented in this chapter are based on the data collected by the Time Projection Chamber (TPC) of the ALICE experiment for pp (elementary) collisions at $\sqrt{s} = 7$ TeV and Pb-Pb (heavy-ion) collisions at $\sqrt{s_{NN}} = 2.76$ TeV. The Time-Of-Flight (TOF) detector information along with TPC, is also used to study anti-helium ($^4\overline{\text{He}}$) particle. The results are based on the data collected and produced at ALICE in the year 2010. All the available production numbers at that time are used for the present analysis which include $LHC10b$, $LHC10c$, $LHC10d$ and $LHC10e$ for pp collisions; and $LHC10h$ for Pb-Pb collisions. Tracks are reconstructed by following the procedure as discussed in section 2.4.4.2. The raw data from each detector are calibrated according to the specialized algorithm obtained after detailed simulation studies. The calibrated data contains all the physical properties obtained from the production run.

6.2.1 Event Selection

The good event selection is needed for the physics analysis. The good events are selected by using the minimum-bias trigger. The vertex reconstruction algorithm determines the primary-vertex position of the collision. The probability to reconstruct the primary-vertex of a minimum-bias (e.g. MB1-triggered) event is 92.5% with the SPD (Silicon Pixel Detector). To select the good primary tracks, the vertex cut along the z-axis is also applied as $|v_z| < 10$ cm. The total number of triggered events analysed are about 381.5 M for pp collisions and about 16.5 M for Pb-Pb collisions.

6.2.2 Track Selection

The tracks used for the physics analysis should also be of good quality. To make sure, we select only good tracks for our analysis, we apply various track cuts. These track cuts are used basically to select primary particles (*primaries*) produced in the collisions

Table 6.1: Track selection cuts

1.	$|v_z|$	< 10 cm
2.	No. of TPC Clusters	≥ 80
3.	χ^2 per TPC Clusters	≤ 4
4.	$|\eta|$	< 0.8
5.	$|DCA_{XY}|$ and $|DCA_Z|$	< 10 cm

and suppress those from secondary particles (*secondaries*). Thus, the main aim of track selection is to lower the contamination from secondaries while retaining high efficiency for primaries.

The various track selection cuts used for our analysis such as vertex cuts, number of clusters measured in the TPC for track reconstruction, χ^2 per cluster, distance of closest approach in XY plane (DCA_{XY}) and in Z direction (DCA_Z) are listed in the table 6.1. In addition to these cuts, we also make sure that there should be at least one cluster in the ITS associated to the track. Also the primary particles having kinks are rejected.

6.3   Particle Identification using TPC

The particle identification in ALICE is mainly done using the TPC. The technical details and principle of TPC is explained in detail in chapter 2. It exploits the ionization energy loss information (dE/dx) of charged particles to identify them in the TPC region. When charged particle passes through the medium (in the TPC case, a mixed gas) in the presence of magnetic field, it ionizes the molecules and atoms of the media along its path. Ionization causes continuous energy loss of the charged particle. The rate of energy loss i.e. dE/dx, is different for different particles, and is described by the Bethe-Bloch function:

$$\frac{dE}{dx} = -\frac{4\pi}{m_e c^2} \frac{nZ^2}{\beta^2} \left(\frac{e^2}{4\pi\epsilon_0}\right)^2 \left[ln\left(\frac{2m_e c^2 \beta^2}{I(1-\beta^2)}\right) - \beta^2 \right], \tag{6.1}$$

in which $\beta = v/c$ (v is the velocity of the particle, and c is the speed of light in the vacuum), E is the energy of the particle, x is the distance traveled, Ze is the charge of the particle, e and m_e are the charge and mass of the electron, n is the electron density of the target, and I is the mean excitation potential of the target. Since the energy loss depends upon the charge and momentum of the incident particle, the energy loss information can be used to distinguish or identify different particles.

In the ALICE experiment, the momentum (p) of the particle is calculated using the applied magnetic field (B) information and the curvature of path travelled by the charge particle in the TPC region. This calculation assumes that the particle is of unit charge ($|Z| = 1$). So, the expected energy loss (dE/dx) of a certain kind of particle is given by a function named 'Bichsel function' [18], which is modified Bethe-Bloch function with $|Z| = 1$ in Eq. 6.1. This is helpful in identifying particles like π, K, and p having unity charge. However, for (anti)-nuclei with charge $|Z| > 1$, some modification is needed. Particles with charge $|Z| > 1$ are converted into the unit charge before using the Bichsel function to make their dE/dx predictions.

Figure 6.1 shows the specific energy loss (dE/dx) as a function of rigidity (momentum/charge) for the TPC tracks in pp collisions at $\sqrt{s} = 7$ TeV [19] (top panel). The lower panel shows the similar plot for Pb-Pb collisions at $\sqrt{s_{NN}} = 2.76$ TeV [16]. Clearly, various nuclei and anti-nuclei are well identified for both pp and Pb-Pb collisions. Thus, the TPC can identify light nuclei and anti-nuclei like d ($\bar{\text{d}}$), t ($\bar{\text{t}}$) and ^{3}He ($^3\overline{\text{He}}$) over a wide momentum range as shown in the figure. The solid curves represent the expected values of Bethe-Bloch function for different particles.

6.4 (Anti) Nuclei Selection

For the present analysis, we select the (anti) nuclei using the specific energy loss (dE/dx) in TPC. The procedure is describes as follows. The difference between the specific energy loss (dE/dx) of (anti) nuclei in the TPC and its expected value using the parametrized Bethe-Bloch curve is plotted as the function of rigidity.

Figure 6.2 show the plots for nuclei identification for Pb-Pb collisions at
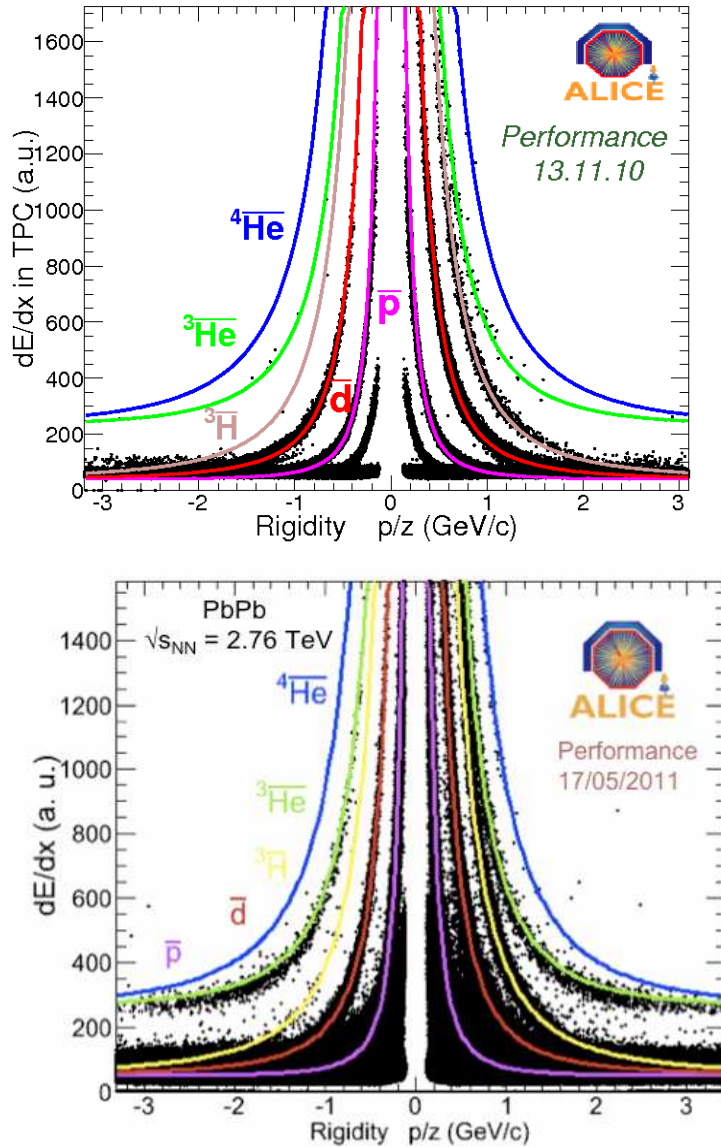
Figure 6.1: Specific energy loss (dE/dx) vs. rigidity (momentum/charge) for TPC tracks in pp collisions at $\sqrt{s} = 7$ TeV (top panel) and for Pb-Pb collisions at $\sqrt{s_{NN}} = 2.76$ TeV (bottom panel). The solid lines are parametrization of the Bethe-Bloch curve.
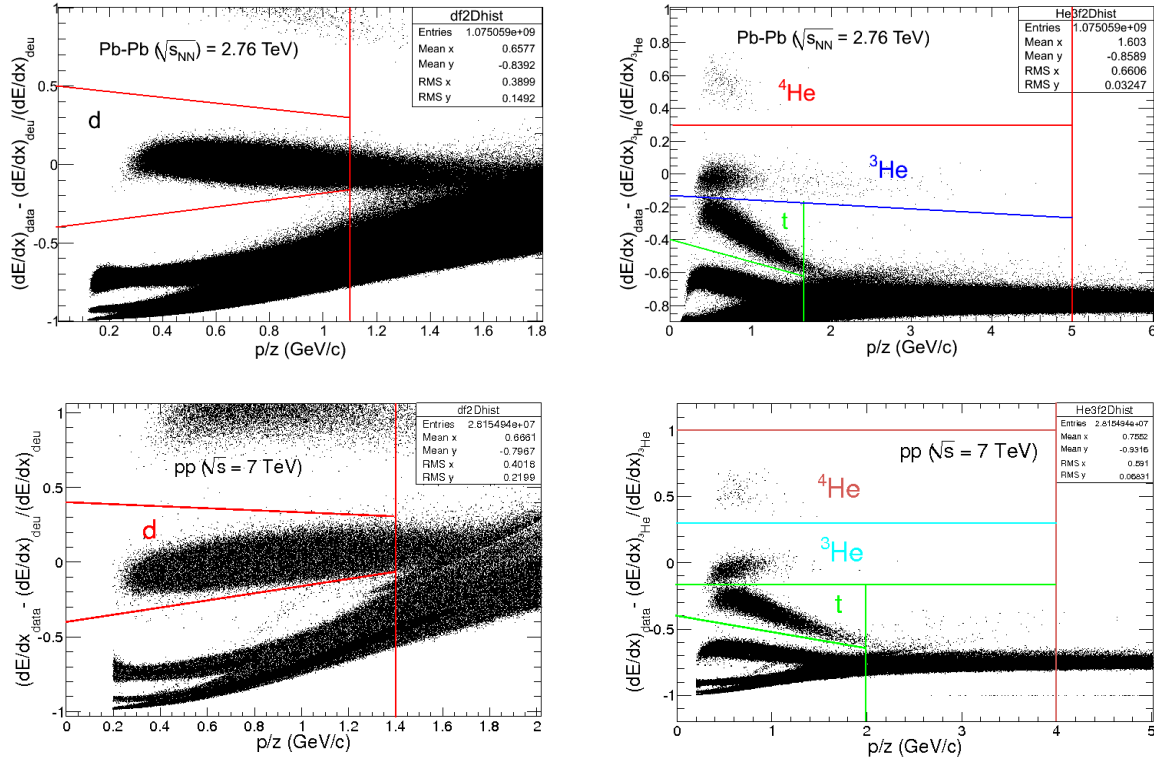
Figure 6.2: Top panels: The difference of specific energy loss between data and theoretical calculations is plotted as a function of rigidity for Pb-Pb collisions at $\sqrt{s_{NN}} = 2.76$ TeV. Left plot shows selection for deuterons; Right plot shows selection for triton, ^{3}He, and ^{4}He. Bottom panels: Similar plots for pp collisions at $\sqrt{s} = 7$ TeV.

$\sqrt{s_{NN}} = 2.76$ TeV in the top panel and for pp collisions at $\sqrt{s} = 7$ TeV in the bottom panel. The deuteron selection is shown in the left panel while that for triton (t), ^{3}He, and ^{4}He are shown in the right panel. As can be seen from the left panel, the deuterons are well separated up to a rigidity value of around 1.1 GeV/c for Pb-Pb collisions (top) and 1.4 GeV/c for pp collisions (bottom). The lines represent the selection of deuterons for the present analysis. Similarly, right panel shows the selection of triton, ^{3}He, and ^{4}He. The different lines represent the selection of different nuclei. The anti-nuclei $\overline{\text{d}}$, $\overline{\text{t}}$, $^3\overline{\text{He}}$, and $^4\overline{\text{He}}$ are also selected using the similar procedure. Since, the ionization energy loss for nuclei and anti-nuclei is similar in the TPC, the identification momentum ranges for the anti-nuclei are similar to those of nuclei.

6.5   Raw Spectra

6.5.1   Background Rejection

The primary particles produced in the collisions interact with the detector material or beam pipe to produce the secondary particles. These secondary particles are background in the sample and should be excluded from the physics analysis. The probability of anti-nuclei production from interaction of produced particles with detector material is very less, whereas nuclei sample may include primary as well as secondary particles from the interaction. So the anti-nuclei sample is mostly background free whereas nuclei sample contains background due to interactions. Most of the secondary particles have large distance-of-closest approach (DCA) to the primary vertex and hence this information can be used to reject these secondary particles or background.

The DCA has three components DCA_X, DCA_Y, and DCA_Z. The DCA_Z is along the direction of the beam axis and the DCA_{XY} represent the DCA in the transverse plane. We use the following procedure to reject the secondary particles. The DCA_{XY} distribution of identified nuclei and anti-nuclei are studied for two different DCA_Z cut. From Fig. 6.3, it can be seen that the DCA_Z cut of 1.0 *cm* reduces large fraction of deuteron background, without affecting primary anti-deuterons for Pb-Pb collisions [19]. Hence, we use $|DCA_Z| < 1.0$ cut for our analysis. Similar cut is used to reject background in the tritons and ^{3}He samples. The procedure to reject background for different nuclei in pp collisions is similar.

6.5.2   Raw Yields of d $(\overline{\text{d}})$

In order to select primary d $(\overline{\text{d}})$, the distance-of-closest approach in XY plane i.e. DCA_{XY} distribution of identified d $(\overline{\text{d}})$ are studied for various transverse momentum slices of size 0.1 GeV/c. Figure 6.4 shows examples for the few transverse momentum regions viz. $0.55 \leq p_t \leq 0.65$ GeV/c, $0.65 \leq p_t \leq 0.75$ GeV/c, $0.75 \leq p_t \leq 0.85$ GeV/c for Pb-Pb collisions at $\sqrt{s_{NN}} = 2.76$ TeV.
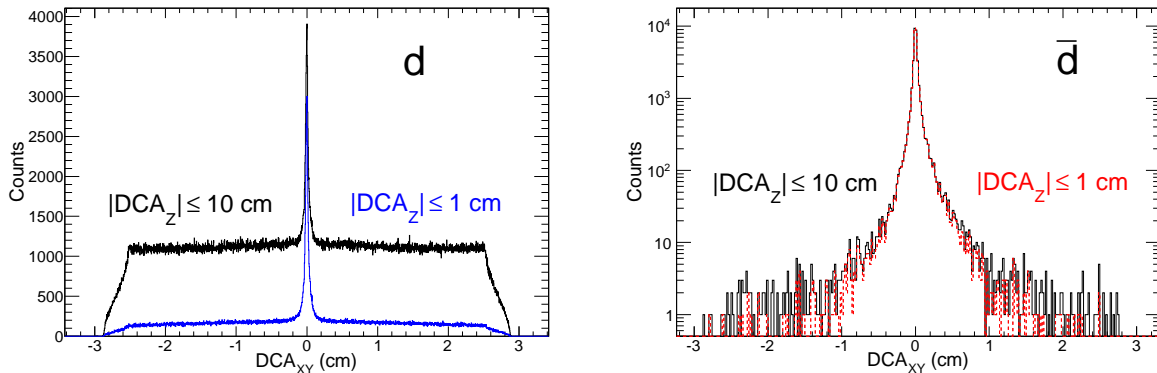
Figure 6.3: DCA_{XY} distribution for deuterons and anti-deuterons in Pb-Pb collisions. Left panel: DCA_Z cut of 1.0 cm reduces large background for deuterons. Right panel: DCA_Z cut of 1.0 cm reduces background without affecting primary anti-deuterons.

1. **Raw yields of $\bar{d}$:**

   As mentioned before, the anti-deuteron sample will contain negligible background due to interactions with material or beam pipe. It is noted from the right panels of Fig. 6.3 that, there are very less counts of $\bar{d}$ outside $|DCA_{XY}| \leq 1.0 \ cm$. The primary anti-deuterons are calculated by integrating the counts in the $|DCA_{XY}| \leq 1.0 \ cm$ for various transverse momentum regions.

2. **Raw yields of d:**

   The nuclei sample contains the background due to interaction with material or beam pipe, which should be subtracted. Figure 6.4 (right panels) shows the DCA_{XY} for deuteron sample. This contains the contribution from primary deuterons as well as background. It may be noted that if there are no interactions with material or beam pipe, the deuterons would behave similar to anti-deuterons sample which contain negligible background. The shape of the deuteron DCA_{XY} distribution should be similar to that of anti-deuteron plus background. This can be seen from the right panels of Fig. 6.4, where the primary deuterons show similar shape as that of anti-deuteron (left panels) but have also the linear background.

   In order to count the primary deuterons, the linear background has to be rejected. For this, we fit the corresponding anti-deuteron ($\bar{d}$) DCA_{XY} distribution (same p_t range) with two Gaussian function, as shown by red line in the left plot of Fig. 6.4.
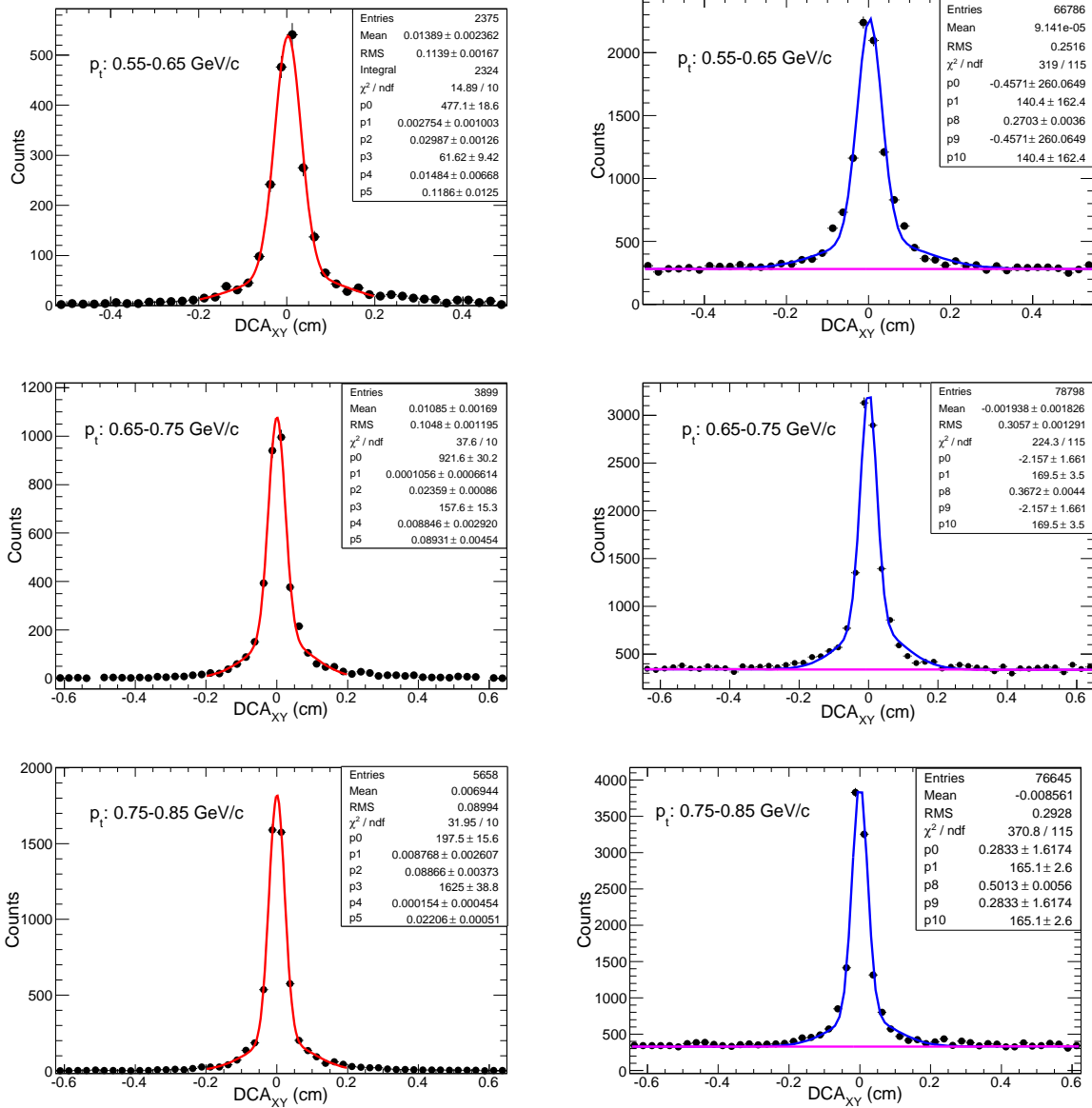
Figure 6.4: DCA$_{XY}$ distribution of anti-deuterons (left panels) and deuterons (right panels) for different transverse momentum regions in Pb-Pb collisions at $\sqrt{s_{NN}} = 2.76$ TeV. See text for details.
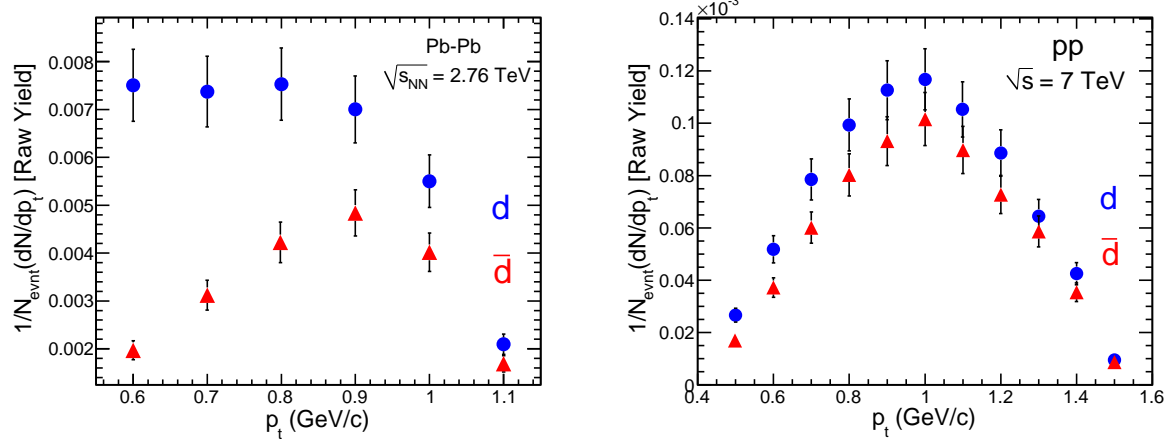
Figure 6.5: Raw yields of deuteron (as blue solid circles) and anti-deuterons (as red triangles) as a function of transverse momentum (p_t). Left plot: for Pb-Pb collisions at $\sqrt{s_{NN}} = 2.76$ TeV; Right plot: pp collisions at $\sqrt{s} = 7$ TeV.

The fit parameters obtained are used in the fit function (two Gaussian function plus one linear background) for deuteron (d) DCA_{XY} distribution as shown by blue line in the right plot of Fig. 6.4. To obtain the primary deuterons we subtract the linear background (pink line in right plot of Fig. 6.4) from the fit function in the $|DCA_{XY}| \leq 1.0$ cm region. For the visibility sake, the plots are shown only for the range $|DCA_{XY}| \leq 0.6$ cm.

Similar procedure is used to extract raw yields of deuterons (d) and anti-deuterons ($\bar{d}$) for pp collisions at $\sqrt{s} = 7$ TeV. Figure 6.5 show the finally obtained raw spectra of deuterons and anti-deuterons for Pb-Pb collisions at $\sqrt{s_{NN}} = 2.76$ TeV (left panel) and pp collisions at $\sqrt{s} = 7$ TeV (right panel). The raw spectra will be finally corrected for the efficiency and acceptance effects to obtain the final spectra. It can be seen that raw anti-deuterons spectra or counts are less compared to the corresponding deuterons counts in Pb-Pb collisions at $\sqrt{s_{NN}} = 2.76$ TeV. This could be due to the fact that the low p_t anti-deuterons are annihilated with the detector material and beam pipe. If the annihilation effect is properly implemented in the simulation, anti-deuteron spectra can be corrected for this effect.
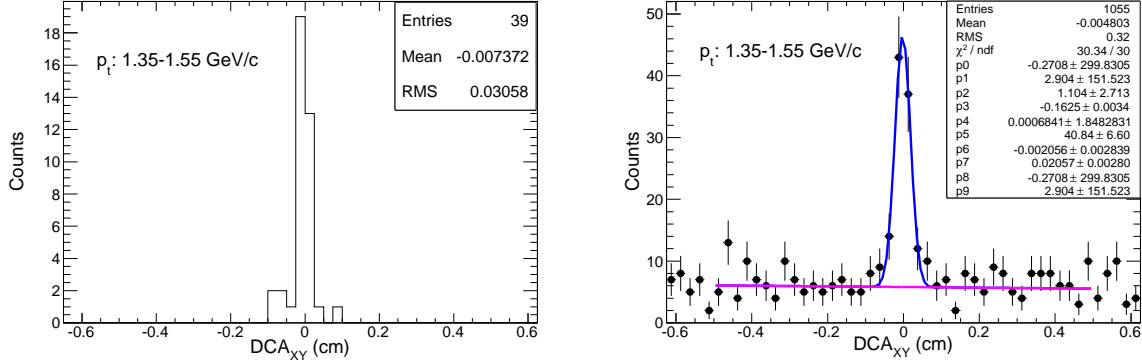
Figure 6.6: DCA_{XY} distribution of anti-tritons (left panel) and tritons (right panel) in the transverse momentum region $1.35 \leq p_t \leq 1.55$ GeV/c for Pb-Pb collisions. See text for details.

6.5.3   Raw Yields of t ($\bar{t}$) and ^{3}He ($^3\overline{\text{He}}$)

To obtain the raw spectra of t ($\bar{t}$), DCA_{XY} distribution is plotted for various transverse momentum (p_t) slices of size 0.2 GeV/c. Figure 6.6 shows the DCA_{XY} distribution for transverse momentum region $1.35 \leq p_t \leq 1.55$ GeV/c for Pb-Pb collisions. For ^{3}He and $^3\overline{\text{He}}$, DCA_{XY} distributions of varying transverse momentum slices are made because of less statistics. Figure 6.7 displays the DCA_{XY} distribution for transverse momentum region $0.85 \leq p_t/2 \leq 1.05$ GeV/c for Pb-Pb collisions at $\sqrt{s_{NN}} = 2.76$ TeV.

Like anti-deuteron, the anti-tritons and $^3\overline{\text{He}}$ are expected to have almost no background, so their raw yields can be directly obtained from the total counts in the DCA_{XY} distribution. The anti-tritons and $^3\overline{\text{He}}$ raw yields are calculated by integrating counts in the region $|DCA_{XY}| \leq 0.5$ *cm*. The DCA_{XY} distributions for anti-tritons and $^3\overline{\text{He}}$ are shown in the left panels of Figs. 6.6 and 6.7, respectively. For tritons and ^{3}He, we employ the same procedure as used for deuterons. We expect that the shape of nuclei DCA_{XY} distribution is similar to that of anti-nulcei plus background. Therefore, the raw counts for tritons and ^{3}He in $|DCA_{XY}| \leq 0.5$ cm region are obtained by fitting the DCA_{XY} distribution with a function (2 Gauss + 1 linear) and then subtracting the linear background as shown by the right panels of Figs. 6.6 and 6.7.

After obtaining the raw counts for each p_t bin, we obtain the uncorrected p_t spectra of t ($\bar{t}$) and ^{3}He ($^3\overline{\text{He}}$) as shown in the Fig. 6.8, for Pb-Pb collisions at $\sqrt{s_{NN}} = 2.76$ TeV.
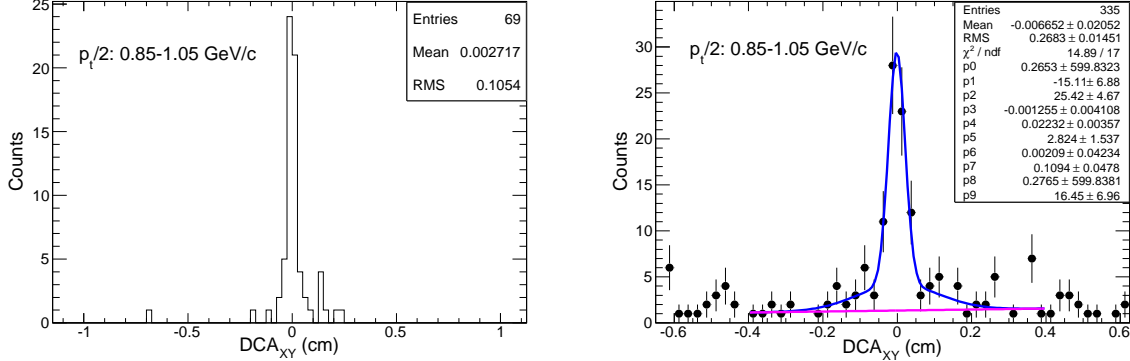
Figure 6.7: DCA$_{XY}$ distribution of $^3\overline{\text{He}}$ (left panel) and ^{3}He (right panel) in the transverse momentum region $0.85 \leq (p_t/2) \leq 1.05$ GeV/c for Pb-Pb collisions. See text for details.
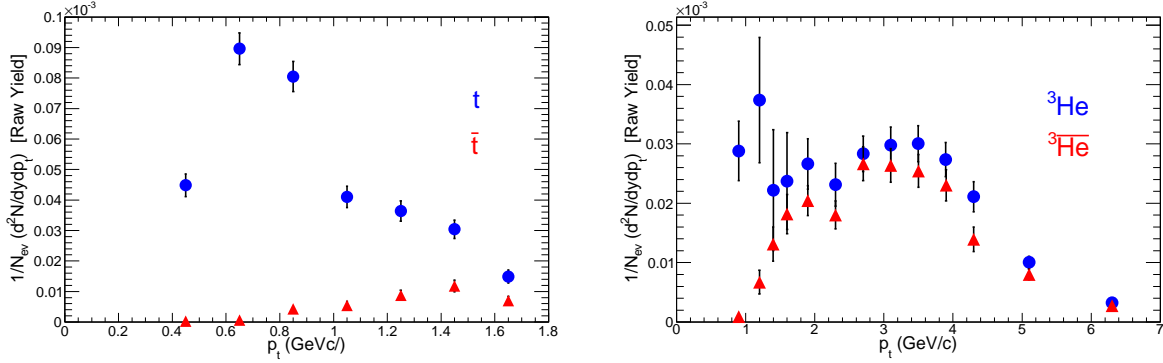

Figure 6.8: Uncorrected p_t spectra of t ($\overline{\text{t}}$) (left panel) and ^{3}He ($^3\overline{\text{He}}$) (right panel) for Pb-Pb collisions at $\sqrt{s_{NN}} = 2.76$ TeV. The solid circles represent the nuclei (t and ^{3}He) while solid triangles represent the anti-nuclei ($\overline{\text{t}}$ and $^3\overline{\text{He}}$). Only statistical errors are shown.

Left panel shows spectra for t ($\overline{\text{t}}$) while right panel shows spectra for ^{3}He ($^3\overline{\text{He}}$). Solid circles are used to represent nuclei (t and ^{3}He) and solid triangles are used to represent anti-nuclei ($\overline{\text{t}}$ and $^3\overline{\text{He}}$). As can be seen from the right plot of Fig. 6.8 that ^{3}He ($^3\overline{\text{He}}$) can be measured over the wide range of transverse momentum in ALICE. Since the statistics is very less, the corresponding spectra for pp collisions are not shown here.

For Pb-Pb data at $\sqrt{s_{NN}} = 2.76$ TeV, nearly 35k $\overline{\text{d}}$, 120 $\overline{\text{t}}$, and 700 $^3\overline{\text{He}}$ candidates are observed. However, for pp collisions at $\sqrt{s} = 7$ TeV, we observed about 20k $\overline{\text{d}}$, 20 $\overline{\text{t}}$, and 20 $^3\overline{\text{He}}$ candidates. The final p_t spectra of identified nuclei and anti-nuclei are obtained by correcting the raw spectra for reconstruction efficiency and detector acceptance. For this simulation study is required which is discussed in the following section.

6.6   Efficiency Correction

To obtain the final p_t spectra of nuclei and anti-nuclei, the raw spectra has to be corrected for the the tracking efficiency and acceptance. For anti-nuclei spectra, the annihilation correction has to be taken into account. For all these corrections, the nuclei or anti-nuclei are generated by the event generators and propagated through the detector material modeled as realistically as possible. The ratio of total reconstructed to incident particles gives the combined efficiency and acceptance for nuclei and also annihilation for anti-nuclei. The simulation of nuclei and anti-nuclei is performed in the AliRoot framework. The interaction of nuclei with the detector material is included in the Geant3. However, the annihilation effect of anti-nuclei in the ALICE detector material is not implemented in Geant3.

1. **Pb-Pb collisions:**

   The various nuclei efficiency for Pb-Pb collisions (heavy-ion collisions) at $\sqrt{s_{NN}} = 2.76$ TeV are calculated by generating minimum bias parametrized HIJING event which include one d, $\bar{\text{d}}$, t, $\bar{\text{t}}$, ^{3}He, $^3\overline{\text{He}}$, ^{4}He and $^4\overline{\text{He}}$ in each event. Since we generate large number of particles ~ 2000 in HIJING at the mid-rapidity region, the inclusion of 8 nuclei at a time does not distort the basic property of the generated events. The Monte-Carlo production number 'LHC11b9_1' was requested for this simulation. In total 30k events were generated for this study. Generated particles are then passed through same detector (ALICE) material, as was present during real data taking time. This help to simulate dead and noisy channels of the detector. Full reconstruction chain is run over simulated events as is done for real data. Various nuclei tracks are looked into in the TPC region and same track selection cuts are applied as is done for real data. Efficiency is defined as the ratio of number of particles detected by a detector $(N_{p_t}^{det})$ to the number of particles incident within its area $(N_{p_t}^{inc})$.

   $$\epsilon_{p_t} = \frac{N_{p_t}^{det}}{N_{p_t}^{inc}} \tag{6.2}$$

   Figure 6.9 shows the efficiency$\times$acceptance of deuteron (top), triton (middle), and
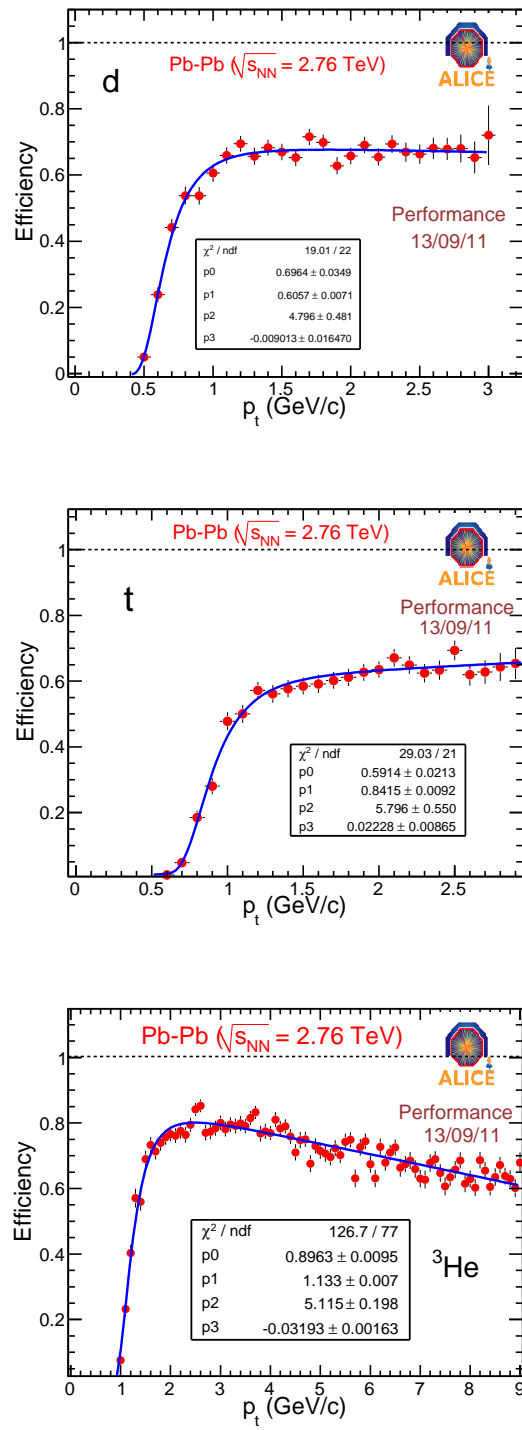
Figure 6.9: Efficiency×acceptance as a function of transverse momentum (p_t) for deuteron (top), triton (middle), and ^{3}He (bottom) in Pb-Pb collisions at $\sqrt{s_{NN}} = 2.76$ TeV.
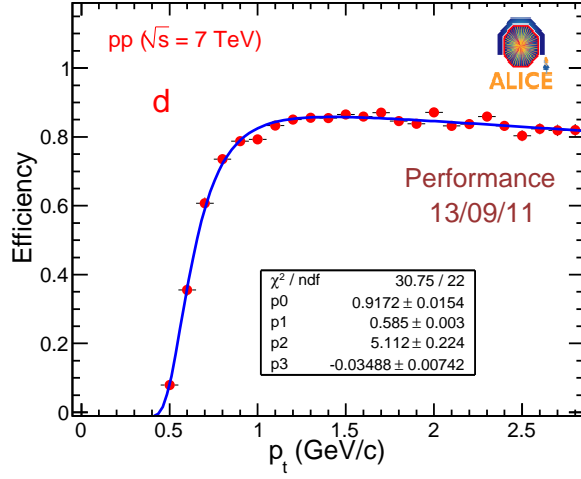
Figure 6.10: Efficiency×acceptance of deuteron (d) as a function of transverse momentum (p_t) for pp collisions at $\sqrt{s} = 7$ TeV.

^{3}He (bottom) as a function of transverse momentum (p_t) for Pb-Pb collisions at 2.76 TeV. The efficiency increases rapidly with increase in p_t for all three nuclei species and then become almost constant for $p_t > 1$ GeV/c, for deuterons and tritons. However, for ^{3}He, it shows small variation after $p_t = 3$ GeV/c. The curve represents the fit to the efficiency data points with functional form: $f(p_t) = p0\, e^{(-p1/p_t)^{p2}} + p3\, p_t$. Here, p0, p1, p2 and p3 are the fit parameters.

2. **pp collisions:**

   'LHC11c4' Monte Carlo production is used for efficiency calculation of the nuclei for pp collisions at $\sqrt{s} = 7$ TeV. The minimum bias PYTHIA generator (used for low multiplicity) is used to generate events which includes one nucleus in each event. The transverse momentum (p_t) of generated nuclei are randomly selected and are produced in the pseudo-rapidity range: -0.8 $\leq \eta \leq$ 0.8. In total 2 million events are generated and analyzed. Particles are transported through the ALICE material in AliRoot framework and full reconstruction chain is run. Figure 6.10 shows the deuteron efficiency×acceptance as a function of transverse momentum (p_t) for pp collisions at $\sqrt{s} = 7$ TeV. The curve is fit to the efficiency data points and has

the same functional form as used for the Pb-Pb collisions discussed above. The efficiency has similar p_t dependence for pp collisions at $\sqrt{s} = 7$ TeV as was obtained for Pb-Pb collisions at $\sqrt{s_{NN}} = 2.76$ TeV (Fig. 6.9).

6.6.1 Momentum Correction

The low momentum particles lose energy while traversing the detector material. The track reconstruction algorithm takes into account the Coulomb scattering and energy loss, assuming the pion mass for each particle. Therefore, a track-by-track correction for the energy loss of heavier particles ($d/\bar{d}$, $t/\bar{t}$ and ^{3}He/$^3\overline{\text{He}}$) is needed. This correction is obtained from Monte Carlo (MC) simulations, in which the p_t difference of reconstructed and MC track is plotted as function of p_t of reconstructed track.

Figure 6.11 shows the energy loss as function of reconstructed track momentum (p_t) for deuterons (top panel), tritons (middle panel) and ^{3}He (bottom panel). The lines represent the function fitted to the data points of the following form -

$$f(p_t) = A + B \left(1 + \frac{C}{p_t^2}\right)^D,$$ (6.3)

where A, B, C and D are the fit parameters. It can be seen that the p_t difference between the reconstructed and the MC track is more towards the lower p_t. The difference is large for the heavier nuclei (^{3}He). Similar energy loss correction is studied for pp collisions at $\sqrt{s} = 7$ TeV. For all the results presented in this chapter, the track p_t is corrected for this energy loss effect.

6.7 Corrected p_t spectra

After obtaining efficiency×acceptance as a function of p_t, the raw spectra are corrected point-by-point with these correction factors. We present the results for corrected spectra of nuclei in the following subsections.

6.7.1 Pb-Pb Collisions

The corrected spectra for nuclei are obtained and fitted with the Blast-Wave (BW) model [13, 20] to extract information about the collision dynamics or fireball. The BW
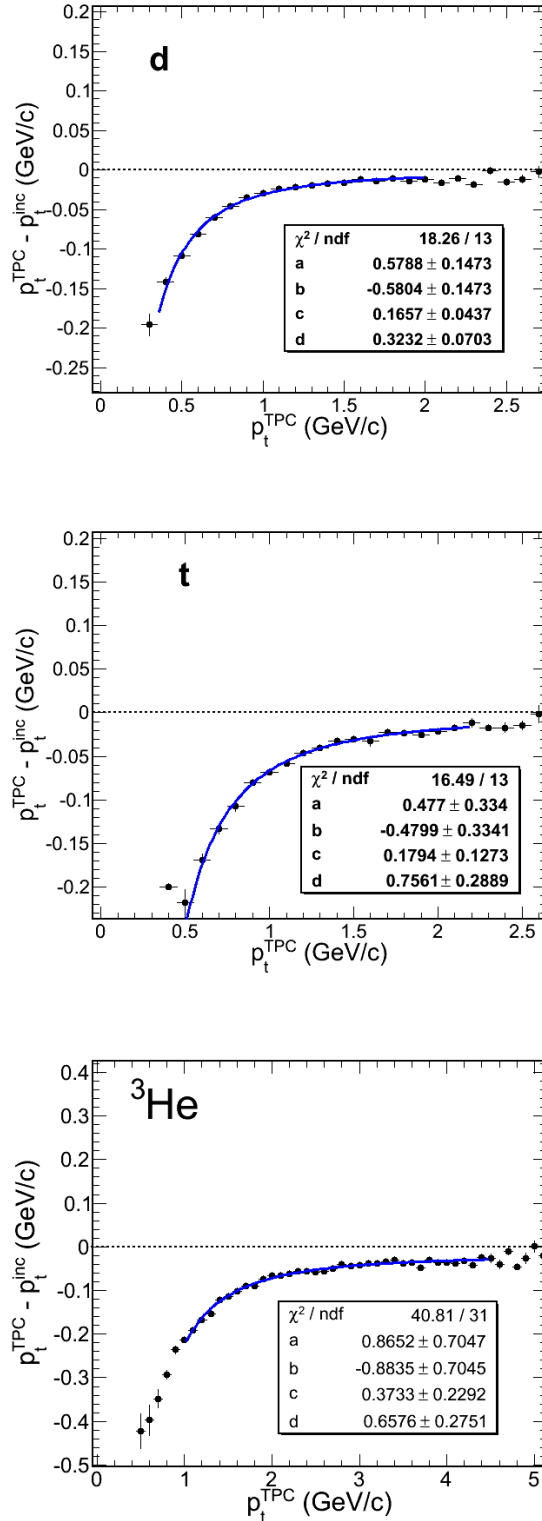
Figure 6.11: The p_t difference of reconstructed and MC track plotted as function of p_t of reconstructed track for deuterons (top panel), tritons (middle panel), and ^{3}He (bottom) for Pb-Pb collisions at $\sqrt{s_{NN}} = 2.76$ TeV. See text for the details.
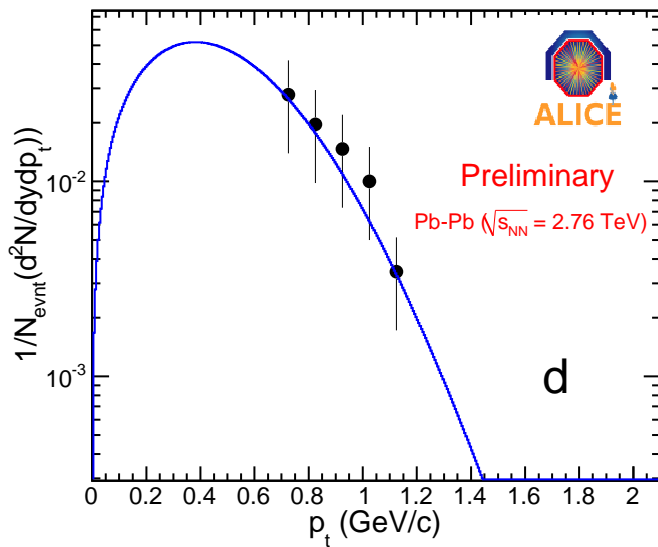
Figure 6.12: Deuteron spectra for Pb-Pb collisions at $\sqrt{s_{NN}} = 2.76$ TeV, fitted with the Blast-Wave function.

model was originally used for the production of hadrons, such as π, K, p, and Λ particles. The model successfully reproduced the momentum spectra and elliptic flow [21] of these particles as a function of transverse momentum and centrality [22]. In this section, the BW model is used to study the production of light nuclei instead of charged hadrons. The light nuclei are treated as heavier particles emitted from the fireball.

The BW model parametrizes the physical features, such as the temperature and geometric dimension of the fireball at the thermal freeze-out stage and gives quantitative predictions for the observable implications such as the transverse momentum spectra. This model calculates particle production properties by assuming, that the particles are emitted thermally on top of a expanding fireball after the collision. The BW model assumes local thermal equilibrium with an expansion velocity profile as a function of transverse radius, modulated by an azimuthal density distribution [22]. The model has the following functional form:

$$\frac{dN}{dp_t} \propto \int_0^R r\,dr\,m_t p_t I_0\left(\frac{p_t sinh\rho}{T_{Kin}}\right) K_1\left(\frac{m_t cosh\rho}{T_{Kin}}\right) \tag{6.4}$$

Here, various parameters are defined as
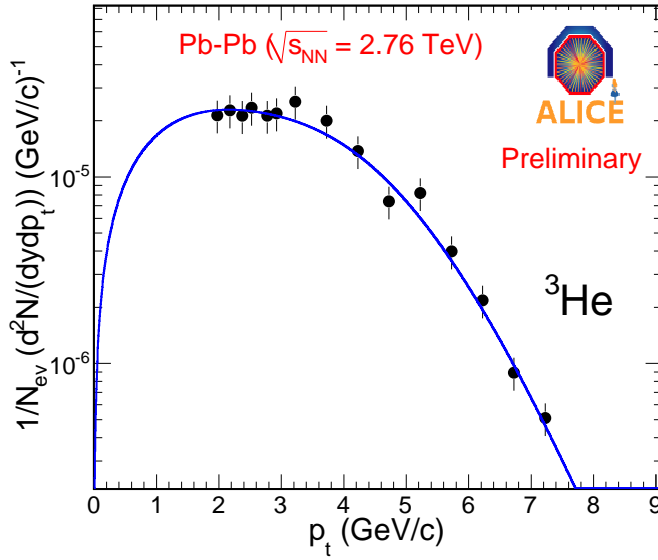
Figure 6.13: ^{3}He spectra for Pb-Pb collisions at $\sqrt{s_{NN}} = 2.76$ TeV, fitted with the Blast-Wave function.

- T_{kin} is the kinetic (thermal) freeze-out temperature;

- $\rho = tanh^{-1}\beta$ is a transverse boost;

- $\beta = \beta_S(r/R)^n$ is radial flow velocity;

- R is transverse geometric radius of the surface at the freeze-out;

- and n is velocity profile.

Figures 6.12 and 6.13 show the final spectra for deuterons and ^{3}He after efficiency and acceptance correction, respectively, for Pb-Pb collisions at $\sqrt{s_{NN}} = 2.76$ TeV. The slope of the deuteron spectra is greater than that of the ^{3}He spectra. The final yields are obtained as one of the BW fit parameters. In order to have the reasonable values of β, T_{kin}, and other parameters of BW fits, the fits have to be preformed simultaneously for different particle species. We fit each nuclei spectra individually and obtain dN/dy from that fit. The deuterons dN/dy is obtained as $7.3 \times 10^{-3} \pm 1.6 \times 10^{-3}$ while ^{3}He dN/dy is $4.3 \times 10^{-5} \pm 2.2 \times 10^{-6}$ for Pb-Pb collisions at $\sqrt{s_{NN}} = 2.76$ TeV.
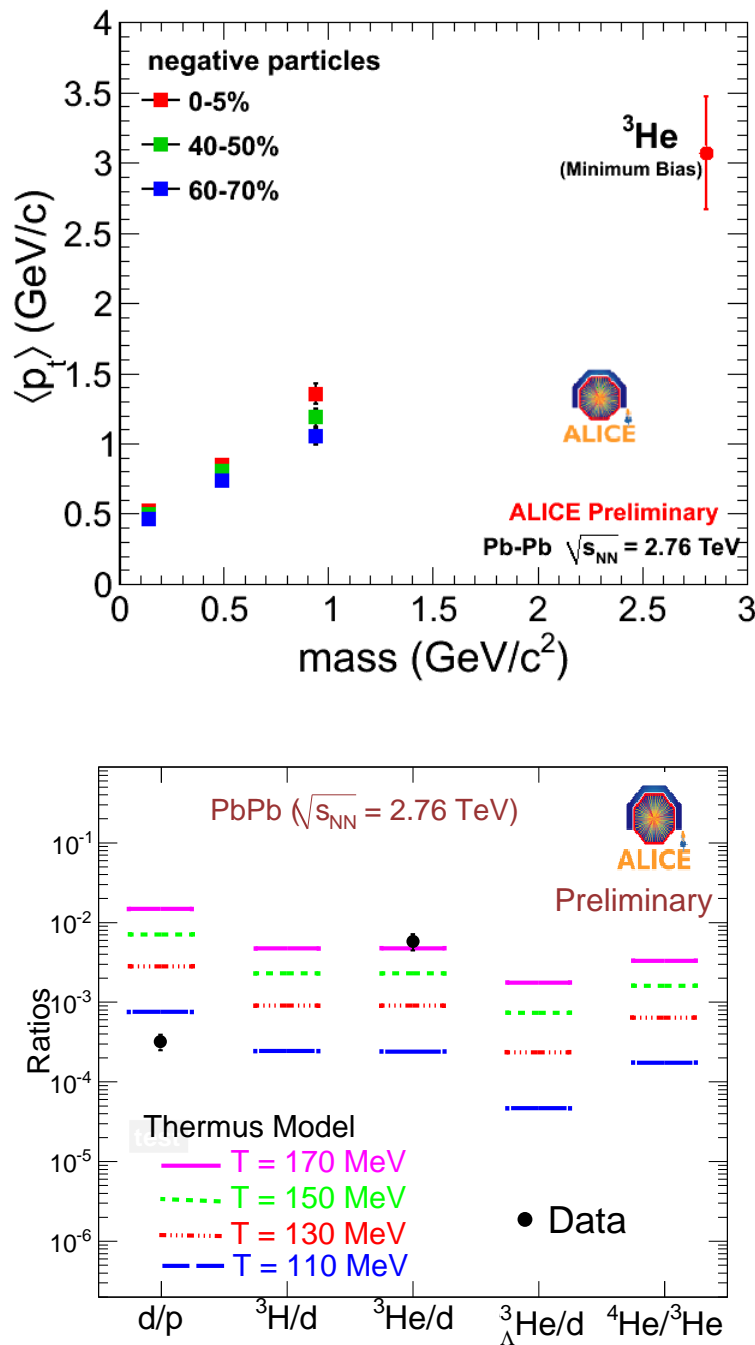
Figure 6.14: Top panel: Mean transverse momentum $\langle p_t \rangle$ as a function of mass for Pb-Pb collisions at $\sqrt{s_{NN}} = 2.76$ TeV. Bottom panel: Particle ratios using THERMUS [23] model for different freeze-out temperatures and their comparison with ALICE data for Pb-Pb collisions at $\sqrt{s_{NN}} = 2.76$ TeV.
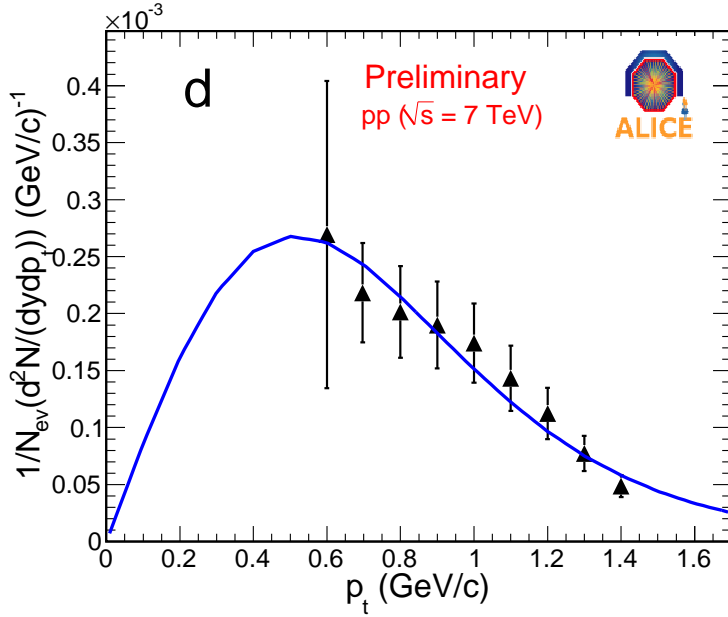
Figure 6.15: Deuteron corrected spectra for pp collisions at $\sqrt{s} = 7$ TeV fitted with the Levy function (see Eq. 6.5).

For ^{3}He, we also obtain the $\langle p_t \rangle$ value from the BW fit and compare with that of different particle species as shown in Fig. 6.14 (top panel). The figure shows that the $\langle p_t \rangle$ increases with increasing mass of the particle. That is, heavier the particle, larger will be it's $\langle p_t \rangle$. Figure 6.14 (lower panel) shows the various particle ratios fitted with the THERMUS model [23]. The details about the THERMUS model are discussed in the previous chapter. THERMUS model calculations are performed using the grand canonical formulation assuming different chemical freeze-out temperatures. The solid circles represent the data points from the ALICE experiment. The yields for deuteron and ^{3}He used for the ratios are from the analysis presented in this chapter for minimum bias collisions while that for proton (p) are used from the available dN/dy for 0–30% collision centrality which is very preliminary. From the figure, it can be seen that the ratio ^{3}He/d favours the higher chemical freeze-out temperature. However, the d/p ratio suggests the lower value. But it may be noted that the proton yields are only for 0–30% centrality and the minimum bias results will be needed for better comparison.

Table 6.2: Levy function fit parameters for deuteron spectra in Fig. 6.15 for pp collisions at $\sqrt{s} = 7$ TeV.

|		
1.	χ^2/ndf	2.9/6
2.	dN/dy	2.6e-04 $\pm$ 2.5e-05
3.	C	1.3e-01 $\pm$ 1.4e-02
4.	n	10.0 $\pm$ 7.95
5.	Mass	1.877 (fixed)
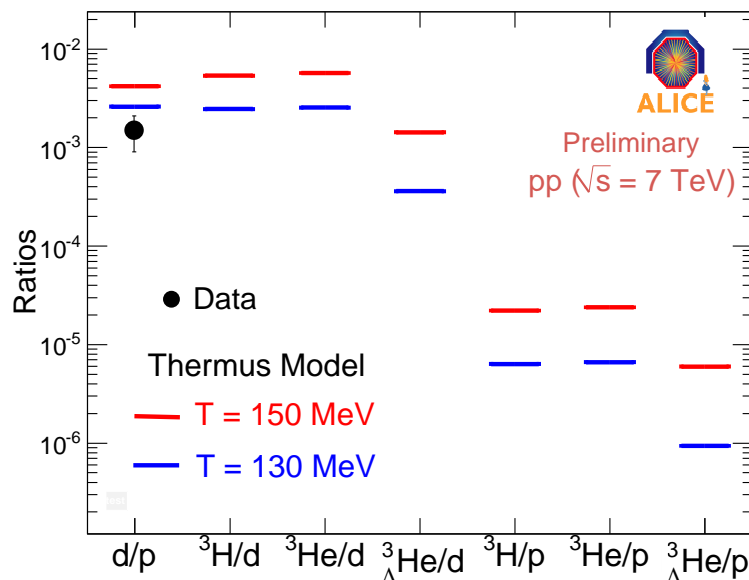
Figure 6.16: Particle ratios using THERMUS model and their comparison with ALICE data (d/p) ratio is shown for pp collisions at $\sqrt{s} = 7$ TeV.

6.7.2 pp Collisions:

After efficiency and acceptance corrections, the final spectra for deuterons is obtained for pp collisions at $\sqrt{s} = 7$ TeV and is shown in Fig. 6.15. The spectra for pp collisions is usually fitted with the Levy (or Tsallis) function [24, 25] as described below,

$$\frac{d^2N}{dp_t dy} = p_t \times \frac{dN}{dy} \frac{(n-1)(n-2)}{nC(nC+m_0(n-2))}(1 + \frac{m_t - m_0}{nC})^{-n} \tag{6.5}$$

Here the fit parameters are C, n and the yield dN/dy. m_0 is the mass of the particle (deuteron) in rest and m_t is transverse mass. The function is fitted well to the deuteron p_t spectra within the statistical errors and is used to extract the dN/dy. The obtained fit parameters are summarized in Table 6.2.

Figure 6.16 shows the particle ratios with different masses for pp collisions at $\sqrt{s} = 7$ TeV [8]. As for the Pb-Pb collisions discussed above, we use the THERMUS model for different predictions. Two different chemical freeze-out temperatures are used as the input parameters. The lines represent the predictions from the THERMUS model. The solid circle represents the data from the ALICE experiment. The yield for deuteron is used from the analysis discussed in this chapter while that for the proton is used from the published results [26]. The strangeness canonical formalism is used where, baryon-chemical potential (μ_B) is fixed using $\bar{p}/p$ ratio. The figure suggests that the data favours the lower chemical freeze-out temperature for pp collisions at $\sqrt{s} = 7$ TeV. Comparing Figs. 6.14 (lower panel) and 6.16 indicates that the chemical freeze-out temperature in pp collisions at $\sqrt{s} = 7$ TeV is lower compared to that for Pb-Pb collisions at $\sqrt{s_{NN}} = 2.76$ TeV.

6.8   Observation of Anti-alpha

The year 2011 is marked with the discovery of anti-alpha and was first reported by the STAR experiment [5, 17]. However, at the same time, the ALICE experiment also confirmed the anti-alpha observation [16], which forms the part of the analysis presented in this chapter. The analysis details are discussed below.

The parametrized Bethe-Bloch curve is used to identify anti-alpha ($^4\overline{\text{He}}$ or $\bar{\alpha}$) from
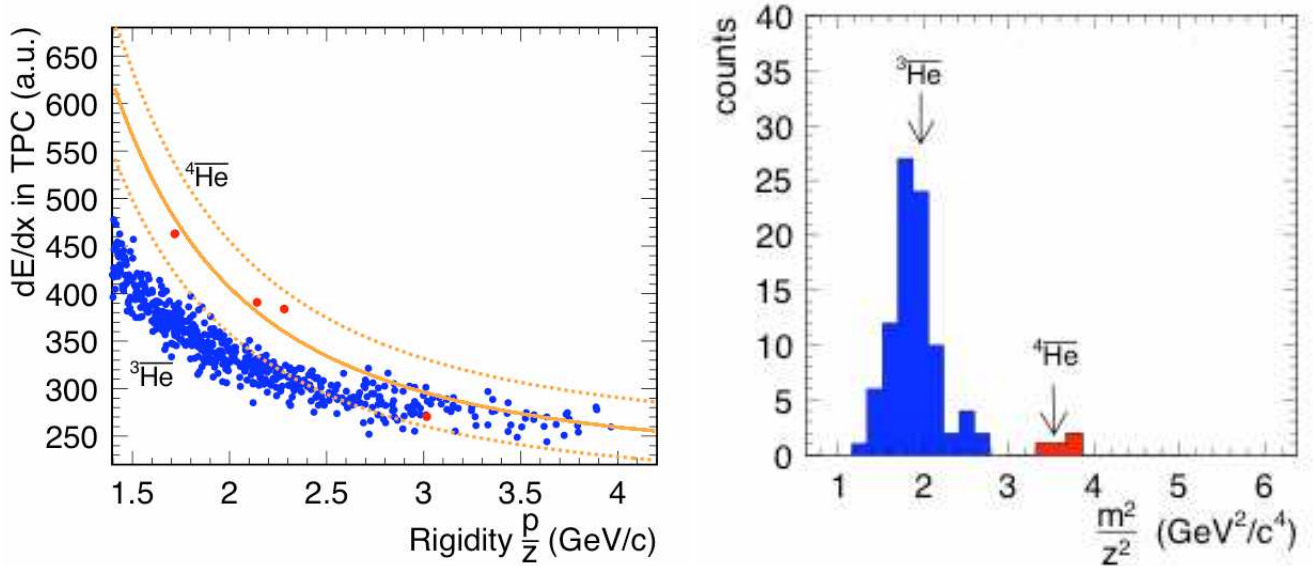
Figure 6.17: Show anti-Alpha ($^4\overline{\text{He}}$) identification; Left plot: Specific energy loss (dE/dx) vs. rigidity for TPC tracks, identified anti-alpha are shown as red points; Right plot: Mass spectrum obtained using TPC and TOF information.

their specific energy loss (dE/dx) vs. rigidity plot in Pb-Pb collisions at $\sqrt{s_{NN}} = 2.76$ TeV, as discussed in Section 6.3 and shown in Fig. 6.1. The left plot of Fig. 6.17 shows negatively charged TPC tracks as blue points, Bethe-Bloch curve parametrised for $^4\overline{\text{He}}$ as orange solid line with dotted lines representing 2-sigma (2σ) band around $^4\overline{\text{He}}$ line. As illustrated in the figure, three anti-alpha ($^4\overline{\text{He}}$) candidates are clearly identified below 2.4 GeV/c rigidity value and are shown as red points.

Since for higher rigidity region $^4\overline{\text{He}}$ and $^3\overline{\text{He}}$ tracks start merging, the Time-Of-Flight (TOF) detector is used to identify $^4\overline{\text{He}}$ in this region. The TOF detector measures time taken (t) by the particles to travel a distance (L) from primary vertex to the TOF detector where they are detected. This gives velocity ($v = L/t$) of the particle. By combining the information of momentum (p) from the TPC detector and velocity (v) from the TOF detector, one can determine the mass (m) of the particle using following formula:

$$m = \frac{z.R}{\sqrt{\gamma^2 - 1}} \tag{6.6}$$

Here, z represents the charge of the particle while R represents it's rigidity (p/z).

Right plot of Fig. 6.17 shows the final mass spectrum obtained with TPC and TOF
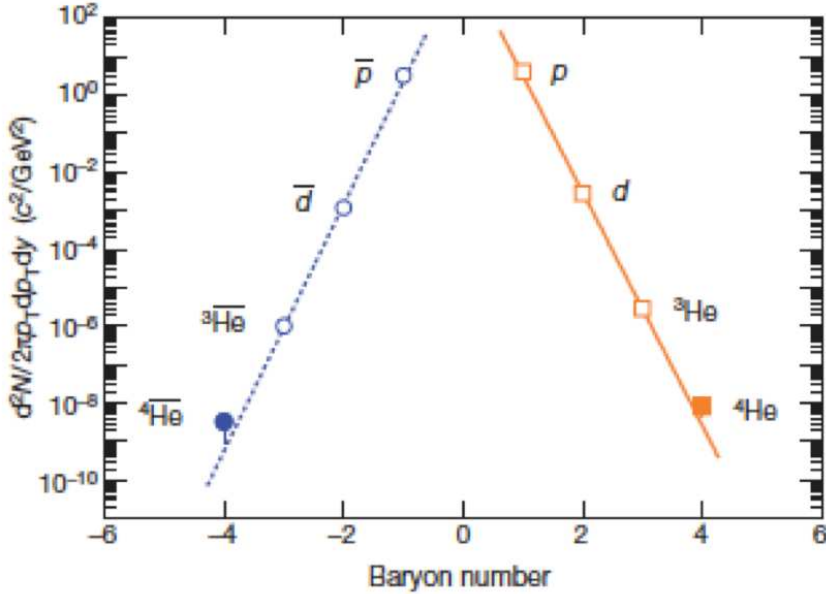
Figure 6.18: Differential invariant yield as a function of baryon number for Au-Au collisions at 200 GeV, measured by the STAR experiment.

showing four visible candidates of $^4\overline{\text{He}}$. Due to large annihilation cross-section for anti-alpha, energy loss, and dead zones in the TOF, not all the TPC tracks give signal in the TOF detector. Hence only two $^4\overline{\text{He}}$ counts are observed in the TOF detector. The mass m for the remaining two candidates are determined based on the mass scaling of the energy loss using inverse function of the Bethe-Bloch parametrisation (Eq. 6.1). The right panel shows all the four $^4\overline{\text{He}}$ candidates using TPC+TOF information. These four anti-alpha candidates are obtained from the 16.5×10^6 triggered events recorded during the first heavy-ion run of the ALICE experiment in the year 2010 for Pb-Pb collisions at $\sqrt{s_{NN}} = 2.76$ TeV.

While the ALICE experiment with only first phase of data taking has found 4 anti-alpha candidates [16], the STAR experiment has observed 18 candidates of anti-alpha in one billion events and reported in the Ref. [5]. Figure 6.18 shows the exponential invariant yields of various particles/nuclei and antiparticles/antinuclei versus baryon number in Au-Au collisions at 200 GeV measured by the STAR experiment. The lines represent the fits with the exponential formula $\propto e^{-r|B|}$ for the negatively and positively charged

particles/nuclei separately, where r is the production reduction factor.

In a coalescence model, the light nucleus produced in the relativistic heavy-ion collision is produced during the last stage of the collision process. The quantum wave functions of the constituent nucleons close enough in momentum and coordinate space will overlap and produce the nucleus. The production rate for a nucleus with baryon number B exhibits the exponential behavior as a function of B. In the thermodynamic model, a nucleus is assumed to have energy $E \approx |B|m_N$, where m_N is the nucleon mass. The production rate is determined by the Boltzman factor $e^{-E/T}$, where T is the temperature. The nuclei yield predicted by this model also goes as exponential.

It is found that the production rate of (anti) particles/(anti) nuclei reduces by a factor of $1.6^{+1.0}_{-0.6} \times 10^3$ and $1.1^{+0.3}_{-0.2} \times 10^3$ for each additional antinucleon and nucleon respectively. This trend is also expected from the coalescent nucleosynthesis models as well as from thermodynamic models. From the consistency of the measurements with thermodynamic and coalescent production, one could predict the yield of the next stable antimatter nucleus in the line ($B = -6$) which is found out to be 2.6×10^6 compared to anti-helium4. Therefore, the sensitivity of current space-based charged particle detectors (e.g. BESS, PaMela, and AMS) is below what would be needed to observe antihelium produced by nuclear interactions in the cosmos, and consequently, any observation of antihelium or even heavier anti-nuclei in space would indicate the existence of a large amount of antimatter elsewhere in the Universe.

6.9 Summary

The first measurements of the nuclei and anti-nuclei production ($d/\bar{d}$, $t/\bar{t}$, and $^3\text{He}/^3\overline{\text{He}}$) in the ALICE experiment at the LHC, for pp and Pb-Pb collisions at $\sqrt{s} = 7$ TeV and $\sqrt{s_{NN}} = 2.76$ TeV, respectively, are presented. This is the first observation of ^3He and $^3\overline{\text{He}}$ candidates by any experiment in the pp (or elementary) collisions. The analysis technique for the identification of (anti) nuclei are presented in details for pp and Pb-Pb collisions in the ALICE experiment. The procedure to reject the background in the nuclei yield due to the interactions from the material and beam pipe, is also presented. The simulation

study is done employing the ALICE simulation framework to obtain the efficiency and acceptance factors to correct the spectra.

The results from the preliminary spectra presented in this chapter, suggest that the deuteron yields in Pb-Pb collisions at $\sqrt{s_{NN}} = 2.76$ TeV is nearly ten times greater than that in pp collisions at $\sqrt{s} = 7$ TeV. The comparison of experimentally obtained ratios of various nuclei and anti-nuclei are done with thermal model predictions. The comparison suggests a higher values of chemical freeze-out temperature in Pb-Pb collisions compared to that in pp collisions.

The observation of anti-alpha by the STAR experiment is re-confirmed, almost at the same time, by the analysis presented in this chapter. While STAR observed 18 counts for the anti-alpha in one billion events, the ALICE experiment observed 4 counts from 16.5 M events collected during its first run.

Bibliography

[1] G. Lemaître Annales de la société Scientifique de Bruxelles **47** (1927) 49.

[2] A. Yamamoto *et al.* Adv. Space Res. **Vol. 14 No. 2** (1994) 75

[3] V. Bonicini *et al.* Nucl. Inst. and Meth. in Phys. Res. A **461** (2011) 262.

[4] J. Alcaraz *et al.* Phys. Lett. B **461** (1999) 387.

[5] H. Agakishiev *et al.* (STAR Collaboration), Nature **473** (2011) 353.

[6] B. Wiebel-Sooth, P. Biermann, and H. Meyer, Astron. Astrophys **330** (1998) 389.

[7] I. Kraus, J. Cleymans, H. Oeschler, K. Redlich, and S. Wheaton, arXiv:0902.0873 [hep-ph].

[8] J. Cleymans, S. Kabana, I. Kraus, H. Oeschler, K. Redlich, and N. Sharma, arXiv:1105.3719v1 [hep-ph].

[9] J. Cleymans, S. Kabana, I. Kraus, H. Oeschler, K. Redlich, and N. Sharma, arXiv:1107.0450v1 [hep-ph].

[10] R. Arsenescu *et. al.* (NA52 Collaboration), New J. Phys. **5** (2003) 150.

[11] J. Cleymans, S. Wheaton, H. Oeschler, and K. Redlich, Phys. Rev. C **73**, (2006) 034905.

[12] J. Cleymans, and H. Satz, Z. Phys. C **57** (1993) 135.

[13] B. I. Abelev *et al.* (STAR Collaboration), Phys. Rev. C **81** (2010) 024911; B. I. Abelev *et al.* (STAR Collaboration), Phys. Rev. C **79** (2009) 034909.

[14] K. Aamodt *et al.* (ALICE Collaboration), Eur. Phys. J. **C71** (2011) 1655.

[15] B.I. Abelev *et. al.* (STAR Collaboration), Science **328** (2010) 58 .

[16] N. Sharma for ALICE Collaboration, Proceeding for Quark Matter Conference 2011, Annecy, France, arXiv:1109.4836v1 [nucl-ex]; A. Kalweit for ALICE Collaboration, Proceeding for Quark Matter Conference 2011.

[17] L. Xue for STAR Collaboration, Proceeding for Quark Matter Conference 2011, Annecy, France.

[18] H. Bichsel, Nucl. Inst. Meth A. **562** (2006) 154.

[19] N. Sharma for ALICE Collaboration, Proceeding for ICPAQGP Conference 2010, Goa, India, arXiv:1104.3311v2 [nucl-ex].

[20] E. Schnedermann *et al.*, Phys. Rev. C **48** (1993) 2462.

[21] B. I. Abelev *et. al.* (STAR Collaboration), Phys. Rev. Lett. **97** (2006) 152301.

[22] F. Retiere and M. A. Lisa, Phys. Rev. C **70** (2004) 044907.

[23] S. Wheaton, J. Cleymans, and M. Hauer, Comp. Phys. Comm. **180** (2009) 84.

[24] C. Tsallis, J. Stat. Phys. **52** (1988) 479.

[25] B.I. Abelev *et. al.* (STAR Collaboration), Phys. Rev. C **75** (2007) 064901, arXiv:nucl-ex/0607033.

[26] K. Aamodt *et al.* (ALICE Collaboration), Phys. Rev. Lett. **105** (2010) 7.